UNIVERSITY OF OXFORD

DEPARTMENT OF ENGINEERING SCIENCE

HYBRID THIN-FILM SOLUTION-PROCESSED LIQUID CRYSTAL LASERS

TAIMOOR ALI

Wolfson College



Michaelmas 2020

A thesis submitted for the degree of Doctor of Philosophy

Department of Engineering Science

University of Oxford

Abstract

HYBRID THIN-FILM SOLUTION-PROCESSED LIQUID CRYSTAL LASERS

by TAIMOOR ALI

The ultimate goal of this thesis is to use low-cost processing techniques to create thin film lasers that are compact in form, exhibit low excitation threshold fluences, and demonstrate the potential for wavelength tuning when the laser is subjected to external stimuli. This thesis explores the use of a combination of liquid crystalline materials and organic & inorganic gain media to fabricate the thin film lasers, which could potentially be important for future bio-medical sensing devices, spectroscopy applications, virtual and augmented reality displays, and environmental sensors. This thesis can be broadly divided into three parts: 1) to investigate the electro-optic properties of novel liquid crystalline materials that could be used to form the optical cavity of these thin film lasers; 2) to employ the use of novel gain materials in the form of perovskite nanocrystals to create photostable liquid crystal (LC) lasers; and 3) to develop thin film lasers with new functionality such as beamsteering through mechanical deformation and polarisation control with the addition of a second LC layer.

Experiments were designed and constructed so as to study the physical parameters, such as the birefringence, elastic and dielectric constants, and the flexoelastic ratio of a newly developed LC dimer. The dimer is found to exhibit a large flexoelastic ratio (2.59 $\approx$ 2.60 V^{-1}) and high birefringence ($\Delta n = 0.312$) that enables it to be used to create fast switching photonic devices at low driving voltages, such as full 2π phase modulators. Furthermore, the high birefringence also makes it desirable for low excitation threshold and wavelength tuneable band-edge LC devices.

The birefringence characteristics and periodic structure of the chiral nematic LC phase, along with its compatibility with solution processing techniques, makes them exciting candidates for thin-film laser devices. As a result, this Thesis aims to explore potential fabrication processes that could be used to disperse alternative gain materials in the form of perovskite nanocrystals ($CsPbI_3$ and $CsPbI_2Br$, $\lambda_{em} = 675 \pm 2$ nm, size = 10 $\sim$ 15 nm) into a chiral nematic LC host. Combining these inorganic and organic semiconducting materials with LC host materials could open up new possibilities in terms of a route towards an electrically pumped LC laser. Therefore, a detailed study is presented on the dispersion of perovskite nanocrystals in nematic and chiral nematic LCs by employing various processing techniques. Results show that for all of the techniques considered in this thesis, nanocrystal aggregates form, which in some cases can lead to an alteration of the emission characteristics. It is believed that the alteration in the emission characteristic is potentially due to a disintegration of the perovskite structure. For several of the processes considered in this work, little to no alteration in the emission spectrum is observed, which indicates that the perovskite structure has remained intact during the dispersion process. Furthermore, thin-films of perovskite (both in the form of a bulk layer and nanocrystals) have also been employed to create a Defect-Mode LC laser structure. After optimising the material combination and fabrication process, a defect-mode structure with perovskite nanocrystals is developed which is found to exhibit multi-mode laser emission.

A novel flexible defect-mode laser is also demonstrated in this Thesis by using a photo-polymerised chiral nematic LC and a laser dye that forms a stack CLC/Barrier/Dye doped PMMA/Barrier/CLC. This laser, which is the first demonstration of a flexible defect-mode laser, is fabricated using a film transfer technique on a transparent flexible polymer. The results show evidence of single mode emission at a wavelength of 582 nm and a low fluence excitation threshold of $12.3\mu J/cm^2$/pulse when optically pumped with a solid-state laser. By the virtue of the mechanical flexibility, the LC laser shows a beam steering phenomenon of up to 42° when the laser is deformed and scanned with a pump laser. Such lasers are potentially useful for creating 3D imaging systems that negate the need for additional optical components.

To conclude this Thesis, a polarisation controllable band-edge LC laser device is presented that shows on-demand control of the polarisation state of the laser using an in-plane electrode configuration combined with a nematic LC layer. The optical anisotropy coupled with the orientation of the electric field results in a laser polarisation along a certain direction. With the use of the in-plane electrode assembly, it is possible to control the polarisation states of light that passes through the device. The device can control the polarisation state of a LC band-edge laser by generating circular and elliptical polarisation with any desired orientation. However, achieving a linear polarisation state was found to be challenging. These polarisation manipulators are potentially important for various imaging applications ranging from the biomedical to the entertainment industries.

"This place is a dream. Only a sleeper considers it real. Then death comes like dawn, and you wake up laughing at what you thought was your grief."

Rumi

To Maa, Baba, my beloved wife, Hira,
& lovely daughter, Manal…

Acknowledgements

First and foremost, I want to express my gratitude to my academic supervisors, Prof Stephen Morris and Prof Steve Elston for giving me an incredible opportunity to come and join SPM and to study at Oxford. Steve M, from the beginning of my studies at Oxford, has kindly been advising me for both my research and non-academic activities. Steve E who has genuinely changed my perception about a professor – has always been there whether I was struggling to understand a theoretical concept or building an experiment. I am very thankful to both of them for always patiently listening to my queries and steering me in the right direction.

I am indebted to my funding organisation, Punjab Educational Endowment Fund (PEEF) for offering me scholarship to study at Oxford and to the Noon Educational Foundation for their generous partial award that helped me in many ways to meet the financial liabilities during my studies.

I must mention Jia-De who had a huge contribution and support during my studies, from discussing novel research ideas to planning the career prospects. I take pride in sharing co-authorship with him. I am also thankful to Olivia, who kindly provided me with perovskite nanocrystals throughout my DPhil. I appreciate her friendly and cooperative behaviour. To my dear friend, Waqas Kamal, for being a humble and kind soul, and an incredible friend who diligently supported me especially during the difficult time of COVID-19 lockdown. I am also thankful to John for being a knowledgeable and honest peer, who was always a help and to Xiuze (Lake) with whom I had a remarkable and productive research collaboration. David and Ellis, you have been incredibly fun persons working in science, I wish both you good luck for your future endeavours. Chole and Serena, I am grateful to both of you for everything from teaching me sample preparation to maintaining a lively social life in the group. To Paul, thank you for help in my research and always welcoming me to work with you; to Julian, for his support in both my research and career advice. Yihan and Andrew, although we spent little time together, I send my best wishes and good luck for your DPhil. Indeed, thanks to Patrick and Asad for their support for using research tools in their labs and to Abhijeet for chatting over lunches.

To my Oxford family that includes, Dr Adeel, Mohsin, Sarah, Humayun Uncle, Talha, Arslan, Iris, Niyati, Yasir, Ali & family. Together with them, Oxford was home away from home. My deepest and special gratitude to Ayesha for her wise advices, moral support, company and being an amazing host in Glasgow.

To one of the most important persons in my life – my beloved wife, Hira. Thank you, for your love and emotional support in every situation and making my time in Oxford unforgettable. To Manal, my lovely daughter, who was born during my DPhil and making the stressful days full of fun with her cackles.

Last but not least, to my Maa and Baba, who grew older making me who I am today. They enabled me to be the first in my entire family to attend a formal university and always supported me despite not understanding my work I find myself at a loss for words to express my gratefulness to them, and I wish I could ever repay them. My love and thanks to my brother, Sharyar, who has been the greatest support for me. To my three beloved sisters, who always cheer me up in my difficult times and to my parents-in-law, who guided and believed in me.

Contents

Abstract i

Publications x

Abbreviations xii

Symbols xiii

1 Introduction 1
- 1.0.1 Chapter Two . . . 2
- 1.0.2 Chapter Three . . . 3
- 1.0.3 Chapter Four . . . 3
- 1.0.4 Chapter Five . . . 4
- 1.0.5 Chapter Six . . . 4
- 1.0.6 Chapter Seven . . . 5
- 1.0.7 Chapter Eight . . . 5
- 1.0.8 Chapter Nine . . . 6

2 Background 7
- 2.1 Introduction to Liquid Crystals . . . 7
  - 2.1.1 LC mesophases . . . 8
    - 2.1.1.1 Nematic LC . . . 8
    - 2.1.1.2 Smectic phase . . . 10
    - 2.1.1.3 Chiral nematic phase . . . 11
    - 2.1.1.4 Blue phase . . . 12
    - 2.1.1.5 Optical indicatrix . . . 13
    - 2.1.1.6 Photonic bandgap in chiral nematic LCs . . . 14
    - 2.1.1.7 Dielectric anisotropy . . . 16
    - 2.1.1.8 Fréedericksz transition . . . 17
    - 2.1.1.9 Other physical properties . . . 18
- 2.2 Laser . . . 19
  - 2.2.1 Laser construction . . . 19
  - 2.2.2 Liquid Crystal (LC) laser . . . 20
    - 2.2.2.1 Band-edge LC laser . . . 21
    - 2.2.2.2 Defect-mode LC laser . . . 22
  - 2.2.3 Emission process in a laser system . . . 25
  - 2.2.4 Jablonski diagram . . . 27
  - 2.2.5 Gain media . . . 29
    - 2.2.5.1 Organic laser dyes . . . 30
    - 2.2.5.2 Quantum dots . . . 32
  - 2.2.6 Functionality . . . 33
  - 2.2.7 Emission characteristics . . . 34

2.2.8 Summary . . . 35

3 Experimental Procedures **37**
3.1 Liquid Crystal Cell . . . 37
3.1.1 Planar aligned LC cell . . . 39
3.1.2 Homeotropic LC cell . . . 40
3.1.3 Chiral LC mixture preparation . . . 42
3.2 Solution Processing Techniques . . . 43
3.3 Characterisation techniques . . . 45
3.3.1 UV-Visible spectrophotometer . . . 45
3.3.2 Optical Polarising Microscopy . . . 48
3.3.3 Optical Fluorescence Microscopy . . . 51
3.3.4 Transmission/Reflection of Chiral Nematic LC Films . . . 52
3.3.5 Photoexcitation of Emissive Liquid Crystal Samples . . . 54
3.3.6 Liquid Crystal Laser Experiments . . . 56
3.3.6.1 Laser Beam Profile and Propagation . . . 56
3.3.6.2 Knife – Edge Measurements of beam waist . . . 57
3.3.6.3 Pump Laser Parameters . . . 58
3.3.6.4 LC Laser characterisation . . . 60
3.4 Summary . . . 62

4 Electro-Optical Study of a New LC Dimer **63**
4.1 Material background . . . 64
4.1.1 Material synthesis . . . 65
4.1.2 Textures and phase identification . . . 66
4.2 Birefringence measurement . . . 67
4.2.1 Background on Berek compensator . . . 67
4.2.1.1 Standard method . . . 68
4.2.1.2 Transmission spectrum method . . . 69
4.2.2 Δn measurement for E7 . . . 71
4.2.2.1 Transmission spectra with Berek compensator . . . 71
4.2.2.2 Standard compensation method . . . 76
4.2.3 Birefringence of the LC dimer . . . 78
4.2.3.1 Temperature dependency of the birefringence . . . 79
4.3 Fréedericksz measurement . . . 81
4.4 Dielectric measurements . . . 84
4.5 Flexoelectro-optic theory . . . 85
4.5.1 Flexoelectro-optic tilt angle (ϕ) measurement . . . 91
4.5.1.1 Rotation method . . . 91
4.5.1.2 Modulation method . . . 92
4.5.2 Flexoelectro-optic measurement of the LC dimer . . . 93
4.6 Conclusion . . . 95

5 Perovskite Nanocrystals for Band Edge LC Lasers **97**
5.1 Introduction . . . 97
5.2 Perovskite Nanocrystals . . . 99
5.3 Ultrasonic Dispersion . . . 104
5.4 Thermal Dispersion . . . 111
5.5 Dispersion at Room Temperature . . . 114
5.6 Summary . . . 121

6 Towards Perovskites Defect-Mode LC Lasers **123**
6.1 Defect-mode structure . . . 123
6.1.1 Background on the simulations of the Defect-mode . . . 124
6.1.2 Simulation on isotropic defect layer in Defect-Mode configuration 127
6.2 Defect-mode structure using bulk perovskite . . . 130
6.3 Defect-mode structure using perovskite nanocrystals . . . 137
6.3.1 Defect-mode structure with printed CLCs . . . 138
6.3.2 Defect-mode structure using delamination . . . 142
6.4 Summary . . . 151

7 Flexible Defect-Mode Laser **153**
7.1 PM597 Laser Dye . . . 154
7.2 Device fabrication and characterisation . . . 156
7.2.1 Spin-coating CLC films . . . 157
7.2.2 Delamination process . . . 158
7.2.3 Dye-doped NLC defect layer . . . 158
7.2.3.1 Flexible laser with no barrier layer . . . 163
7.2.3.2 Flexible defect-mode laser with a barrier layer . . . 165
7.2.3.3 Beam steering . . . 172
7.2.4 Summary . . . 175

8 Polarisation Controllable Band-Edge LC Laser **177**
8.1 Waveplate . . . 178
8.1.1 A tuneable waveplate . . . 181
8.1.2 A tuneable LC waveplate . . . 184
8.2 In-plane switching device . . . 192
8.2.1 IPS Device Preparation . . . 195
8.2.2 Polarisation controllability with an LC IPS device . . . 199
8.3 Polarisation Controllable Band-Edge LC Laser . . . 202
8.4 Summary . . . 209

9 Conclusion and Future Work **211**
9.1 Optical Characteristics of a Novel LC Dimer . . . 211
9.2 Perovskites for LC Lasers . . . 213
9.3 Thin-film flexible laser . . . 216
9.4 Polarisation Controllable LC laser . . . 217

A High Birefringence LC Dimer **219**
A.1 Twist-Bend Nematic ($N_{TB/X}$) phase of LC . . . 219

B Towards Defect-Mode LC Laser **220**
B.1 Material details on the printed LC . . . 220
B.1.1 Paliocolor® LC 242 (Nematic phase) . . . 220
B.1.2 Paliocolor® LC 756 (Chiral Dopant) . . . 220

C Polarisation Controllable Laser **221**
C.1 Signal and Reference waveforms . . . 221
C.2 Field estimation . . . 223
C.3 Linearity test of Nd:YAG pump laser . . . 223

Bibliography **224**

List of Tables

2.1 Photo-physics of different laser dyes (Rhodamine dyes: Rh-123 & Rh-B), 4-dicyanomethylene-2-methyl-6-p-dimethylamino-styryl-4H-pyran (DCM), Coumarin 151 (C-151) and Pyrromethene 597 (PM597)) in different solvents. 31
2.2 The fluence excitation threshold in band-edge and defect-mode LC laser configurations created with different dyes. 35

4.1 Phase behaviour of the LC dimer (compound 7). Temperatures in °C. . . . 66
4.2 The comparison of the ratio of the Frank (elastic) constants for the LC dimer compound-7 (measured at 140°C) with other nematic LCs. 83
4.3 Comparison of the measured flexo-elastic ratio for the LC dimer (compound 7) with other LC materials. Measurement for the compound 7 were carried at 140°C. 95

5.1 Summary of results showing the approximate cluster diameter of perovskite nanocrystals in nematic (NLC) and chiral nematic (CLC) mixtures prepared with different methods. 122

7.1 Photo-physics of Pyrromethene PM597 dye in a range of different solvents*. 155

C.1 The estimate of the applied voltage on the four electrodes (A, B, C and D) of the IPS device to generate the field in different orientations. 223

Publications

1. **Taimoor Ali**, Chris Welch, Julian Fells, Steve Elston, Stephen Morris, Georg H. Mehl, "Birefringence & Flexoelectro-optic Study of a High Birefringent Liquid Crystal Dimer." [In-submission]

2. **Taimoor Ali**, Jia-De Lin, Stephen Morris, Steve Elston, "Polarisation Controllable Liquid Crystal Band-Edge Laser." [In-submission]

3. **Taimoor Ali**, Jia-De Lin, Benjamin Snow, Xiuze Wang, Steve J Elston and, Stephen M Morris, "A Thin-Film Flexible Defect-Mode Laser." *Advanced Optical Materials*, **8**, 1901891, 2020.

4. **Taimoor Ali**, Jia-De Lin, Steve J Elston and, Stephen M Morris, "Developing Flexible Liquid Crystal Defect-mode Lasers." *Proc. SPIE 11303, Emerging Liquid Crystal Technologies XV*, 113030Q, 2020.

5. Waqas Kamal, Jia-De Lin, Steve J Elston, **Taimoor Ali**, Alfonso A Castrejón-pita, and Stephen M Morris, "Electrically Tunable Printed Bifocal Liquid Crystal Microlens Arrays." *Advanced Materials Interfaces*, **7**, 2000578, 2020.

6. Xiuze Wang, Julian A. J. Fells, Yuping Shi, **Taimoor Ali**, Chris Welch, Georg H. Mehl, Timothy D. Wilkinson, Martin J. Booth, Stephen M. Morris, and Steve J. Elston, "A compact full 2π flexoelectro-optic liquid crystal phase modulator." *Advanced Materials Technology*, **11**, 2000589, 2020.

7. Xiuze Wang, Julian A. J. Fells, **Taimoor Ali**, Jia-De Lin, Chris Welch, Georg H. Mehl, Timothy D. Wilkinson, Martin J. Booth, Stephen M. Morris, and Steve J. Elston, "Transmissive flexoelectro-optic liquid crystal optical phase modulator with 2π modulation." *AIP Advances*, **10**, 055011, 2020.

8. Xiuze Wang, Julian A J Fells, Larry Yip, **Taimoor Ali**, Jia-De Lin, Chris Welch, Georg H Mehl, Martin J Booth, Timothy D Wilkinson, Stephen M Morris, and Steve J Elston, "Fast and low loss flexoelectro-optic liquid crystal phase modulator with a chiral nematic reflector." *Scientific Report*, **9**, 7016, 2019.

NB. Articles 5 – 8 are not related to this Thesis but are based on the collaborative work with the group members.

Conference presentations

1. **28th International Liquid Crystal Conference** (Poster)
   Lisbon, Portugal - July 2020
   "Polarisation Tuneable Liquid Crystal Laser"
   (Conference cancelled due to COVID-19)

2. **Materials Research Society** (Oral)
   Arizona, US - April 2020
   "Beam-steering with Comfortable Defect-Mode Liquid Crystal Laser"
   (Conference cancelled due to COVID-19)

3. **Emerging Liquid Crystal Technologies, SPIE Photonics West** (Invited Oral)
   San Francisco, US - April 2020
   "A Flexible Defect-Mode Liquid Crystal Laser"

4. **Materials Research Society** (Poster)
   Boston, US - Dec 2019
   "Photo-polymerised Defect-Mode Liquid Crystal Lasers"
   (Could not attend the conference due to late approval of US visa)

5. **University of Oxford Photonics Day**
   Oxford - April 2019 (Poster)
   "Laser Emission from a Dye-doped Nematic Liquid Crystal"

6. **University of Oxford Photonics Day**
   Oxford - April 2018 (Poster)
   "Towards the Liquid Crystal Lasers using Perovskites"

List of Abbreviations

Ab	**Ab**sorbance
AR	**A**ugmented **R**eality
ASE	**A**mplifid **S**pontaneous **E**mission
CCD	**C**harge **C**oupled **D**evice
CLC	**C**hiral **L**iquid **C**rystal phase
Cr	**C**r**y**stalline phase
CN	**C**ya**n**o
DoS	**D**ensity **o**f **S**tates
FWHM	**F**ull **W**idth **H**alf **M**aximum
He-Ne	**H**elium **N**eon
HTP	**H**elical **T**wisting **P**ower
HWP	**H**alf **W**ave **P**late
I or $\mathbf{I}_{so}$	**I**sotropic phase
IPS	**I**n **P**lane **S**witching
ITO	**I**ndium **T**in **O**xide
LASER	**L**ight **A**mplification by **S**timulated **E**mission of **R**adiation
LC	**L**iquid **C**rystal
LCD	**L**iquid **C**rystals **D**isplay
LED	**L**ight **E**mitting **D**iode
N	**N**ematic phase
NC	**N**ano**c**rystals
Nd:YAG	**N**eodymium-**d**oped **Y**ttrium **A**luminum **G**arnet
OPM	**O**ptical **P**olarising **M**icroscope
PBG	**P**hotonic **B**and **G**ap
PL	**P**hoto**l**uminescence
PLQE	**P**hoto**l**uminescence **Q**uantume **E**fficiency
PR	**P**hoto**r**esist
QD	**Q**uantum **D**ots
QWP	**Q**uarter **W**ave **P**late
RM	**R**eactive **M**esogen
SLM	**S**patial **L**ight **M**odulator
Sm	**S**mectic phase
TEM	**T**ransmission **E**lectron **M**icroscope
TN	**T**wisted **N**ematic
UV	**U**ltra**V**iolet
UV-Vis	**U**ltra**V**oilet-**V**isible spectrophotometer
ULH	**U**niform **L**ying **H**elix
USH	**U**niform **S**tanding **H**elix
VR	**V**irtual **R**eality
WP	**W**ave **P**late

List of Symbols

Symbol	Name	Unit
C	Capacitance	F
c	Concentration of chiral dopant	$wt.$ %
d	Thickness of LC device	µm
d_{bar}	Thickness of barrier layer	nm or μm
d_{CLC}	Thickness of CLC layer	nm or μm
d_{def}	Thickness of defect layer	nm or μm
E	Electric field strength	V/m
E_{th}	Excitation fluence	μJ/cm^2/pulse
$(e_1 - e_3/k_1 + k_3)$	Flexo-elastic ratio	V^{-1}
f	Free energy density	J/m^2
k_{11}, k_{22} or k_{33}	Splay/Twist/Bend elastic constant	N
n	Refractive index	Dimensionless
n_{avg}	Average refractive index	Dimensionless
n_o or $n_\perp$	Ordinary refractive index	Dimensionless
n_o or $n_\parallel$	Extra-ordinary refractive index	Dimensionless
$\mathbf{P}_{flexo}$	Flexoelectric polarisation	$-$
p	Pitch of CLC helix	nm
$\hat{\mathbf{n}}$	LC director	unit vector
V_{th}	Threshold driving voltage for planar LC device	V
V_{th}^{IPS}	Threshold driving voltage for IPS LC device	V
α	Orientation of analyser w.r.t. polariser	$^\circ$
β	Helical twisting power	μm^{-1}
χ	LC device azimuthal orientation w.r.t. analyser	$^\circ$
Δn	Birefringence	Dimensionless
$\Delta\epsilon$	Dielectric anisotropy	F/m
ϵ_o	Permittivity of free space	F/m
ϵ_r	Relative permittivity	Dimensionless
$\epsilon_\perp$	Perpendicular dielectric permittivity	F/m
$\epsilon_\parallel$	Parallel dielectric permittivity	F/m
η	Slope efficiency of laser	%
λ	Wavelength	nm
λ_{ab}	Maximum of absorbance wavelength	nm
λ_{em} or λ_{fl}	Maximum of emission wavelength	nm
λ_c	Centre wavelength of PBG	nm
λ_S	Short-edge of PBG	nm
λ_L	Long-edge of PBG	nm
ψ	Electric field orientation in IPS device	$^\circ$
τ	Lifetime	ns

Chapter 1

Introduction

Photonics can be broadly interpreted as relating to the generation, manipulation, transport, detection, and use of light. Light behaves as a wave while propagating in free-space but in certain circumstances acts as a particle with quantised energy, which can either be emitted or absorbed. Light-matter interactions are some of the most interesting phenomena that paves the way for the development of advance optoelectronic and photonic devices such as light emitting diodes and lasers. The possibility of laser emission has its origins with Albert Einstein who introduced the concept of stimulated emission in the early twentieth century followed by the pioneering experimental demonstration in 1960 by Theodore Maiman, which opened up a new prospective for photonic devices. Over the past half century, the continual development in the technology has progressed laser technology from huge sizes to compact packages in the form of micro-/nano-lasers that have revolutionised various industries from communications, manufacturing, robotics, sensors, biomedical diagnostics, consumer electronics to entertainment.

While the miniaturisation of laser technology enables its transition from high-tech research laboratories to everyday consumer applications, the fabrication of micro-/nano-lasers poses a number of challenges. To-date numerous micro-/nano-lasers have been proposed using inorganic semiconductor materials that are fabricated both with top-down and bottom-up techniques, requiring stringent processing conditions and sophisticated equipment that eventually leads to high device costs. In-contrast, solution processing techniques involve simple and cost-effective fabrication routes that offer new

functionality and thereby reduce the device cost. This unlocks the potential of finding alternative materials and exploring the processes that can bring about simple, cost effective and easy-to-deploy processing techniques for the realisation of micro-/nano-lasers.

This Thesis aims to investigate potential advance materials that could be employed as soft optical resonators and gain media for micro-/nano-lasers which are compatible with solution processing techniques. In this regard, advanced liquid crystalline (LC) mesogens, their phase behaviour and electro-optic characteristics are considered. The fabrication process of photo-polymerised thin-films of chiral nematic LCs are discussed along with the need for alternative gain media such as perovskite are considered. The challenges associated with combining perovskite emitters with LC materials are investigated in detail leading to the creation of the first flexible defect-mode laser, which demonstrates beam-steering by virtue of mechanical flexibility. Finally, a polarisation controllable band-edge LC laser is fabricated and demonstrated using the electro-optic characteristics of a nematic LC. Figure 1.1 illustrates the flow and structure of this Thesis, which is followed by a brief description of the contents and subject of each chapter.

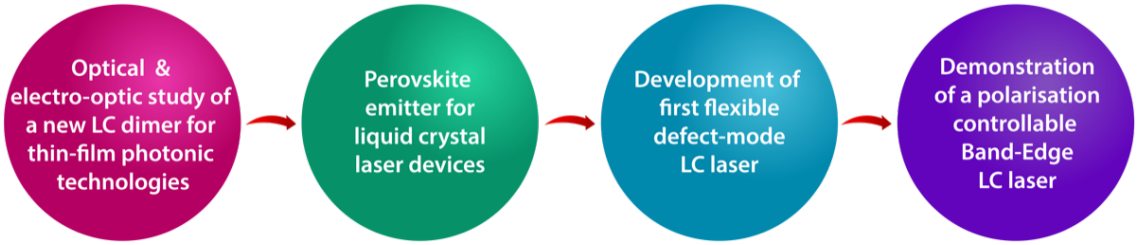


FIGURE 1.1: Illustration depicting the flow and structure of this Thesis.

1.0.1 Chapter Two

This chapter provides the general background and the relevant literature LC materials and corresponding LC laser technology. It opens with an introduction of the different LC phases, the physical and optical characteristics, particularly related to the nematic and chiral nematic phases (that are used in this Thesis) and the identification of these phases using an optical polarising microscope. This is followed by a discussion on the advantages of using LC materials for thin-film lasers. Since the gain material of the laser is vital in determining the laser efficiency, this chapter also considers available gain media that are currently suitable for use with LC laser technology, which follows a brief

background on their photo-physical characteristics with the help of the Jablonski diagram. A general introduction to the underlying laser physics of the different types of LC laser: Band-Edge and Defect-Mode, their working principle, and their recent progress is presented. Finally, the chapter discusses the potential of creating LC lasers with advanced emissive materials for future photonics technologies.

1.0.2 Chapter Three

This chapter describes the core experimental techniques employed in this thesis ranging from the fabrication of single pixel LC devices to their characterisation. The fabrication processes that are described include the preparation of glass substrates with different types of alignment layer (planar or homeotropic), the preparation of LC mixtures, and the solution processing techniques used to form thin-film laser devices. The principle underlying the spectroscopy and microscopy techniques that are used in this work are described in detail along with the use of characterisation tools such as a UV-Vis spectrophotometer, optical polarising microscopes and a fluorescence microscope. The free-space optical setup used to study the reflection spectrum of the chiral nematic phase is presented and finally, the optical excitation experiments employed to characterise the LC lasers either with light emitting diodes or Nd:YAG pulsed laser are introduced and discussed.

1.0.3 Chapter Four

The optical cavity typically employed in thin-film LC lasers are chiral nematic LCs. In this chapter, the optic and electro-optic characteristics of a newly developed LC dimer have been studied. Results are presented on the birefringence measurements of the new LC dimer. The reliability of the experiments was ensured by measuring the birefringence of other well-characterised LC materials. Other relevant material parameters such as the ratio of the splay elastic constant to the dielectric anisotropy ($k_{11}/\Delta\epsilon$) and the ratio of the bend to splay elastic constants (k_{33}/k_{11}) have also been determined. In addition, the flexoelectro-optic behaviour of this LC dimer has been investigated, which is compared and confirmed using two different experimental methods. Throughout the measurements, results presented for this new material are compared with other well-known nematic and chiral nematic LC mixtures. The high birefringence and relatively strong flexoelectric coupling for this LC dimer make it possible to create a thin photonic

device with fast response time and low driving voltages. This combination of material properties is potentially of interest for band-edge and defect-mode LC lasers with low excitation thresholds and wavelength tuneability. *This work has been prepared for submission to the peer-reviewed journal*.

1.0.4 Chapter Five

After investigation of a potential new candidate for the optical resonator, this thesis then considers advanced emissive materials that could replace conventional laser dyes as the gain media in LC lasers. In this regard, the chapter is concerned with the study of perovskite nanocrystals for band-edge LC lasers. It addresses the challenges associated with fabricating LC lasers using perovskite nanocrystals dispersed directly into a chiral nematic LC host. Different fabrications routes are considered, and results are presented showing the impact of the distribution of the nanocrystals along with the photoluminescence that is observed when these materials are used in combination with nematic and chiral nematic LCs. In contrast to conventional laser dyes that are typically used in band-edge LC lasers, this new form of gain medium could provide a viable route towards electrical rather than optical pumping.

1.0.5 Chapter Six

With the challenges encountered in creating band-edge LC lasers using perovskite nanocrystals, an alternative device configuration, known as the defect-mode, was explored. This device architecture has the benefit of avoiding the need for the gain medium to be dispersed directly into the LC host. In this chapter, results are presented on combining defect-mode architectures with perovskite nanocrystals. The advantage of this approach is that the gain material is confined within a separate layer between two chiral nematic LC reflectors, which potentially circumvents the issues of aggregation and degradation when the perovskite nanocrystals are dispersed directly into a LC host, as seen in the previous Chapter for the case of the band-edge laser configuration. This chapter starts with an overview of defect-mode lasers and presents results from simulations in terms of cavity design. This is then followed by an experimental study on the fabrication of a perovskite-based LC defect-mode laser. For this work, perovskite was used either as a bulk layer or by embedding perovskite nanocrystals into a thin polymer film to form the defect layer. Results are presented on the optical properties of the defect-mode

structure and the emission characteristics for the complete device stack. *Results from this chapter were selected for oral presentation for Materials Research Society (MRS), Boston USA, 2019.*

1.0.6 Chapter Seven

Following on from the development of a defect-mode structure in the previous chapter, a flexible defect-mode LC laser is proposed and demonstrated in this chapter. Experimental methods are presented to create an aligned photo-polymerised film of chiral nematic LC using various surface alignment layers. A number of fabrication techniques are considered for the fabrication of a single mode flexible defect-mode laser. These thin-film lasers are then characterised in terms of the film quality, laser emission wavelength, input-output characteristics, and laser polarisation. Finally, a beam steering feature of the flexible laser is demonstrated. The proposed flexible laser can be used to form lasers that could be integrated into conformable platforms and that could be used to control the beam direction without the need for additional optical components. *This work has been published in a peer-review journal, Advanced Optical Materials (1901891, 8, 2020), was selected as the Back-Cover Article (2070034, 2020). Part results from this chapter were also presented at SPIE Photonic West 2020 and published in the Conference Proceedings – SPIE (11303, Emerging Liquid Crystal Technologies XV; 113030Q, 2020).*

1.0.7 Chapter Eight

Having demonstrated beam-steering through mechanical deformation of a flexible defect-mode LC lasers, in this chapter the objective is to demonstrate control of another characteristic of LC laser emission, namely the polarisation. This chapter first provides background on the working principle of a waveplate and explains the use of a nematic LC for the purposes of a tuneable waveplate. It discusses the theory underpinning the electro-optic characteristics of an LC device and presents the relevant experimental results in terms of the transmission properties for a Fréedericksz transition, which is essential for understanding the control of the polarisation state with a nematic LC. This is followed by the design of the in-plane electrode LC device configuration and a discussion of the COMSOL Multiphysics based simulation models used to estimate the electric field in order to achieve a polarisation state at the desired orientation. A bench-top demonstration is presented by first showing the polarisation controllability of a continuous wave

He-Ne laser with the proposed in-plane switching (IPS) device followed by a demonstration when this device is used in combination with a band-edge LC laser. Results are presented showing that the IPS device can be used to attain any polarisation state, which could be of importance in polarimetric and holographic imaging applications and AR/VR technologies. *This work is being prepared for submission to the peer-reviewed journal and was selected for a poster presentation at 28th International Liquid Crystal Conference 2020.*

1.0.8 Chapter Nine

In the final chapter, results are summarised by providing an overall conclusion of the studies that were carried out in this Thesis that relate to the creation of thin-film lasers. This ranges from the characterisation of advanced LC and gain materials along with the development of new device fabrication routes. This chapter also considers possible future work for each of the strands of research explored in this thesis. In particular the process development and initial characterisation of a conjugate light emitting polymer, F8BT, as an alternative gain material for future defect-mode LC laser.

Chapter 2

Background

2.1 Introduction to Liquid Crystals

The most common phases of condensed matter are crystalline solids and isotropic liquids, which are distinguished based on their physical characteristics. Crystalline structures have both positional and orientational order with distinct lattice points. However, molecules in an isotropic liquid phase are randomly oriented and diffuse throughout the phase with their molecular axis tumbling in all directions. Interestingly, there is a phase of matter that exhibits more order than an isotropic liquid, but less order than the crystalline phase and is called the Liquid Crystal phase (LC) [1].

LCs can be broadly divided into two main categories: 1) lyotropic, and 2) thermotropic LCs [2]. Lyotropic LCs form an LC phase when they are combined with a certain solvent; the concentration level of such solvent is critical in determining the LC phase. Lyotropic LC are generally form a molecule with a hydrophobic group at an end and a hydrophilic group at the another end and generally consist of a polar head attached to a hydrocarbon tail. Thermotropic LC, on the other hand, do not require any solvent and can exhibit an LC phase within a certain range of temperature and beyond that temperature, they behave like an isotropic liquid. In this Thesis thermotropic LC are considered.

Thermotropic LC can be formed with different types of molecules: one of the most common types are rod-shape molecules, as shown in Figure 2.1 (a), in which one axis is longer than other. This is called a calamitic LC [3, 4]. Generally, they have a rigid polarisable core made of two or more phenyl rings and have a flexible aliphatic tail

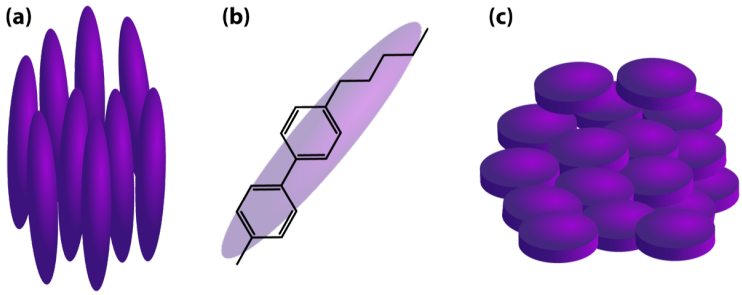


FIGURE 2.1: A simplified illustration of (**a**) rod-like calamitic, (**b**) the molecular structure of 5CB, and (**c**) disc-shaped discotic LC molecules.

(carbon—hydrogen chain). It is essential that the calamitic molecules have an elongated structure to attain an intramolecular interaction that complements the alignment. An example of a calamitic LC is the well-known 5CB molecule, its molecular structure is shown in Figure 2.1 (b). Another type of thermotropic LC are ones that are based on molecules that resemble a disc and are called discotic LC (as shown in Figure 2.1 (c)) [4, 5]. For discotic molecules, the rigid core is essential and is made from multiple phenyl rings or truxene that offers six or eight connections to further chains similar to calamitic molecules.

2.1.1 LC mesophases

Thermotropic LC formed with calamitic molecules can exhibit various phases including the nematic, chiral nematic (or cholesteric), smectic C, and blue phase. In the following sub-sections, the phases are briefly discussed.

2.1.1.1 Nematic LC

The nematic LC phase is the most simple form of calamitic LC molecules. The long axis of the molecule spends more time oriented in a specific direction while they can also remain diffuse. In other words, they have orientational order but no positional order. Their preferred direction is represented by a dimensionless quantity, a unit vector, called the director and is represented by $\hat{\mathbf{n}}$ as shown in Figure 2.2 (a) [6]. Although nematic LC can be polar in nature, in the bulk material the ordering is such that $\hat{\mathbf{n}} = -\hat{\mathbf{n}}$. However, under the application of external electric fields or with strong distortion, polar ordering can be induced. The coupling between distortion and polar ordering leads to phenomenon referred to as flexoelectricity, which will be discussed later in this Thesis. Nematic LCs are non-polar in nature and therefore $\hat{\mathbf{n}} = -\hat{\mathbf{n}}$. The extent to which the LC has orientational order can be quantified by the order parameter $\langle S \rangle = \langle \frac{3}{2} \cos^2 \theta - \frac{1}{2} \rangle$,

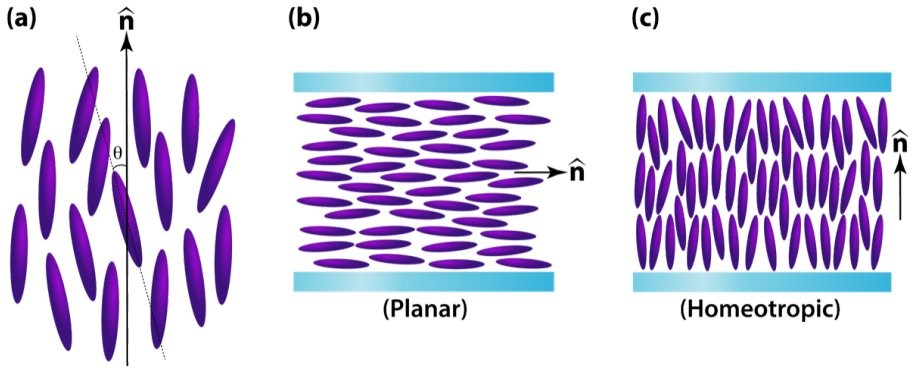


FIGURE 2.2: (**a**) An illustration of typical calamitic nematic LC showing orientational order defined by the director, $\hat{n}$. Illustration of (**b**) planar/homogeneous and (**c**) homeotropic alignment of a nematic LC in a glass cell.

where θ is the angle that the long axis of a local LC molecule makes with the LC director $\hat{\mathbf{n}}$ as depicted in Figure 2.2 (a) [2]. The '$\langle\rangle$' indicates either an average of orientation of a single molecule averaged over time or spatial average of many molecules at an instantaneous time. When $\theta = 0^\circ$, the order parameter would be $S = 1$, i.e., the LC system has perfect orientation along $\hat{\mathbf{n}}$. However, order parameter $S = 0$ implies that the molecules orient in random directions corresponding to an isotropic liquid. The order parameter is temperature dependent and for thermotropic LC, the order parameter would become zero as the LC is heated above the clearing temperature (temperature above which the LC exhibits an isotropic phase).

Nematic LCs can be filled between two glass plates separated by spacers varying in thickness from a few microns to tens of microns. The glass plates are typically treated with a material to encourage a particular alignment of the LC nematic phase. There are generally two types of alignments: 1) homogeneous and 2) homeotropic alignment [7]. The preparation of LC glass cells will be discussed in detail in §3.1 of Chapter 3. For homogeneous/planar alignment, the LC director is aligned parallel with the glass substrate, which is illustrated in Figure 2.2 (b). Based on the desired application, planar alignment can be further divided in two categories such as parallel and anti-parallel planar alignment and is defined by the direction each substrate is rubbed. For parallel planar alignment both substrates are rubbed in the same direction whereas for anti-parallel alignment, the rubbing direction is in opposite directions for both substrates. Alternatively, for homeotropic alignment, the LC director is aligned perpendicular to the substrate; this is shown with an illustration in Figure 2.2 (c). Such alignments are of interest

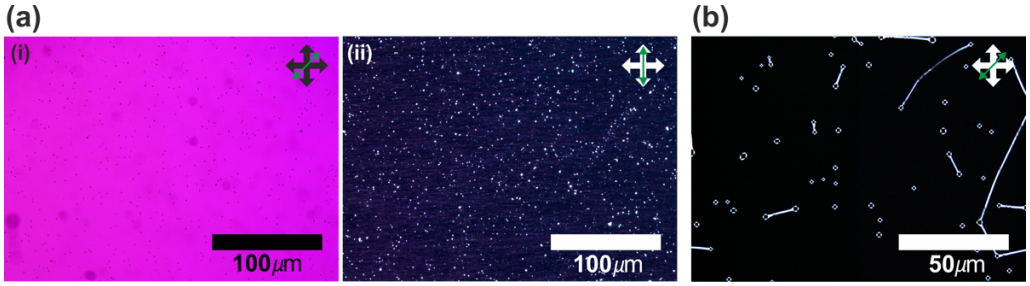


FIGURE 2.3: Optical polarisation microscope images of nematic LC (**a**) planar (i) 45° and (ii) 0° or 90° with respect to the polariser and analyser, and (**b**) homeotropic aligned nematic LC.

in particular when out-of-plane switching is desired [8].

Identification of the nematic LC phase is highly important and relevant to the study undertaken in this Thesis. The optical texture that is observed depends on the alignment of the nematic LC and is identified by viewing the LC in the brightfield of an optical polarisation microscope with crossed polariser and analyser. For a planar aligned nematic LC that is placed such that the macroscopic optic axis is aligned at $\chi = 45°$ with respect to the transmission axes of the polariser and analyser, a bright coloured state can be observed [9]. The transmitted light through the LC device varies between a dark and bright state as the sample is rotated from $\chi = 0°$ to 90°. Example images taken with an optical polarisation microscope of the bright and dark states of a planar nematic LC are shown in Figure 2.3 (a). The lines in the nematic phase are defects in the LC director alignment, typically referred to as disclination lines, and are the reason of for the name 'nematic', which comes from a Greek word meaning thread. Similarly, Figure 2.3 (b) shows the texture of a homeotropic aligned nematic LC device when observed with an optical microscope image with crossed polariser and analyser. Since in the homeotropic aligned LC, light travels through the device only sees n_o (as explained later in §2.1.1.5) and therefore the appears dark.

2.1.1.2 Smectic phase

The calamitic molecules that give rise to a nematic LC phase can also exhibit other mesophases that, in addition to exhibiting orientational order (as seen in the nematic phase), can also have positional order forming layer-like structures and known as Smectic (Sm) phase as illustrated in Figure 2.4 [10]. Based on the tilt angle of the LC director and their packing, the smectic phase can be sub-divided into several types such as SmA to SmK. SmA and SmC are the most studied types. In the layered structure of

Smectic A, molecules have orientational order similar to nematic phase and is illustrated in Figure 2.4 (a). Smectic C also exhibits the layered structure, however, molecules within the layers are tilted (Figure 2.4 (b)).

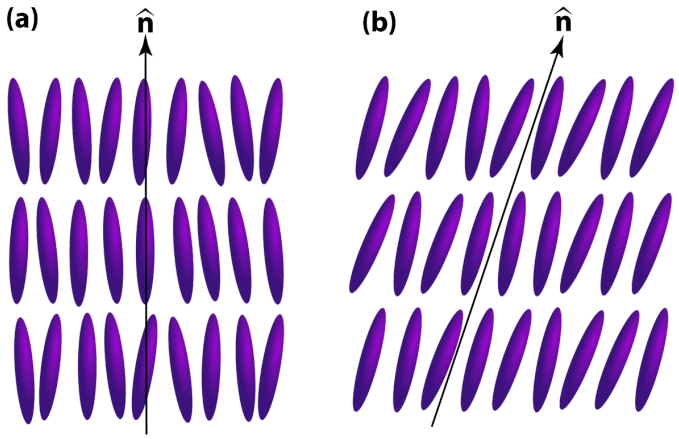


FIGURE 2.4: Illustrations of the smectic A (**a**) and smectic C (**b**) phases.

2.1.1.3 Chiral nematic phase

The chiral nematic phase is of importance for potential photonics devices and is a modified form of the nematic phase [11]. This is also known as the cholesteric phase as the early compounds that exhibited this phase were derivatives of cholesterol [12]. The chiral nematic phase can be formed from LC molecules that are either inherently chiral in nature (cannot be superimposed on their mirror image due to absence of inversion symmetry) or through the use of chiral additives or dopants (which is the approached used in this Thesis). Depending on the helical twisting power (HTP) and the concentration of the dopant, the pitch of the helix can be adjusted, and this is explained in detail in Chapter 3. Due to the presence of chirality, the LC director is rotated about a single axis to form a macroscopic helix as shown in Figure 2.5. The distance over which the director rotates through the angle of 360° is referred to as the pitch (p) and is an important parameter for chiral nematic LCs as together with optical anisotropy it defines the position of photonic bandgap (that is discussed in detail later) [13]. Since the LC molecules are non-polar, i.e. $\hat{\mathbf{n}} = -\hat{\mathbf{n}}$, the structure repeats after each half of the pitch (180°). The pitch can range from $\approx$ 100 nm to 10s of microns. When the pitch is of the order of the wavelength of light interesting optical effects can be observed.

The alignment of the chiral nematic phase in glass cells can take the form of one of the following: 1) uniform standing helix (Grandjean texture), 2) uniform lying

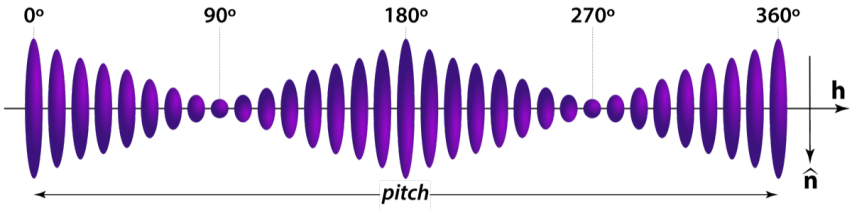


FIGURE 2.5: Illustration of the helical structure of a chiral nematic liquid crystal illustrating the local director ($\hat{\mathbf{n}}$), helix/optical axis ($\mathbf{h}$) and pitch (p).

helix (short pitch) or fingerprint texture and 3) a focal conic texture [14]. For the uniform stand helix (USH), the helical axis of the chiral nematic LC is oriented normal to the substrates as shown in Figure 2.6 a (i). The substrates are treated to encourage planar alignment of the LC director at the substrate surfaces, resulting in a helical axis that is aligned along the normal of the substrates. When observed with an optical polarising microscope, a Grandjean texture (example image is presented in Figure 2.6 a (ii)) can be observed. The disclination lines (or oily streaks/defects) are typically regions of pseudo-lying helix between different domains of standing helices. This alignment is important for the LC lasers considered in this thesis [15]. For the uniform lying helix (ULH) texture, the helical axis is aligned parallel to the surface of the substrates, Figure 2.6 b (i). An example of a ULH texture is shown in Figure 2.6 b (ii). The ULH texture can be induced into a USH device by cooling the device in the presence of an electrical field. This texture is key for studying the flexoelectro optic effect which is described in detail in Chapter 4. In contrast to the USH or fingerprint textures, if the chiral nematic LC phase is injected into a cell that does not have any alignment, the helices are oriented in a random fashion, Figure 2.6 c (i); this texture is called the focal conic texture and is illustrated with an example optical microscope image in Figure 2.6 c (ii).

2.1.1.4 Blue phase

The LC Blue phases are an exotic thermotropic LC phase that appears on cooling from the isotropic phase in chiral nematic LC mixtures with a high twisting power. In contrast to the chiral nematic phase that exhibits a one-dimensional photonic structure, blue phases possess a three-dimensional photonic structure, an illustration of which is shown in Figure 2.7 (a) [18, 19]. They form a lattice (cubic) arrangement of line defects and generally appear as platelets when observed under the microscope, Figure 2.7 (b) [20]. They were first observed in 1888 as blue-violet colour, but also exist in other colours depending on the lattice constants. Until relatively recently, blue phases were

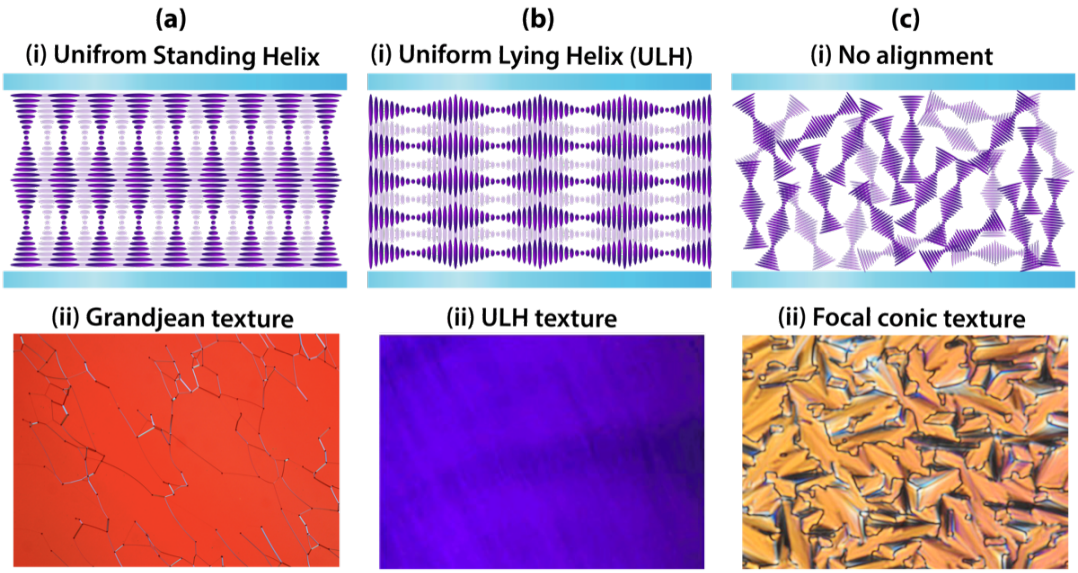


FIGURE 2.6: (**a**) The uniform standing helix (USH) (**b**) the uniform lying helix (ULH) [16] and (**c**) randomly aligned chiral nematic LC helix [17]. The label (i) depicts the schematic illustration and (ii) shows the optical polarising microscope images.

found to be stable only within a small range of temperatures, although wider temperature ranges have now been observed in polymer-stabilised blue phases [21] and mixtures of LC dimers. There are three different types of blue phase: I, II and III. which can appear with increasing temperature.

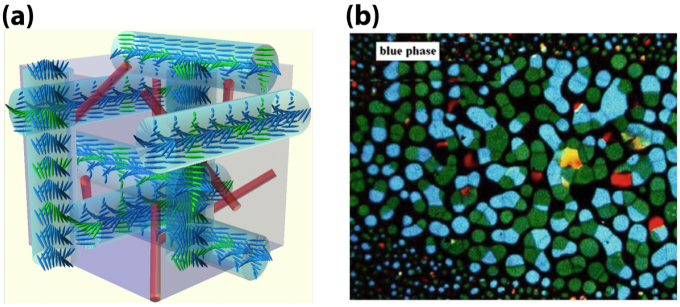


FIGURE 2.7: (**a**) An illustration of a typical blue phase configuration consisting of double-twist cylinders [18] and (**b**) the blue phase platelets observed with an optical polarising microscope [20].

2.1.1.5 Optical indicatrix

When light enters an optical material, its speed and wavelength can change as governed by the refractive index (n), which for a non-magnetic material such as a LC is equal to the square-root of the optical dielectric permittivity. For an isotropic material, the refractive index is constant in all directions and therefore light entering from any direction would experience the same change in speed and wavelength. However, for anisotropic materials (such as LCs), the refractive index is not constant in all directions;

this implies that, for an LC, a light ray entering from one direction would slow down by a different factor to a light ray which enters from a different direction. Generally, the refractive indices of a nematic LC along the three principal axes x, y and z are denoted n_x, n_y and n_z, respectively, and are related as follows [22]:

$$\frac{x^2}{n_x^2} + \frac{y^2}{n_y^2} + \frac{z^2}{n_z^2} = 1 \tag{2.1}$$

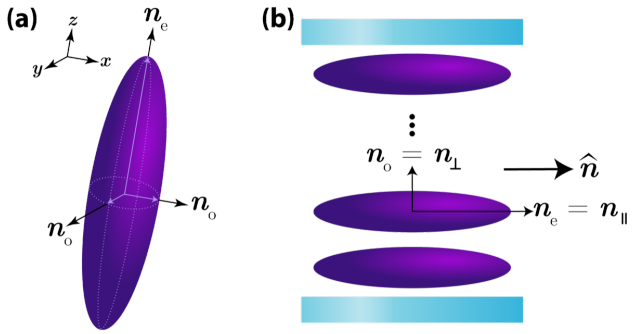


FIGURE 2.8: Illustrations of (**a**) optical indicatrix in a typical calamitic nematic LC representing the refractive indices along different directions, the representation of the ordinary (n_o) and extraordinary (n_e) refractive index of a nematic LC. (**b**) Schematic showing a planar-aligned nematic LC illustrating $n_e = n_{\parallel}$ and $n_o = n_{\perp}$

.

Calamitic nematic LC molecules have an elongated shape and are uniaxial, the optical axis is along one of the said directions, say $z-$axis. Two of the three refractive indices say n_x and n_y are equal and are known as the ordinary refractive index, which is denoted as n_o. This is shown in Figure 2.8 (a). This means that light travelling along the z-axis would experience n_o. The refractive index along the z-direction, however, is the extraordinary refractive index and is represented with n_e so that $n_e > n_o$, Figure 2.8 (a). For a planar aligned nematic LC, the optical axis is parallel to the director $\hat{\mathbf{n}}$ and therefore the refractive indices are also often written as $n_e = n_{\parallel}$ and $n_o = n_{\perp}$, as shown in Figure 2.8 (b). The variation in the refractive index along different viewing directions gives rise to the optical anisotropy that is also known as birefringence (Δn) and given as [9]:

$$\Delta n = n_e - n_o \tag{2.2}$$

The optical anisotropy or birefringence enables LCs to be exploited in photonic devices such as displays, tuneable waveplates, optical phase modulators and optical resonators.

2.1.1.6 Photonic bandgap in chiral nematic LCs

As explained earlier in §2.1.1.3, the chiral nematic LC exhibits a one-dimensional macroscopic helix that can be created by adding chiral dopants to a nematic LC. For the

USH configuration, when the transmission of light is considered, interesting optical effects can be observed. The chiral nematic helix has a sense of rotation that is either left- or right-handed, depending on the type of chiral dopant added. When light propagates parallel to the helical axis, the structure acts as a one-dimensional Bragg reflector for the circularly polarised light whose wavelength matches with the pitch (p) of the helix and has the same sense of rotation as the helix. This implies that when such light is incident on the chiral nematic LC, it will not transmit through the helix and will be reflected [23, 24]. This comes down largely to the typical definitions of left and right circularly polarised light. These are usually defined such that left circularly polarised light rotates counter-clockwise relative to the observer whereas right circularly polarised light rotates clockwise. By this definition, this means that when right circularly polarised light is incident on a right-handed helix it will rotate in the opposite sense to the helix and will thus see a variation in the refractive indices, resulting in a reflection band if the pitch is of the order of the wavelength of light. Left circularly polarised light however will have the same screw sense as the right-handed helix and so does not see a variation in the refractive indices and is thus able to propagate through the structure.

Chiral nematic LCs can reflect a certain range of wavelengths of light depending on the refractive indices and the pitch of the helix through the expressions [25]:

$$\lambda_S = p \times n_o \tag{2.3}$$

$$\lambda_L = p \times n_e \tag{2.4}$$

where λ_S and λ_L are the short and long-wavelength edges of the reflection band as illustrated in Figure 2.9 (a). The refection spectrum is also known as the photonic bandgap as it stops the transmission of light of certain wavelengths through the helix. The width of the photonic bandgap ($\Delta\lambda$) depends on the birefringence of the LC, for a given pitch. As a result, a larger optical anisotropy leads to a wider photonic bandgap and is given by:

$$\Delta\lambda = \lambda_L - \lambda_S = \Delta n \times p \tag{2.5}$$

Similarly, for a given birefringence, the position of the photonic bandgap can be tailored by adjusting the pitch of the helix: in general, a short pitch results in a photonic bandgap that appears at shorter wavelengths whereas a longer pitch moves the photonic bandgap toward longer wavelengths. An example of the transmission spectra for a chiral nematic

LC with long and short pitch values are presented in Figure 2.9 (b). Furthermore, for a planar aligned nematic LC, $n_{\parallel} = n_e$ and $n_{\perp} = n_o$, as seen earlier. However, in the chiral nematic phase, the optic axis is parallel to the helical axis (as shown in Figure 2.5); this implies: $n_{\perp} = n_e$ and $n_{\parallel} = \sqrt{\frac{n_o^2+n_e^2}{2}}$.

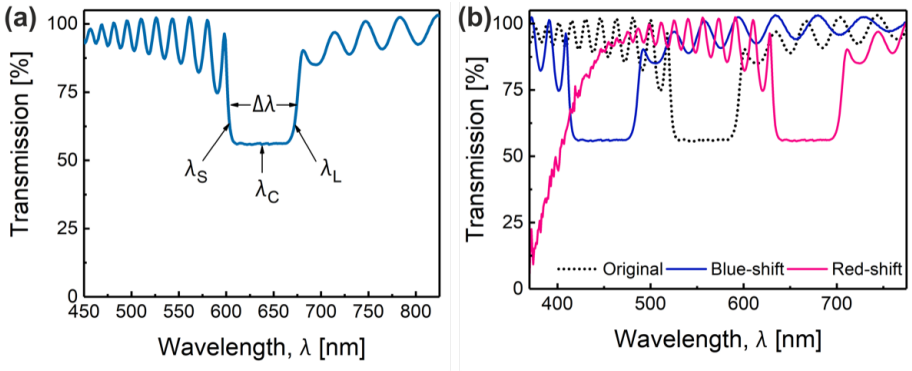


FIGURE 2.9: (**a**) Example transmission spectrum of a typical chiral nematic LC illustrating the positions of the short (λ_S) and long wavelength (λ_L) band-edges and (**b**) example transmission spectra illustrating a blue and red shift in the photonic bandgap due to a variation in the pitch of the helix.

2.1.1.7 Dielectric anisotropy

The permittivity of a material measures its electric polarisability and is denoted by the Greek symbol, ϵ. Generally, the permittivity of a material is constant in all directions; however, for LCs the permittivity varies along different directions relative to the director. In the nematic phase, the permittivity is defined by two principal components, that is, parallel and perpendicular components to the director and is represented by $\epsilon_{\parallel}$ and $\epsilon_{\perp}$, respectively [26, 27]. The anisotropy in the permittivity ($\Delta\epsilon$), therefore, is defined:

$$\Delta\epsilon = \epsilon_{\parallel} - \epsilon_{\perp} \tag{2.6}$$

There are two factors that contribute towards the permittivity of a nematic LC when an electric field is applied:

1. It induces a polarisation in the LC molecules and therefore a dipole moment. The induced polarisation in the LC molecules depends on the chemical structure such as the aromaticity, and hence the polarisability can be different along the molecule and perpendicular to the molecule.
2. It interacts with permanent dipoles in the molecules. In the bulk nematic phase, the uniaxial $\hat{\mathbf{n}} = -\hat{\mathbf{n}}$ symmetry means that although individual molecule tends to be polar, the bulk average polarisation is zero. However, under electric field application along the molecular axis the $\hat{\mathbf{n}} = -\hat{\mathbf{n}}$ symmetry is broken, and a bulk polarisation can be induced along the molecular axis. Similarly, under field application perpendicular to the molecular axis the uniaxial ordering is broken, and a

bulk polarisation can be induced perpendicular to the original molecular axis. Depending on the orientation of the molecular dipole and the nature of the ordering, the polarisability can be stronger along the molecular axis or perpendicular to the molecular axis.

Depending on the combination of effects (1) and (2), the overall polarisability can be either stronger along $\hat{\mathbf{n}}$ or perpendicular to $\hat{\mathbf{n}}$, leading to either positive or negative dielectric anisotropy. LC materials that exhibit a positive $\Delta\epsilon$ orient along the direction of an applied electric field whereas for a negative $\Delta\epsilon$, the director orients perpendicular to the applied field.

2.1.1.8 Fréedericksz transition

To understand the response of a nematic LC to an electric field, consider the arrangement as shown in Figure 2.10 in which a nematic LC is aligned between glass plates that have been treated with a layer that encourages a planar alignment so that the director is aligned in the x-direction. An electric field is applied across the device in the z-direction. When an electric field is applied, the LC director reorients in the direction of the applied electric field, i.e., from the $x-$direction to the $z-$direction. This deformation of the LC molecules from the uniform director configuration in response to a sufficient electric field is called the Fréedericksz transition [28, 29]. The threshold transition voltage (V_{TH}) is given as:

$$V_{TH} = \pi \times \sqrt{\frac{k_1}{\epsilon_o \Delta\epsilon}} \tag{2.7}$$

where k_1 is the splay elastic constant, ϵ_o is the permittivity of free-space and $\Delta\epsilon$ is the dielectric anisotropy. Below the threshold voltage or field, the LC director remains undistorted, after passing the threshold the LC director reorients until collinear with the applied electric field. When the electric field is removed, the director returns to the original state due to the elastic restoring force. This enables the LC to create several interesting electro-optic devices such as a light intensity modulator.

$$T = T_o \sin^2(2\chi) \sin^2\left(\frac{\pi \Delta n_{eff}(V) \times d}{\lambda}\right) \tag{2.8}$$

The transmission of light through the such LC device between crossed polarisers can be modelled with Equation (2.8) where T_o is the maximum transmission intensity, χ is the angle of the optical axis of the LC device with respect to the polariser/analyser axis, Δn is optical anisotropy, d is the device thickness and λ is the wavelength of light. To

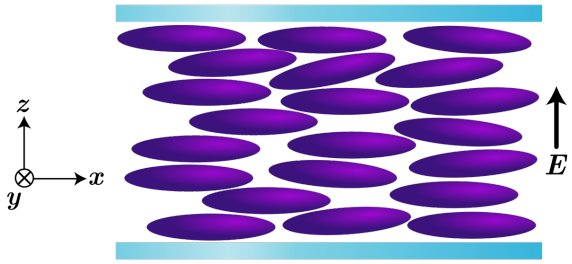


FIGURE 2.10: A typical planar aligned nematic LC system illustrating the directions for LC director and electric field.

illustrate this behaviour, an LC device was placed on a polarising optical microscope such that $\chi = 45°$, and when a changing electric field was applied, the transmission of light was found to vary. An example of a Fréedericksz transmission curve is presented in Figure 2.11, which highlights the location where the transition occurs and defines the threshold driving voltage of the device. The variation in the transmission by increasing the electric field strength shows the LC director orients towards the direction of the electric field and when the director become parallel to the electric field, the transmission has eventually reduced to zero. This electro-optic effect is exploited later in this thesis to form a tuneable waveplate so as to control the polarisation of an LC laser, as discussed in detail in Chapter 8.

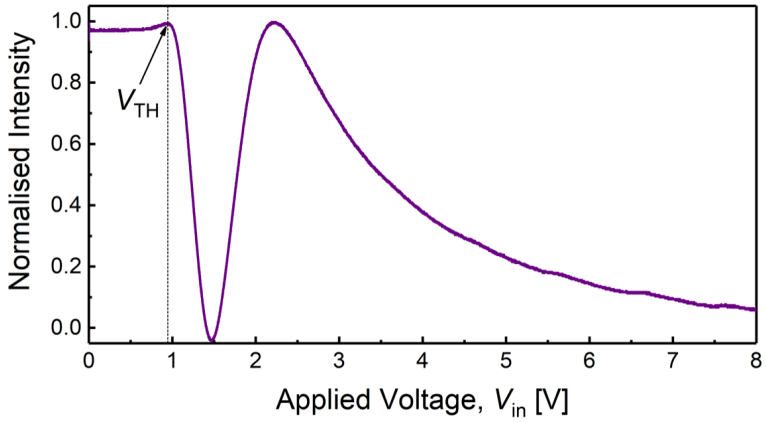


FIGURE 2.11: An example Fréedericksz transmission curve illustrating the threshold voltage and variation of the light intensity that is transmitted through the device.

2.1.1.9 Other physical properties

In addition to the birefringence and dielectric properties, LCs also exhibit elastic behaviour, which is relevant for studying their electro-optic characteristics. The director orientation in a nematic LC without an external electric field is determined by the physical parameters such as the type of alignment. However, if the LC is perturbed with

an external electric field, the director reorients in response to the applied field as so to minimise the free-energy of the system and cause a distortion in the LC. The elastic properties are considered in more detail when the flexoelectro-optic characteristics [30, 31] of a new LC dimer, an electro-optic effect relating to a distortion-induced polarisation due to shape asymmetry, are discussed in §4.5, Chapter 4.

2.2 Laser

Light Amplification by Stimulated Emission of Radiation or simply LASER is a process involving the emission of light that has been amplified through stimulated emission. Laser radiation has unique emission properties that enable it to be used in a variety of applications such as holography, spectroscopy, communication systems, information storage, and bio-medical diagnostic techniques. The laser is characterised by a [32]:

1. High degree of temporal coherence, narrow spectral width or monochromatic radiation
2. High spatial coherence, diffraction limited or highly collimated, and a very small focussing spot

2.2.1 Laser construction

Physically, a typical laser comprises two major parts: 1) an optical gain or amplifier and 2) a resonator or cavity that provides the optical feedback. An arrangement of optical components that permits light to circulate in a closed path form an optical resonator or resonant optical cavity, which is an essential part of a laser. Typically, the optical resonator surrounds the gain within which light bounces back and forth for amplified emission or laser action.

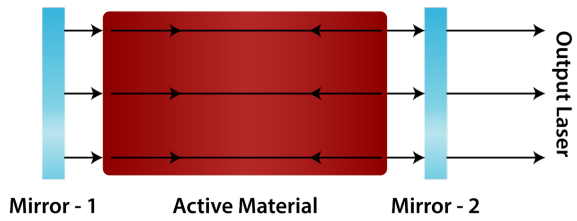


FIGURE 2.12: A simple schematic of a conventional laser comprising two reflective surfaces (mirror) and an emissive material between them.

The simplest optical feedback is the Fabry-Perot resonator (Figure 2.12) which

consists of two plane mirrors facing each other placed at either end of the optical amplifier at a distance of $^{m\lambda}/_{2}$ (where m is an integer and λ is the wavelength of stimulated emission). The mirror spacing is crucial as the correct distance enables the reflected light to be in-phase with the incident light, thereby resulting in the formation of a standing wave between the mirrors. One mirror is fully reflective, while the second mirror is slightly transmissive allowing a small proportion of the light to be emitted as laser light.

Many different types of lasers have been studied and developed, varying in construction, size and material. Examples of lasers include crystal lasers that use doped crystals such as Nd:YAG, Er:YAG, Ti:Sapphire or Yb:glass. Alternatively, semiconductor lasers from semiconductor materials such as GaAs, InGaAs and AlGaAs that generally forms quantum wells and are electrically pumped. In addition, there are lasers that used other phases such as gases (He-Ne or CO_2) and liquid (dyes) as the gain material.

2.2.2 Liquid Crystal (LC) laser

The optical cavity can be built with a variety of materials and vary in size from metres (crystal or gas laser) to micro/nano lasers (semiconductor laser). For micro/nano-lasers, the optical cavity can be constructed in various forms such as ring [33–35] and waveguides [36, 37]. While these lasers offer benefits in terms of miniature photonic devices, the fabrication of the laser cavity with these materials requires stringent processing conditions that eventually increases the device cost. On the other hand, the self-assembly of LC molecules in the chiral nematic LC phase enables the facile fabrication of a 1D photonic structure without the need for sophisticated fabrication processes. Provided that the periodicity of the helix is of the same order as the wavelength of light, a gap in the photonic bands exists where light within a particular frequency range and circular polarisation cannot propagate. This is also true for a chiral smectic-C* phase, which also exhibits a macroscopic helicoidal arrangement of the LC molecules. For both the chiral nematic and chiral smectic-C* phases the photonic bandgap is one-dimensional in nature (i.e. it only exists along the helix axis).

In this Thesis, laser cavities are manufactured from the chiral nematic phase in two different configurations: 1) band-edge LC laser [38–40] and 2) defect-mode LC laser [41–43]. The following sections provide general background on both types of LC lasers.

2.2.2.1 Band-edge LC laser

The photonic bandgap in optics is analogous to the electronic bandgap in semiconductors and can be realised, in principle, in 1, 2, or 3D periodic structures. These photonic structures have been studied considerably as they can control the propagation of light for a certain range of frequencies. Within the bandgap, emission is suppressed due to the low photonic density of states (DOS). The DOS, however, diverges at the band edge leading to higher photon dwell times that result in amplified emission in the presence of gain. These band-edges, one on either side of the band gap, thus act as the modes of the resonator, which are well-separated in terms of frequency space and can lead to laser emission when the frequency of these modes overlap with the emission spectrum of a gain medium [44].

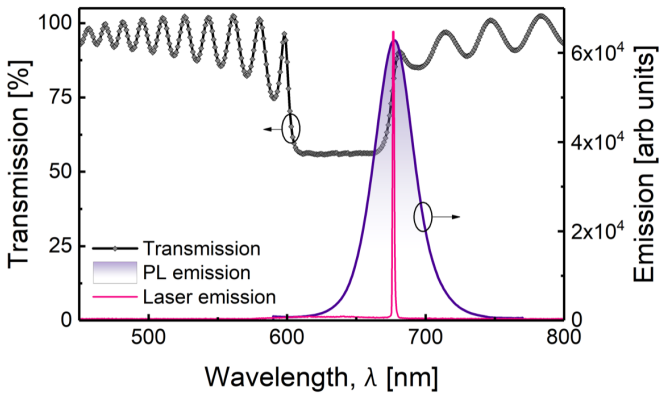


FIGURE 2.13: Example of laser emission at the long wavelength band-edge, primary axis is the transmission spectrum for a chiral nematic whereas the secondary axis represents the emission intensity.

For an LC band-edge laser, two factors are important: the spectral position of the light emitter and the relative spectral position of the photonic bandgap. To ensure laser emission at the photonic band-edge, the emission spectrum of the emitter must overlap with one of the band-edges of the photonic bandgap (Figure 2.13). For a low threshold laser, the gain maximum of the emissive medium must overlap with one of the band-edges so as to maximise the coupling efficiency. In most cases, the long-wavelength band edge tends to exhibit a lower excitation threshold [45].

The photonic bandgap of a chiral nematic LC can alter the emission spectrum of the guest emitters by suppressing the fluorescence within the band gap whilst enhancing it at the edges because of the increase in the photonic density of states (ρ). Originally, *de*

Vries analysed the optical properties of a chiral nematic LC by considering chiral structure as a series of rotating layers [25] as explained by Dowling *et al.* [44] by proposing the gain enhancement at the edges of photonic bandgap:

$$\rho = \frac{d}{d\omega}\left(\Re(k)\right) \tag{2.9}$$

where ω is the frequency and $\Re(k)$ is the real part of the wavevector. The photonic DOS can also be expressed as $\rho = \frac{1}{v_g}$, where v_g is the group velocity. As noted in the original theoretical work on the band-edge laser by Dowling *et al.* [44], for the region near the band edge, the group velocity (v_g) is real but tends towards zero. A good way to visualise the effect is to consider that near the band edge a photon is undergoing many multiple reflections in the structure, and it only slowly propagates through the structure with a mean velocity given by v_g. If a gain material is present, the large increase in optical path length would enhance the effective gain – leading to amplified stimulated emission. [44, 45].

When the excitation wavelength falls within the wavelength range of the band-gap, half of the power is lost due to unwanted reflection from the band-gap. It is therefore best to optically pump the sample with a solid-state laser that has a circular polarisation that is of the opposite sense of the helical structure of the chiral nematic phase. The laser pumping excitation wavelength depends on the absorption spectrum of the gain medium. Regardless of the optical geometry of the pumping, the emission from the LC laser is always along the helical axis. Nevertheless, if the laser is photo-pumped at an angle greater than 18°, the laser emission can depend significantly on the incident polarisation of the pump source [46] and therefore requires the correct polarisation. The laser threshold can be decreased using the identical sense of rotation of the helix as the polarisation handedness of the incident light [47, 48].

2.2.2.2 Defect-mode LC laser

The second important lasing mechanism that has been demonstrated in LCs is the defect mode laser. As its name suggests, a structural defect has to be created within the macroscopic helical arrangement of the chiral nematic phase. This in turn leads to a resonant channel inside the photonic bandgap where the energy is confined within a very small volume. This can be obtained by inducing either a phase slip into the structure,

by adding a defect-layer or a combination of both [49–51]. Provided that the emission spectrum overlaps the entirety of the band-gap, it is possible to excite both the defect and band-edge modes simultaneously.

To elucidate the defect created in the photonic bandgap, let us consider a chiral nematic LC forming a helix as in Figure 2.14 (a). It has a pitch (p) and due to the helical structure, the local director $\hat{\mathbf{n}}$ rotates about the helix axis with a handedness defined by the chiral dopant. As explained by Schmidtke and Stille [45, 49], the DOS inside the photonic bandgap is zero meaning no spontaneous emission. If, however, somehow this helical structure no longer remains uniform or gets disturbed, it will allow to pass the opposite sense polarisation to the helical structure (which was previously blocked within the PBG). This creates a region where the DOS is no longer zero but becomes large as a certain wavelength of light is not suppressed. For either side of this 'leaky' mode no emission takes place due to the existence of the band gap and thus the mode is only localised at the defect.

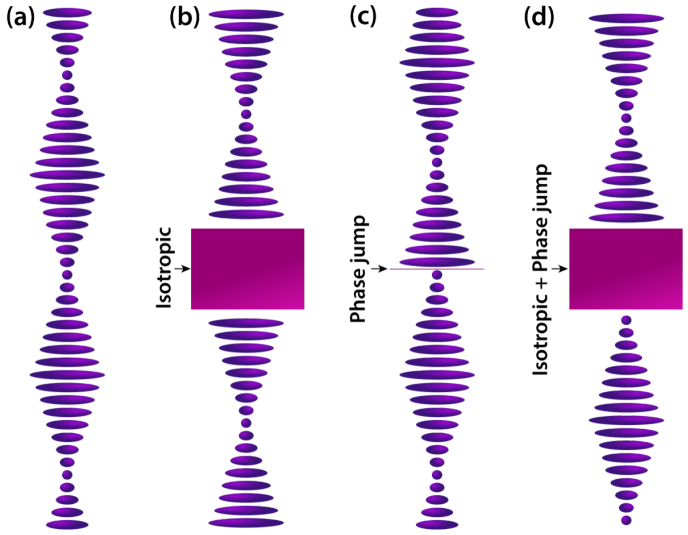


FIGURE 2.14: (**a**) A generic chiral nematic LC helix. A perturbation or defect introduced in a CLC helix by (**b**) isotopic defect layer, (**c**) twist defect, and (d) a hybrid approach having both defect layer and twist defect.

Generally, there are two ways to create the defect in the chiral nematic phase. One is to break the helix and add an isotropic or anisotropic layer between two identical CLC layers, which is called the defect layer approach (Figure 2.14 (b)). This defect layer can simply be a nematic layer doped with a fluorescence compound. A defect can also be created with a sudden phase change in the helix, referred to as a twist defect (Figure

2.14 (c)). In addition, a hybrid approach of using both techniques can also be used to create a defect in which an isotropic/anisotropic layer is sandwiched between two layers of chiral nematic LC that introduces a defect in the helix while also having a phase jump in the twist of the helix as shown in Figure 2.14 (d).

There can be single or multiple modes existing inside the band gap depending upon the size of the defect, which in turn can give rise to multimode lasing provided there is sufficient gain available for each mode analogous to a Fabry-Perot laser. In addition, instead of using a thin defect layer, a relatively thick layer ($\approx 10\mu$m) can also be sandwiched between the CLC reflector layers, giving rise to multiple resonant modes within the band gap [52]. Examples of single mode and multimode laser emission in the defect-mode structure are shown in Figure 2.15.

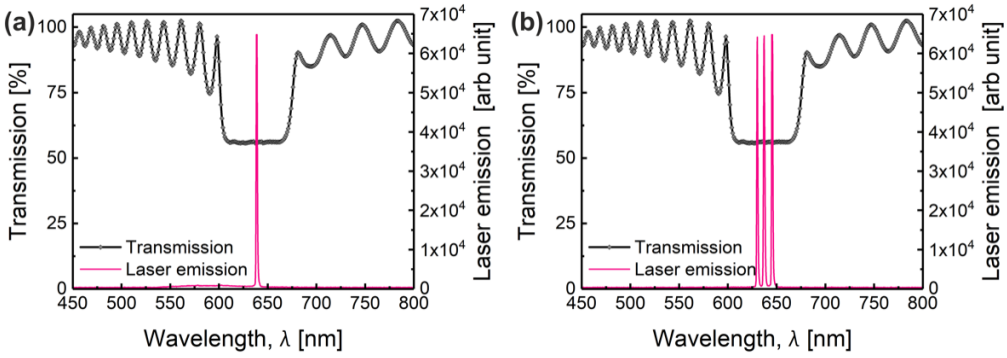


FIGURE 2.15: Example illustration of a CLC-based defect mode laser. (**a**) the existence of single mode and (**b**) multiple modes.

The presence of a defect layer or twist defect in a CLC can lead to resonance behaviour under the right experimental conditions. The 1D photonic crystal having a defect layer is considered as a 'micro-resonator' and is identical to an optical resonator. The defect layer behaves as an optical resonator cavity, which is sandwiched between two reflecting surfaces i.e. a dielectric or a mirror. The modes in the optical resonator comprise three parts: a standing wave within the defect layer, and two exponentially decaying (evanescent) waves within the dielectric mirrors. As the thickness of the defect layer is small, this makes the evanescent tails became a substantial part of the standing waves. Their decay length gives the spatial extension of the defect mode. Surprisingly, the twist defect can also act as an optical resonator; however, this is not identical to the conventional micro-resonator concept, as no defect layer exists that could potentially act

as a resonant cavity. Thus, the resonator only comprises two out-of-phase chiral nematic reflectors.

Defect-mode LC lasers have been shown to exhibit a low excitation threshold when compared with band-edge lasers. Initial demonstrations included using dye-doped nematic polymer layers, which were sandwiched between two CLC layers [52–56]. Recently, a wavelength tuneable white-light laser has been fabricated from an organic-inorganic hybrid system. It comprises of a dye-doped CLC layer sandwiched between inorganic periodic and identical (but imperfect) structures that exhibited mono, bi or trichromatic laser emission when pumped optically [57]. Defect mode lasers, due to the wide range of possible device architectures and the potentially low excitation threshold characteristics, have attracted researchers attempting to enhance the DOS. While affixing a mode to the defect potentially reduces the pumping threshold, it also reduces the maximum emission energy of the device when compared with the corresponding band-edge laser devices. Therefore, a trade-off must be made between the excitation threshold and the maximum achievable emission energy.

2.2.3 Emission process in a laser system

There are three fundamental mechanisms that can occur when light interacts with an atom – absorption, spontaneous emission and stimulated emission and these are illustrated in Figure 2.16. Absorption occurs when an atom in a lower energy level absorbs a photon of energy, $h\nu$ (where h is Planck's constant and ν is the frequency) transferring the electron to a higher energy level as depicted in Figure 2.16 (a).

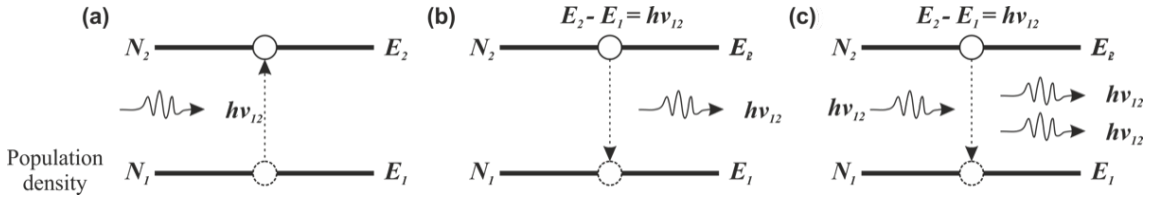


FIGURE 2.16: A two-level energy system for (**a**) absorption, (**b**) spontaneous, and (**c**) stimulated emission

Spontaneous emission occurs when an atom from a higher energy level relaxes back to a lower energy electronic level by releasing its energy in the form of the emission of a photon. To understand this phenomenon, consider a two-level energy system E_1 and E_2 such that $E_2 > E_1$ with E_1 being the ground state as shown in Figure 2.16 (b). Following

the absorption of a photon and the excitation to E_2 from E_1, the electron relaxes back to E_1 and releases energy in the form of a photon equal to the energy difference ($\Delta E = h\nu$) between the two levels. The emitted photon has an arbitrary polarisation and random direction.

On the contrary, stimulated emission as illustrated in Figure 2.16 (c) occurs as a result of the interaction of an excited electron in (E_2) with external radiation such that the electron relaxes back to ground level (E_1) via the emission of a photon with the same energy, frequency and direction as the incident photon. This can only occur when the external radiation possesses energy in a frequency range that matches the energy which is lost when returning to the ground state.

Optical amplification requires the rate of stimulated emission to be greater than the rate of radiative absorption, which means that a higher proportion of electrons must exist in the excited state than the ground state, referred to as a population inversion. This, however, under normal circumstances does not exist as more electrons tend to reside in the ground state and can population inversion only be achieved by elevating more electrons to the excited state through external means, i.e. optical or electrical pumping. Additionally, for a simple two – level system, the absorption rate is equal to the emission rate, and therefore it is impossible to produce a population inversion in a simple two-level energy system.

In a three– or four – level system, energy differences (ΔE) exist such that the absorption and emission do not balance, making it possible to achieve a net gain. For molecules, in particular, at each electronic energy level there exists additional rotational and vibrational sub-levels thus forming multiple excitation and de-excitation routes, Figure 2.17 (a).

In the four – level system (Figure 2.17 (b)), the electron is excited from the ground state (E_0) with an external pumping mechanism to the level (E_3) from where it rapidly decays in a non-radiative way to the upper laser level (E_2). While the decay from E_3 to E_2 is very fast ($<ps$), it produces a higher proportion of electrons in E_2 whereas E_1 remains empty – a population inversion. The electrons from E_2 then relax to E_1 over a longer timescale through stimulated emission, where they then quickly drop back to E_0

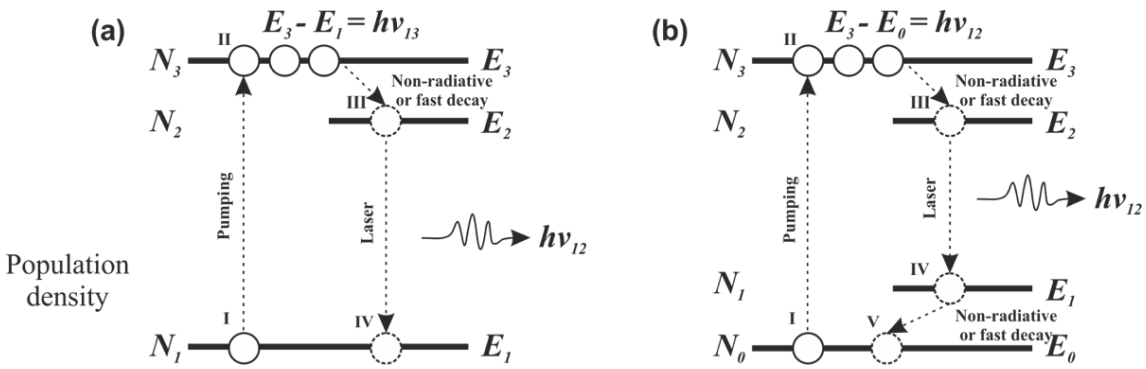


FIGURE 2.17: Illustration of (**a**) three-level and (**b**) four-level laser systems.

from E_1. For continuous wave operation, the transition from $1 \rightarrow 0$ must be fast and the decay should be non-radiative. The operation of the three-level system is similar to the four-level system, although the population inversion in four-level systems is much easier to establish than for three-level systems [58].

2.2.4 Jablonski diagram

The Jablonski diagram is an illustration to represent the electronic states of a molecule and the transition between the electronic states that help understand the emission process [59]. Figure 2.18 shows the Jablonski diagram where the horizontal bold lines represents the electronic states. Along the vertical axis, energy of the system increases, i.e. S_0 being lowest. S_0 is the ground electronic state whereas S_1 is the excited electronic state. In S_0, electrons exist as a pair, one spin up and other spin down with a net spin = 0, which implies a singlet electronic state and is denoted with S. However, if electron spin flips, and the net spin $\neq 0$, it will be in the triplet electronic states, that is represented with T_1. Within each electronic state, the sub-levels (shown with the thin lines) are the vibrational states, i.e., electrons within the ground state would have different vibrational energies.

When the electron in the ground state absorbs light of energy higher than the energy difference between S_0 and S_1, an electron transits from the ground state S_0 to S_1. Since the spin of the electron remains unchanged, it therefore stays in the singlet state. Notice that electron transits to the higher vibrational state of excited state S_1, which implies the electron is excited both electronically and vibrationally – this is the *absorption* and represented with '**1**' (blue line) in Figure 2.18. After this, the electron gives off energy and relaxes to the lowest vibrational state in the excited electronic state S_1. This is called

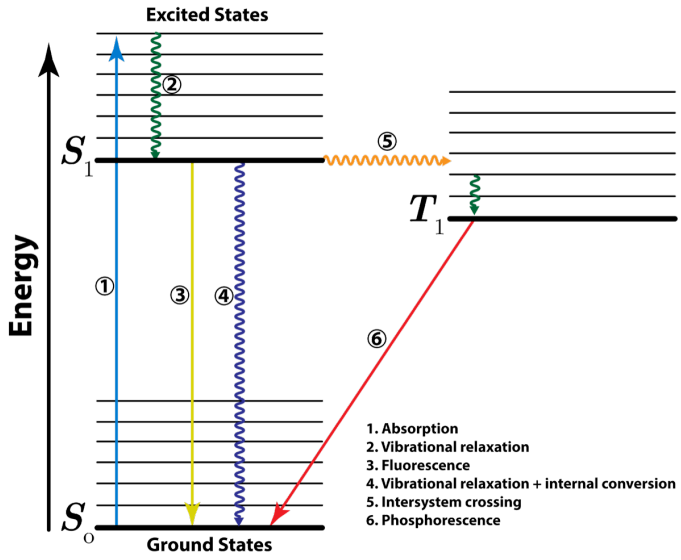


FIGURE 2.18: Jablonski diagram of a light emitting system illustrating the different radiative and nonradiative mechanisms involved.

vibrational relaxation and is a non-radiative process as the energy released by electron is in form of heat. This is shown with '**2**' (green line) in Figure 2.18.

From here, there are multiple possibilities that an electron can undertake. One of them is relaxation from the lowest vibration excited electronic state to the lowest ground state and radiates energy as a photon. This is *fluorescence* and is a radiative process as an electron releases energy in the form of a photon. It is shown with '**3**' (yellow colour) in Figure 2.18. A second possibility is to relax non-radiatively by giving off energy in the form of heat from the lowest excited stated (S_1) to the lowest ground state (S_0). This is called *vibrational relaxation + internal conversion* and shown with '**4**' (purple line). Vibrational relaxation means the energy is released in the form of heat and internal conversion means that the electron is changing electronic state from S_1 to S_0.

The third possibility is, after the vibrational relaxation from higher vibrational excited states in S_1, the electron flips spin and pairs with an electron so that the net spin is no longer zero, this means, the electron is now in the triplet state (T_1). This is the *intersystem crossing* (transition from singlet to triplet state) and is illustrated with '**5**' (orange colour). From the excited vibrational the triplet state, electron undergoes vibrational relaxation to the lowest vibrational state in triplet state and eventually radiatively relaxes to the lowest ground electronic state (S_0). During the radiative relaxation, an electron releases energy in the form of light, this process is called *phosphorescence* and shown with

'**6**' (red colour).

The absorption energy is highest as the energy absorbed by the electron is released both radiatively and non-radiatively. The fluorescence energy is higher than the phosphorescence as some of the energy in phosphorescence is released non-radiatively. In general, $E_{abs} > E_{fluor} > E_{phos}$ where E_{abs}, E_{fluor} and E_{phos} are the energies at absorption, fluorescence and phosphorescence emission, respectively. Furthermore, phosphorescence is a slower process than fluorescence as before it takes places as it is a forbidden transition. As vibrational relaxation is a non-radiative process and therefore causes heat in the system. Examples of materials that show fluorescence emission include organic dyes, quantum dots, conjugate polymers whereas metal-based clustomesogens exhibit phosphorescence.

2.2.5 Gain media

A gain-medium or optical amplifier is simply a material that can be 'pumped' into a population inversion and generates an amplified output. Once excited into a higher energy level, the electrons relax back to the ground state from the excited state which were previously populated by the pumping process.

The gain medium has a variety of important physical properties that make it suitable for use in a laser device. These properties include transition characteristics, quantum efficiency, emission spectrum and pump threshold. Transition cross-sections are used to measure the probability of optically introduced transition events, i.e. absorption or stimulated emission. For a particular electronic state, the rate of transitions (event/sec) is defined as the corresponding cross-section times the photon-flux as $R = \sigma\left(I/h\nu\right)$ where R is the transition rate (s^{-1}), σ is the transition cross-section, I is the optical intensity and $h\nu$ is the photon energy. Transition cross-sections depend on the wavelength and involve resonances that cause a strong peak in the cross-section spectra. For a laser, the most relevant transition cross-sections are the absorption and emission cross-sections at the pump and laser emission wavelength, respectively. For crystal-based lasers, these cross-sections are typically of the order of $10^{-20} \sim 10^{-18}$ cm^2 whereas for dye lasers, the emission cross-section is of the order of 10^{-16} cm^2.

The quantum yield or efficiency is an important quantity in laser physics which

is the fraction of the input photons that contributed to the desired effect. For example, in the laser gain media, pumping requires the transfer of electrons from one electronic state to an upper state of the laser transition. The pump quantum yield is the percentage of the absorbed photon from the pump source that gives rise to the population inversion and this efficiency can ideally be unity (100%) but practically is substantially smaller.

Doped insulator lasers have demonstrated a wide amplification bandwidth that allows a larger wavelength tuning range and ultrashort pulses as compared to crystalline lasers. However, they exhibited lower laser cross-sections and thermal properties (limited output power), higher pump thresholds and inferior Q-switching instabilities. The doping concentration of glass, crystal and ceramic needs to be optimised carefully as higher doping concentration can be good for pump absorption over a short length scale but leads to energy losses related to quenching. Furthermore, dye-based lasers are relatively easy to fabricate, have higher PL and wavelength tuneability, but exhibit shorter lifetimes as the dyes become photo-bleached when optically pumped. In this regard, a solution processed gain medium with a high quantum efficiency that is insensitive towards photo-bleaching is required. Therefore, owing to such characteristics, perovskite [60], as bulk and nanocrystals, and quantum dots [61, 62] are considered as potential optical gain medium. In this Thesis, two kinds of gain materials are considered for use in thin-film LC lasers, 1) laser dyes and 2) nanocrystals. In the following sections, both of these gain materials are introduced.

2.2.5.1 Organic laser dyes

Organic dyes have been used in various applications from spectroscopy studies for chemical analysis to microscopic investigation of biological species. The organic dye chloro-aluminum phthalocyanine solution was used by Fritz *et al.* in simple cavity of plane-parallel cuvettes and pumped with a pulse ruby laser to demonstrate the first dye-based liquid laser [63]. Organic dyes in comparison to the inorganic dyes offer benefit in terms of wavelength tunning across the visible spectrum. They can dissolve in various solution and are compatible with solution processing techniques to create a thin film. This opens up the potential to further progress the synthesis of organic dyes and has been used to create several dye-based lasers [64–66]. Table 2.1 summaries photophysical characteristics such as maximum absorption, emission, and fluorescence quantum yield

of widely used laser dyes in solvent (ethanol or methanol).

TABLE 2.1: Photo-physics of different laser dyes (Rhodamine dyes: Rh-123 & Rh-B), 4-dicyanomethylene-2-methyl-6-p-dimethylamino-styryl-4H-pyran (DCM), Coumarin 151 (C-151) and Pyrromethene 597 (PM597)) in different solvents.

Dye	**Solvent**	λ_{ab} (nm)	λ_{fl} (nm)	ϕ_f ± 0.05	**Ref**
Rh-123	Ethanol	507	530	0.86	[67]
Rh-B	Polyethylene glycol	550	650	0.80	[68]
DCM	Methanol	465	630	0.44	[69]
C-151	Ethanol	383	485	0.49	[70]
PM597	Ethanol	525	563	0.43	[71]

Maximum of wavelength of absorbance (λ_{ab}) and fluorescence (λ_{fl}), and fluorescence quantum yield (ϕ_f).

The choice of the laser dye is important for the laser process and generally the potential candidate needs to fulfil key requirements for the successful demonstration of a dye-based laser. A laser dye should possess a strong absorption at the excitation wavelength and lowest absorption at the emission wavelength. In other words, their absorption and emission spectra should not overlap. They should exhibit good photo-chemical stability when they dissolve into solvent and pumped. Laser dyes also have higher quantum yield of more than 50 percent and exhibit shorter fluorescence lifetimes of about 5 to 10 ns. As seen in an earlier section, for the fluorescence action, intersystem crossing should be minimised in order to avoid populating the triplet states. Furthermore, impurity in the dyes can cause photo-quenching, which is highly undesirable for stable laser emission [72].

The composition and structure of a laser dye is essential for emission. Laser dyes are complex molecules that mainly consist of phenyl ring(s) that can be classified into different categories based on their structures: coumarins [73], xanthenes [74] and pyrromethenes [75–77]. Coumarins dyes are the derivative of coumarins molecules that show emission from blue to green. Coumarins molecules are non-fluorescent in nature, however by adding a suitable functional group to the molecules, emission from coumarins can be achieved. The first coumarin dye-based laser contained 7-diethylamino-4-methylcoumarin, which showed laser emission at 460 nm upon photoexcitation with a lamp. Examples of other coumarin dyes include Coumarins-102 [78] [80], Coumarins-151 [70] and Coumarins-522 [79]. Coumarin-based dyes show photo-instability and decompose due to the laser. The product formed after the degradation

can absorb output laser that can affect the device performance.

Xanthene dyes are considered one of the most efficient laser dyes and exhibit emission from green to red. Rhodamine B [80] and Fluorescein [81] are the two commercially available xanthene dyes. Rhodamine 6G is one of the example dyes of the class Rhodamine B and is a highly photostable laser dye that is also used as a reference to measure the efficiency of the other laser dyes. By modification to the molecular structure, the dye emission performance can be improved; for example, if the phenyl ring in Rhodamine 6G is replaced with $-CF_3$ it forms the Rhodamine 700, which improves the emission stability of the dye.

Pyrromethene, dipyrromethene or boron-dipyrromethene dyes are some of the most efficient laser dyes. These dyes consist of phenyl rings attached to a boron atom (BF_2) and show tuneable emission from green to yellow region in the visible spectrum. They exhibit excellent photostability, low intersystem crossing, high emission quantum yield and absorption coefficient. Example dyes include pyrromethene PM567 (λ_{ems} = 567 nm) [82] and PM597 (λ_{ems} = 597 nm) [83] and are solute in various solvents. In this Thesis, pyrromethene PM597 dye laser is used to create a flexible defect-mode laser. Further background on the photo-physical characteristics of PM597 are presented in Chapter 7.

While, in general, laser dyes are compatible with solution processing techniques, demonstrate photostability, high fluorescence quantum yield, larger absorption coefficient and peak emission wavelength across the entire visible region, the output laser intensity in dye-based lasers cannot exceed a certain level even when increasing the pump energy which can cause photo-quenching. It is therefore imperative to investigate alternative gain materials that are compatible with LC materials and solution processing and could be used as a potential gain material for the LC laser. In this regard, colloidal quantum dots are considered that can show several interesting characteristics (such as photo-stability, wavelength tuning) that are desirable for the laser.

2.2.5.2 Quantum dots

Semiconductor quantum dots (QD) are synthesised from group II-VI, III-V, and IV-VI elements ranging in size from $2 - 10$ nm with diverse electronic and optoelectronic properties which make them suitable for photonic, biomedical and photovoltaic (PV) devices. With their shape- and size-dependent optoelectronic properties, they exhibit

a quantum confinement effect i.e. strong confinement of holes and electrons when the particle size is less than the exciton Bohr radius of the material. The relationship between size and band gap energy of nanocrystals is given as [84]:

$$E_{g,Qd} = E_{g,b} + \left(\frac{\hbar}{8R^2}\right)\left(\frac{1}{m_e^*} + \frac{1}{m_h^*}\right) - \left(\frac{1.8e^2}{4\pi\varepsilon\varepsilon_0 R}\right) \tag{2.10}$$

Here R is the radius of the QD, $E_{g,Qd}$ and $E_{g,b}$ are the bandgap energies of the QD and the bulk material, m_e^* and m_h^* are the effective mass of electron and holes, respectively, $\hbar$ is the reduced Planck's constant and e is the electron charge. The band gap energy of a QD directly relates to its size – reducing the size of a QD results in a higher band gap energy thereby tuning the emission wavelength, Figure 2.19 (a & b).

In addition to tuning the emission wavelength by changing the size, QDs emit at a longer wavelength than is expected for a given size. The problem arises due to surface defects also called surface traps. These defects result from dangling bonds and imperfections, and have their own electronic states localised within the QD, which leads to non-radiative recombination, thus reducing the PL efficiency while emitting at lower energy. This can be overcome with the *core – shell* approach in which the surface of the QD is passivated with another material with larger band gap that results in a reduction of these surface trap sites (Figure 2.19 (c)). Furthermore, while synthesising QDs, ligands play a vital role in changing the physical and chemical states of the QD surface and disturb their photo-physical properties by interacting with surface atoms [85]. Therefore, much research have been done on their type, concentration, precursor ratios, growth rate and temperature to enhance the stability of QDs [86]. In this Thesis, perovskite quantum dots/nanocrystals are used as a potential gain material for LC lasers and are discussed further in Chapter 5.

2.2.6 Functionality

Liquid crystals are compatible with solution processing techniques and have been used in several laser structures when combined with different laser dyes to create either a band-edge or defect-mode laser [87]. In recent years, thin films of bulk perovskite and perovskite nanocrystals have also attracted considerable attention for use in such devices. To date, perovskite materials have been used in configurations to demonstrate amplified spontaneous emission in a corrugated polymer structure [88] and also been

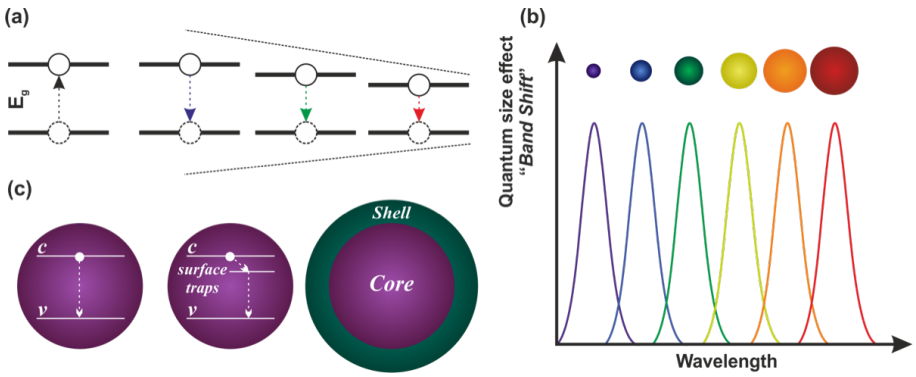


FIGURE 2.19: (**a**) Quantum size effect, (**b**) size dependent emission wavelength, and (c) core-shell approach in QD synthesis.

combined with LC and metal reflectors that showed laser emission [89]. For perovskites, the emission wavelength can be changed by varying the composition of the halide group [90, 91]. It is also possible to achieve multi-colour emission from these materials either by using blends or modifying the construction of the laser cavity so that it can support multiple modes. Furthermore, unlike conventional inorganic materials, thin films of both LC and organic dyes or perovskites can be used with flexible and conformable substrates, which can be mechanically deformed and are of interest for wearable technologies and gadgets [92–96].

2.2.7 Emission characteristics

The slope efficiency and laser excitation fluence threshold are critical in determining the performance of a laser. In an optically pumped laser system, the slope efficiency (η) is the slope of the curve that is obtained by plotting the output laser emission versus input pump power and can be defined as $\eta = {}^{\Delta P_o}/_{\Delta P_i}$ where ΔP_o is the change in the output laser power and ΔP_i is the change in input pump power. The excitation threshold is the state when the optical gain is equal to the cavity losses. This implies that to achieve a lower excitation threshold, the laser system should be created with an optical cavity with lower losses and a highly efficient gain material [97]; example fluence threshold plot is present and explain in Figure 3.21 (b) in Chapter 3.

Several laser dyes have been used in various configurations to create micro/-nano lasers that demonstrate low excitation threshold; for example, Rhodamine dye-based laser systems have shown pump thresholds as low as a few tens of $\mu J/cm^2/pulse$ [103, 104] in a whispering gallery mode configuration. For LC lasers, the laser pump

TABLE 2.2: The fluence excitation threshold in band-edge and defect-mode LC laser configurations created with different dyes.

LC Laser Type	Materials	f (Hz)	E_{th} (cm^2/pulse)	Ref
Band-Edge	Flexible CLC + DCM	10	1.53 mJ	[96]
	CLC + pyrene dye	10	8.1 mJ	[98]
	Stretchable CLC + PM597	10	3.1 mJ	[99]
	PhCLC + PM597	10	0.75 μJ	[87]
	Printed PDLC + PM597	1	5.66 mJ	[38]
	CLC + PM597	10k	1.1 mJ	[100]
	CLC + Chromophore	1	20 mJ	[101]
Defect-Mode	PhCLC + T-PPV† dye	-	1.3 mJ	[53]
	CLC + DCM	10	16.7 mJ	[102]
	PhCLC + DCM	10	30 mJ	[94]
	CLC + DCM (twist defect)	1000	25.5 nJ	[42]
	PhCLC + T-PPV† dye	10	4 mJ	[55]

Repetition rate of pump laser (f) and fluence excitation threshold (E_{th}), PhCLC is photo-polymerised chiral nematic LC and †T-PPV: triptycene poly(p-phenylene vinylene).

threshold depends on the gain media and the type of LC laser. For a band-edge LC laser, the pump threshold is typically of the order of a few mJ/cm^2/pulse [98, 100, 105] whereas for LC defect-mode lasers the pump threshold is found to be lower and is typically in the range of hundreds of μJ/cm^2/pulse to tens of mJ/cm^2/pulse [42, 53, 94, 102]. Table 2.2 summaries the excitation fluence threshold in LC laser configurations either of band-edge or defect-mode created with different dyes. Furthermore, one aspect of creating the optical cavity with LC materials is that they offer optical anisotropy and the high birefringent LC can benefit in reducing the excitation fluence threshold as the excitation threshold is inversely proportional to the birefringence of the material [106–110]. In this regard, the electro-optic study of a newly developed high birefringent LC dimer is also investigated and presented in Chapter 4.

2.2.8 Summary

This chapter provides general background on liquid crystals and gain materials relevant to the studies carried out in this thesis. In the first half of the chapter, the physical and optical properties of certain LC phases were introduced, including discussion on the distinction between thermotropic and lyotropic LCs. The different LC mesophases such as the nematic, chiral nematic, smectic, and blue phase were briefly discussed, which was followed by an introduction to the optical and electro-optic characteristics of the nematic

LC phase, including birefringence, dielectric anisotropy, and the Freedericksz transition. Furthermore, the optical properties of a chiral nematic phase were also discussed. Different types of alignment were introduced, such as planar and homeotropic alignment, as well as the different optical textures observed for a chiral nematic phase.

In the second half of the chapter, a brief background on laser devices was presented, highlighting the salient features relevant to this thesis. Since this Thesis uses two types of gain media, laser dyes and perovskites, a general description of the 3 and 4-level emission processes was provided with the help of the Jablonski diagram. A short summary of the properties of quantum dots/nanocrystals and their emission characteristics was also presented. Combining advanced gain materials with LCs enables functionality such as wavelength tuning, compatibility with solution processing techniques, and compatibility with flexible substrates platform to be realised and in this regard, the relevant literature has been presented. The emission characteristics for an optically-pumped laser, such as the slope efficiency and excitation threshold, were briefly explained, and a comparison with the reported excitation fluence threshold for lasers based on either organic dyes or perovskites in LC hosts has been considered.

Chapter 3

Experimental Procedures

Liquid crystals (LC) are the primary material that are used to create the different photonic devices considered in this thesis. To investigate the optical and electro-optic characteristics of these materials, and to create a band-edge LC laser, glass cells that range in thickness from 10 - 15 μm are required [107]. The assembly of the glass cells is critical in order to study the optical characteristics under different conditions. The following section outlines the construction of a typical industrially-manufactured LC glass cell and explains the preparation process of such cells in the laboratory using different alignment layers.

3.1 Liquid Crystal Cell

The LC cells consist of two transparent glass substrates (typically 0.7 mm-thick) that are combined together using glue leaving an air-gap that ranges from 5 μm to 50 μm, depending upon the spacers (spacer beads or Kapton film) that have been used. The LC compound is then capillary-filled between these two glass substrates. LC cells can vary in a number of different ways such as the type of alignment layer, the gap between the two substrates, the use and layout of electrodes, as well as the type of spacer. Figure 3.1 illustrates a typical commercially-manufactured LC cell showing spacer beads that are uniformly distributed across the device to define the thickness of the air-gap and subsequently the LC film thickness.

Typically, a LC cell is prepared by adding a number of different layers as shown in Figure 3.1 (a). Fabrication starts with a pair of glass substrates that consist of patterned

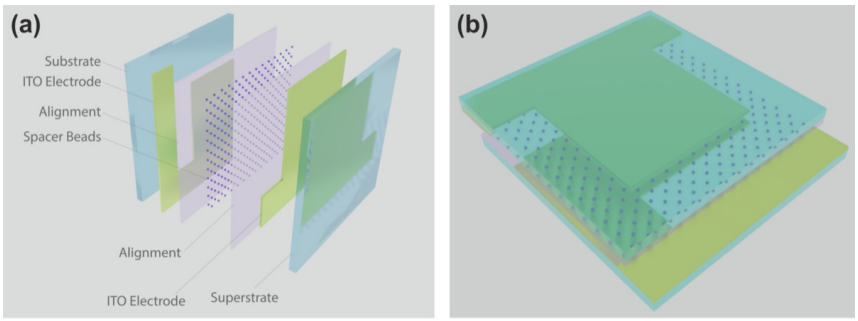


FIGURE 3.1: **(a)** An example of the architecture of a liquid crystal (LC) cell used in this work and **(b)** the construction in a typical commercially-available LC cell.

transparent electrodes, usually in the form of an indium tin oxide (ITO) layer. Next, the alignment layer is deposited, which is needed to define the arrangement of the LC director at the glass/LC interface and consequently throughout the bulk of the LC layer. This defines the type of cell that is fabricated e.g. planar, homeotropic or a combination of both (i.e., hybrid alignment). Generally, rubbed polyvinyl alcohol (PVA) or polyimide (PI) are used to give a planar alignment whereas a thin layer of lecithin results in a homeotropic arrangement of the director. The glass substrates with the electrode and alignment layers are then combined by sandwiching spacers between them. The spacers provide a gap between the two substrates where the LC mixture can be inserted. The spacers, in general, are made of silica (and called silica spacer bead) and vary in diameter from 5, 7, 10 and 20 μm. An illustration of a complete LC cell is presented in Figure 3.1.

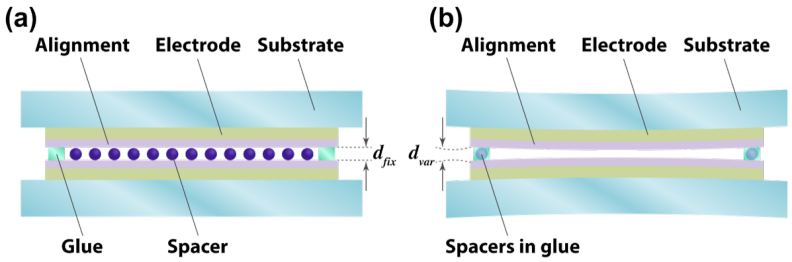


FIGURE 3.2: The cross-section of an LC cell illustrating the variation in the cell gap when **(a)** the spacer beads are distributed across the device and **(b)** spacer beads are mixed in the glue.

The spacer beads can be spread across the device so as to maintain a uniform cell gap between the substrates as shown Figure 3.2 (a). Alternatively, they can be mixed directly into the glue and applied at the edges of the cells that holds the two substrates together. In such an arrangement, the cell gap may vary across the device due to a bulge created at the centre of the device as shown in Figure 3.2 (b).

The following sub-sections describe the experimental methods used in this work to prepare planar-aligned and homeotropic-aligned LC cells.

3.1.1 Planar aligned LC cell

The planar alignment of the LC director is explained in detail in §2.1.1.1, Chapter 2, whereby the LC molecules align parallel to the surface of the substrates. Figure 3.3 illustrates the fabrication process employed to prepare a planar aligned LC cell. Either bare glass or ITO-coated glass substrates can be used. The process begins by immersing the substrates in a beaker filled with acetone that is placed in an ultrasonic bath (Barson 2510) [111] to clean any organic impurities from the substrates. Each substrate was sonicated for 20 min at 25°C. During sonication, the beaker was covered with parafilm tape to avoid the evaporation of the acetone.

The substrates were then transferred onto the platform of a spin-coater where, before dispensing any solution, they were further cleaned by gently rubbing across the surface of the substrate using an optical wipe (ThorLab MC-5, Lens Tissues) [112] that is dipped in acetone. This additional cleaning step removes any residual particles on the substrate when transferring the substrates to the spin coater (Figure 3.3 (ii)). 1 wt. % PVA mixture homogeneously dissolved in deionised water was dispensed on the substrate and the substrate was then spun at 1000 rpm for 30 sec before being baked in an oven at 90°C for 20 mins to remove any residual water content; this created a thin layer of PVA on the substrate, Figure 3.3 (iii – iv).

The substrates were then transferred onto a translational stage of a rubbing machine. The translation stage was connected to a suction pump which secured the substrate in place while it was rubbed. The rubbing machine consists of a drum covered with a clean velvet cloth that rubs the PVA-coated substrate. The drum can rotate either in a clockwise or anti-clockwise direction at different spin speeds, which can be adjusted depending upon the requirements. During the rubbing process, the stage moves in one direction, say towards the '$+x$' direction as shown in Figure 3.3 (v), whereas the drum rotates in an anti-clockwise direction. The drum spin speed was adjusted to 2000 rpm in an anticlockwise direction while rubbing the PVA coated substrate. In order to encourage a strong alignment, the substrate was rubbed multiple times; for example, in this process, the number of rubs was found to be optimised at 2 – 3 times by preparing substrates and

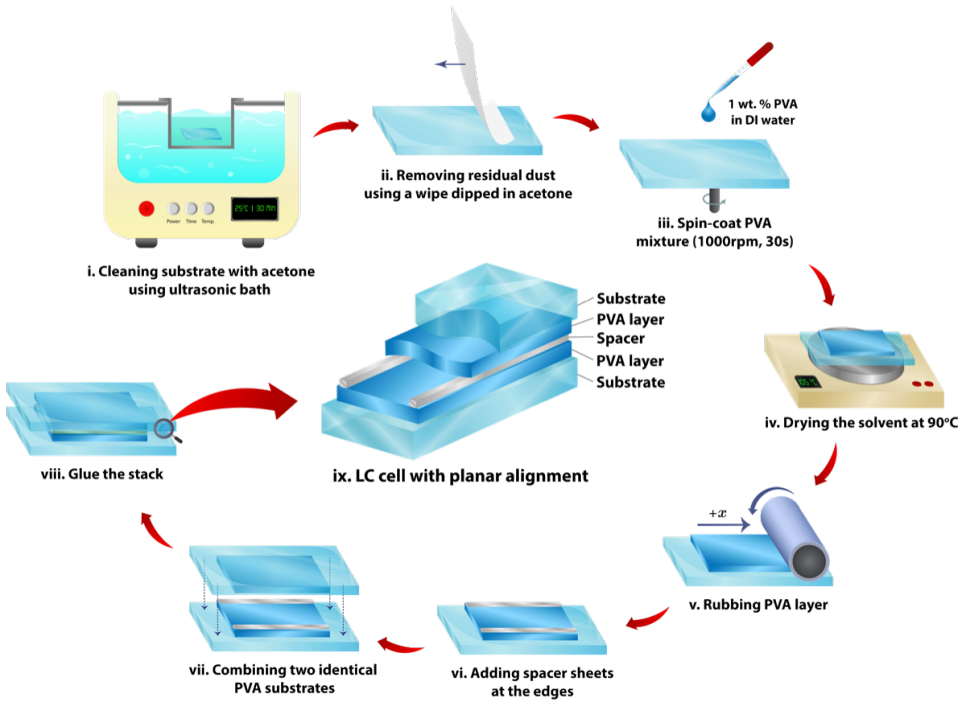


FIGURE 3.3: Illustration of the process used to create a LC cell with planar alignment layers.

filling them with nematic LC to achieve planar alignment. It is also important to keep the substrate position and the rubbing direction the same throughout the process. Two identical substrates were prepared using this process that were used to create one LC cell.

The next step is to add the spacers: one choice is to use Kapton film, which are available in different thicknesses including 5, 10, 23, and 50 μm. Small pieces of spacer sheet are placed on two edges of one of the two substrates before attaching the top substrate and applying the glue at the edges. Alternatively, silica spear beads are mixed into Norland UV-curable glue [113]. The stack of the two substrates were then held together with clips and the spacer beads-glue mixture was then applied using a glue dispenser (Nordson Performus V, 0 $\sim$ 100 psi) with syringe (Nordson Percision Tips, 30GA Lavender). The glue is then photo-polymerised using UV radiation (ThorLab CS2010 UV 365 nm curing LED System) [112] at 20 mW/cm^2 for 40 sec. The complete LC cell consists of a glass substrate/PVA/spacers/PVA/substrate. A cross-sectional view of a planar aligned LC cell is shown in Figure 3.3 (ix).

3.1.2 Homeotropic LC cell

For the homeotropic LC cell, the LC director is aligned at 90° with respect to the plane of the substrate. When observed between the crossed polariser and analyser of

an optical polarising microscope the device appears dark. Further detail on homeotropic alignment is given in §2.1.1.1, Chapter 2. The fabrication process for the homeotropic cell is illustrated in Figure 3.4. First, the substrates were cleaned using the ultrasonic bath while immersed in acetone for 20 min at 25°C. This was followed by wiping the substrates with an optical tissue dipped in acetone. 0.02 wt. % of Lecithin (L-α-Phosphatidylcholine purchased from Merck) [114] was dissolved in polyimide and the mixture was stirred at 200 rpm at room temperature for 24 hrs. Once a homogeneous mixture had been prepared, the mixture was injected into a pipette that was attached to a filter to remove any residue from the mixture. The sample was then spin-coated at 1000 rpm for 30 sec and baked on a hot-plate at 70°C for 5 min to evaporate the solvent. These steps are shown in Figure 3.4 (i - iv). An identical substrate was also prepared following the same processing steps. Spaces were then added on the substrates as explained earlier and glue was applied to seal the cell, Figure 3.4 (v – viii). The complete device arrangement consists of glass substrate/lecithin/spacer/lecithin/substrate as shown in Figure 3.4 (ix).

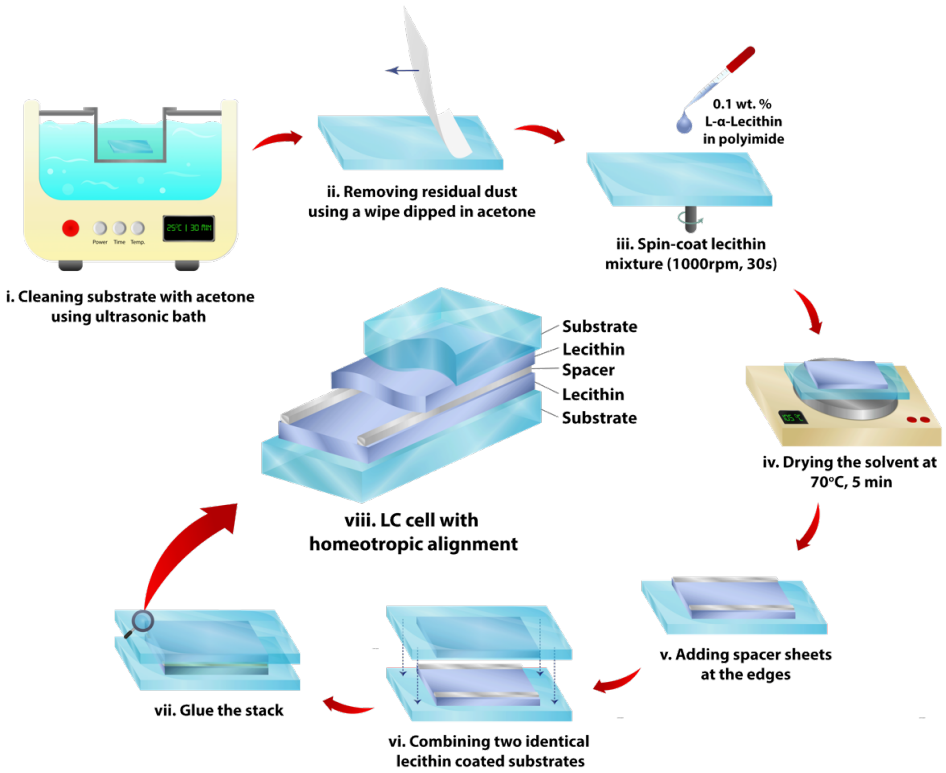


FIGURE 3.4: Illustration of the process used to create a LC cell with homeotropic alignment.

Once the device was ready, the LC mixture was injected into the cell. For cell gaps that were greater than 20 μm it was found that devices had to be left for a couple of

hours after filling to enable the LC director to assume a homeotropic alignment.

3.1.3 Chiral LC mixture preparation

The chiral nematic LC phase is used in this Thesis to create the optical cavity for the laser and to investigate the flexoelectro-optic effect. To prepare chiral nematic LCs, nematic LCs can be combined with a chiral dopant. Chiral dopants are chosen based upon their helical twisting power (HTP) and the handedness of the helix (i.e. left or right-handed). For a chiral nematic phase, the pitch can be adjusted by varying the concentration of the chiral dopant and obeys the relationship [115]:

$$p = \frac{1}{c_w \beta e_e} \tag{3.1}$$

where c_w is the concentration and β is the helical twisting power (HTP) of the chiral dopant (measure in μm^{-1}), and e_e defines the enantiomeric purity. Numerous chiral dopants are available such as ZL14572 [116], S811 [117], R5011 [118], R1011 [118], CB15 [118] and BDH1281 [116, 119], each one has a different HTP value when doped into a nematic LC to form a chiral nematic LC phase. Among them, BDH1281 and R5011 have been found to exhibit large values of HTP. Chiral dopants with higher twisting powers are advantageous as a lower concentration by weight is required to form a helical structure with a pitch of the order of the wavelength of light. Furthermore, the lower concentration of chiral dopant means that the properties of the pseudo-nematic layers of the chiral nematic mixture will closely resemble that of the host nematic LC.

The mixture constituents used to prepare the chiral nematic phase in this study were measured precisely using a microbalance (Mettler Toledo AB104-S) [120] with weight measuring accuracy of ± 0.05 mg. The mixture composition throughout the thesis is quoted as the weight percentage, conventionally denoted as wt. % and given as (weight of solute)/(weight of host). To prepare the mixture, an empty vial was placed on the measuring balance and the chiral dopant was added to the desired amount followed by the nematic LC using a micropipette. Once the required concentration was achieved, a small magnetic stirrer was added to the vial, which was then transferred to a hotplate that was equipped with magnetic stirring control. The mixture was heated to 10°C above the clearing temperature of the host nematic LC and mixed at least 200 rpm for about 24 hr to form a homogeneous mixture. An empty cell was placed on the hotplate and the

mixture was then injected into a glass cell.

3.2 Solution Processing Techniques

Solution-processing techniques that function in atmospheric conditions offer several benefits over conventional vacuum-deposition of thin-films, which typically require stringent processing conditions. Solution processing enables the use of a wide range of materials and is compatible with many different kinds of substrates including flexible substrates. This form of processing also enables large scale production and inexpensive manufacturing [121]. Scalable deposition techniques can be divided into two categories: 1) direct growth of a substance on a substrate during deposition and 2) using a solution to coat the material that requires further processing such as thermal annealing after deposition [122, 123].

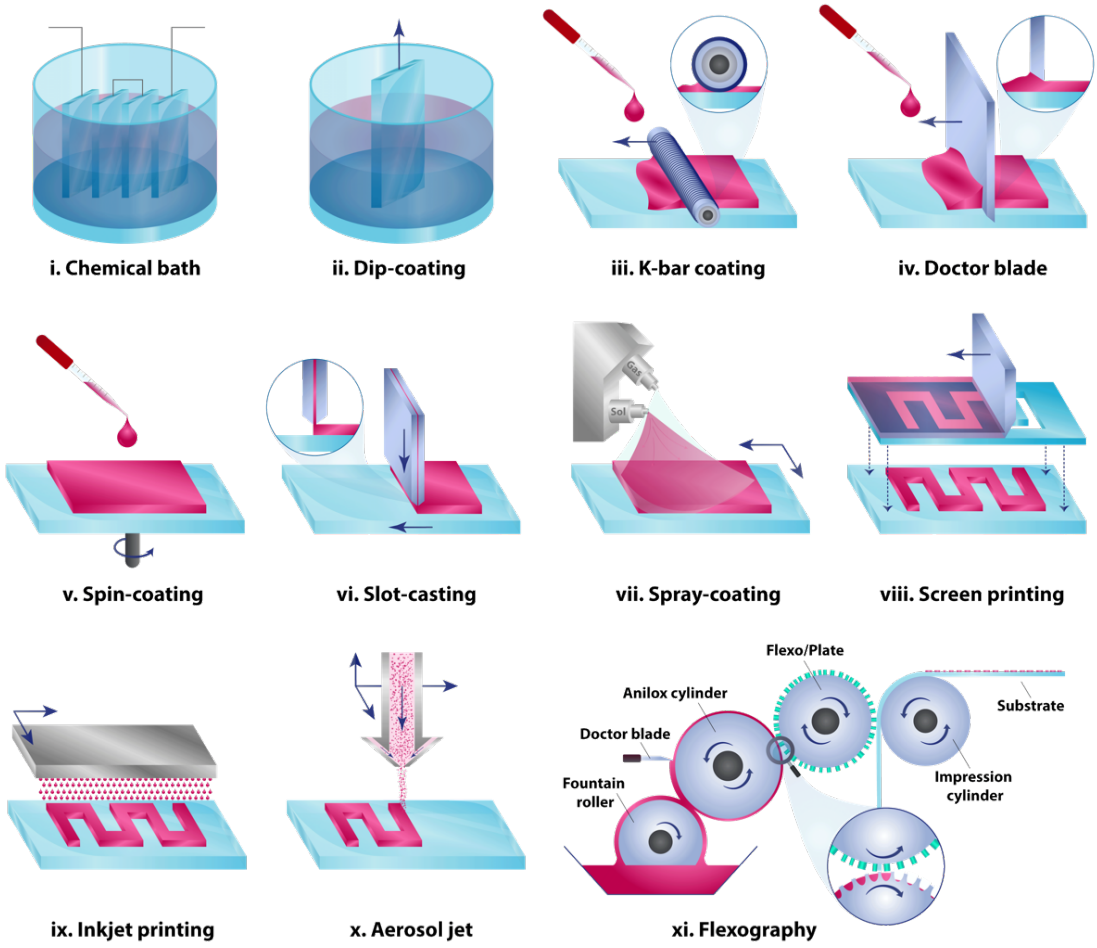


FIGURE 3.5: Solution processing techniques **(i)** chemical bath, **(ii)** dip coating, **(iii)** K-bar coating, **(iv)** doctor blading, **(v)** spin coating, **(vi)** slot casting, **(vii)** spray-coating, **(viii)** screen printing, **(ix)** inkjet printing, **(x)** aerosol jet, and **(xi)** flexography.

Figure 3.5 illustrates commonly used solution processing and patterning techniques to deposit thin-films. These include chemical bath, dip and K-bar coating, doctor blading, spin-coating, slot or slit casting, screen printing, inkjet printing, spray coating, aerosol jet and flexography. For the chemical bath method, Figure 3.5 (i), both the substrates and the source materials are immersed into a solution to form an electrochemical cell. During electrolysis, the material is directly deposited onto the substrate via the precipitation of species under a controlled reaction. The disadvantage of this method is the appearance of a waste by-product. Alternatively, for the dip-coating method (Figure 3.5 (ii)) the solution can be used again to prepare multiple samples. A thin film is created while withdrawing the substrate from the solution reservoir either in batches or as a continuous process. This method deposits a thin film on both sides of the substrates.

There are other methods that can deposit thin-films only onto one side of the substrate such as K-bar coating, doctor blading and spin-coating. For K-coating method, Figure 3.5 (iii), wire-wound metal rods (also called Mayer/Meyer rods) are used that rub across the surface containing the material that needs to be deposited. The film thickness is determined by the diameter of the wire. Instead of using rods, a blade can be used to spread the material on the substrate, known as doctor blading, as shown in Figure 3.5 (iv). The gap between the blade and substrate determines the thickness of the film.

Spin-coating is a widely used solution processing technique for the small-scale production of thin-films in research laboratories due to its simplicity and compatibility with various solution processable materials, Figure 3.5 (v). It can be divided into two main types: 1) static spin-coating and 2) dynamic spin-coating. For static spin coating, the substrate is placed on the coater stage and secured using vacuum suction; the material is then dispensed on the substrate before it is spun (typically for several thousand rpm). For dynamic coating, however, the substrate is first spun, and the solution is then dispensed while the substrate is spinning. For both methods, a uniform thin film can be created through the radial flow of the solution across the substrate. Once the film has been deposited, the sample is then thermally annealed to evaporate the residual solvent. In general, the thickness of these thin films (t) depends on the spin speed (ω) and the viscosity of the solution and in the most simplified form varies as $t \propto \sqrt{\omega}$.

Slot-casting (also known as slit or die casting), Figure 3.5 (vi), uses a slotted head

filled with a solution above the substrate that moves with a constant line speed. To deposit a thin and uniform layer, the line speed is maintained at a higher speed than that by which the material is dispensed through the slot. Spray coating (Figure 3.5 (vii)) enables large area printing that uses either liquid coating or a direct deposition method while heating the substrate above the decomposition temperature of the precursors. The process generates an atomised solution via a pneumatically controlled system and is directed via a carrier gas onto the substrate.

Patterned thin films are also important in various electronic and optoelectronic devices such as creating the contact electrodes. This is traditionally performed using masks or screen printing (Figure 3.5 (viii)) by using a screen with a desired pattern. The screen is placed on the substrate and material is dispensed and wiped with a fine blade to create a thin film. This method usually requires a high viscosity material and has limited resolution. In contrast, direct writing methods such as inkjet printing (Figure 3.5 (ix)) and aerosol jets (Figure 3.5 (x)) are an attractive choice as they are non-contact methods and can create features with resolutions down to a few tens of microns.

For large-scale production, one method that is generally used in the printing industry is known as flexography or flexo-printing. This is illustrated in Figure 3.5 (xi). The process involves a reservoir or ink tray containing the material with a fountain roller. This is physically in-contact with an anilox roller with anilox cells that contain a controlled amount of material. As the anilox roller rotates, it transfers the material to a third roller called the plate cylinder which consists of a flexo plate (small features that form the desire pattern). Material from here is eventually transferred onto a flexible substrate that wraps around the impression cylinder. This method is used to create some of the photo-polymerised chiral nematic LCs in the thesis that will be presented in Chapter 7.

3.3 Characterisation techniques

3.3.1 UV-Visible spectrophotometer

Ultraviolet-Visible (UV-Vis) spectrophotometry is a quantitative technique that is widely used in photochemistry to measure the light absorbance of a material. This is measured by comparing the intensity of light that passes through the material with respect to the intensity of light through a reference sample (or blank). This technique is

equally suitable for determining the absorbance of different types of samples including glass, solids, liquids, or thin films.

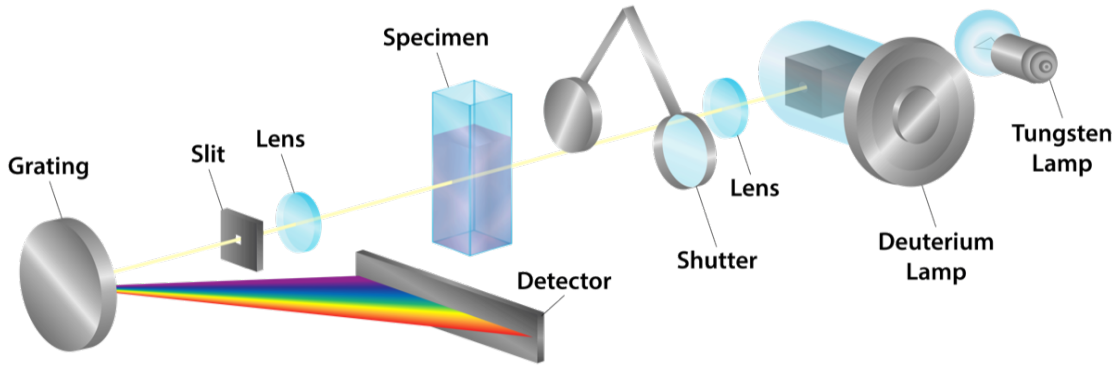


FIGURE 3.6: Arrangement of components of the UV-Vis spectrometer.

In principle, a UV-Vis spectrometer consists of a combination of light sources, a monochromator, and a detector. Figure 3.6 illustrate the basic configuration of the UV-Vis spectrophotometer (Agilent Cary 8454 UV-Vis) [124] used in this thesis, which consists of two light sources: a tungsten lamp that generates light from visible to infrared wavelengths and a deuterium lamp that can produce ultraviolet (UV) radiation. The measurement process takes two signals: 1) blank/reference signal and 2) sample signal. The measurement begins with a blank signal in which a reference sample (usually an empty cuvette or cell) is used. An internal control system opens the shutter enabling light to pass through the empty cuvette after passing through the lens. Light is then directed onto a grating by passing through another lens; the grating disperses light into all wavelengths that which is then detected by an array of sensors attached to the detector. This records a blank signal. The next step is to replace the empty cuvette or cell with the LC cell and the measurement process is repeated.

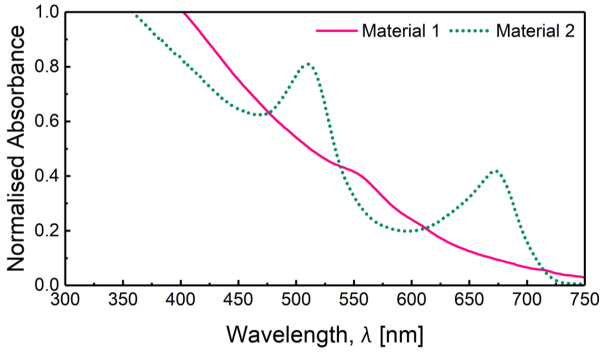


FIGURE 3.7: Example absorbance spectra of light absorbing substances, Material 1, and Material 2.

Some of the thin-films and LC cells considered in this thesis absorb certain wavelength bands, depending on the type and the concentration of the absorptive species. The sample signal is then compared with the blank signal and using the Beer-Bouguer-Lambert law, the absorbance of the compound can be estimated. The Beer-Bouguer-Lambert law (also known as the Beer-Lambert law) [125] relates the absorbance (A) of light through a substance that is given as:

$$A = \log\left(\frac{I_t}{I_r}\right) = \varepsilon l c \tag{3.2}$$

where I_t and I_r are the intensities of the transmitted and reference light, respectively, l is the path length and c is the concentration of absorbing species and ε is the molar absorption or extinction coefficient and is an important characteristic of a substance and provides information about how much and what set of wavelengths a given substance can absorb. Example spectra of two light absorbing substances are shown in Figure 3.7. While both materials show peak absorbance in the UV region, Material-2 exhibits two additional absorbance peaks at 510 nm and 675 nm.

In addition to measuring the absorbance of a substance, in this thesis, the UV-Vis spectrometer was used to estimate the thickness of the LC cells. An empty LC cell consists of a pair of parallel glass substrates with a thin gap typically of the order of a few tens of microns. When white light is transmitted along the normal of the surface of an empty cell, it generates an interference fringe pattern through the Fabry – Perot etalon effect, as shown in Figure 3.8 (a). From this fringe pattern, the cell thickness (d) can be estimated using [126, 127].

$$2nd\left|\frac{\lambda_{i+1}}{\lambda_i}\right| = k \tag{3.3}$$

where n is the refractive index of the material between the glass substrates (i.e., air, n_{air} = 1.0006), λ_{i+1} and λ_i are the wavelengths of two consecutive maxima or minima of transmitted light and k is the number of fringes between λ_{i+1} and λ_i. A Matlab script was written to calculate the thickness of the LC cell. The Matlab script plots the inverse of the wavelength (λ^{-1}) as a function of k and extracts the thickness as a gradient of linear best fit of the plot as shown in Figure 3.8 (b). The cell thickness was typically measured at five locations on a cell such as left (L), right (R), centre (C), top (T) and bottom (B) that ensures the thickness variation is minimum across the device. Cells that differ in terms of

the average measured thickness relative to the nominal thickness by more than 5% were discarded.

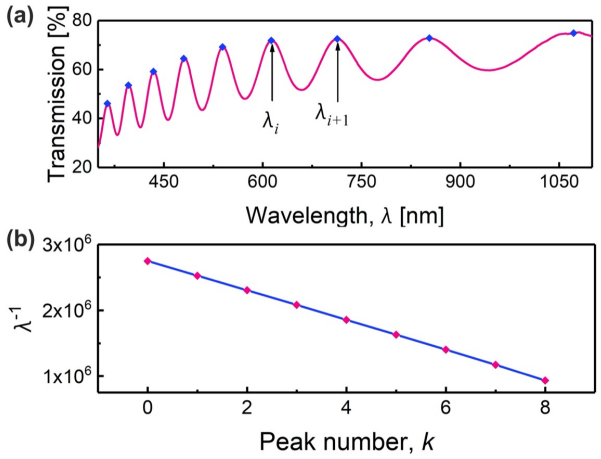


FIGURE 3.8: (**a**) The interference fringe pattern for transmitted white light through a thin LC cell, and (**b**) the locations of the consecutive interference peaks as a function of the order (peak) number. The gradient of this plot is used to estimate the cell thickness. In the given example, the thickness was 2.4 μm, which is within 5% of the nominal thickness of 2.5 μm.

3.3.2 Optical Polarising Microscopy

An optical polarising microscope (OPM) is one of the most used metrology techniques in this thesis. It is used to determine the alignment of the LC samples and confirm the type of LC mesophase. The OPM consists of a pair of polarisers and their optical axes can be adjusted to form a crossed position; between these polarisers a LC sample is placed. Figure 3.9 (a) shows the arrangement of a generic optical polarisation microscope. In this work, bright field microscopy was performed using an Olympus BX-51-P [128] optical polarisation microscope.

The microscope contains a halogen lamp as the illumination source, which can emit light from 400 – 700 nm. Unpolarised light passes through a polariser that allows only linear polarised light to pass along the optical axis of the polariser. After this, light is transmitted through the condenser and directed onto the specimen. Infinity-corrected objective lenses are used in which light beam after passing through the objective lens does not create the image and enters the tube lens as infinity parallel beam and forms the intermediate image. Different magnifications of such objective lenses, from 4$\times$ to 50$\times$, were used to collect light after transmitting through the LC. Before reaching the eyepieces or a camera placed in the phototube, light passes through a second polariser with the optical axis placed at 90° with respect to the first polariser. A 6.0MP CCD camera

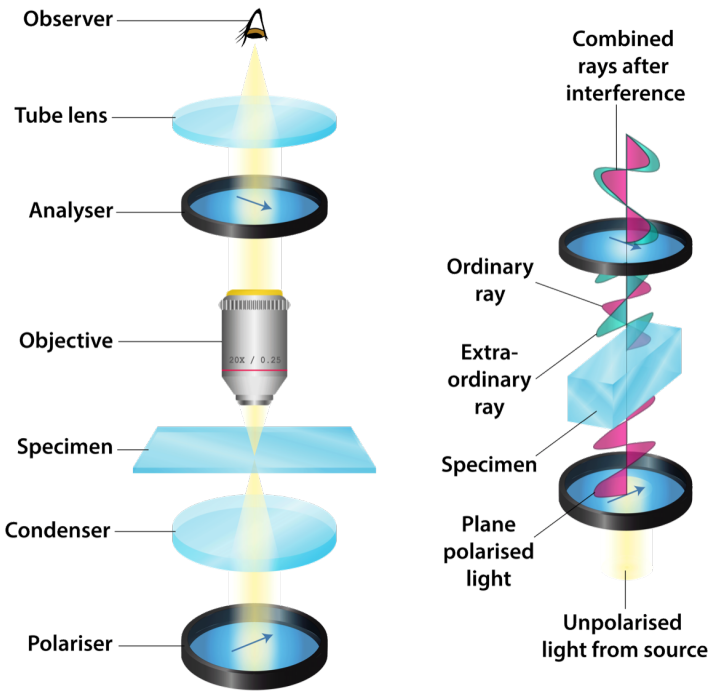


FIGURE 3.9: (**a**) Illustration of the arrangement of components of the OPM and (**b**) working principle of an optical polarisation microscope.

(QImaging Retiga R6) [129] was fitted to the microscope and was used to obtain high resolution photographs of the optical textures.

Figure 3.9 (b) illustrates the arrangement of a pair of crossed polarisers with a birefringent material – a planar aligned LC cell – placed between them that affect the polarisation state of incoming light. In its simplest form, this arrangement can help to understand the working principle of an optical polarising microscope. The birefringent specimen is placed so that its optical axis makes an angle of $\chi = 45^{\circ}$ with respect to the optical axis of both the polariser and analyser. When linearly polarised light passes through the birefringent material, it produces two orthogonal components that see either the ordinary (n_o) or extra-ordinary (n_e) refractive index of the material. Since $n_o \neq n_e$, both components travel with different velocities through the specimen. After leaving the material the light components become out-of-phase resulting in constructive and destructive interference when they pass through the analyser. Depending on the optical anisotropy (Δn) and thickness (d) of the material, light encounters different retardation, $\Delta n \times d$, and as result different colours can be seen when looking through the eyepiece. Furthermore, if the birefringent material is rotated through $0 \leqslant \chi \leqslant 360^{\circ}$, bright and dark states are observed at the eyepiece, and the corresponding intensity is given by [130].

$$T(\chi) = \sin^2(2\chi)\sin^2\left(\frac{\pi\Delta n d}{\lambda}\right) \tag{3.4}$$

where χ is the azimuthal angle of the device with respect to the polariser and Δn is the optical anisotropy as a function of wavelength and d is the thickness of LC device.

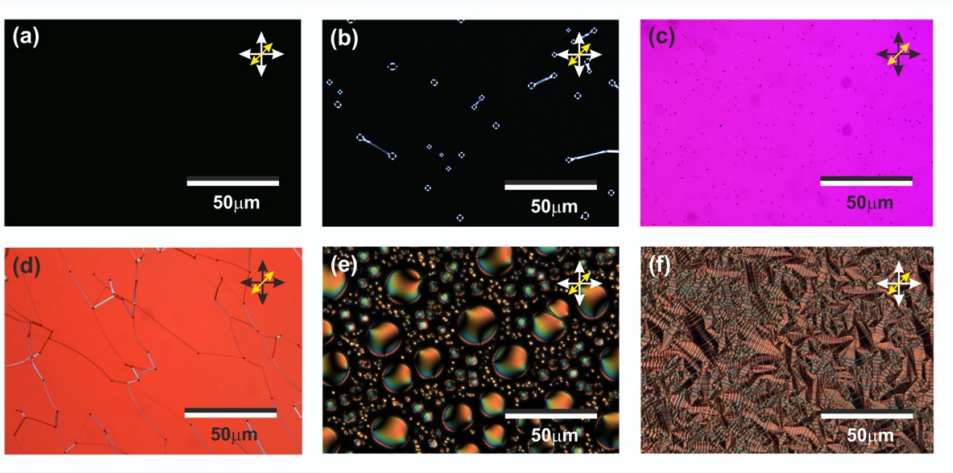


FIGURE 3.10: Examples of OPM images of different LC phases considered in this work (**a**) isotropic liquid, (**b**) homeotropic-aligned nematic, (**c**) planar-aligned nematic, (**d**) Grandjean texture of the chiral nematic phase, (**e**) polymer dispersed LC, and (**f**) focal conic chiral nematic LC between crossed polarisers.

Figure 3.10 depicts some example images taken with the optical polarisation microscope including an isotropic liquid phase and the nematic and chiral nematic LC phases. When an optically isotropic material is placed between crossed polarisers, it does not affect the polarisation state of the transmitted light and thus a dark state is observed, Figure 3.10 (a). Similarly, when a homeotropically-aligned LC sample is observed, it also appears dark. This is because both components of linearly polarised light see the ordinary refractive index along both directions (x and y) as light passes through the sample along the z-direction and therefore they leave the sample in-phase, Figure 3.10 (b). Note: In a very thick homeotropic sample, (e.g., $>50\mu$m), when observed between crossed polarisers light leakage can occur due to light scattering effects and therefore thick homeotropic layers can appear grey when observed between crossed polarisers.

Alternatively, when a planar-aligned nematic LC (Figure 3.10 (c)) is observed, it appears as a bright colourful image as explained previously. The colour depends on the optical anisotropy of the material (i.e. n_o and n_e), and the thickness of the device. A uniform standing helix (USH) of a chiral nematic LC sample shows defects or disclination lines; this texture is known as the Grandjean texture, shown in Figure 3.10 (d).

The microscope can also be used in reflection mode with the addition of a reflection arm and a halogen light source (Olympus TH4 – 200) [131]; this allows light to shine onto the top surface of the sample and reflected light is then collected and directed towards the eye-piece or camera. When a USH chiral nematic LC is observed in reflection mode, the colour of the sample corresponds to the central wavelength of the photonic bandgap; a uniform monodomain structure confirms a uniform pitch. Similarly, other LC phases/-textures can be studied such as polymer dispersed LCs (PDLC) and focal conic textures, which also show bright states as shown in Figure 3.10 (e & f).

3.3.3 Optical Fluorescence Microscopy

Optical fluorescence microscopy is used to study the light absorbing materials that can emit light upon photoexcitation. In this thesis, various types of gain media were investigated for use in LC lasers; in particular, different types of perovskite nanocrystals were doped into nematic and chiral nematic LC phases. In order to investigate the distribution and emission stability of perovskite nanocrystals in LC, an optical fluorescence microscope was used.

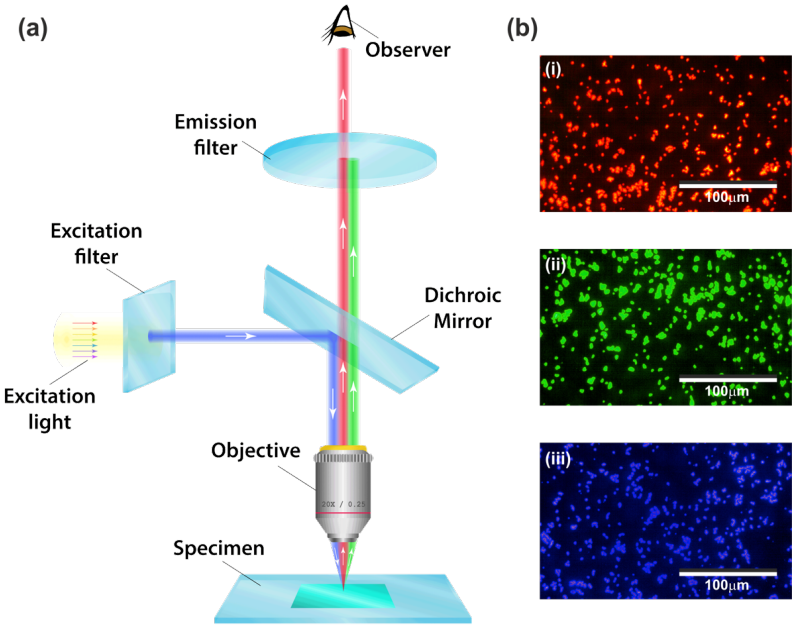


FIGURE 3.11: (**a**) Illustration of construction and working principle of optical fluorescence microscope, and (**b**) the examples of different compounds emitting (i) red, (ii) green and (iii) blue captured using a fluorescence optical microscope.

Figure 3.11 (a) illustrates the construction and working principle of a fluorescence microscope. In this work, a custom-built fluorescence microscope (Zeiss Axioplan

2 + LSM 5 Pascal with ebq 100 isolate power supply) [132] was used and a CMOS camera (Ximea xiQ USB 3.0) [133] captured the images of the emission from the samples. A fluorescence microscope enables a choice of excitation and emission filters. The narrow band of light after passing through the filter is then incident onto a dichroic mirror that is placed at 45° with respect to the incident light and sample, which directs the filtered light onto the sample through an objective lens. The incident light excites the specimen resulting in fluorescence emission. The emitted light, which is generally at longer wavelengths than the excitation light, was collected by the objective lens and passed through a dichroic mirror. Finally, an emission filter was inserted to cut-off the entire band of excitation wavelengths so that only the emission from the material was observed at the eyepiece or camera. Figure 3.11 (b) depicts example images obtained on the fluorescence optical microscope for three different materials emitting at (i) red, (ii) green and (iii) blue wavelengths when photoexcited with light that is close to the absorbance peak of the emitter.

3.3.4 Transmission/Reflection of Chiral Nematic LC Films

The transmission (or reflection) of light through (or from) the chiral nematic LC sample has been studied throughout this thesis. Chiral nematic LC exhibits a 1D photonic bandgap in the transmission spectrum when the incident light is of a wavelength that is of the order of the helical pitch. The spectral position and reflection quality of the photonic bandgap is an important indicator for the creation of an LC laser. Therefore, it was necessary to record the transmission/reflection spectrum at each stage of the development process.

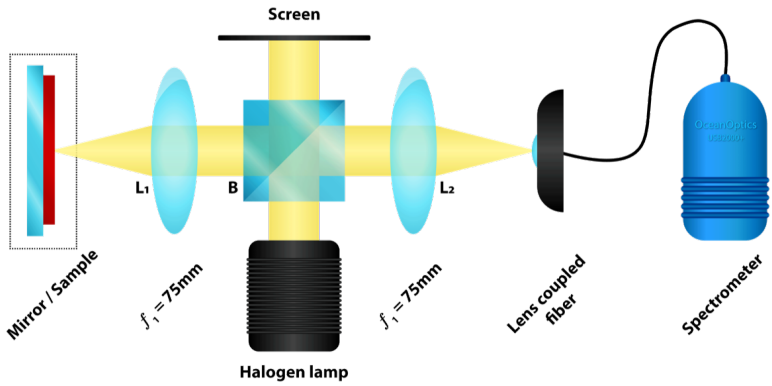


FIGURE 3.12: A free space optical setup to study the reflection properties of chiral nematic LCs using a halogen white light source.

Generally, transmission spectra were recorded while probing the optical characteristics of the LC sample; however, for certain devices/films it was necessary to record the reflection spectrum from the chiral nematic LC sample as both can provide the same information – spectral position and width of the band gap. In this thesis, the reflection spectrum was recorded to determine the quality of the band-gap and the alignment of the chiral nematic LC. The reflection spectrum was preferred in some cases as the transmission spectrum of the band-gap can be obscured when a dye is present in the host chiral nematic LC as part of the light is absorbed by the gain material. However, by studying the reflection properties, the band-gap can be viewed in its entirety.

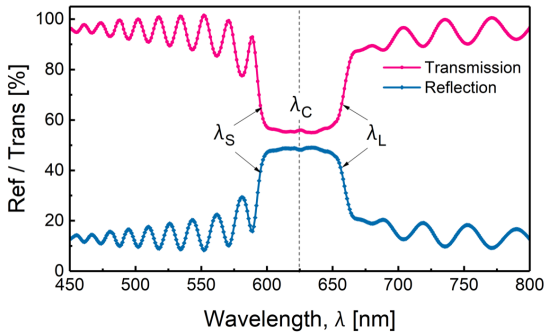


FIGURE 3.13: Examples of the transmission and reflection spectra from the chiral nemtic LC sample indicating the wavelengths relevant for designing the LC lasers.

Figure 3.12 presents the free space optical setup used to investigate the reflection from chiral nematic LC samples. Initially, a mirror was placed as shown in the illustration to record the reference spectrum. Light from a halogen lamp (Ocean Optics HL-2000-FHSA) [131] passes through a beam splitter (B): one of the beams is directed onto the mirror by passing through the lens L_1 (f_1 = 75 mm). From the mirror, light is reflected and transmitted through the lens L_1 back to the beam splitter B and another focusing lens L_2 (f_1 = 75 mm) was used to focus the light onto the entrance of an optical fibre (Ocean Optics QP600-1-UV-VIS, 600 μm diameter) [131] that was connected to a broadband spectrometer (Ocean Optics USB2000+ UV-VIS; 200-850 nm range, resolution 1.7 nm, 600 lines/mm) [131]. A reference signal was recorded with the mirror, and the mirror was then replaced with a chiral nematic LC sample to record the spectrum of reflected light from the sample. The reference signal was then subtracted from the sample signal to obtain the correct intensity level of sample signal. An example of the transmission and reflection spectra of a chiral nematic LC are presented in Figure 3.13 showing

the central wavelengths (λ_C) of the band-gap as well as the short band-edge (λ_S) and long band-edge (λ_L).

3.3.5 Photoexcitation of Emissive Liquid Crystal Samples

The photoluminescence (PL) spectrum of both the neat gain media and the gain medium-doped LC mixtures were studied by exciting the material with a Thorlabs fibre-coupled light emitting diode (LED) that was driven by a Thorlabs four channel LED current controller (DC4100, current: 0 to 1000 mA) [112]. Different types of gain materials such as organic dyes, thin films of metal-halide perovskite, perovskite nanocrystals and conjugated liquid crystalline polymers were studied in this thesis. These materials exhibit different peak absorbance, which was determined using the spectrophotometer as explained earlier in §3.3.1. Depending upon the wavelength corresponding to the peak absorbance, the relevant LED was chosen from a wide range of wavelengths from 365 nm to 780 nm (spectra shown in Figure 3.14). For example, in the case of the perovskite samples, the peak absorbance was found to occur in the UV spectral region, and therefore a fibre-coupled Thorlabs LED (M365F1, I_{max} = 700 mA) [112] emitting at λ_{ex} = 365 nm was used to excite the samples. In each set of measurements, while studying the PL emission of a gain material at different concentrations by weight, the excitation power level was kept the same for comparison.

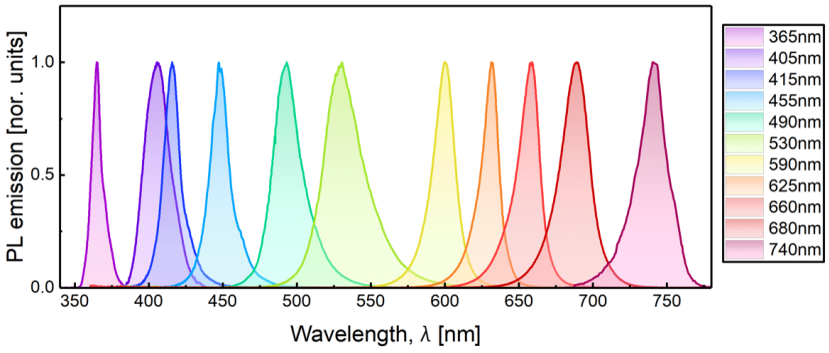


FIGURE 3.14: The photoluminescence spectra of the excitation LEDs used in this study. Reproduced from [2].

The experimental arrangement used to study the photoluminescence emission spectrum of the gain material is shown in Figure 3.15. Light from the LED was focused on the sample using a focusing lens f_1 = 75 mm. The emitted light was collected by an objective lens 20× and 0.4 N.A. that directs the emitted light to the fibre-coupled spectrometer (Ocean Optics USB2000+) by passing through another focusing lens f_2 = 25

mm. A wavelength cut-off filter was added before the spectrometer to prevent the excitation light from the LED from entering the spectrometer. All PL emission spectra were recorded by first taking the dark signal that was subtracted from the LED excited signal to correct the intensity level.

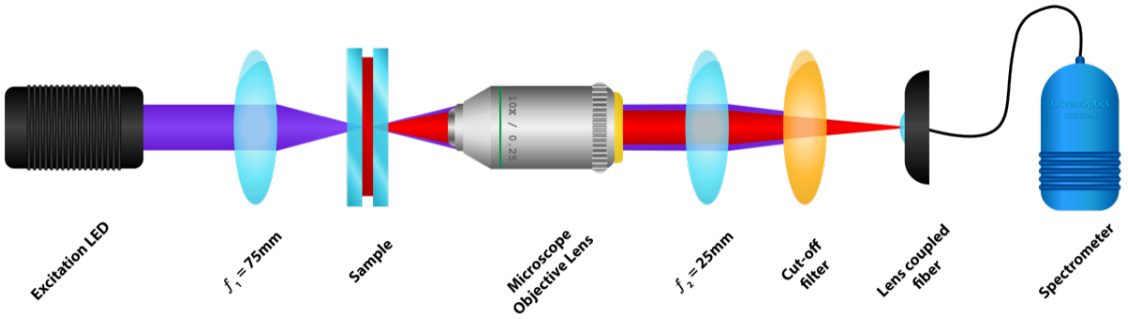


FIGURE 3.15: Free-space optical set-up for studying the PL spectrum of the different gain media.

An example photoluminescence (PL) spectrum of an emissive material is presented in the Figure 3.16 (a). In the example, the centre wavelength of the emission spectrum was at λ_c = 645 nm, which corresponds to the position where it has a maximum intensity. The shape of a PL spectrum, in general, is analogous to a gaussian distribution. The width of the spectrum is important and relevant in terms of determining the colour purity of the emissive material. The important quantity used to describe the width of the PL emission spectrum is the Full Width Half Maximum (FWHM); it is the difference in the wavelengths where peak intensity is reduced to 50%. This is illustrated in Figure 3.16 (b).

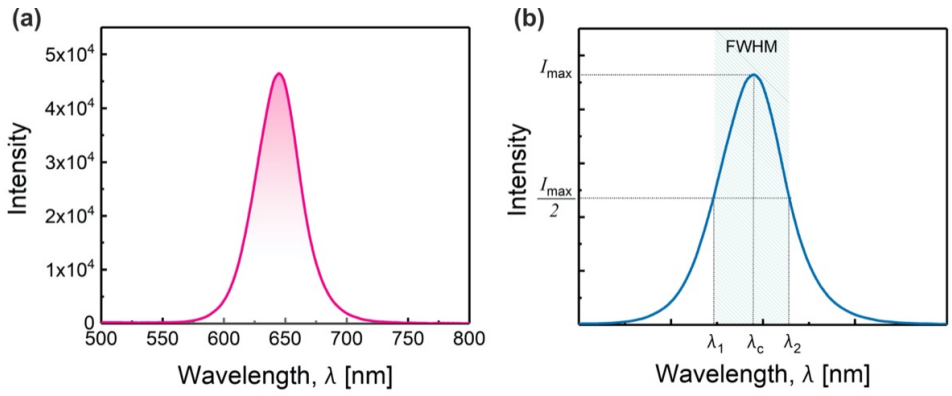


FIGURE 3.16: (**a**) An example photoluminescence (PL) spectrum and (**b**) the definition of the full-width half-maximum (FWHM) illustrated on the PL spectrum.

3.3.6 Liquid Crystal Laser Experiments

The LC lasers created in this work were optically excited with a short-pulsed (nanosecond) laser. For most of this work, the second harmonic of an Nd:YAG (Neodymium-doped Yttrium Aluminum Garnet) laser (CryLas 6FTSS355-Q4-S) [134] emitting 1.4 ns pulses at λ_{ex} = 532 nm with a variable repetition rate from 1 Hz to 1000 Hz was used. It was important to understand the stability of the pump laser to characterise the optical properties of the LC laser. This section describes the free-space optical setup used to characterise the LC lasers.

3.3.6.1 Laser Beam Profile and Propagation

Generally, a laser beam is considered to exhibit an irradiance that follows an ideal Gaussian distribution. For a Gaussian distribution, the beam profile is symmetric around the centre and is shown with examples in Figure 3.17 (a & b). As the laser beam travels along the optical path, the beam diameter is continually varying. In an ideal case when a Gaussian beam is considered, the width of the beam, i.e., radius (w), along the propagation axis (z) is given as [135]

$$w(z) = w_o \sqrt{1 + \left(\frac{z}{z_R}\right)^2} \tag{3.5}$$

where w_o is the beam waist, that is, the smallest radius of Gaussian beam and z_R is the Rayleigh range, the distance over which the beam area become twice as big as the waist area and given as $z_R = \pi w_o^2/\lambda$. When the Gaussian beam is focused with a lens of focal length (f), as shown in Figure 3.17 (c), the beam waist (w_f) becomes:

$$w_f = \frac{\lambda f}{\pi w_o} \tag{3.6}$$

The focus spot size is become very small and increases rapidly along the beam propagation axis. One of the common ways to define the beam diameter is as $1/e^2$, i.e., 13.5% of maximum. It can be understood from the simplified form of the Gaussian beam radial distribution, $I(r)$, that is:

$$I(r) = I_o \exp\left(\frac{-2r^2}{w^2}\right) \tag{3.7}$$

where I_o is the peak irradiance at the centre of the beam and r is the radial distance away from the axis. In the beam distribution, when beam radius equals to the beam waist, i.e., $r = w$, the Equation (3.7) becomes:

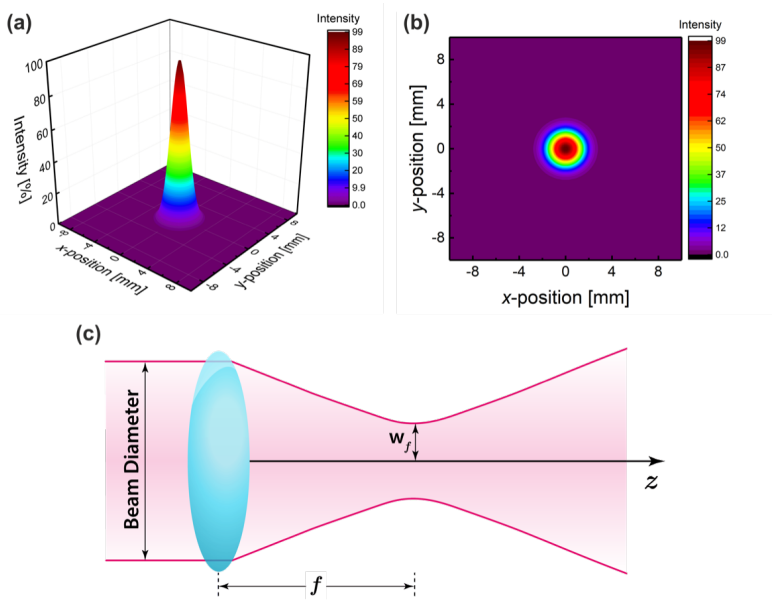


FIGURE 3.17: A typical Gaussian beam profile of a laser (**a**) isometric view, (**b**) top view and (**c**) the illustration of laser beam waist when a focus lens is used.

$$I(r = w) = I_o \times \frac{1}{e^2} \tag{3.8}$$

which is 13.5% ($\because e = 2.71828\ldots$). This is shown in Figure 3.18.

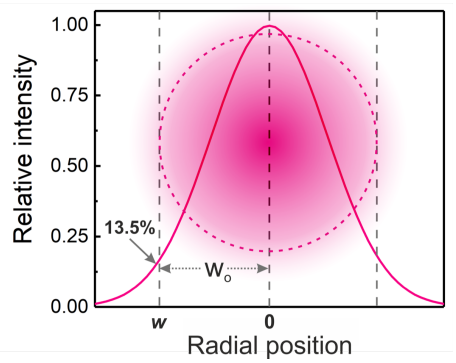


FIGURE 3.18: The laser beam distribution profile illustrating the beam waist at $1/e^2$.

3.3.6.2 Knife – Edge Measurements of beam waist

The Knife $-$ Edge method is a widely adopted characterisation technique used to estimate the laser beam waist [136]. Since the laser beam waist gives information about the size of the pump laser at the LC, it is required for the pump excitation fluence threshold of the LC lasers studied in this thesis. The principle of the knife $-$ edge measurement is illustrated in Figure 3.19 (a), that consists of a blade and a focusing lens. The laser beam is completely cut-off by a sharp blade mounted on a translational stage capable of moving in the $x - z$ direction.

To ensure a large fluence is achievable using the pump laser setup, a focusing lens was included to increase the laser fluence; the knife − edge was then placed at the focus f of the lens by precisely adjusting its position in z direction. The blade is then gradually moved across (in the x direction) so that the laser beam is now exposed to a pyroelectric laser energy meter (Ophir PE9-ES-C; detection range: <0.05 μJ up to 200 μJ, up to 25 kHz, spectral range: 0.15 – 12 μm, 8 mm aperture) [137]. As the blade is moved away from the central position, for each position of the knife, the laser energy is recorded and plotted as a function of the knife position and shown in Figure 3.19. For this work, the pump excitation rate was set at 10 Hz to avoid photo-bleaching of the gain medium and therefore the knife-edge measurement was also performed at 10 Hz repetition rate. A Matlab script was used to extract the beam waist; using a 75 mm focusing lens the beam waist was estimated to be $w_o = 0.163 \pm 0.025$ mm.

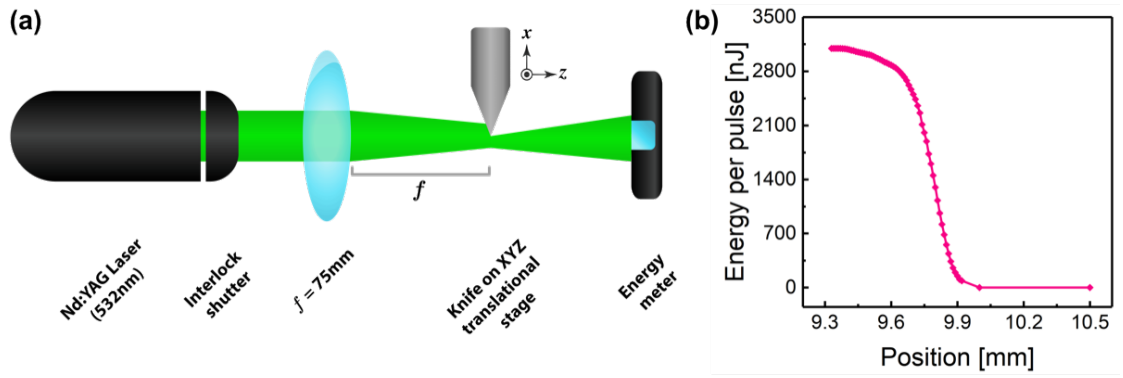


FIGURE 3.19: (**a**) Free space optical setup for the Knife edge experiment to measure the pump spot size and (**b**) Plot of the energy as a function of the position of the knife-edge. The beam waist is the width at $1/e^2$ (13.5%) between the position at 417 nJ to 2677 nJ. Measurements were carried out at 10 Hz repetition rate.

3.3.6.3 Pump Laser Parameters

Before optically pumping the sample, the pump laser energy fluence needed to be calibrated as a function of position of the variable neutral density filter, which was used to control the pump fluence at the LC laser. The free-space optics arrangement for the calibration of the laser energy fluence is shown in Figure 3.20. A round continuously variable metallic neutral density filter wheel (ThorLab NDC-50C-4: optical density, OD $= 0.04 \sim 4.0$) [112] was used to control the intensity of the laser beam that the sample receives. A 25 mm focusing lens was used to focus the laser onto the detector for maximum collection of light. The laser energy meter that detects the individual pulses was used as the detector. Initially, the neutral density filter wheel was positioned to block the laser

and was then rotated such that the laser emission could be detected by the energy meter. The position of the neutral density filter was adjusted from minimum transmission to maximum transmission and the detected laser energy per pulse was then recorded as a function of angle. The results are presented in Figure 3.21 (a); this shows an increase in the energy per pulse detected as the transmittance of the neutral density filter wheel increases while it was rotated from the minimum transmission settings towards the maximum transmission.

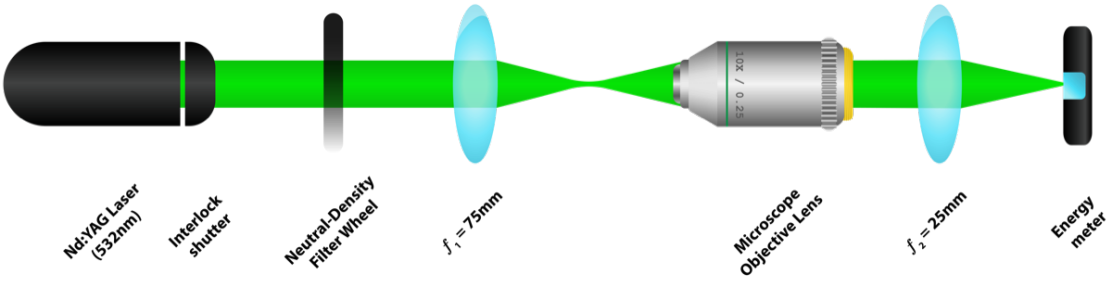


FIGURE 3.20: Free-space optics experiment to calibrate the pump fluence of the Nd:YAG laser.

The energy per pulse at a given repetition rate and the spot size of the pump where the device under investigation is to be placed are used to determine the fluence excitation threshold of the device. An example plot of input-output energy characteristics is presented in the Figure 3.21 (b), the excitation threshold corresponds to the point that shows a discontinuity in the gradient. The fluence excitation threshold is (output energy at threshold)/(spot size) and is usually quoted in J/cm^2/pulse.

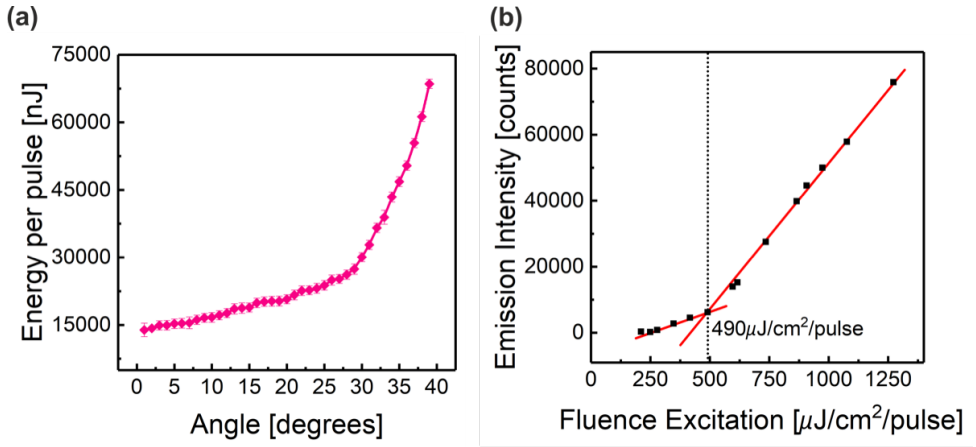


FIGURE 3.21: The pump Nd:YAG 532 nm laser parameters. (**a**) Energy per pulse as a function of position of the neutral density filter, and (**b**) an example plot of input-output characteristic of a device illustrating threshold.

Other laser parameters were also studied to check the stability of the pump laser.

These parameters include the energy per pulse and the pulse frequency detected by the energy meter for different repetition rates. The temperature of the laser is also important and therefore any change in temperature was also monitored as the repetition rate was varied. These measurements were performed using the experimental setup as shown in Figure 3.20. To avoid damage to the energy meter, the position of the neutral density filter wheel was set to the lower transmission setting (OD $\approx$ 2). The repetition rate was varied from 1 Hz to 1000 Hz for all measurements and readings were recorded at 500 pulse counts for consistency.

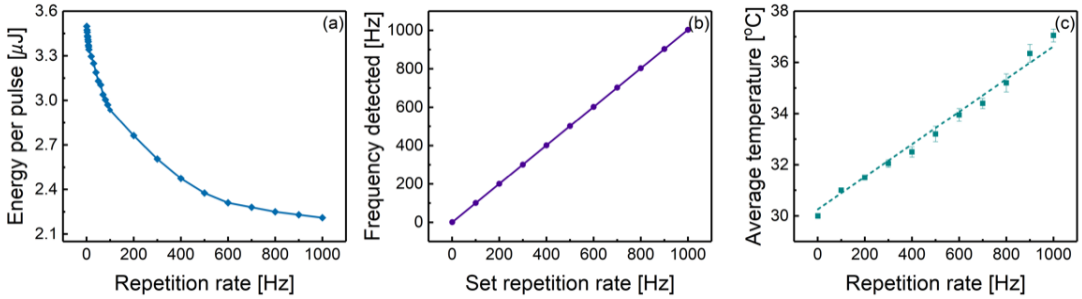


FIGURE 3.22: The pump Nd:YAG 532 nm laser parameters. (**a**) Energy per pulse, (**b**) frequency, and (**c**) temperature as a variation of the repetition rate.

Figure 3.22 (a) shows the energy per pulse as a function of the repetition rate of the pump laser, which decreases when the repetition rate was increased from 1 Hz to 1000 Hz; the reduction in the energy per pulse was more than 35%. Results for the frequency detected by the energy meter are presented in Figure 3.22 (b) after 500 pulses and showed a linear behaviour. Therefore, the pulse frequency detected by the meter was in agreement with the set repetition rate of the pump laser. Figure 3.22 (c) shows a linear variation in temperature with a 23% increase in the pump laser temperature as the repetition rate increases from 1 Hz to 1000 Hz, which is within the operating temperature range (18 – 38°C) of the Nd:YAG laser.

3.3.6.4 LC Laser characterisation

Following calibration, the free space optical setup shown in Figure 3.23 was used to optically pump the LC sample with the Nd:YAG pulse laser (λ_{ex} = 532 nm). An LC laser sample was placed at the focal plane (f_1) of the lens, which was perpendicular to the propagation of the pump beam. The focusing lens f_1 = 75 mm focused the beam onto the sample to a pump beam waist (radius) of 0.163 mm.

Light from the pump laser first passes through the neutral density filter wheel to

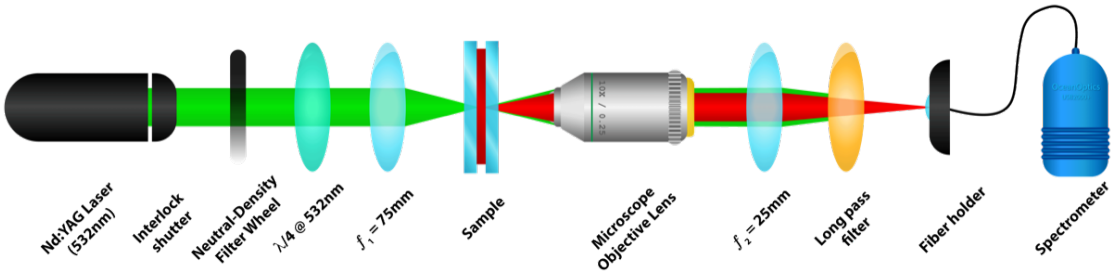


FIGURE 3.23: Free-space optics experiment for studying the emission characteristics from a liquid crystal laser.

attenuate the pump power and avoid photo-bleaching of the LC laser sample. A quarter-wave plate was then placed in between the neutral density filter and focusing lens. The $\lambda/4$ was used to convert the input linearly polarised light into circularly polarised light of the opposite handedness of the chiral nematic LC structure to avoid being reflected by the band-gap. The output laser light from the LC sample was collected by a microscope objective lens of 20× and 0.4 NA that collimated the beam before a second focusing lens, f_2 = 25 mm, directed the beam to an Ocean Optics USB 2000+ spectrometer, which detected the output emission spectrum from the LC laser. A 532 nm EdgeBasic™ long-pass long pass filter (BLP01-532R-25, $\lambda_{cut-off}$ = 542 nm and OD > 5: 270 – 425.6 nm & OD > 6: 425.6 – 532 nm, example transmission spectrum is presented in Figure 3.24) [138] was placed between the lens f_2 and the spectrometer to stop the pump excitation from reaching the spectrometer.

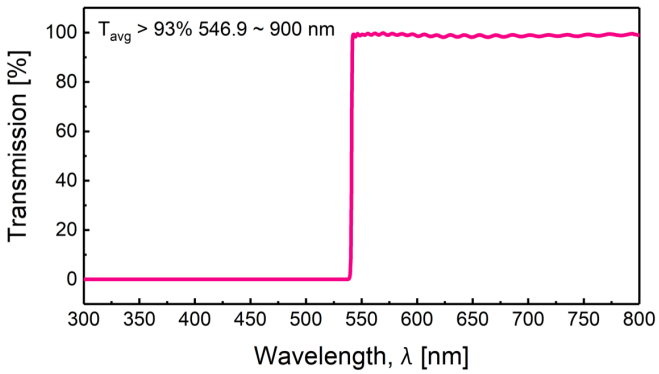


FIGURE 3.24: The transmission spectrum of a long pass filter ($\lambda_{cut-off}$ = 542 nm) used to cut-off the Nd:YAG (532 nm) pump laser.

3.4 Summary

In summary, in this Chapter, the core experimental methods that are used to fabricate and characterise the LC devices in this Thesis are described in detail. The fabrication methods for creating LC cells with planar and homeotropic alignment layers are presented. A brief discussion on the processes and advantages of solution processing techniques such as spin coating, K-bar coating, flexography is also reviewed, these techniques were used in the fabrication of different devices as explained elsewhere in this Thesis.

The spectroscopic and microscopic characterisation techniques, their working principle and examples of relevant results as used in this Thesis were presented and discussed. A general background on laser beam theory such as beam profile and beam propagation has also been discussed briefly. The LED and laser optical excitation setups have been introduced and explained. In the following chapters, these techniques are utilised to fabricate and characterise the LC samples and LC laser devices.

Chapter 4

Electro-Optical Study of a New LC Dimer

Liquid crystals (LC) are potential candidates for thin-film lasers [15], tuneable waveplates [139] and light modulating devices [140]. As explained in Chapter 2, the 1D photonic bandgap of the chiral nematic phase acts as a forbidden band for the transmission of certain wavelengths of light for a specific handedness of circular polarisation. This forbidden (or photonic) band gap plays a vital role in determining the spectral position and number of modes of an LC laser. The width of the photonic bandgap depends on the optical anisotropy (Δn) of the LC materials and the pitch of the helix – higher birefringent LCs exhibit a wider photonic bandgap and vice-versa [25]. Thus, with the correct combination of optical anisotropy and pitch of the helical structure, the photonic bandgap can effectively cover a large part of the visible spectrum. When such material is used to form an optical resonant cavity and is subsequently combined with a suitable gain material that exhibits a wide emission spectrum, a wavelength tuneable laser can be created. As this Thesis considers advanced optical and emissive materials for LC lasers along with the fabrication challenges of using such materials, an understanding of the optical and electro-optic characteristics of the core LC materials for the laser cavity is particularly relevant. For the laser cavity, it would be highly desirable to have an LC host that exhibited a high birefringence, to ensure good coverage of the visible spectrum and potentially low threshold laser emission [108].

In this chapter, the synthesis process of a newly developed LC dimer is summarised, which has been prepared by our collaborators in the Department of Chemistry at the University of Hull, UK (Dr Chris Welch and Prof Georg Mehl). The measurement of the birefringence of this new LC dimer is studied as both a function of wavelength of

light and temperature. In this regard, the reliability of experimental methods was first confirmed by estimating the birefringence of a well-known nematic LC, E7 followed by the measurement of the new LC dimer. Throughout the measurements, equivalent theoretical models for the transmission characteristics for both E7 and the LC dimer were simulated and compared with experimental results in order to estimate the birefringence of the nematic LC. Furthermore, the transmission characteristics for the Fréedericksz transition were also studied for the dimer and analysed to extract the splay and bend elastic constants ratios, $k_1/\Delta\epsilon$ and k_3/k_1. A study of the flexoelectro-optic properties was also performed by preparing a chiral nematic LC that was based upon the new dimer and a small concentration by weight of chiral additive. Measurements are presented of the flexoelectro-optic tilt angle and flexo-elastic ratio, which are important metrics used to compare the degree of flexoelectro-optic coupling in comparison to monomeric LC mixtures and other dimers.

4.1 Material background

The birefringence (optical anisotropy) results from a combination of the molecular polarisability, which is typically larger along the long axis of the molecule than it is perpendicular to it, and the order parameter. The molecular polarisability originates from the distribution of the $\pi-$electrons. Molecules that consist of high polarisability units such as aromatic rings in the core and terminal cyano groups have a high birefringence. Linking groups are also used to extend the length and polarisability anisotropy [141].

When light impinges upon an anisotropic material along a path that does not coincide with the optic axis it splits into two rays: an ordinary ray ($O-$ray) and an extraordinary ray ($E-$ray), which are polarised at mutually perpendicular angles, and these rays subsequently move at different velocities through the material. This is known as double refraction and the larger the difference in velocity, the larger will be the birefringence of the material. Molecular structures based around conjugated π-electrons have been shown to confer high birefringence to a material by retarding the $E-$ray relative to the $O-$ray and aromatic groups such as phenyl, naphthyl, thiophene and alkynyl groups have all been used to achieve this [142, 143]. A polarisable end group that extends the

conjugation such as −CN (cyanide) or −NCS (isothiocyanate) has been shown to further increase the birefringence [143]. For example, in the terminal group −NCS, $\pi-$electrons are distributed over the three atoms of the group that influence the retardation of the $E-$ray and hence increases the birefringence of the material.

The new LC dimer compound studied here is comprised of two selectively fluorinated terphenyl systems linked with a flexible spacer and terminated with NCS groups; the molecular structure of the LC compound is shown in Figure 4.1. The terphenyl system was chosen as this group is compatible with the existence of the NTB phase in dimeric materials [144, 145] without the broadened molecular envelope that a naphthyl group would give [143]. An ethynyl link was discounted due to the UV instability and increased rigidity of this functionality [143, 146]. The isothiocyanate group extends the molecular conjugation of the π-electron system by three atoms which is known to increase the birefringence by more than the analogous cyano compounds, [146–150] and additionally they exhibit lower viscosity and higher UV stability [148].

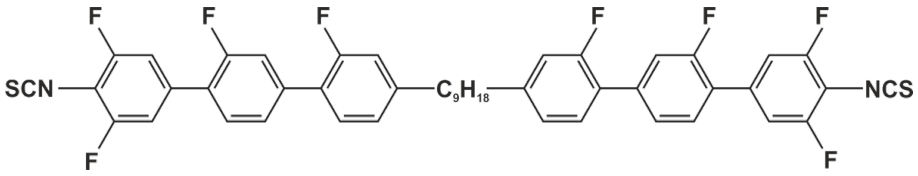


FIGURE 4.1: The molecular structure of the LC dimer designed to give both strong flexoelectro-optic coupling and a high birefringence.

In order to suppress potential underlying smectic phases [150] and promote a stable nematic phase over a wide temperature range, lateral fluoro substitution was used. The specific fluorination pattern used in the compound was chosen based on the work of the Dabrowsky group [151]. The use of terphenyl−NCS monomeric system enables the substitution arrangement to give a high value of the birefringence (Δn = 0.46) whilst the fluoro substituent completely suppresses the presence of smectic phases.

4.1.1 Material synthesis

The molecular structure of the LC dimer was prepared using convergent synthesis by the team of Prof Mehl at the University of Hull. This is a strategy in organic chemistry to improve the efficiency of a multistep synthesis – when several individual pieces of a complex molecule are created in a single stage and then combined together to form the final compound in another stage [152]. Using this approach, the LC dimer

(compound 7) was synthesised by combining compound 2 and compound 5 as shown in Figure 4.2. In summary, the central part of the molecule comprising the alkyl spacer and the two innermost phenyl rings, compound 2, was synthesised separately to the outer biphenyl ring system 5. These parts were then coupled together using a Suzuki Miyaura reaction [153–156] to create compound 7.

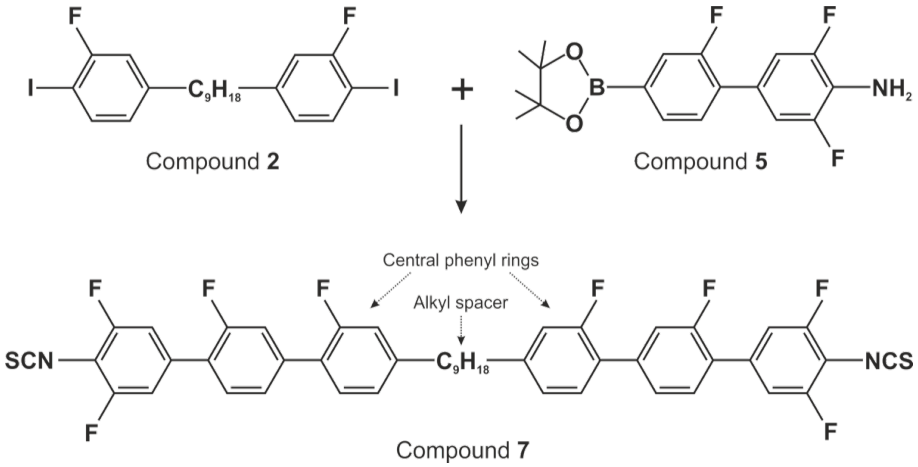


FIGURE 4.2: Molecular target designed to give a high birefringence LC dimer (compound 7) created by convergent synthesis of compound 2 and compound 5. Synthetic route was devised and carried out by collaborators at the University of Hull.

4.1.2 Textures and phase identification

The phase transition temperatures for the LC dimer are presented in Table 4.1. To estimate the phase transition temperature, a thin sample was placed on an untreated glass slide under a cover slip, heated at 10°C/min and observed under crossed polarisers. On the first heating cycle it was found to melt at 119°C into a flowing phase showing a birefringent texture and clear striations. However, it was not possible to clearly identify this phase. Further heating showed a transition to a nematic phase at 132°C which persisted until the clearing point at 217°C.

TABLE 4.1: Phase behaviour of the LC dimer (compound 7). Temperatures in °C.

Heating	Cr	119	N_{TB}	132	N	217	I_{SO} (Decomp)
Cooling	Cr	85	N_{TB}	131	N	200	-

Cr – crystalline, N_{TB} – twist bend nematic, N – nematic, I_{so} – isotropic.

The sample was found to degrade after reaching the isotropic phase and so a new sample was prepared and heated up to 200°C before cooling where a transition was observed at 131°C from the nematic phase, Figure 4.3 (a), into the N_{TB} phase, exhibiting a birefringent, blocky texture typical of these materials, Figure 4.3 (b). Further cooling

showed development of this texture and the sample crystallised at 85°C. No higher order phases were observed even under a monotropic regime (fast cooling of >30°C/min). Further heating and cooling cycles showed the same transition temperatures, indicating no degradation of the sample providing it was not allowed to pass the clearing point of 217°C.

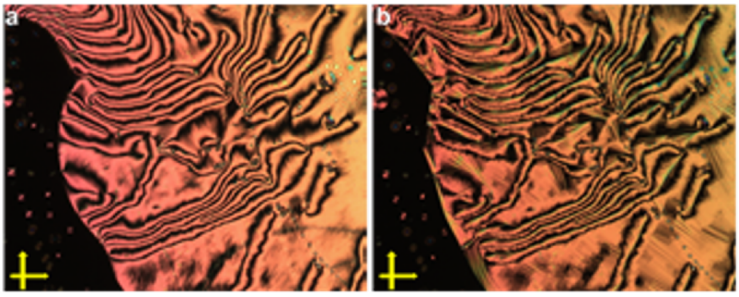


FIGURE 4.3: Optical polarisation microscope images of LC dimer (7) on cooling (**a**) 140.0°C, Schlieren texture of the nematic phase and (**b**) 130.0°C blocky texture of the N_{TB} phase. Sample was mounted on an untreated glass slide. The cooling rate was 10°C/min, 200× magnification between crossed polariser and analyser. The measurements were obtained from our collaborators at University of Hull.

4.2 Birefringence measurement

4.2.1 Background on Berek compensator

The birefringence of the new LC material was determined with the Berek Compensation approach, which is a standard procedure used to measure the retardation of a birefringent material [157]. An illustration of a standard Berek compensator is shown in Figure 4.4 (a). The Berek compensator consists of an optically anisotropic crystal (Δn) that can be used to quantitatively determine the optical retardation of the material as its crystal axis is either rotated or tilted. This tilt (θ) of the Berek crystal changes the effective path length (i.e. Δd) and the effective anisotropy for light passing through the crystal. The change of path length and effective anisotropy changes the retardation ($\Gamma = \Delta n_{eff} \times d$) introduced by the Berek crystal as illustrated in Figure 4.4 (b). The retardance is a unit of length and is generally expressed in nm; however, it can also be specified in units of degrees or waves. The commonly used unit is the $milli - mu$ meters because the thickness is measured in μm, Δn is a unitless quantity and to achieve equality of units, the thickness is multiplied by 1000 (that is 1000 nm/μm) in order to express retardation in $milli - mu$.

Here the Berek compensator was used in two ways to estimate the birefringence

of the nematic LCs. One is the 'standard method' for Berek compensator use, and the other investigates the transmission spectra with varying levels of Berek compensation. These are described in more detail in the following subsections.

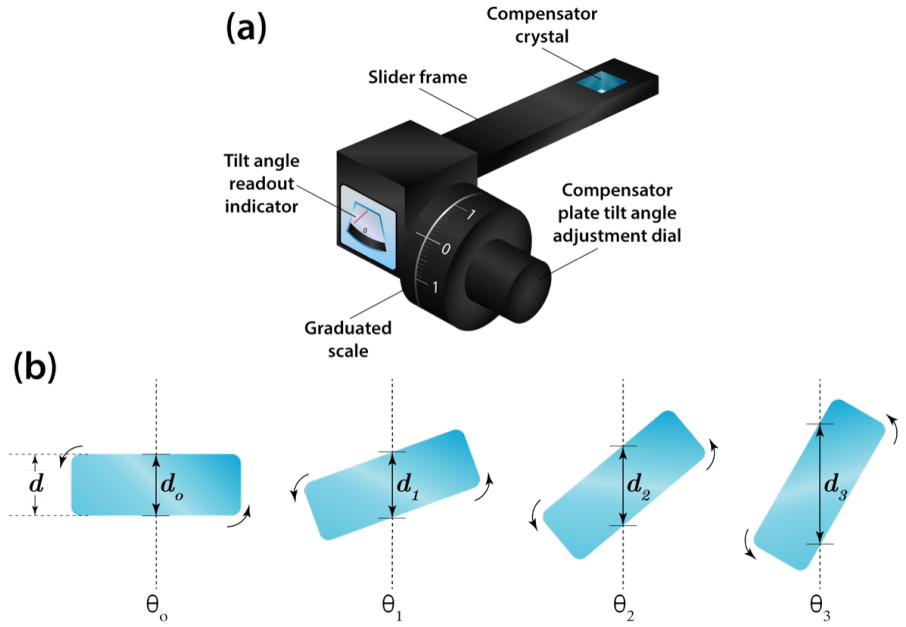


FIGURE 4.4: (**a**) An example of a typical Berek Compensator, and (**b**) the side-view showing the rotation of the Berek crystal plate resulting in different path lengths d_o to d_3 when titled from θ_o to θ_3.

4.2.1.1 Standard method

An optical polarising microscope that was equipped with a polariser and analyser and a slot for a Berek compensator was used to determine the unknown birefringence of the LC material or sample. The optical axes of the polariser and analyser of the microscope were aligned orthogonally (i.e., crossed) and fitted on the body of the microscope. The LC sample was placed on the optical stage so that the optical axis of the LC device makes an angle of 45° with respect to the axes of each polarisers. The Berek compensator was then inserted such that its optical axis was at 45° with respect to the optical axis of the polariser or analyser and was at 90° (i.e., perpendicular) with respect to the optical axis of the LC device. This arrangement is illustrated in Figure 4.5 (a & b).

When the Berek compensator is rotated, it changes the effective path length of light passing through the crystal and hence the retardation. At a given wavelength, and at a certain tilt angle (say, at θ_1), this retardation becomes equal in magnitude to the retardation of the layer of material whose birefringence is to be determined. When examining through the eyepiece of a microscope while rotating the Berek crystal to the position,

where the birefringence of both Berek crystal and material under investigation become equal, a fairly black line can be seen (Figure 4.5 (c)) and is referred to here as the Black Compensation Line (BCL).

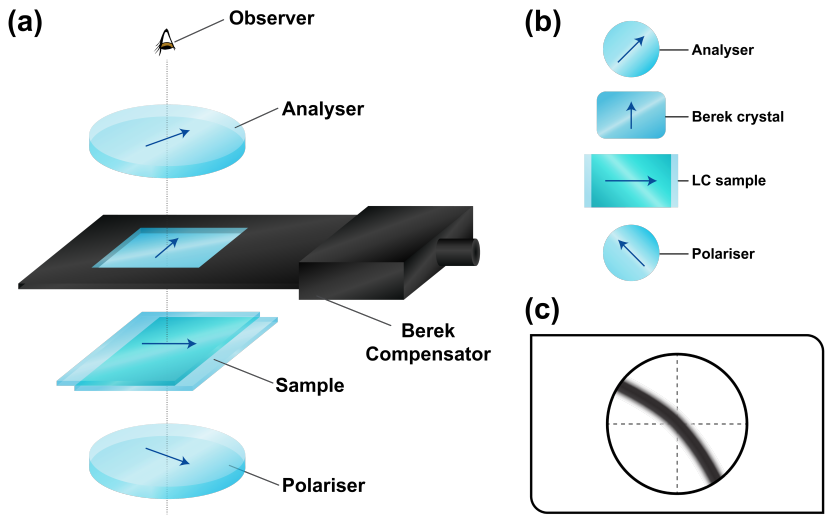


FIGURE 4.5: (**a**) The experimental arrangement for the standard method using a Berek compensator, (**b**) the orientation of optical axis of the components, and (**c**) an example of the Black Compensation Line of the Berek Compensator when examined through the eyepiece of the microscope.

The measured tilt angle of the compensator translates into a retardation, which is a pre-determined retardation as a function of tilt angle of the Berek compensator and is provided by the manufacturer of the compensator. This is then the retardation of the unknown layer of material at that particular wavelength. If the thickness of the device that contains the material is known, the birefringence (Δn) can then be estimated using:

$$Retardance = (\Delta n \times d)_{\lambda} \tag{4.1}$$

This method can be repeated over a range of wavelengths to determine the birefringence dispersion of the unknown material as a function of wavelength. Similarly, the birefringence at a particular wavelength, but over a range of different temperatures can also be determined.

4.2.1.2 Transmission spectrum method

Another method that is based upon the use of a Berek compensator to find the retardation of an unknown material is to use a spectrometer together with the compensator. In this method, instead of directly 'looking through the eyepiece' of the microscope to find the black compensation line, a spectrometer is attached to the microscope

(as shown in Figure 4.6) and the spectrum is observed as the Berek crystal is rotated and the compensation level adjusted.

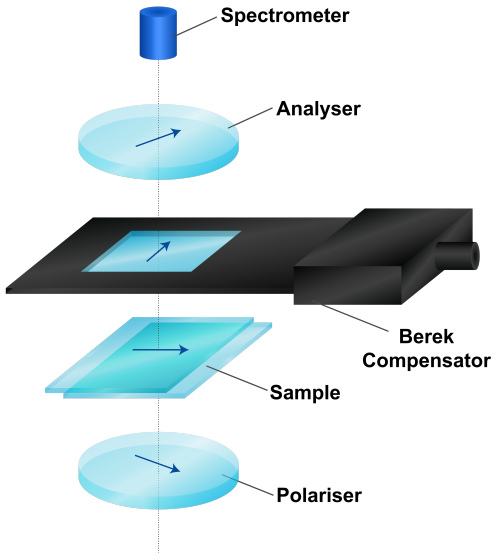


FIGURE 4.6: The experimental arrangement for using a spectrometer with a Berek compensator.

For a given sample with a particular birefringence at a certain wavelength, setting the Berek crystal at an appropriate tilt angle should compensate the retardation at that point in the spectrum, i.e. light at that particular wavelength will not pass through the combination of the sample under investigation and the compensator system between crossed polarisers. If the transmission is considered as a function of wavelength then a dip or a minimum should be observed at that wavelength in the spectrum. Using this approach, the spectra at a range of compensation points (i.e. for a number of different tilt orientations of the Berek crystal) were recorded. From these spectra, the points were chosen where the dip or minima occurs that indicate "correct compensation" enabling the results to be translated into a measure of the retardation.

To confirm the consistency of the process, a standard nematic LC, E7, was first used and then the new LC dimer, of unknown birefringence, was studied. The spectra were taken by rotating the Berek compensator to adjust the compensation level so that a minimum appeared in the transmission spectrum at the desired wavelength. Furthermore, because in the above method, the transmission spectra for the samples were investigated with varying degrees of compensation, it enables the dispersion of the birefringence of the material to be determined. It will be seen in the following that this is key

to ensuring that correct results are obtained.

4.2.2 Δn measurement for E7

A commercially manufactured glass cell (LC-2, Instec) with antiparallel rubbed polyimide layers and a nominal thickness of 5 μm were used in this experiment. The cell gap was carefully measured using an Agilent 8454 UV-Vis spectrophotometer. Measurements of the transmission spectrum of each empty glass cell resulted in the appearance of interference fringes from the Fabry – Pérot etalon effect when white light was transmitted at normal incidence to the empty glass cell. The thickness of the device was extracted from the interference fringes using a MATLAB script based on Equation 3.3 as explained in §3.3.1 of Chapter 3. The device was found to be d = 4.85 μm-thick in the central region of the cell and this region of the device was marked so that it could be easily located after filling with the nematic LC. The nematic LC, E7, was then filled into the device above the clearing temperature at 65°C via capillary action.

4.2.2.1 Transmission spectra with Berek compensator

An Olympus U-CBE Berek compensator was used in this study with an optical polarising microscope, Olympus BH-2. The planar-aligned glass cell containing E7 was placed in between a pair of crossed polarisers and the Berek compensator was inserted between the sample and the analyser as shown in the experimental arrangement in Figure 4.6. An Ocean Optics 2000+ USB spectrometer was attached to the phototube to record the spectra with a resolution of 1.5 nm. An "uncompensated" spectrum for the E7 Instec device (placed at an orientation angle of χ = 45°) was taken and is shown (solid line) below in Figure 4.7.

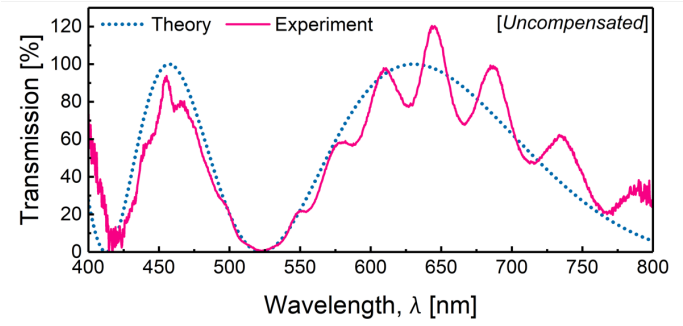


FIGURE 4.7: The uncompensated experimental transmission spectrum and the predicted spectrum from theory for the nematic phase of E7 filled in an Instec glass cell. Measurement were taken at 25°C.

Additionally, a number of simple models were also run to calculate transmission

spectra, where the control parameters are the device thickness, the birefringence of the LC material and the compensation from the Berek compensator. To understand this, consider the general expression for the transmission (T) of light through a birefringent layer placed between crossed polarisers, given as:

$$T = \sin^2(2\chi)\sin^2\left(\frac{\pi\Delta n \times d}{\lambda}\right) \tag{4.2}$$

where χ is the device orientation, Δn is the optical anisotropy, d is the device thickness and λ is the wavelength of light. Assuming that the device is placed such that the optic axis is at 45° between the crossed polarisers, and modifying this expression to allow for optical dispersion of the LC material and also for the presence of the Berek compensator, the optical transmission through the system can then be expressed as:

$$T = \sin^2\left(\frac{\pi(\Delta n_{eff}(\lambda)d - Berek)}{\lambda}\right) \tag{4.3}$$

where $\Delta n_{eff}(\lambda)$ is the optical anisotropy as a function of wavelength for the LC material under investigation and *Berek* is the retardation of the Berek compensator (i.e., the effective $\Delta n \times d$ of the compensator). Equation 4.3 can then be used to compare the simulated transmission spectrum with the experimental spectrum.

The uncompensated spectrum was calculated using Equation 4.3 by setting $Berek = 0$. The data for $\Delta n_{eff}(\lambda)$ are then taken from the predetermined values of E7 in [158] and were fit based on Cauchy's equation [159] as:

$$\Delta n_{eff}(\lambda) = A + \frac{B}{\lambda^2} \tag{4.4}$$

where A and B are the coefficients, which were determined for a material by fitting the equation to determine the refractive indices at the desired wavelength. Using Equation (4.4), the modelled results for $\Delta n_{eff}(\lambda)$ were obtained and substituted in Equation 4.3. This allowed us to re-write the transmission in Equation 4.3 as function of A, B and *Berek* as: $T = \sin^2\left(\frac{\pi(A+B/\lambda^2)d-Berek}{\lambda}\right)$. *Berek* was set for the mid-spectrum value, (i.e., around $e-$line $\approx$ 550nm) as the dispersion in the Berek compensator was $\pm\frac{1}{2}$%; therefore, for simplicity in the modelling, the dispersion effect in the Berek was ignored. To achieve the uncompensated spectrum, the Berek in Equation 4.3 was set to zero and the resulting model for the uncompensated spectrum for E7 in an Instec glass cell is shown (dotted line) in Figure 4.7.

The uncompensated spectrum of E7 in a planar-aligned device is in good agreement with the equivalent model. There are some additional interference fringes in the experimental results which are not reproduced in the simple theory, but the key behaviour is consistent. Importantly, the peaks (which correspond to half-wave-plate conditions where $\frac{\Delta nd}{\lambda} = \frac{1}{2}, 1\frac{1}{2}, 2\frac{1}{2} \ldots$) and the dips (which correspond to full-wave-plate conditions where $\frac{\Delta nd}{\lambda} = 1, 2, 3 \ldots$) are well reproduced.

Let us consider a wavelength in the middle of the visible spectrum (550 nm) as the set wavelength. From the "fit" between the experiment and theory shown in Figures 4.7, it can be determined that at this wavelength the device retardation is approximately 1014 milli-mu meter (that is 1014×10^{-9} or 1014 nm). The model spectrum was re-determined by removing the effects of birefringence dispersion and fixing the retardation to this value at all wavelengths; that is, by setting $\Delta n_{eff}(\lambda) \times d = \Delta n(550 \text{ nm}) \times d = 1014 \times 10^{-9}$.

Now, having considered the transmission spectrum behaviour of an "uncompensated" device, the effect of adding Berek compensation can be included, again choosing to concentrate on a mid-spectrum wavelength 550 nm as a key point. The Berek crystal was tilted to change the retardation compensation until a minimum appeared at 550 nm; this spectrum was then recorded. The Berek crystal was tilted in both clockwise (CW) and counter-clockwise (CCW) directions, which were identical and for simplicity the CW tilt spectra are used here. An equivalent theoretical model was run. Both the experimental and modelling results are shown in Figure 4.8 (a); this is referred to as the first minimum. The spectrum for E7 in a planar-aligned Instec cell at the first minimum of 550 nm is compared with its equivalent model.

At this point, for the selected wavelength (550 nm) the Berek compensator appears to compensate the retardation of the device. Therefore, if monochromatic illumination at 550 nm were used then the conventional observation of the device at this wavelength would show a Black Compensation Line for this level of compensation. However, from the calibration data provided with the Berek compensator it is known that at this point the compensation is in fact 462 $milli - mu$ (that is 462×10^{-9}), whereas the device retardation at this wavelength is approximately 1014 $milli - mu$ (that is 1014×10^{-9}). The device is therefore clearly not fully compensated. At this point it

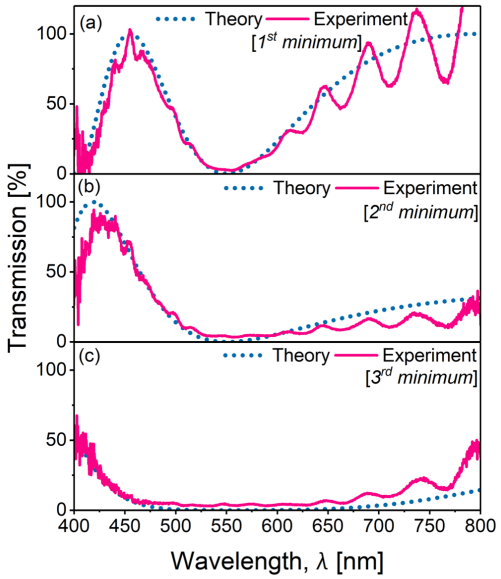


FIGURE 4.8: The experimental transmission spectra (solid lines) with their equivalent theoretical model (dashed lines) of the nematic E7 device at 25oC for various compensation levels with compensated minima in the transmission set at 550 nm. The compensated spectrum at (**a**) 1^{st}, (**b**) 2^{nd}, and (**c**) 3^{rd} minimum at 550 nm.

can also be seen that the device and Berek compensator are close to a full-wave-plate by working out the total retardation of the device plus compensator combination. That is: $\Delta n_{eff}(\lambda) \times d - Berek = 1014 \times 10^{-9} - 462 \times 10^{-9} = 552 \times 10^{-9}$ which is close to the full-wave-plate condition at 550 nm (which would of course equate to a retardation on 550 $milli - mu$).

Now, if the Berek crystal is further rotated, more minima would appear at 550 nm. As the crystal rotates from the initial position (i.e. $\theta = 0°$), it adds further compensation. Therefore, after seeing a first minimum at 550 nm (where the compensation was around 462 $milli - mu$) a second minimum appears, and so on. These minima are termed as the 2^{nd} and 3^{rd} minimum or simply higher orders. Experimental and modelling results for the second and third minimum at 550 nm are shown in Figure 4.8 (b) and Figure 4.8 (c), respectively.

In the theoretical model used to reproduce the results shown in Figure 4.8 (b) (the spectrum of the E7 in a planar-aligned Instec cell for the second minimum at 550 nm) it was necessary to add compensation of around 1014 $milli - mu$. That is, its equivalent model spectrum (Figure 4.8 (b)) was calculated under the condition:

$\Delta n_{eff}(\lambda) \times d - Berek = \Delta n_{eff}(\lambda) \times d - 1014 \times 10^{-9}$. Since at 550 nm the E7 device retardation is approximately 1014 $milli - mu$ (that is 1014×10^{-9}), under this condition at 550 nm the device is fully compensated. If there were no dispersion in the E7 birefringence, then under this condition there would be no transmission across the entire spectrum.

Now, in this context it is interesting to consider the results for what are termed the third minimum. Figure 4.8 (c) shows the third minimum at 550 nm; at this point the compensation added at 550 nm (both experimentally as determined by the Berek compensator, and theoretically in the model) is around 1566 $milli - mu$ (that is 1566×10^{-9}). Knowing the actual retardation of the device is around 1014 $milli - mu$ at 550 nm, it can be seen from: $\Delta n_{eff}(\lambda) \times d - Berek = 1014 \times 10^{-9} - 1566 \times 10^{-9} = -552 \times 10^{-9}$ that this is "one order too-much" compensation.

It is very interesting to consider the spectra in Figure 4.8 (b) compared with those shown in Figure 4.8 (c). It is observed that the third minimum shows a broader dark spectrum across the visible spectrum. Therefore, it is the third minimum spectrum which appears to show the best Black Compensation Line, of the type illustrated in Figure 4.5 (b), when looking through the eyepiece of the microscope after removing the spectrometer. This means that at the point of the darkest broad-spectrum line the Berek compensator is effectively compensating at the incorrect order. Therefore, importantly, if we use a visual observation of the Berek compensation line with white light as a measure of compensation, it will not provide the correct compensation to cancel the retardation of E7. This is generally true for materials with substantial birefringence dispersion – normally the case for LC materials. The interplay between the spectral dependence of the transmission given in Equation 4.3 (mainly due to the λ in the denominator of the term in brackets in this equation) and the birefringence dispersion of the material under investigation (the LC, E7 in the above case) means that the higher order compensation shows the darkest broad-spectrum line.

The above result means that care must be taken when using the Berek compensator to measure the birefringence of materials with substantial birefringence dispersion when using the conventional approach of observing the Black Compensation Line. However, it is relatively simple to "correct" the results if a different order is observed, as illustrated in the following.

4.2.2.2 Standard compensation method

The same E7 sample in the 4.85 μm-thick device was placed between the two crossed polarisers in an optical polarisation microscope as shown in the arrangement in Figure 4.5 (a). After setting the device orientation so that the optic axis is at $\chi = 45^{\circ}$ by rotating the sample stage, the Berek compensator was then inserted in between the analyser and the sample. The compensator crystal was rotated and in doing so a series of coloured fringes appeared. The compensator crystal was rotated until a black line appeared, as seen in Figure 4.9. Initially, one might think that this tilt should now be completely compensating the retardation of the sample in white light. However, as seen from the transmission spectra shown previously in Figure 4.8, in fact this black compensation line represents one order more compensation than the correct compensation at the mid-spectrum ($\sim$550 nm) point. Nevertheless, this tilt angle (θ) was recorded.

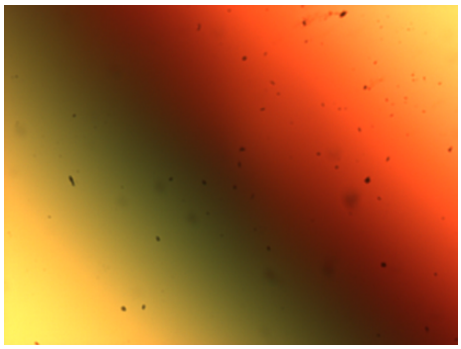


FIGURE 4.9: The black compensation line under white or chorochromatic light when observed with an optical polarising microscope.

The white light source of the microscope was then replaced by quasi-monochromatic light sources of particular wavelength in the visible spectrum (ThorLab LED presented in Chapter 3). The compensator tilt angle was adjusted for each wavelength to ensure that the compensator black line was in the centre of the field of view, as illustrated in Figure 4.5 (b). The tilt angle can then be recorded, and this can be converted to a compensation using the data supplied with the Berek compensator. (In fact, this data was supplied at only certain wavelengths, so a fitting and interpolation procedure was used to determine the appropriate values at other wavelengths).

It is important to note when using monochromatic light, it is impossible to directly determine the appropriate black compensation line. This is why the process is to

first find a black line using white light and then to switch to monochromatic light. Alternatively, the series of coloured fringes which appear as the Berek crystal is tilted when using white light could be counted until the Berek compensation line appears in the view field (as seen in Figure 4.9). Counting and recording the number of orders of fringes until the black compensation fringe appears that informs which is the order of the blackest line. Then, when monochromatic light is used, the same order can again be identified by counting the black fringes until that compensation fringe appears. However, it is important to further note, that based on the observations in Figure 4.8, this is not be the correct compensation order − it is simply the one which corresponds to the broadest dark spectrum. Using this method, E7 dispersion was obtained at an 'over-compensated' order (beyond the true compensation point) which follows an incorrect behaviour as a function of wavelength and therefore is not included here.

It is noted that the correct order was one lower than the broad-spectrum black compensation line point. Therefore, one order (i.e. $m \times \lambda$, where m is the number of orders, i.e. $m = 1$ in this case) is subtracted from the retardation data in order to determine the correct compensation. Dividing by the device thickness then gives the correct birefringence. The corrected birefringence for E7 as a function of wavelength is shown as a solid line in Figure 4.10, together with compared values that were reported in the literature (the reported values are obtained with modified ellipsometry to adapt high-leaky guided mode (HLGM) technique as explained in [160]), and shown as a dotted line. The small difference between the reported and experimental values may be due to different experimental condition such as temperature.

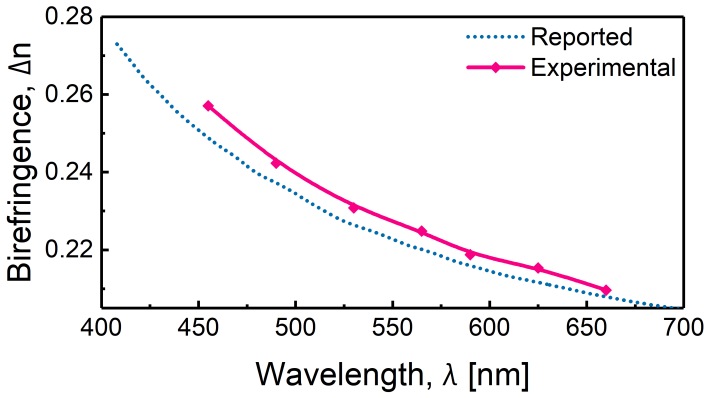


FIGURE 4.10: The measured and reported values of birefringence dispersion in E7. The reported values were obtained from [160].

4.2.3 Birefringence of the LC dimer

Following confirmation of the understanding of the birefringence of a well-known LC material E7, the unknown birefringence of the newly developed LC dimer (compound 7) was measured using the identical experimental setup as explained earlier. Since the LC dimer exhibits a nematic phase over a temperature range of 132°C $\leqslant T_N \leqslant$ 217°C, measurements were taken within this range. For the birefringence measurement, 150°C was chosen as a test point in the temperature range where the material exhibited a nematic phase.

A commercially manufactured LC cell with planar alignment of nominal thickness 2.5 μm was used to prepare the sample. The cell gap was confirmed by taking a spectrum of an empty cell with the Agilent Cary 8453 UV-Vis spectrophotometer and using Equation 3.3 as explained in Chapter 3; the cell thickness in this case was found to be 2.41 μm. This region was marked to ensure all measurements were carried out within this region. The device was then filled with the LC dimer at 135°C (which is in the nematic temperature range).

Measurements of the birefringence of the LC dimer were carried out by studying the transmission spectrum method as explained earlier in §4.2.1.2. Since the material exhibits a nematic phase from 132°C, the sample was heated to 150°C using a Mettler Toledo hot-stage and controller (FP82HT and FP90). The hot-stage containing the sample was then placed between the crossed polariser and analyser of the optical polarising microscope as shown in Figure 4.7. The microscope stage was rotated through χ = 45° with respect to the optical axis of the polarisers. The Berek compensator was inserted into the compensator slot of the microscope, however, the compensator was adjusted to the no-tilt position (i.e. $\theta = 0°$); a spectrum was then recorded without any compensation. The data are shown in Figure 4.11 (a). To obtain a 'fit' to this data the device thickness was set to its measured value of 2.41 μm and then the birefringence values and dispersion adjusted using the form shown in Equation 4.4 until a good comparison was achieved.

After this, retardation was added, and the behaviour of the spectra was studied as the level of compensation was adjusted to match the mid-spectrum point at 550 nm. The retardation was increased by tilting the Berek crystal and for every time that the spectrum showed a minimum at 550 nm, the spectrum was recorded and referred to as

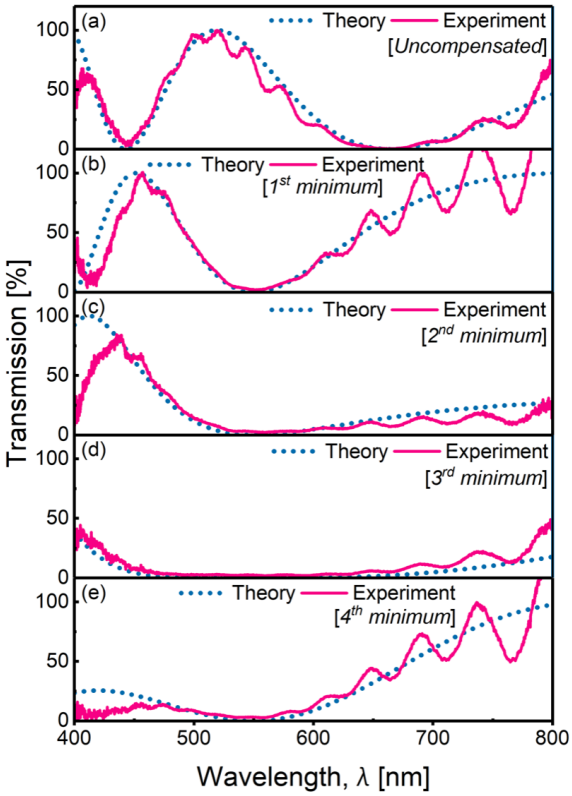


FIGURE 4.11: Experimentally-measured transmission spectra (solid lines) and results from the equivalent theoretical model for the new LC dimer at 150°C for various compensation levels with compensated minima in the transmission set at 550 nm. (**a**) The uncompensated spectrum, and compensated spectra (**b**) 1^{st}, (**c**) 2^{nd}, (**d**) 3^{rd}, and (**e**) 4^{th} minimum at 550 nm. The cell gap was 2.41μm.

1^{st}, 2^{nd}, 3^{rd}, and 4^{th} minimum at 550 nm. The experimental spectra (solid lines) as a function of wavelength at 150°C that simultaneously provided all of the fits (dotted blue lines) are shown in Figures 4.11 (b – e). Each experimental spectrum for a given order is in agreement with their corresponding theoretical model spectrum. Using this comparison between the data and theory it was then possible to estimate the birefringence of the new LC dimer as a function of wavelength at 150°C – this is shown in Figure 4.12. This indicates a mid-spectrum (550 nm) value for the birefringence at 150°C of $\Delta n = 0.312$, with strong dispersion across the visible spectrum.

4.2.3.1 Temperature dependency of the birefringence

The birefringence of a LC also depends on the temperature. The order parameter $\langle S \rangle$ of a nematic LC material decreases with increasing temperature and is zero beyond the isotropic temperature; Δn follows this variation in the order parameter. An example of the dependence of the birefringence on the temperature of a typical nematic LC is

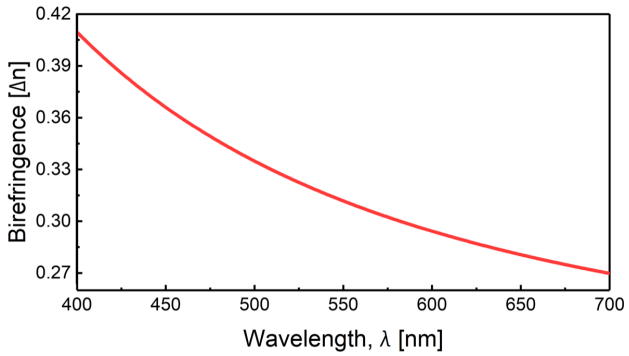


FIGURE 4.12: Birefringence as a function of wavelength for the nematic LC dimer at a temperature of 150°C estimated using the transmission spectra.

shown in Figure 4.13. Since the birefringence also varies with the wavelength (as seen earlier), it is therefore important to study the temperature dependency of the LC dimer at a fixed wavelength.

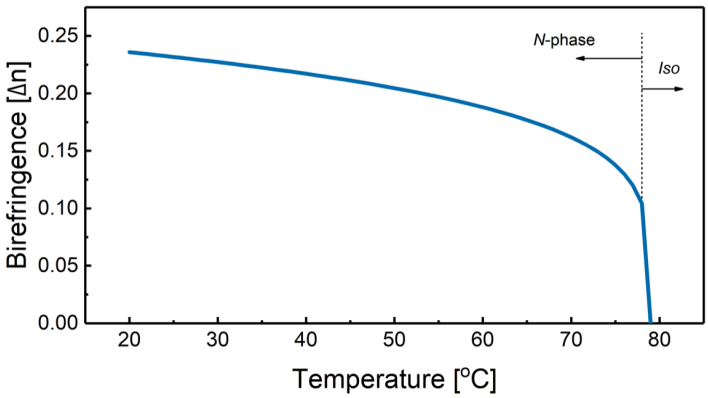


FIGURE 4.13: An example of the temperature dependency of the birefringence of a typical nematic LC.

The birefringence of the LC dimer was studied as a function of temperature ranging from the $N_{TB/X}$ phase through the $N-$ phase to the I_{SO} phase at a fixed wavelength of 550 nm; the results are presented in Figure 4.14. The results were taken with the same method as explained above by heating the sample from 105°C to 207°C. In general, the temperature dependence observed for the nematic phase was similar to that observed for other nematic LCs. The behaviour shows a slight decrease in Δn as the materials enters to the $N_{TB/X}$ phase from the $N-$phase. The molecular arrangement of a typical $N_{TB/X}$ phase is illustrated and presented in Figure A.1, Appendix A. As shown in the Figure A.1, in the $N_{TB/X}$ phase, the tilt in the molecule would result in a decrease in the effective value of n_e and an increase in the effective value of n_o compared to the nematic phase; therefore, it results in an overall decrease in the Δn of the material in the $N_{TB/X}$

phase and supports the phase identification. The increase in birefringence with increasing temperature appears to continue a little way into the $N-$phase, which might not be expected, then levels off and drops from 150°C until it reaches a lower level at the I_{SO}-phase transition temperature. Overall, a high birefringence was observed for the nematic LC dimer with the maximum Δn of 0.312 at 150°C. The minimum value of $\Delta n = 0.184$ was observed at 207°C, which is the just at the limit of the N-phase. There is, however, an unusual drop in Δn within the N phase before the $N_{TB/X}$ phase is entered. This may be due to a change in the molecular ordering before the formation of a tight tilted chiral structure within the molecular arrangement in the $N_{TB/X}$ phase itself.

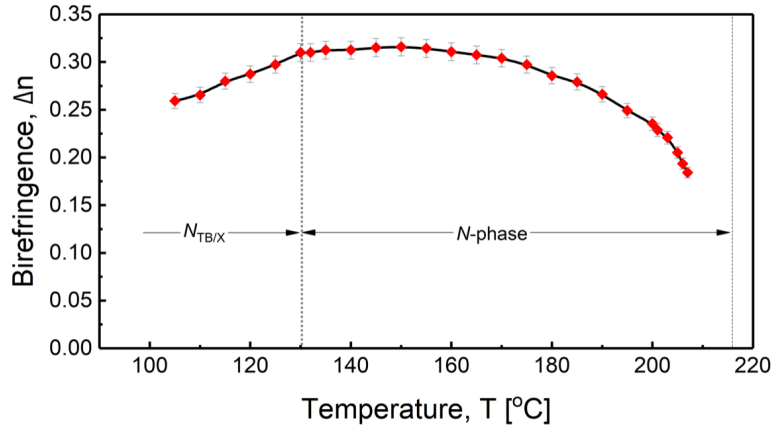


FIGURE 4.14: The temperature dependency of the birefringence of the new LC dimer when the device was heated from the $N_{TB/X}$ at 105°C to the N phase at 207°C. Measurements are for a wavelength of 550 nm.

4.3 Fréedericksz measurement

To investigate the electro-optic behaviour of the LC dimer, the Fréedericksz transition [161] in the nematic phase was investigated using the optical setup as shown in Figure 4.15. A continuous wave (CW) He-Ne laser of emission wavelength at 543.5 nm (close to 550 nm) was used to illuminate the sample. Electrodes and wires were attached to the same device used in the birefringence measurement. The sample was then placed on a hot-stage (set at 140°C) and placed between two crossed polarisers at an orientation of 45°. An electric field was applied across the planar aligned device and the laser passed through the centre of device which was then detected by a photodetector (Thorlab PDA36A-EC $\pm$12V, 200mA) attached to an oscilloscope.

The electric field will cause the reorientation of the LC director if the material

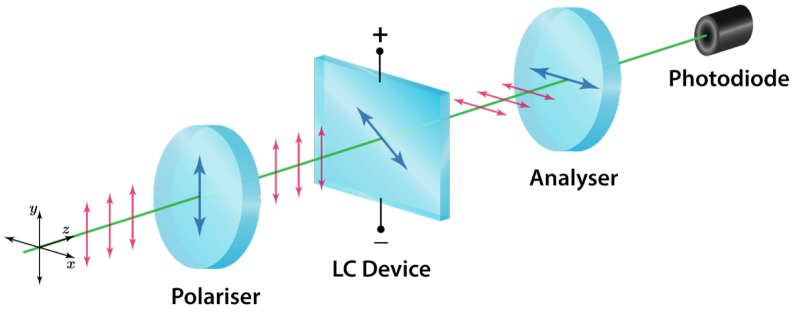


FIGURE 4.15: The experimental arrangement for the Fréedericksz measurement of LC dimer (compound 7) using a pair of crossed polarisers and a continuous wave He-Ne (543.5 nm) laser at 140°C.

has a positive dielectric anisotropy. This reorientation or tilt in the LC director in the presence of an applied electric field is illustrated in Figure 4.16. Due to the tilt in the LC director, the effective retardation experienced by the light passing through the LC device changes. Since the LC device was placed at 45° with respect to the incident linearly polarised monochromatic light, it travels with different velocities through the LC device due to the optical anisotropy of the material. As a result, the components leave the device at different times leading to a phase difference. Depending upon the magnitude of the applied voltage, which produces a certain amount of tilt in the LC director, the output light after coming from the device could be linear, elliptical, or circularly polarised. This transmission of monochromatic 543.5 nm light was measured as a function of the applied electric field and is referred to as a Fréedericksz transmission curve.

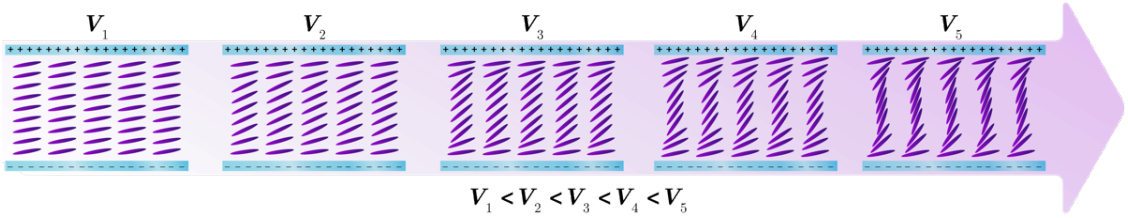


FIGURE 4.16: The variation in the director orientation of a nematic LC when an electric field of varying amplitude is applied across a planar aligned LC device.

In a truly planar cell this results in a change in the transmission of light after passing the threshold voltage (V_{TH}) that is given as:

$$V_{TH} = \pi \sqrt{\frac{k_1}{\Delta\epsilon \times \epsilon_0}} \tag{4.5}$$

where k_1 is the splay elastic coefficient (explained later) for the given LC and $\Delta\epsilon$ is the dielectric anisotropy. In practice, the device is not truly planar so we fit the transmission

curve, which also allows the k_3/k_1 ratio to be estimated. Note: these measurements were taken manually, that is, by apply a certain level of voltage and then recording the output voltage from the photodiode connected to an oscilloscope. Since the measurements were take manually with a step-size of 0.2V, at each point the device reached equilibrium before the data was recorded, therefore, this allows for critical slowing down at the Fréedericksz transition voltage. The results for the nematic LC dimer with 543.5 nm light are presented in Figure 4.17. A theoretical model is also added in Figure 4.17 (blue line) to fit with the experimental dataset.

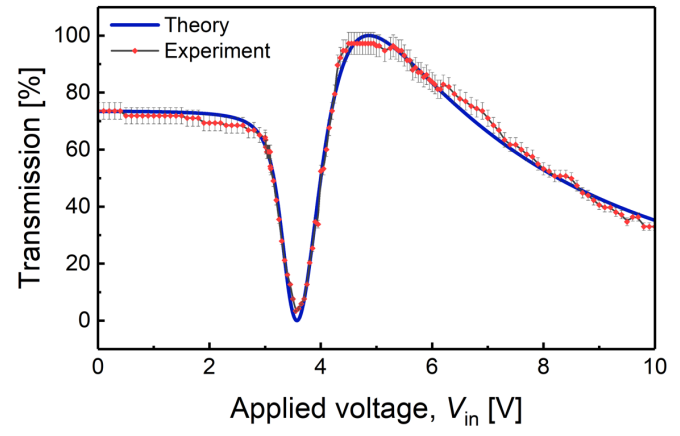


FIGURE 4.17: The Fréedericksz curve of the LC dimer studied with monochromatic He – Ne (543.5 nm) laser light with the device between crossed polarisers.

Modelling and experimental results are used to estimate the $k_1/\Delta\epsilon$ and k_3/k_1 ratios. These are presented and compared with other widely used and related nematic LCs in Table 4.2. A couple of interesting observations can be made: (i) the $k_1/\Delta\epsilon$ value is lower in the other materials listed. It is substantially lower in common materials such as E7, but of a similar magnitude to the dimer CB7CB; (ii) the k_3/k_1 value is less than unity. This is also somewhat different from common materials such as E7 (where the k_3/k_1 ratio is generally larger than one). However, interestingly, it can be seen that the k_3/k_1 ratio for CB7CB is also less than unity.

TABLE 4.2: The comparison of the ratio of the Frank (elastic) constants for the LC dimer compound-7 (measured at 140°C) with other nematic LCs.

Compound	$k_1/\Delta\epsilon$ (pN)	k_3/k_1	**Ref**
E7	0.78	1.54	[162]
5CB	0.44±0.09	1.31±0.12	[163]
CB7CB	2.98±1.87	0.24±0.13	[164]
7	10±1	0.41±0.01	–

4.4 Dielectric measurements

Nematic LCs also exhibit a dielectric anisotropy – this means that the dielectric permittivity varies with direction. In other words, for a given applied electric field, the response of the LC director varies when an electric field is applied along different directions relative to the director. For example, the dielectric permittivity perpendicular to the director is typically denoted as $\epsilon_{\perp}$ whereas $\epsilon_{\parallel}$ represents the dielectric permittivity parallel to the director [165, 166]. Under the presence of electric field and with the mechanical rotation of the LC director, the dielectric permittivity of the LC is no longer constant. In this study, the variation of the dielectric permittivity of the LC dimer is studied.

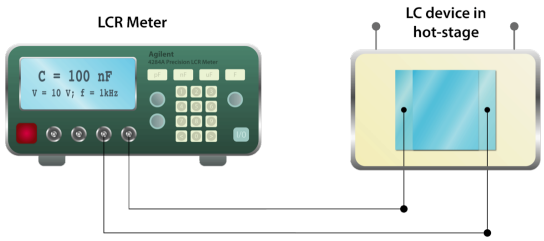


FIGURE 4.18: The experimental arrangement for the measurement of the dielectric permittivity in the nematic phase of the LC dimer (compound 7).

Measurement of the dielectric constant as a function of the applied electric field at 1 kHz at a temperature of 140°C was performed using an Agilent 4284A Precision LCR Meter (20Hz – 1 MHz); the experimental arrangement is shown in Figure 4.18, which measures the capacitance of the LC device under an applied electric field. It is important to note that an ac signal was applied to the device as dc voltages can cause ion migration and can affect the dielectric measurements. The same LC device was used to estimate the dielectric constant as that used to determine the birefringence and the ratios of the Frank elastic constants; this cell had a gap of 2.41 μm and an electrode area of 10 $\times$ 10 mm^2.

The configuration of a LC device can be considered as a parallel plate capacitor that is separated by a distance (d) and filled with LC (in this case the LC dimer). Using the capacitance of a parallel plate capacitor, $C = \epsilon_0 \epsilon_r A/d$, the dielectric constant (ϵ) of the LC was calculated by substituting the capacitance determined using the setup as shown in Figure 4.18. The results of the dielectric measurement as a function of the applied electric field are presented in Figure 4.19. It can be seen that the dielectric constant

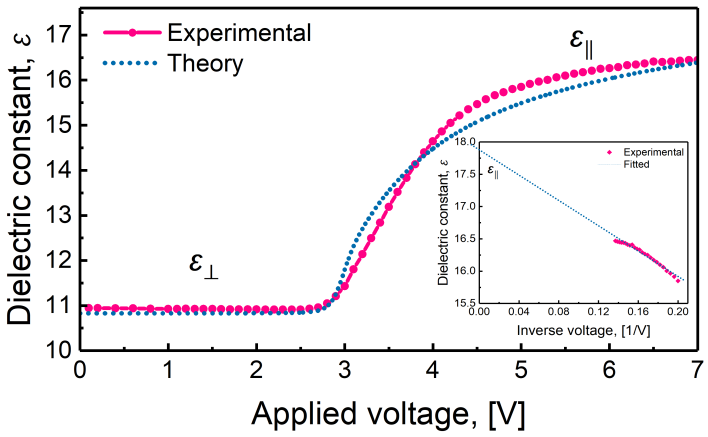


FIGURE 4.19: The dielectric constant of the LC dimer as a function of an applied voltage at 1kHz ac signal at 140°C, inset shows the dielectric constant curve as a function of inverse applied voltage, $1/V$.

increases with the applied voltage, which indicates that the dimer has a positive dielectric anisotropy. As explained earlier, when the applied voltage is less that the threshold voltage, the LC director is aligned in a planar arrangement corresponding to $\epsilon_{\perp}$. As the applied electric field increases above the threshold, the director experiences a change in the tilt leading eventually to a homeotropic alignment as the voltage tends to infinity. Therefore, at higher voltages, the dielectric constant saturates which means that the LC director has adopted an alignment close to that of a homeotropic alignment and thus the equivalent dielectric constant is $\epsilon_{\parallel}$. In order to estimate $\epsilon_{\parallel}$, the dielectric constant is plotted as an inverse function of the applied voltage and presented in the inset plot in Figure 4.19. By extrapolation, it gives the approximate value of $\epsilon_{\parallel}$. The dielectric constant for the LC dimer is found to vary from $\epsilon_{\perp}$ ≈10.9 to $\epsilon_{\parallel}$ ≈17.8. Note: The value of k_1 (as shown in Table 4.2) is unusually large (i.e., $k_1 \approx 70p$N given $\Delta\epsilon \approx 7$) for the compound-7. This could be either due to the unusual nature of LC molecule or some unreliability in the experimental measurement of $\Delta\epsilon$. In the latter case, it is likely that the measured value of $\Delta\epsilon$ is not reliable as this value is unusually larger.

4.5 Flexoelectro-optic theory

In an unperturbed LC system, the LC director is uniform as determined by the physical parameters such as the type of surface alignment or a uniform electric/magnetic field. Nevertheless, if the LC system is disturbed (either by different surface alignment or electric fields), a distortion would occur in the LC director $\hat{\mathbf{n}}(r)$. LCs can be thought of as

an elastic system in which the distortion in the director needs energy (or work done) provided by an external force. The distorted structure stores the elastic energy and returns to the equilibrium (or natural) states when the applied force is removed. A uniaxial LC nematic phase can exhibit distortion that results in three fundamental structures: splay, twist and bend as illustrated in Figure 4.20 [167].

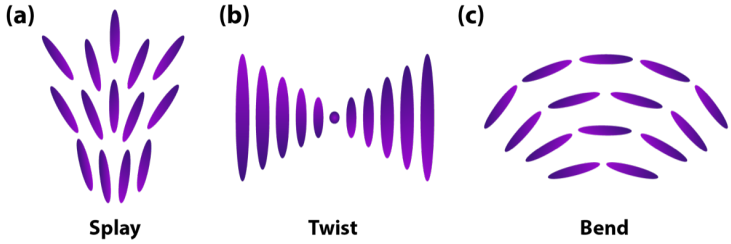


FIGURE 4.20: The three fundamental elastic distortions of a uniaxial LC: (**a**) splay, (**b**) twist and (**c**) bend.

It is considered that the distortion in the LC system occurs over a larger length scale than the molecular length scale. Mathematically, the distortion in the director of an LC system can be described as:

$$Splay : [\hat{\mathbf{n}}(\nabla \cdot \hat{\mathbf{n}})] \tag{4.6}$$

$$Twist : [\hat{\mathbf{n}} \cdot (\nabla \times \hat{\mathbf{n}})] \tag{4.7}$$

$$Bend : [\hat{\mathbf{n}} \times (\nabla \times \hat{\mathbf{n}})] \tag{4.8}$$

The amount with which each kind of distortion (i.e., splay, twist or bend) increases the energy of the system is established by its respective elastic coefficient denoted as k_{11}, k_{22} and k_{33} so as the Frank-Oseen free energy density [167, 168], $f(\hat{\mathbf{n}})$, including the effect of an external electric field and is given by:

$$f(\hat{\mathbf{n}}) = \frac{1}{2}k_{11}[\nabla \cdot \hat{\mathbf{n}}]^2 + \frac{1}{2}k_{22}[\hat{\mathbf{n}} \cdot (\nabla \times \hat{\mathbf{n}})]^2 + \frac{1}{2}k_{33}[\hat{\mathbf{n}} \times (\nabla \times \hat{\mathbf{n}})]^2 - \frac{1}{2}\epsilon_0 \Delta\epsilon[\hat{\mathbf{n}} \cdot \mathbf{E}]^2 \tag{4.9}$$

where ϵ_0 is the permittivity of free space and $\Delta\epsilon$ is the dielectric anisotropy of the nematic LC, given as $\Delta\epsilon = \epsilon_{\parallel} - \epsilon_{\perp}$.

Flexoelectricity is an interesting phenomenon in LCs that relates to the asymmetric shape of the LC molecules, which can introduce a distortion-induced polarisation if the molecules contain a permanent dipole. Generally, flexoelectricity is associated with molecules that are either banana-shaped possessing transverse dipoles or pear-shaped

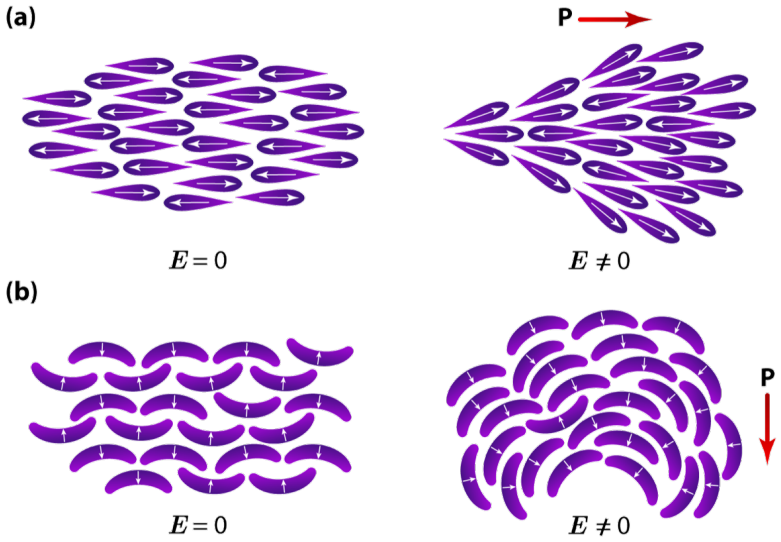


FIGURE 4.21: Illustration of (**a**) pear-shaped molecules and (**b**) banana-shaped molecules and the resulting flexoelectric coupling with an external electric field. In the presence of an electric field, the shape asymmetry of the pear-shaped molecules forms a splay distortion whereas the banana-shaped molecules create a bend deformation of the LC director.

having longitudinal dipoles as illustrated in Figure 4.21 (a & b) [169]. The shape of the LC molecules can play a vital role in determining the flexoelectric coefficient (e_3) of the LC. Unlike to the conventional calamitic rod-shape nematic LCs, the LC dimer possessing a so-called bent-shaped configuration can demonstrate a higher value of e_3 about 3 orders of magnitude greater than that of conventional nematic LC due to their distinctive shape (i.e., banana or pear shape) [170, 171]. As a schematic of a typical bent-core LC molecule is shown in Figure 4.22 (a), which illustrates the presence of a kink angle (θ_0) in the molecular core that directly relates to $e_3 = \left(\frac{\mu_T k_3}{2k_3 T}\right)\theta_0\left(\frac{b}{a}\right)^{2/3} N^{1/3}$, where μ_T is the dipole moment perpendicular to the molecular long axis, k_3 is the elastic constant, T is absolute temperature, N is the number of density of the molecules and a & b are the length and breadth of the molecule, respectively. For an LC where $\theta_0 < 1^\circ$, the flexoelectric coefficient is expected to be between $1{\sim}10 pC/\mathrm{m}$ [172]. However, for a bent-core structure, for instant, in the LC where $\theta_0 \approx 60^\circ$, the flexoelectric coefficient could be 100-times higher than in the conventional nematic LC. Example bent-core LC molecules are shown in Figure 4.22 (b & c).

Without an electric field, the LC molecules arrange with nematic ordering and their dipoles are random and have net polarisation zero. Under the presence of an external electric field, however, the LC molecules reorient to align their dipoles along the

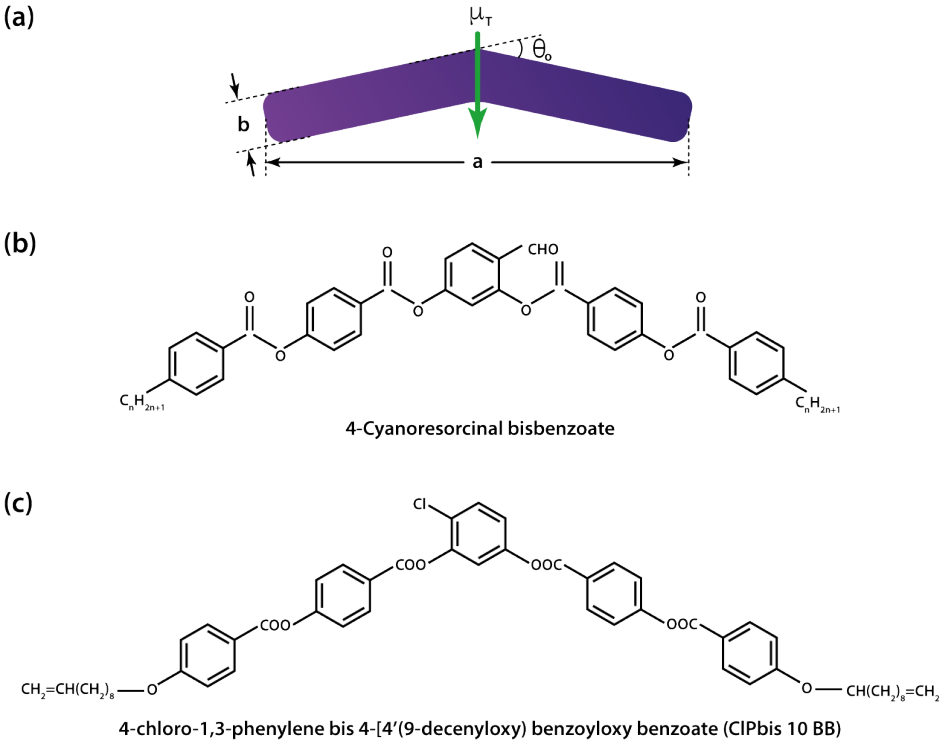


FIGURE 4.22: (**a**) Schematic of a typical bent-core molecule illustrating the kink-angle and dipole moment, and (**b & c**) example bent-core LC molecules. Molecular structures in (**b**) and (**c**) are adapted from [173] and [170], respectively.

electric field. As a result of this reorientation, their shape asymmetry can produce a distortion in the director. This distortion arises either as a bend or splay deformation in the bulk that depends on the shape of the LC molecules.

R. B. Meyer explained the formation of domains in the nematic phase using flexoelectricity when an electric field was applied to the device [174]. If a material with zero dielectric anisotropy, that was uniformly aligned and that had properties of both banana and pear-shaped molecules, it can form an alternating structure of splay and band distortion in the presence of electric field that couples that with flexoelectricity (i.e. the shape asymmetry). Such an LC system is shown in Figure 4.23 [174].

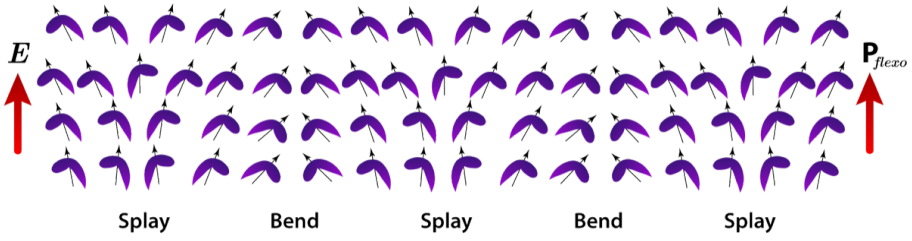


FIGURE 4.23: A hypothetical flexoelectric LC system (possessing banana and pear-shape molecules) forming alternating splay and bend deformation in the presence of external electric field.

Patel and Meyer studied the flexoelectro-optic effect in chiral nematic LCs [175] and concluded it is unlikely to have such a splay-bend alternating structure as, in reality, conventional LC materials have non-zero dielectric anisotropy that would dominate over flexoelectricity. However, they found that in chiral nematic LCs, tilting the director plane with respect to the helix axis can create an alternating splay-bend structure. This deformation produces a flexoelectric polarisation ($\mathbf{P}_{flexo}$) that is orthogonal to the helix axis and a rotation of the director planes. This means that when an external electric field is applied perpendicular to the helix axis, it induces a tilt in the director planes with respect to the helix axis in the plane perpendicular to the applied field, which results in flexoelectric polarisation; the applied field couples with the flexoelectric polarisation. The flexoelectrooptic effect is linear in the applied field and is reversed when the electric field is applied in the opposite direction; this is illustrated in Figure 4.24.

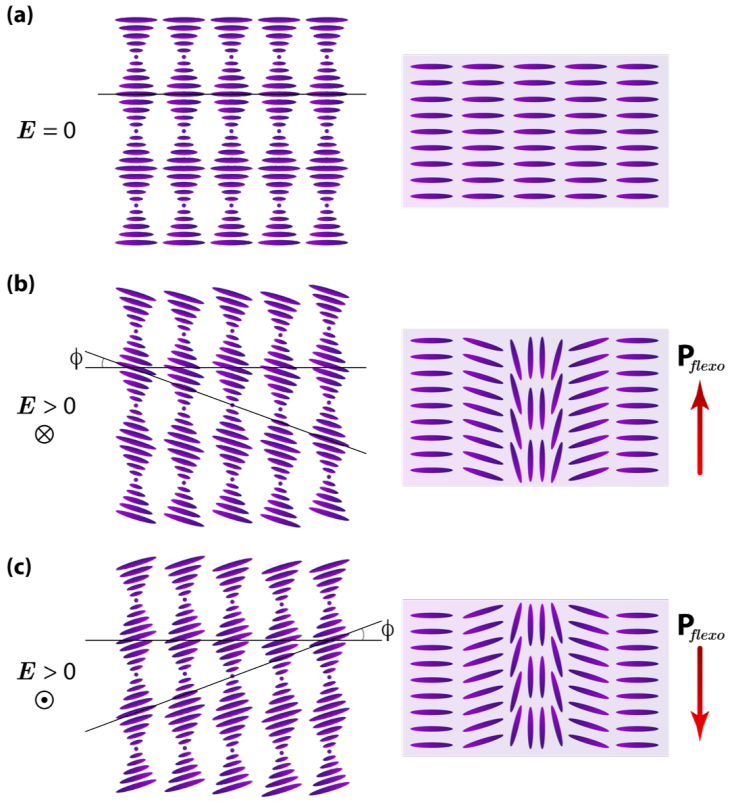


FIGURE 4.24: A chiral nematic helix (*left*) and Bouligand cut-through a plane showing the arrangement of the molecules (*right*), when applied field (**a**)$\mathbf{E} = 0$, and (**b & c**) when $\mathbf{E} \neq 0$: the respective helices show the tilt and the corresponding cut-through planes illustrates the alternating splay-band distortion.

In essence, the coupling between an electric field applied orthogonally to the

helical axis and the flexoelectricity can rotate the molecular orientation resulting in in-plane switching of the optical axis. This is illustrated in Figure 4.25 [175, 176]. The effect therefore results in a coupling between polarisation and distortion, and the flexoelectric polarisation, $\mathbf{P}_{flexo}$, can mathematically be written as:

$$\mathbf{P}_{flexo} = e_1\hat{\mathbf{n}}(\nabla \cdot \hat{\mathbf{n}}) + e_3(\nabla \times \hat{\mathbf{n}}) \times \hat{\mathbf{n}} \tag{4.10}$$

where e_1 and e_3 are the flexoelectric coefficients for splay and bend deformation of the director profile, respectively.

For a given optical anisotropy, choosing the thickness can potentially form a useful electrically rotatable wave-plate. When such a device is observed between a pair of crossed polarisers, the electro-optic effect can be studied in terms of light intensity modulation due to the reorientation of the macroscopic optical axis. The switching angle and switching time depend on the helical pitch and physical characteristics of the LC, such as the elastic constants and viscosity.

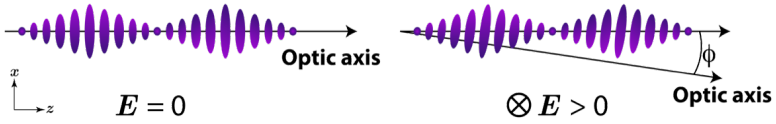


FIGURE 4.25: Illustration of the flexoelectro-optic effect in a chiral nematic LC. ϕ is the tilt angle induced by the electric field applied perpendicular to the helix axis.

The flexoelectro-optic effect is therefore associated with the elastic energy of the system and the coupling between an electric field and flexoelectricity. Assuming $\Delta\epsilon = 0$, mathematically the free energy density of the system can be written as:

$$f = f_{elastic} + f_{flexo} \tag{4.11}$$

$$f(\hat{\mathbf{n}}) = \left[\frac{1}{2}k_{11}[\nabla \cdot \hat{\mathbf{n}}]^2 + \frac{1}{2}k_{22}[\hat{\mathbf{n}} \cdot (\nabla \times \hat{\mathbf{n}}) - q_0]^2 + \frac{1}{2}k_{33}[\hat{\mathbf{n}} \times (\nabla \times \hat{\mathbf{n}})]^2\right] - \left[[e_1\hat{\mathbf{n}}(\nabla \cdot \hat{\mathbf{n}}) + e_3(\nabla \times \hat{\mathbf{n}}) \times \hat{\mathbf{n}}] \cdot \mathbf{E}\right] \tag{4.12}$$

where k_1, k_2 and k_3 are the splay, twist and bend elastic constants, respectively, E is the applied electric field and q_0 is given by $^{2\pi}/_{p_0}$ where p_0 is the natural pitch of the helix. In the current situation, the electric field is applied in the y-direction across the device perpendicular to the helical axis (oriented along the z-direction). Note: Although in real LCs the dielectric anisotropy is not zero, nevertheless, because the flexoelectric coupling

is proportional to **E** whereas the dielectric coupling is proportional to $\mathbf{E}^2$ at low fields it is generally reasonable to ignore the dielectric term. The free energy of the system then becomes:

$$f = \frac{1}{2}k_{11}q^2\cos^2 qz\sin^2\phi + \frac{1}{2}k_{22}[q_0 - q\cos\phi]^2 + \frac{1}{2}k_{33}q^2\sin^2 qz\sin^2\phi - [e_1 q\cos^2 qz\sin^2\phi + e_3 q\sin^2 qz\sin\phi]E_y \quad (4.13)$$

where $q = {}^{2\pi}/_{p}$ with p is the actual pitch of the helix and ϕ is the reorientation in the optical axis or tilt angle as illustrated in Figure 4.25 and E_y is the component of the electric field perpendicular to the helix axis. If the pitch is unchanged with electric field, minimisation of the free-energy gives a relationship between the applied electric field and the tilt angle as:

$$\tan\phi = \left(\frac{e_1 - e_3}{2q_0k_{22}}\right)E - \frac{k_{11} - 2k_{22} + k_{33}}{2k_{22}}\sin\phi \quad (4.14)$$

For small angle switching under the electric field, Equation (4.14) can be simplified by using a small angle approximation to give:

$$\Rightarrow \phi = \left(\frac{e_1 - e_3}{k_1 + k_3}\right)\frac{E}{q_0} \quad (4.15)$$

where $\left(\frac{e_1-e_3}{k_1+k_3}\right)$ is the flexo-elastic ratio and is measured in V^{-1}.

4.5.1 Flexoelectro-optic tilt angle (ϕ) measurement

Generally, two methods are employed to estimate the flexoelectrically-induced tilt angle (ϕ) of the optical axis under an applied electric field. These are (i) a direct estimation of the tilt angle using device rotation and (ii) measuring the electro-optic modulation to determine the tilt angle. In both methods, the transmission (T) through the chiral nematic device placed between a crossed polariser and analyser pair is studied as a function of rotation angle (χ) and given as:

$$T(\chi) = \sin^2(2\chi + 2\phi)\sin^2\left(\frac{\pi\Delta n_{eff}d}{\lambda}\right) \quad (4.16)$$

4.5.1.1 Rotation method

In the first method, to estimate the flexo-electric optical tilt, under an external electric field, the device is placed on the rotation stage of a microscope at $\chi = 22.5^\circ$ with respect to the polariser axis; this gives a modulation signal having a maximum difference

in the intensities of transmission between the positive and negative fields. The corresponding average intensity is denoted by $\langle T \rangle$; this is shown in Figure 4.26. The device is then rotated through an angle of χ_1 until the intensity due to the positive polarity electric field (T_{E^+}) is equal to $\langle T \rangle$. Similarly, the device is rotated in the opposite direction through an angle of χ_2 where $T_{E^-} = \langle T \rangle$. The full switching range (2ϕ) is given by:

$$\Delta\chi = |\chi_1 - \chi_2| = 2|\phi| \tag{4.17}$$

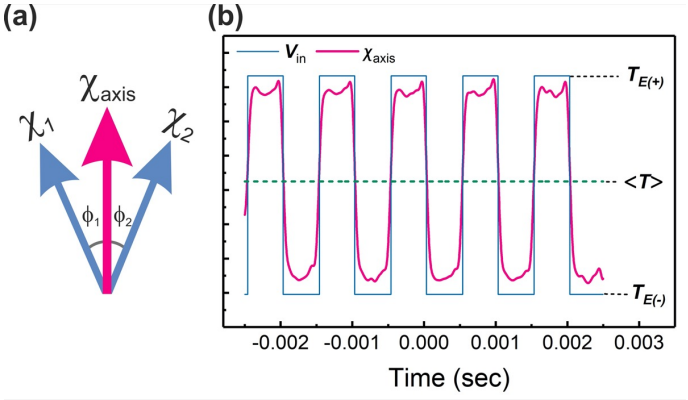


FIGURE 4.26: (**a**) Illustration showing the tilt angle at different orientations of the optic axis, and (**b**) the input and modulation waveform observed using the rotation method when $\chi = 22.5°$.

4.5.1.2 Modulation method

The rotation method does not require any calibration, but the resolution is limited to the accuracy of the rotation stage, which is usually 1°. In the second method, the LC device is first rotated between the crossed polariser and analyser to determine the maximum and minimum levels of the light observed. The stage is then rotated in one direction to an angle of χ_1 so that the modulation waveform levels-off to the minimum, i.e., T_{min}; this allows us to record the T_{E^-} below the mean position of $\langle T \rangle$ (as shown in Figure 4.27). Similarly, the stage is rotated in the opposite direction to the angle of χ_2 that causes the modulation waveform to level-up to T_{max}; this is T_{E^+} and is recorded. With the square-wave electric field ON, the rotation stage is then positioned to the angle of χ_{axis} which is half-way between χ_1 and χ_2 that also gives the maximum modulation of ΔT. This maximum modulation ΔT is recorded and used to calculate the tilt angle as:

$$T = T_0 \sin^2(2\chi_{axis}) \tag{4.18}$$

$$\frac{\partial T}{\partial \chi} = 4T_0 \sin(2\chi_{axis}) \cos(2\chi_{axis}) \tag{4.19}$$

when $\chi_{axis} = 22.5°$,

$$\frac{\partial T}{\partial \chi} = 2T_0 \tag{4.20}$$

This allows us to write,

$$\frac{\Delta T}{\Delta \chi} = 2T_0 \tag{4.21}$$

$$\Rightarrow \Delta\chi = \frac{\Delta T}{2[T_{max} - T_{min}]} \tag{4.22}$$

$$\because T_0 = T_{max} - T_{min} \tag{4.23}$$

$$\therefore \Delta\chi = 2\phi \tag{4.24}$$

(See Equation (4.17) and Figure 4.26 (a) for definitions). Thus;

$$2\phi = \frac{\Delta T}{2[T_{E^+} - T_{E^-}]} \tag{4.25}$$

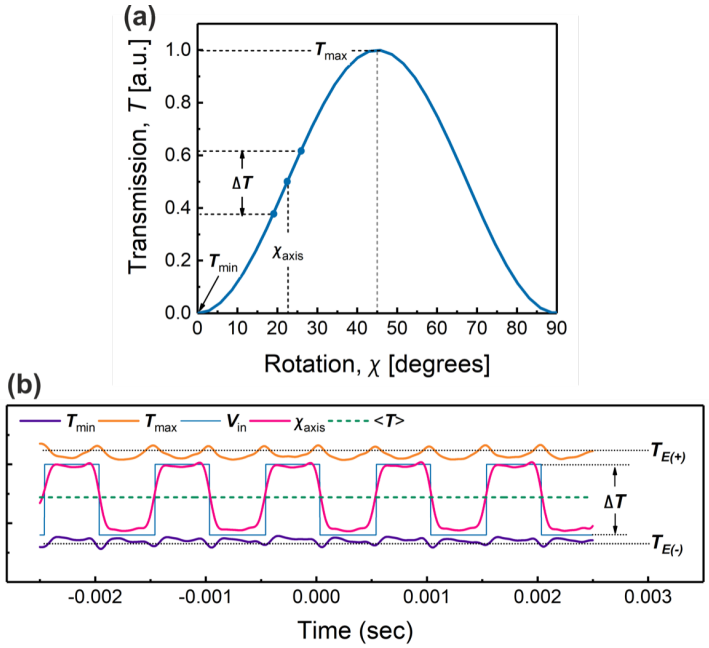


FIGURE 4.27: (**a**) The transmission (T) of light through the LC device as a function of rotation angle (χ) of the stage and (**b**) the modulation signal at the three different rotation positions.

4.5.2 Flexoelectro-optic measurement of the LC dimer

To study the flexoelectro optic measurements of the LC dimer (compound 7), a chiral nematic phase was prepared by mixing it with 3wt. % of the chiral dopant, BDH1281 (Merck). A nominally 5μm-thick glass cell with anti-parallel rubbed polyimide alignment layers and ITO electrodes (Instec) was then filled by adding a small amount of the LC mixture in solid form at one of the entrances of the cell while it was heated to 135° to form the chiral nematic phase. Once the device was filled, wires were attached using

indium shot. The sample was then placed on to a hot-stage and heated to the test point temperature of 140° to form the chiral nematic phase and the transmission spectrum was used to estimate the pitch of the helix using $\lambda_S = n_o \times p$ and $\lambda_L = n_e \times p$. Since LCs generally exhibit an ordinary refractive index of $n_o = 1.5$, the value for n_e was then estimated from $\Delta n = n_e - n_o$. Using these values, the pitch was determined so that the estimated value of pitch satisfies the equations for λ_S and λ_L. The pitch of the helix was found to be $\approxeq 322\ nm$. A percentage error of 1∼2% is expected in the pitch of the helix if n_o is assumed to be 1.55 instead of 1.5. While the sample was at 140°, a $\pm 7V$ square pulse of 700 Hz was applied across the device. The sample was then gently rubbed in one direction to obtain a uniform lying helix (ULH) texture. As the sample was rotated under crossed polarisers, bright and dark states were observed.

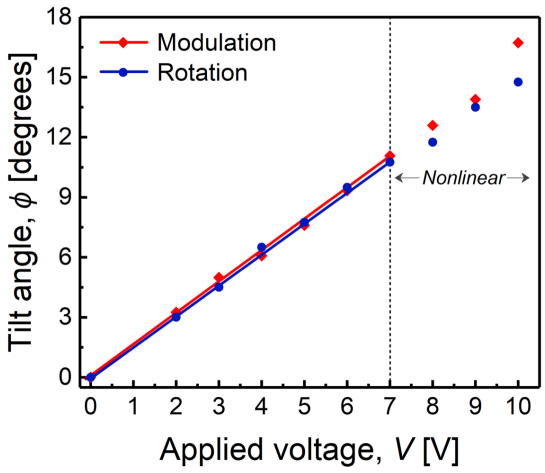


FIGURE 4.28: The flexoelectro-optic tilt angle as function of an external applied electric field for the chiral nematic mixture consisting of the LC dimer (compound 7) and 3 wt% BDH1281. Measurements were conducted for a cell gap of 5μm and a temperature of 140$^{\mu}$C.

Both the 'rotation' and 'modulation' methods were used to estimate the flexoelectrically induced tilt angle of the optical axis of the LC mixture under the presence of an electric field and the results are presented in Figure 4.28. The results suggest a chiral nematic mixture formed from the LC dimer can exhibit large tilt angles of the optical axis up to $15° \pm 1°$ with an electric field of $2\text{V}\mu\text{m}^{-1}$. However, a non-linearity is observed in the behaviour of tilt angle after 1.4 $\text{V}\mu\text{m}^{-1}$ (i.e. 7V) – this may be due to dielectric coupling leading to helix distortion as noted above dielectric coupling can be become important with larger fields. Within the linear regime, the two methods show flexoelectric tilt angles that are in good agreement.

Using the form of the tilt angle as given in Equation (11), the flexo-elastic ratio for this mixture comprising the LC dimer was also determined. Both methods give the flexo-elastic ratio $(e_1 - e_3)/(k_1 + k_3)$ to be approximately 2.59 $\sim$ 2.6 V^{-1}. There have been a number of previous studies on the measurement of the flexo-elastic ratio for E7 + chiral dopant as well as for a range of other materials in different device configurations. Some values are summarized in Table 4.3. To benchmark the results for the new compound, using known values of k_{11} and k_{33} [162] the flexo-elastic ratio for E7 + chiral dopant is found to vary between 0.33 – 0.45 V^{-1} [162, 177–179]. The chiral nematic form of 5CB exhibits a flexoelastic ratio between 0.48 - 0.49 V^{-1} that changes with temperature [180]. On the other hand, a large flexo-elastic ratio of 3.67 V^{-1} has been measured for the material CB7CB when combined with a chiral additive [171].

TABLE 4.3: Comparison of the measured flexo-elastic ratio for the LC dimer (compound 7) with other LC materials. Measurement for the compound 7 were carried at 140°C.

Compound	$(e_1 - e_3/k_1 + k_3)$ (V^{-1})	**Ref**
E7	0.39±0.06	[162, 177–179]
5CB	0.39±0.06	[180]
CB7CB	3.67	[171]
7	2.595±0.005	–

Clearly, the flexo-elastic ratio of this new mixture (compound 7 + chiral dopant) is found to be much larger than that of conventional monomeric mixtures such as E7 and 5CB, but not quite as large as that for chiral nematic mixtures based upon the dimer CB7CB. Nevertheless, the results presented here suggest that the dimer could potentially be used to form a flexoelectro-optic modulator, with the added benefit that due to the high birefringence of the material it could be used to achieve half-wave-plate modulation in much thinner devices i.e. those that are around 2 μm-thick, leading to low driving voltages. Furthermore, the high birefringence is particularly desirable for potential LC laser technologies as it could lead to lower excitation thresholds. However, the high temperature of the LC phase is not desirable for use with conventional laser dyes, which can degrade if subjected to prolonged periods at elevated temperatures.

4.6 Conclusion

The birefringence of a new LC dimer has been measured with a Berek compensator approach. Before the characterisation of this new compound, the reliability

of the experimental method was first confirmed by measuring the birefringence of the well-studied nematic LC, E7. The birefringence of the LC dimer showed dispersion and varied with the wavelength and temperature. Within the nematic phase, Δn varied from 0.312 to 0.184 as the temperature increased from 150°C to 207°C. In addition, the ratios $k_1/\Delta\epsilon = 9 \sim 4$ and $k_3/k_1 = 0.40 \sim 0.42$ were estimated from measurements of the Fréedericksz transition and the dielectric permittivities $\epsilon_\perp$ and $\epsilon_\parallel$ were also investigated and estimated to be 10.9 and 16.4, respectively.

When the new LC dimer was dispersed with a small concentration by weight of chiral additive, the material was found to exhibit a large flexo-elastic ratio of 2.59 $\sim$ 2.60V^{-1}. The relatively large flexo-elastic ratio for the LC dimer (compound 7) coupled with the added benefit of high birefringence enables it to be used in fast switching LC devices that can operate at low voltages. Furthermore, this combination of material properties is potentially of interest for LC laser devices. However, the high temperature (>132°C) of the LC mesophase is not readily compatible with many laser dyes. In the next chapter, alternative gain media in the form of perovskite structures are considered for use with liquid crystalline materials.

Chapter 5

Perovskite Nanocrystals for Band Edge LC Lasers

5.1 Introduction

The gain medium plays an important role in the performance of a laser device as it influences the excitation threshold, slope efficiency and emission stability [58]. Depending on the nature of the optical cavity, the gain medium can be of various forms ranging from doped crystals, to ceramic materials doped with rare earth ions, gases, and fluorescent dyes. For liquid crystal (LC) lasers, fluorescent (laser) dyes have been the gain medium of choice as they can be readily dispersed into a LC host [15, 41, 71]. Dye-based lasers are attractive because they can exhibit both large photoluminescence (PL) quantum efficiencies and wavelength tunability. However, laser dyes generally suffer from photobleaching when optically pumped over long periods of time [64]. Irreversible photo-bleaching, which is due to the breaking of covalent or non-covalent bonds of the fluorophore caused by high intensity photoexcitation, is one of the biggest challenges limiting the performance of dye-based system [181]. In addition to the chemical and photo-instabilities, other drawbacks associated with organic dyes include nonlinear thermal effects when optically excited with high energy beams and the presence of nonradiative triplet states [182, 183].

An alternative form of gain material for LC lasers are quantum dots (QDs) or nanocrystals (NC). QD-LC nanocomposites have been studied for the past few years to study the electro-optic and emission characteristics of a range of the LC systems. In this regards, functional nanocrystals (Au: 1.5$\sim$2 nm) were utilised to attain the alignment

in LC systems [184] and to improve the electro-optic response [185]. For example, CIS-ZnS ($CuInS_2$-ZnS: core/shell) QD (2.2nm) presented in [186] were dispersed in the 5CB nematic LC to reduce the threshold voltage (V_{th}), and electrically tune the birefringence of the LC. In another study, CIS-ZnS (6.5nm) dispersed into into a ferroelectric LC (Felix 17/000) to reduce the order parameter of FLC, spontaneous polarisation and cone angle, enhance the electro-optic response, and photoluminescence intensity at elevated temperature [187]. Alternatively, InP/ZnS (core/shell) (3∼4 nm) QDs in a nematic LC (1823A) were demonstrated an enhancement (∼35%) in the optical birefringence of LC, and to reduce the physical parameters such as the switching time, rotational viscosity and splay constant (k_1) [188]. Furthermore, size-dependent tuning of the photoluminescence intensity and a blue shift in the spectra position in ZnO QDs was achieved when they were combined with ferroelectric LC (KCFLC7S) LC [189]. Similarly, an enhancement in the photoluminescence intensity was demonstrated for MPA (3-mercaptopropeonic acid) capped ZnS (2∼7nm) that was doped into ferroelectric LC (Felix 17/000) [190] and for a ZnS/ferroelectric LC(SCE4) nanocomposite [191].

One of the suitable nano-emitters gain materials for LC lasers are perovskite quantum dots [192], which are compatible with solution processing techniques. Perovskite quantum dots, which can exhibit emission across the entire visible electromagnetic spectrum depending upon the size and composition of the nanocrystals, also appear to exhibit a high quantum efficiency ranging from 70% (methylammonium based in Dimethylformamide) [193] to 90% (Caesium-based in toluene) [194] and high absorption coefficients of the order of 10^4 to 10^5 cm^{-1} [195]. Research has demonstrated that they are also insensitive to photo-bleaching and have the potential for electrical pumping. Perovskite nanocrystals have been used in a number of different configurations to create micro/nano laser devices and have exhibited amplified spontaneous emission (ASE) as well as single and multimode laser emission [88, 89, 196–198]. For example, $CsPbX_3$ perovskite nanocrystals have demonstrated ultralow fluence excitation in different configurations such as whispering gallery mode microspheres ($2\mu J/cm^{-2}$/pulse) [199], micro/-nanowires ($3\mu J/cm^{-2}$/pulse) [200] and quantum dots or nanocrystals ($5\mu J/cm^{-2}$/pulse) [201].

The combination of compatibility with solution processing along with the remarkable emission characteristics (wavelength tuning, narrow emission spectrum and low excitation threshold) make perovskite nanocrystals a potential candidate for micro-lasers based upon liquid crystalline materials. One of the simplest configurations would be to combine the perovskite nanocrystals (NC) directly with the chiral nematic LC phase to form a band-edge laser. The effective dispersion of the nanocrystals is critical as it can affect the LC alignment as well as the emission characteristics of the perovskite. The dispersion of nanocrystals in LC materials can be achieved in variety of ways [202–204]; one widely used method is to add the required amount of nanocrystals with their host solvent into the LC phase, the nanocrystal's doped mixture is then ultra-sonicated to achieve a uniform dispersion [205–209]. In addition to the creation of nanocrystal-doped LC lasers, nanocrystals have also been employed to improve LC electro-optic characteristics for the purposes of display applications [204, 205, 210–213]. Because of these desirable photophysical characteristics, in this chapter, perovskite nanocrystals [214–216] are considered as an alternative optical gain medium for band-edge LC laser devices and for other optoelectronic devices.

5.2 Perovskite Nanocrystals

The *perovskite structure*, or simply *perovskite*, was originally attributed to the mineral composed of calcium, titanium, and oxygen, known as $CaTiO_3$ [217]. It was given the name perovskite by the German mineralogist, Gustav Rose, in honour of the Russian mineralogist Lev A. Perovski. Today, the term perovskite is ascribed to structures that have an identical crystallographic form to that of the perovskite mineral, and which are of the general configuration, ABX_3, as depicted in Figure 5.1, where A is a monovalent cation that can be either organic (e.g.$CH_3NH_3)^+$ or inorganic (e.g. Cs^+), B is an inorganic metal anion (typically lead $(Pb)^{2+}$, but can also be $(Sn)^{2+}$), and X^- is a halide (Cl, Br, I) or mixture of halides. Hybrid perovskite structures have attracted considerable attention in recent years due to their incredible light-absorbing properties, which has led to a revolution in the performance of photovoltaic technologies enabling solution-processed devices to reach efficiencies of up to 25% by 2020 [218].

While perovskite materials have demonstrated great potential in photovoltaics,

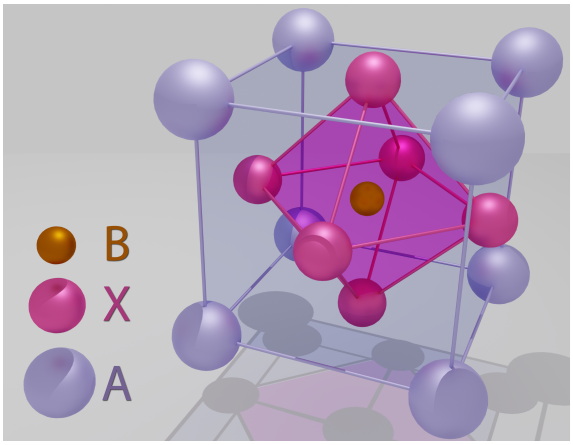


FIGURE 5.1: The structure of a perovskite crystal, where A is a cation, which can be organic (e.g. $CH_3NH_3^+$) or inorganic (e.g. Cs), B is an anion (metal) and mostly lead (Pb^{2-}) and X is a halide (Cl, Br or I) or a mixture of halides.

they are also an exciting prospect for light emitting diodes [219] and thin-film lasers [220, 221]. Previous reports on perovskite films have demonstrated amplified spontaneous emission [89] and/or laser emission from a variety of configurations and architectures including thin films [222], whispering gallery modes [223, 224], nanowires [214, 225], nanorods [226], and corrugated distributed Bragg reflectors [88]. Many of these configurations are not readily compatible with LC materials. Perovskite-based colloidal quantum dots or nanocrystals [192, 201], however, are more suited as they could, in principle, be dispersed directly into a LC host [203], negating the need for a complex fabrication process of the resonant cavity/photonic structure. The fundamentals of an LC band-edge laser are explained in detail in Chapter 2.

Nanocrystals are typically synthesised using one of a number of different methods such as hot-injection [227, 228], ligand-assisted re-precipitation [229, 230], one-pot synthesis [231, 232], or a vapour cross-linked method [233, 234]. The emission wavelength of perovskite nanocrystals exhibits a size-insensitive narrow emission spectrum that can be tuned over a wide wavelength range (400 nm $\leqslant \lambda \leqslant$ 780 nm) by varying the composition of the anion halide group. Due to their narrow emission spectrum (FWHM $\sim$ 20 nm), they exhibit a very wide colour gamut and are promising candidates for high colour purity light emission [235]. These distinct features make them superior to other inorganic quantum dots such as ZnO [236] and CdSe – CdS [237] that have comparatively larger FWHM ($\sim$30 nm), and size sensitive emission spectrum [238]. In the perovskite 3D

emitter, the lead-halide bond prompts a Fröhlich interaction (between longitudinal optical (LO) phonons and charge carriers) resulting in phonon-electron coupling and LO-phonon scattering that determines the FWHM [239]. Furthermore, the impurities and defects in perovskite arising from poor crystallinity do not appear to affect the FWHM as trap-assisted relaxations that lead to non-radiative recombination are negligible as are the impurities that typically introduce line broadening. As a result, the FWHM of 3D perovskite emitters are found to be insensitive to their physical size [239, 240].

Other distinct characteristics include the sharp electronic bandgap, free-carrier densities greater 10^{17} cm^3 [214], high charge carrier mobilities [241], bright emissivity driven by lower threshold voltages, low charge trapping enabling efficient radiative recombination, high photo-luminescence quantum yield [242] and high brightness [243]. Being a semiconductor material, they can also be electrically pumped as demonstrated in various perovskite-based LEDs [244], which provides a potential pathway to electrically-driven perovskite lasers [245].

Perovskites are created either as organic–inorganic hybrids (usually methylammonium or formamidinium) or all-inorganic such as those based upon Caesium (Cs) occupying the A-site. The organic–inorganic perovskite hybrids can become chemically unstable either due to exposure to a moist environment or photo-degradation. Predominantly, the cation in these hybrids is hygroscopic in nature, which can easily decompose the crystal lattice structure [246, 247]. In contrast, Cs-based perovskite nanocrystals exhibit stable emission characteristics and they appear to be more immune to environmental conditions that can typically lead to a disintegration of the structure. These nanocrystals also exhibit good optical characteristics such as photoluminescence quantum efficiency $\geqslant$ 90% [194, 248]. Furthermore, structures based upon the composition $CsPbX_3$ have been widely studied in the past few years and for these combined reasons, all-inorganic (Cs-based) hybrids of perovskite nanocrystals are considered in the following sections.

Two types of Cs-based nanocrystals were used in this study: (1) $CsPbI_3$ and (2) $CsPbI_2Br$, both of which were synthesised and provided by the team of Professor Henry Snaith in the Department of Physics at Oxford, UK. These nanocrystals were synthesised using ligand-assisted reprecipitation techniques using a method similar to that

reported [249]. They were supplied in the host solvent, hexane. The concentration of the $CsPbI_3$ nanocrystals in hexane was 10 mg/ml while for $CsPbI_2Br$ it was 1 mg/ml. Squared shaped perovskite nanocrystals were used in this study. Perovskite nanocrystals have zero dimensionality (measure from several to hundreds of nanometres) and offer remarkable light-emitting characteristics (as explained earlier). While single crystal nano-emitters with an anisotropic shape may offer benefits in terms of the dispersion in an anisotropic medium (such as an LC) and show different absorption coefficients along different directions, the isotropic-shaped metal halide perovskite nanocrystal exhibits higher electron and hole confinement in three dimensions compared to the 2D (microplates) or 1D (nanorods) structures, which could potentially lead to a lower excitation threshold of the laser [250]. To control the overall size and shape of the nanocrystals, and to avoid aggregation and the passivation of electronic trap states, both types of nanocrystals were caped with oleic acid and oleylamine. TEM (Transmission Electron Microscope) micrographs of these nanocrystals are shown in Figure 5.2 (a & b) demonstrating that the sizes of both types of nanocrystals were relatively monodisperse at 10 – 15 nm. The absorbance and photoluminescence for the nanocrystals dispersed in hexane were studied using a Horiba Fluorolog-3 with FluorEssence. The results of the absorbance and PL emission are presented in Figure 5.2 (c & d) indicating that both types of nanocrystals show a strong absorbance at shorter wavelengths and emit light with a peak wavelength at 675 ± 2 nm when illuminated with UV (365 nm) radiation.

The photo-physical characteristics of the gain medium can influence the laser efficiency, which can vary dramatically depending upon the properties of the host material. The gain medium can be combined with LCs to form an optical cavity in a number of different ways. However, due to its appeal in terms of simplicity of fabrication, a band-edge configuration is considered here. In the following sections, attempts are made to combine the perovskite nanocrystals with LCs in order to demonstrate band-edge laser emission in chiral nematic LCs. The uniform dispersion of QD or nanocrystals in the LC systems is critical for the LC lasing operation and to maintain the LC alignment structure. As summarised above, in the previous reports, the QDs were dispersed into LC systems to improve the electro-optic characteristics and enhance the birefringence of the LC. Precautions were taken into account to create the QD-doped LC nanocomposites.

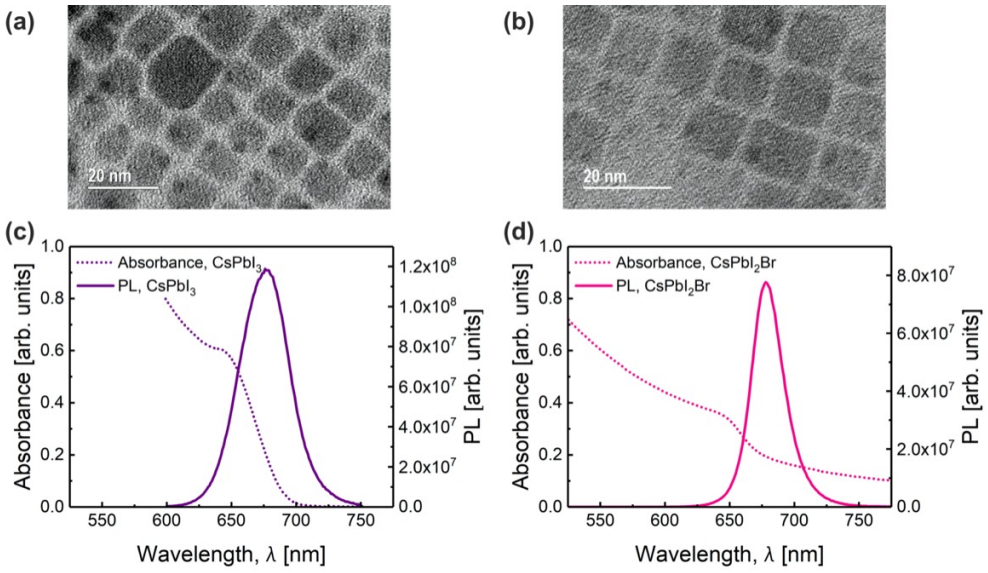


FIGURE 5.2: TEM micrographs of (**a**) $CsPbI_3$ and (**b**) $CsPbI_2Br$, and absorbance and photoluminescence spectra of (**c**) $CsPbI_3$ and (d) $CsPbI_2Br$ perovskite nanocrystals in hexane when excited with UV (365 nm) radiation. These results were obtained by the group of Professor Henry Snaith, Physics, Oxford, UK.

These include [251]:

1. The concentration of the QDs needs to be optimised since a lower concentration may not provide enough gain for the laser action whereas a higher concentration may result the aggregation of QDs in the LC.
2. The physical experimental conditions such as temperature can also play an important role in determining the physical and chemical properties of the QD-LC nanocomposites. High temperature can damage the capping or ligands of the QDs that would affect their dispersion and may cause aggregation, it can also lead to chemically decomposition of the LC materials.
3. The host solvent of the QD must evaporate completely from the QD-LC composite to ensure a uniform phase of the nanocomposite.

In attempting to prepare the perovskite nanocrystals doped in host nematic LC mixtures for the purpose of fabricating band-edge LC lasers, the abovementioned considerations were taken into account. The dispersion of the perovskite nanocrystals in the LC were achieved using different methods including ultrasonication, thermal and room temperature dispersion by optimising the concentration of perovskite nanocrystals.

5.3 Ultrasonic Dispersion

For this study, perovskite nanocrystals were dispersed into nematic and chiral nematic LCs using ultrasonication. This method was selected so as to avoid direct physical contact of a magnetic stirrer with the nanocrystals. This section describes the mixture preparation process and the relevant metrologies employed to study the nanocrystals dispersed in the LC host.

Inorganic Cs-based ($CsPbI_3$ and $CsPbI_2Br$) perovskite nanocrystals were used for this study because they have been well-characterised previously and are more stable in comparison to organic – inorganic hybrid material (as explained earlier) [246–248]. The weight of the nanocrystal/hexane mixture and the nematic LC, E7, were carefully measured using a precision microbalance (Mettler Toledo AB104-S). Mixtures were prepared for three different concentrations of nanocrystal: 1, 2.5 and 5 wt. % for both $CsPbI_3$ and $CsPbI_2Br$ nanocrystals. In order to understand the effects of sonication on the dispersion, the nematic phase of the LC (E7) was first considered. E7 is a thermotropic LC that exhibits an isotropic phase above 60°C and as the temperature is decreased to that of room temperature the viscosity increases. It was expected that the perovskite nanocrystals might not disperse uniformly in the nematic phase due to the larger viscosity. Therefore, to encourage a successful homogeneous dispersion of the nanocrystals in the nematic E7, the LC was first diluted with a solvent. This solvent was chosen to be same as the host solvent for the perovskite nanocrystals, i.e. hexane.

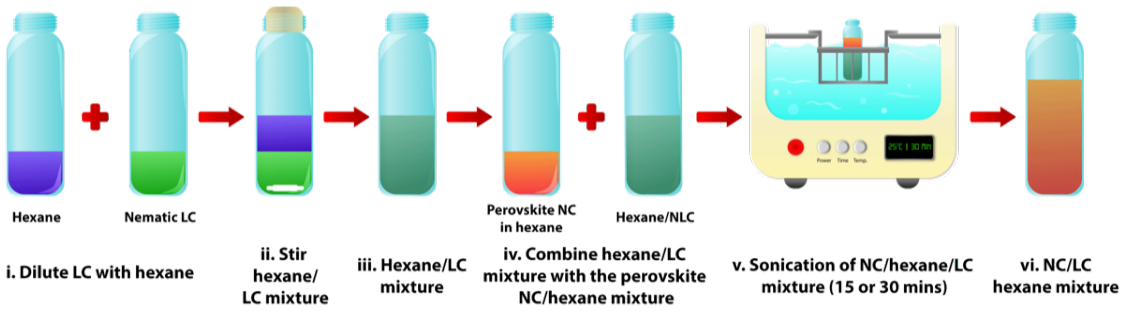


FIGURE 5.3: Mixture preparation process that involved diluting the nematic LC (E7) with hexane before adding it to a solution of perovskite nanocrystals and hexane. This was followed by an ultrasonication process.

The mixture preparation process is illustrated in Figure 5.3. To begin with, the nematic LC was mixed with hexane using a magnetic stirrer at a speed of 200 rpm and a temperature of 25°C for 2 hr. During mixing, the vial was capped to avoid evaporation

of the hexane, Figure 5.3 (i – iii). Once the mixture was prepared, the $CsPbI_3$ or $CsPbI_2Br$ nanocrystals in hexane were added (Figure 5.3 (iv – vi)). Mixtures were prepared so as to achieve a final concentration of nanocrystal in the LC of 1, 2.5 and 5 wt. % for both types of nanocrystal. In the vials, each mixture exhibited two separate phases: one that was clearly dominated by the nanocrystals and the other that was believed to be the diluted LC (e.g. see Figure 5.4 (a) for $CsPbI_3$ nanocrystals in a hexane-diluted LC host). Sonication was then performed by immersing the vials in an ultrasonic bath (Branson 1550, f = 40 kHz, temperature control up to 69°C). At 5 minute intervals, the mixtures were inspected under UV illumination to see if the nanocrystals had been uniformly dispersed in the mixture by observing whether the emission from the vials appeared uniform. It was found that mixtures that were sonicated for 15 min resulted in homogenous emission (see Figure 5.4 (b & c)). During sonication, the lids from the vials were removed to allow the hexane solvent to evaporate. 7 μm-thick glass cells with anti-parallel rubbed polyimide layers were then filled with these mixtures via capillary action and were sealed with a UV-curable glue.

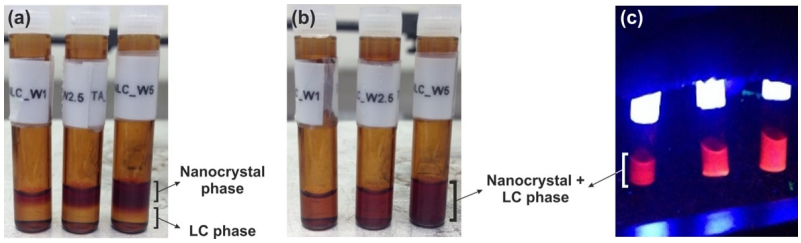


FIGURE 5.4: Photographs of diluted LC doped with $CsPbI_3$ nanocrystals in hexane: (**a**) before the ultrasonication process when the mixture shows two separate phases consisting of nanocrystal in hexane and LC/hexane and (**b**) after the ultrasonication process where it was found that the mixture forms a single phase. (**c**) Photograph of mixtures under UV (365 nm) illumination after the ultrasonication process showing emission from the $CsPbI_3$ nanocrystal dispersed in the diluted nematic LC host.

The samples were then observed with an optical polarisation microscope with crossed polarisers. Example images for samples consisting of the $CsPbI_3$ nanocrystals doped in a nematic LC are presented in Figure 5.5. Due to aggregation, the nanocrystals can be seen clearly in the 2.5 and 5 wt. % samples for both types of nanocrystals and are more noticeable when viewed in the dark state (i.e. the optic axis of the nematic phase is aligned with one of the transmission axes of the polarisers). However, the presence of the nanocrystals was not so obvious for the 1 wt. % sample and images are not included here. Even though the nanocrystals for both the 2.5 and 5 wt. % samples tend to aggregate, the

distribution of these clusters appears to be relatively uniform.

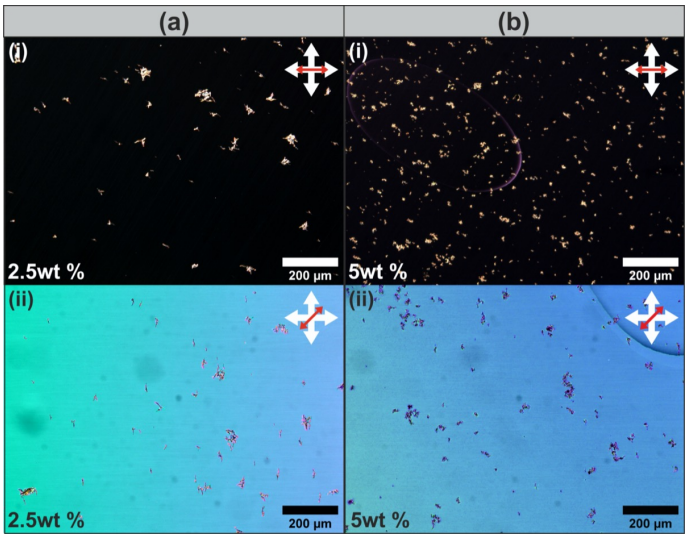


FIGURE 5.5: Optical polarisation microscope images of the nematic LC (E7) doped with $CsPbI_3$ nanocrystals at concentrations by weight of (**a**) 2.5 wt. % and (**b**) 5 wt. %. Images are of a dark state (i), with the optic axis aligned with one of the transmission axes of the polarisers, and a bright state (ii), whereby the optic axis of the LC is at 45° to the crossed polarisers. Samples (7 μm-thick) were prepared by diluting the LC mixture and dispersing the nanocrystals via an ultrasonication process. The samples were prepared, and the measurements were carried out, at a temperature of 25°C.

The optical microscope images were subsequently analysed by generating images based on an edge-detection method. For the edge-detection method used in this study, the function *edge* in MATLAB was used and amongst the available filters, the Sobel filter was chosen as this was found to give optimised selectivity between the edge of the cluster domains and the surrounding LC background. As an example, the images generated for the $CsPbI_3$ nanocrystals are presented in Figure 5.6, which indicate that the nanocrystal aggregate size increases as the concentration increases from 2.5 to 5 wt. %. Specifically, the average cluster size observed for the 2.5 wt. % and 5 wt. % samples were found to be 10 ± 1.5 μm and 18 ± 1.7 μm, respectively.

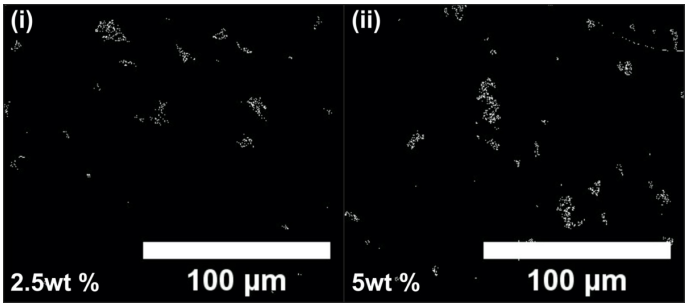


FIGURE 5.6: Images generated using an edge-detection method showing the presence of $CsPbI_3$ nanocrystal clusters in the nematic LC for (i) 2.5 wt. % and (ii) 5 wt. % concentrations by weight of the nanocrystals.

The samples containing $CsPbI_2Br$ were also observed with an optical polarisation microscope with crossed polarisers and images are shown in Figure 5.7. For all concentrations, the samples were found to retain the planar alignment of the LC director as evidenced by the bright and dark states observed when the samples were rotated between crossed polarisers. Again, there was no clear evidence of the nanocrystals in the 1 wt. % mixtures in accordance with that observed for the $CsPbI_3$ nanocrystals and hence results are not included here. Similarly, the nanocrystals are found to form aggregates for the 2.5 and 5 wt. % samples and the aggregate size clearly increases as the level of concentration is increased to 5 wt. %. The sizes of the nanocrystal clusters in the 2.5 and 5 wt. % samples were again estimated using the edge-detection method. In this case, the average cluster size for the 2.5 wt. % sample was 10 ± 3.2 μm and 15 ± 2.1 μm for the 5 wt. % sample, which are comparable to the results obtained for the samples containing the same weight concentration of the $CsPbI_3$ nanocrystals.

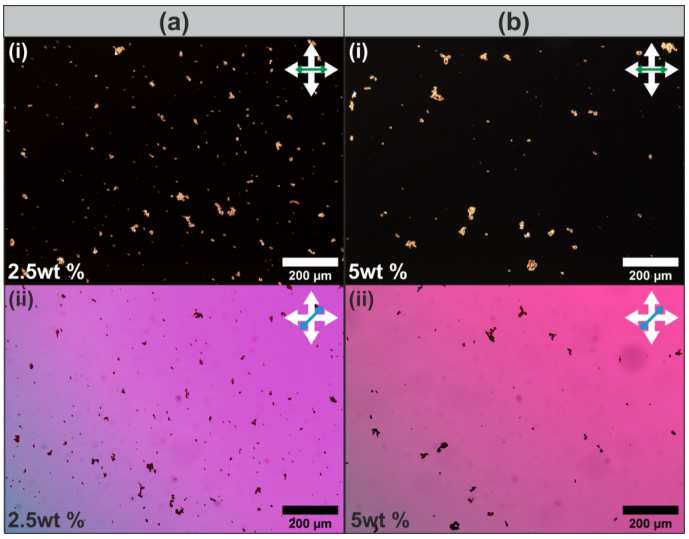


FIGURE 5.7: Optical polarisation microscope images of the nematic LC (E7) doped with $CsPbI_2Br$ at two different concentrations by weight: (**a**) 2.5 wt. % and (**b**) 5 wt.%. Images are of a dark state (i) and a bright state (ii). Samples were prepared by diluting the LC with hexane before the dispersion of the nanocrystals using an ultrasonication process. The samples were 7 μ m-thick. Both sample preparation and measurements were carried out at a temperature of 25°C.

To investigate the emission from the nanocrystals in the nematic LC host after the ultrasonication process, the samples were studied with a fluorescence microscope using UV (λ = 365 nm) illumination. Examples of the fluorescence optical micrographs are depicted in Figure 5.8. The nanocrystals showed red emission as expected from the emission spectrum recorded when they are dispersed in hexane (see Figure 5.2). In accordance

with the optical microscope images, the nanocrystals appear to aggregate for the 2.5 and 5 wt. % samples, as can be seen by the bright fluorescent regions, and the cluster size is increased as the concentration changes from 2.5 to 5 wt. %.

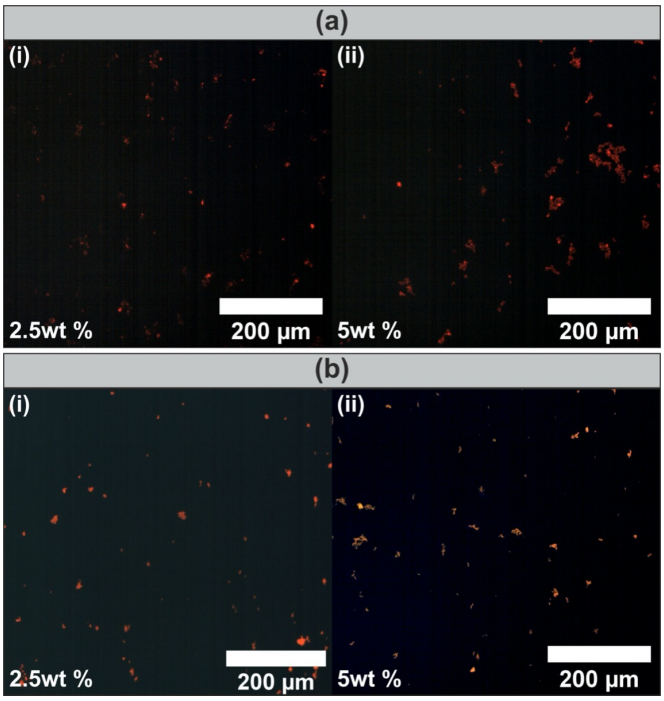


FIGURE 5.8: Fluorescence microscope images of the nematic LC (E7) doped with either (**a**) $CsPbI_3$ or (**b**) $CsPbI_2Br$ nanocrystals at 2.5 wt. % and 5 wt. % concentration by weight. The samples were prepared by diluting the LC mixture with hexane and dispersing the NC into the hexane/LC mixture using ultrasonication. The samples were 7 μm-thick and measurements were carried out at a temperature of 25°C.

To excite the nanocrystals and study their PL emission spectrum, a fibre-coupled UV LED (λ = 365 nm, Thorlabs M365F1) was used; this experimental setup is discussed in more detail in Figure 3.15, Chapter 3. In order to compare the different samples, the excitation intensity and the integration time of the spectrometer was kept the same throughout measurements. The results are presented in Figure 5.9. The samples with 2.5 and 5 wt. % concentration of nanocrystals showed significant PL emission when excited with UV radiation, although no emission spectrum was recorded for the 1 wt. % samples (not shown here). The peak emission for the nematic LC samples doped with the $CsPbI_3$ nanocrystals was found to be centred at λ_p = 678$\pm$1 nm, which is a small red-shift from that observed for the perovskite nanocrystals dispersed in hexane (dotted line) (λ_p = 677$\pm$1 nm). A small solvatochromic shift is not unexpected given the difference in polarity between the LC and hexane hosts.

Generally, a positive solvatochromic shift (i.e., a red-shift in the peak emission

wavelength) is expected when the emission characteristics of the solute are studied in a polar solvent in comparison to the behaviour observed in a non-polar solvent. For example, fluorescence emission from the DCM laser dye has been studied in both a *n*-hexane host (non-polar solvent) [252] and the nematic LC mixture, E49, which is a polar solvent [253]. Upon photo-excitation, a positive solvatochromic shift of ∼60nm (red-shift) was observed for the mixture containing the LC host when compared to the mixture with the hexane solvent ($\lambda_{hexane} = 530$ nm and $\lambda_{E49} = 589$ nm). In the case of perovskite-doped nematic LC, the solvatochromic red-shift was found to be rather small, typically of the order of 3∼4 nm ($\lambda_{hexane} = 675$ nm whereas $\lambda_{E7} = 678$ nm). It is not entirely clear why there is such a small solvatochromic shift for these mixtures. It is speculated that the aggregation of the perovskite nanocrystals reduces the solvatochromic shift as the nanocrystals are not uniformly diluted into the LC host.

The FWHM of the spectrum for the $CsPbI_3$-doped LC samples was also found to be reduced by a small amount of ≈ 4 nm compared with that observed for the solution of nanocrystals in hexane. Nevertheless, despite these small differences, the overall shape of the PL emission spectrum is found to closely resemble that observed for the nanocrystals in hexane and is a strong indication that the nanocrystals have largely remained intact during the dispersion process.

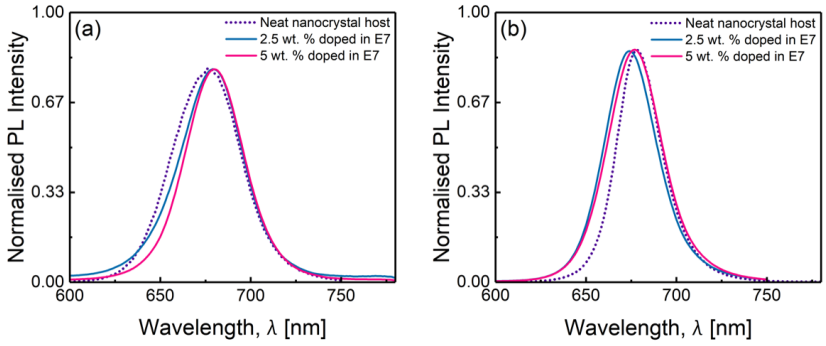


FIGURE 5.9: PL emission spectrum from samples containing the nematic LC (E7) doped with either the (**a**) $CsPbI_3$ or (**b**) $CsPbI_2Br$ nanocrystals at 2.5 wt. % and 5 wt. % concentrations by weight. The samples were prepared by diluting the LC mixture with hexane before dispersing the nanocrystals using an ultrasonication process. For comparison, the emission spectrum for the nanocrystals in hexane are also presented (dotted lines). The samples were 7 μm-thick films and measurements were carried out at a temperature of 25°C.

Samples containing the $CsPbI_2Br$ nanocrystals exhibited a peak in the emission intensity at 676 nm for the 5 wt. % sample, which is close to the peak emission recorded for the nanocrystal in hexane sample (λ_{PL} = 677±1nm). However, the 2.5 wt. % samples

exhibited a slight blue shift of about 2.5 nm with the emission peak occurring at 674.5 nm, Figure 5.9 (b). It is not clear why there is a small blue shift for the lower concentration. The FWHM for the $CsPbI_2Br$ doped E7 sample was also found to increase slightly ($\approx$ 4 nm). In accordance with that observed for the $CsPbI_3$ samples, the overall shape of the PL emission did not change significantly when the nanocrystals were doped into the nematic host, indicating that the perovskite structure had not disintegrated during the dispersion process. It should be noted that the 1 wt. % sample did not exhibit any notable emission specta and so are not presented here. The measurements of the PL emission spectra were recorded at approximately 3 to 4 different locations around the centre of each LC cell and that the emission spectrum and intensity were found to remain relatively constant across the measurements for a specific concentration of the nanocrystal. Some variation was noted at the edges of the cells where more clustering of the nanocrystals was observed.

Following dispersion of the nanocrystals in the LC host, albeit in the form of clusters, the next step was to combine them with a chiral nematic LC. In this regard, a mixture of the nematic LC, E7, and 2.8 wt. % of the chiral dopant BDH1281 (Merck) was prepared. The concentration of the chiral dopant was chosen so that the long wavelength edge of the photonic bandgap would overlap the peak PL emission wavelength of the nanocrystals recorded in the nematic host. To obtain a photonic bandgap with a long wavelength band edge located at λ_L = 675 nm using E7 as the nematic host, the pitch of the chiral nematic LC had to be adjusted to $\sim$387 nm. The mixture was then stirred for 24 hours at 300 rpm at a temperature of 60°C. Using the process outlined in Figure 5.3, the nanocrystals were then doped into the chiral nematic LC mixture at concentrations by weight of 1, 2.5 and 5 wt. %. Following this, the mixtures were filled into planar aligned 7 μm thick devices. Each sample was investigated with an optical polarising microscope, which revealed multi-domain Grandjean textures whereby nanocrystal clusters appeared to form at the disclination lines. To confirm the presence of the nanocrystals, the samples were further interrogated with the fluorescence microscope under UV illumination but no detectable emission was observed within the LC domains. These results are not presented here as no detectable emission was observed in any of these chiral nematic samples, which suggest that nanocrystals may damage following the dispersion. As a result, while the sonication method appeared to show some limited dispersion of

the nanocrystals in a nematic LC phase, albeit in the form of aggregates, it was therefore deemed necessary to consider an alternative method to disperse the perovskite nanocrystals.

5.4 Thermal Dispersion

As shown in the previous section, ultrasonication did not appear to result in measurable PL emission when the nanocrystals were doped into a chiral nematic LC host. Therefore, an alternative process was considered based upon thermal diffusion. This involved raising the temperature to the isotropic phase so as to reduce the viscosity of the LC in order to encourage the dispersion of nanocrystals in the undiluted LC host. An illustration of the mixture process is shown in Figure 5.10. The process begins by combining the nematic LC, E7 (without diluting in hexane), with the $CsPbI_3$ nanocrystals dissolved initially in hexane. These were mixed to attain a desired concentration by weight of 2.5 wt. % and 5 wt. % in the final solution. After adding the nanocrystals into the LC, the mixture was then stirred at 200 rpm at a temperature of 60°C for 2hrs, which is just above the clearing temperature of the LC.

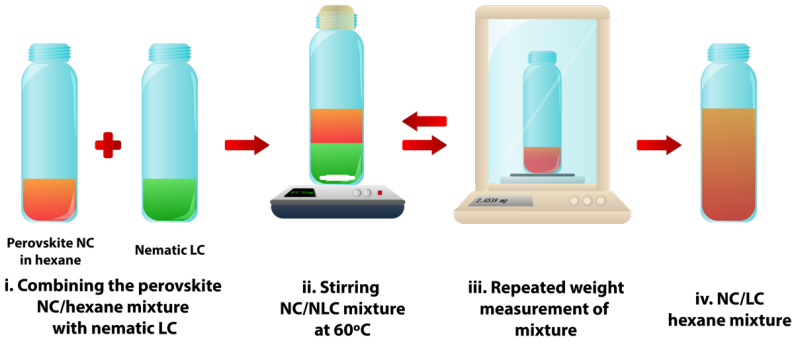


FIGURE 5.10: Mixture preparation by doping perovskite nanocrystals into a nematic liquid crystal (E7) using a thermal stirring process.

During the preparation process, it was critical to evaporate the host solvent to form a single phase of LC/nanocrystal. In order to confirm the removal of the host solvent, the weight of the mixture was measured repeatedly during the preparation process. Once no further change in the weight had been observed, it was considered that the host solvent (hexane) had completely evaporated. The nanocrystal/LC mixture was then filled into commercially available glass cells with anti-parallel rubbed polyimide alignment layers that had a nominal thickness of 7 μm.

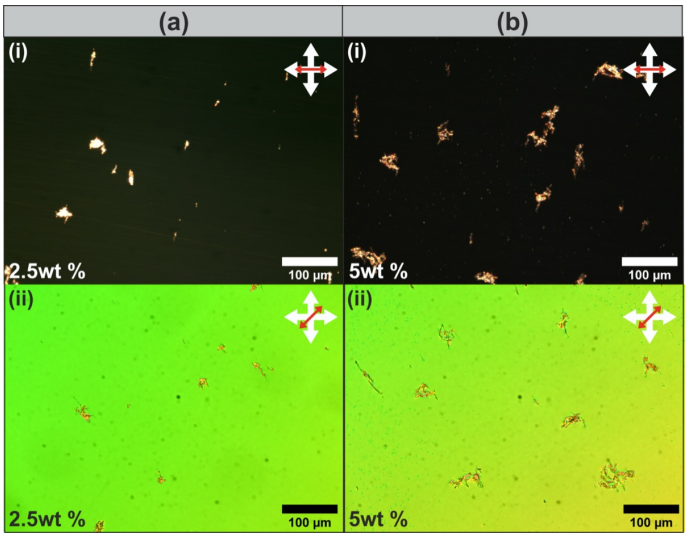


FIGURE 5.11: Optical polarisation microscope images of samples prepared using a thermal diffusion process at 60°C. The samples consist of the nematic LC (E7) doped with $CsPbI_3$ perovskite nanocrystals at different concentrations by weight: (**a**) 2.5 wt. % and (**b**) 5 wt. %. Images are of a dark state (i), with the optic axis aligned with one of the transmission axes of the polarisers, and a bright state (ii), whereby the optic axis of the LC is at 45° to the crossed polarisers. The samples were 7 μm-thick and measurements were carried out at a temperature of 25°C.

The samples were investigated initially with an optical polarising microscope by placing them between a pair of crossed polarisers as shown in Figure 5.11. As seen in the previous section, the nanocrystals did not dramatically alter the alignment of the LC director, which remained parallel to the substrates. The samples containing 2.5 wt. % and 5 wt. % concentration of nanocrystals appeared to reveal the existence of the nanocrystals, although in the form of aggregates. The cluster size was found to increase with concentration, with the 5 wt. % concentration showing larger clusters compared with the 2.5 wt. % concentration of nanocrystals. As before, an edge-detection method and was used to determine the average aggregate size for the 2.5 wt. % and 5 wt. % samples, which were found to be 3.5 ± 4.8 μm and 8 ± 2.3 μm, respectively. Interestingly, these sizes are at least 45 % smaller than that observed using the ultrasonication process (Figure 5.3). Evidently, the thermal diffusion process results in smaller cluster sizes; however, the distribution of the nanocrystals is still relatively non-uniform and aggregation is observed.

Samples were investigated on a fluorescence optical microscope and example images are presented in Figure 5.12. Clearly, images obtained for both the 2.5 wt. % and 5 wt. % samples reveal the existence of the perovskite nanocrystals as seen by the

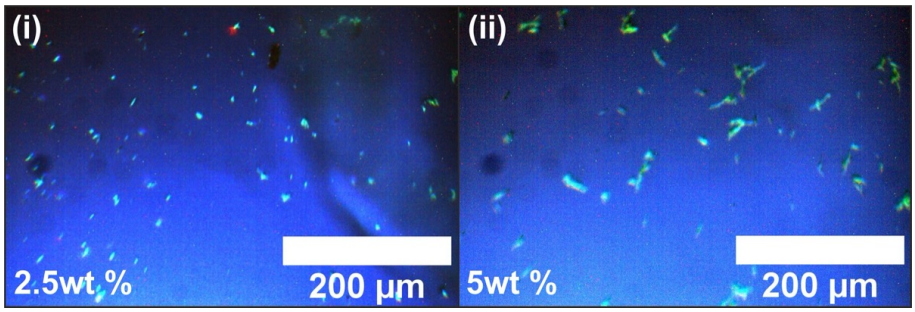


FIGURE 5.12: Fluorescence microscope images for samples prepared using a thermal diffusion process at 60°C. The samples consist of the nematic LC (E7) doped with $CsPbI_3$ at different concentrations by weight (i) 2.5 wt. % and (ii) 5 wt. %. Samples were illuminated with UV light (λ_{ex}= 365 nm). The samples were 7 μm-thick and measurements were carried out at a temperature of 25°C.

green emissive regions; however, both samples exhibited green emission under UV illumination rather than the red emission expected from the PL emission spectrum from the nanocrystals dispersed in hexane. Additionally, the samples showed some degree of distribution of the nanocrystals in the nematic host albeit with the formation of aggregates in accordance with the optical polarisation microscope images as shown in Figure 5.11.

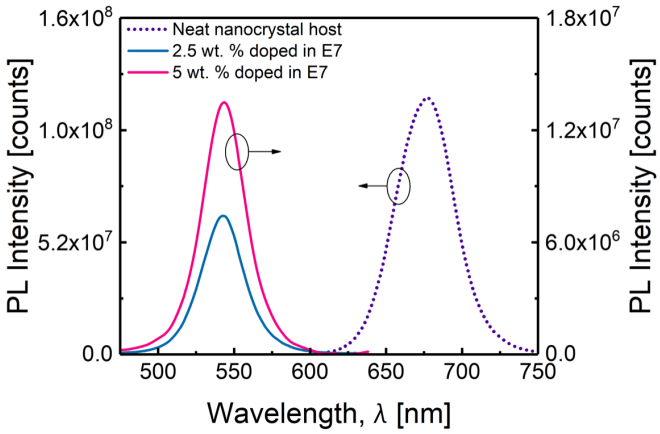


FIGURE 5.13: PL emission spectrum for the nematic LC (E7) samples doped with $CsPbI_3$ perovskite nanocrystals when excited with UV illumination (365 nm). The samples were prepared using thermally-assisted diffusion at 200 rpm at a temperature of 60°C. The samples were 7 μm-thick and measurements were carried out at a temperature of ~25°C. Emission from the neat nanocrystal sample in hexane is shown on the primary axis while the emission from the nanocrystal-doped LC samples are shown on the secondary axis.

To confirm the PL emission band for these perovskite/LC films, samples were photo-excited with UV (365 nm) radiation. The results for the PL emission spectra are shown in Figure 5.13. As observed in the fluorescence microscope images in Figure 5.12, samples for both concentrations of nanocrystals showed green rather than red emission, which is supported by the results for the spectrum which show a peak emission wavelength of λ_{PL} = 543±1 nm, indicating a $\Delta\lambda$ = 135±1 nm blue shift compared with that

observed for the same nanocrystals in hexane (dotted line, λ_{PL} = 675±1 nm). Given that the blueshift is quite substantial it is unlikely that this is the result of a solvatochromic shift and may be more likely indicative that the perovskite structure underwent an irreversible photoaccelerated reaction in the presence of oxygen, light and possibility moisture (as these samples were not sealed) causing the decomposition of the perovskite and resulting in a blue-shift in the emission spectrum [254]. This mixing process is clearly not desirable and so an alternative approach was investigated.

5.5 Dispersion at Room Temperature

Since the nanocrystals showed a blue-shift in samples prepared with the thermal dispersion method as explained in §5.4, new samples were prepared using the same process as explained in Figure 5.10; however, this time, dispersion was carried out at room temperature. The mixtures were prepared by using both types of Cs-based perovskite nanocrystals ($CsPbI_3$, and $CsPbI_2Br$) to form nanocrystal-doped nematic LC (E7) mixtures. For $CsPbI_3$, 2.5, 5 and 10 wt. % concentrations of nanocrystals in the nematic LC host were targeted. Due to the limited supply of $CsPbI_2Br$ in hexane, only 2.5 and 5 wt. % nanocrystal-doped LC mixtures were prepared.

To begin with, the nanocrystals in the hexane solvent were added to the nematic LC at the desired concentrations. The mixture was then stirred with a magnetic stirrer at 200 rpm at 25°C. As employed in §5.4, the LC/nanocrystal + hexane mixture was continuously stirred to evaporate the host solvent to form a single phase of LC/-nanocrystal; to achieve this, the weight of the mixture was repeatedly measured during the stirring process. After confirmation of no further change in the weight of the mixture, the nanocrystal/LC mixture was then filled into commercially available planar 7 μm-thick planar glass cells.

Once the glass cells had been filled with the nanocrystal-doped LC mixtures, they were inspected on an optical polarisation microscope. Figure 5.14 shows example optical polarising micrographs of samples containing $CsPbI_3$ under crossed polarisers. When the samples were rotated between crossed polariser and analyser pair, bright and dark states were observed with the exception of the samples containing 10 wt. % of $CsPbI_3$ nanocrystals. This might be due to the collection of the nanocrystals near the

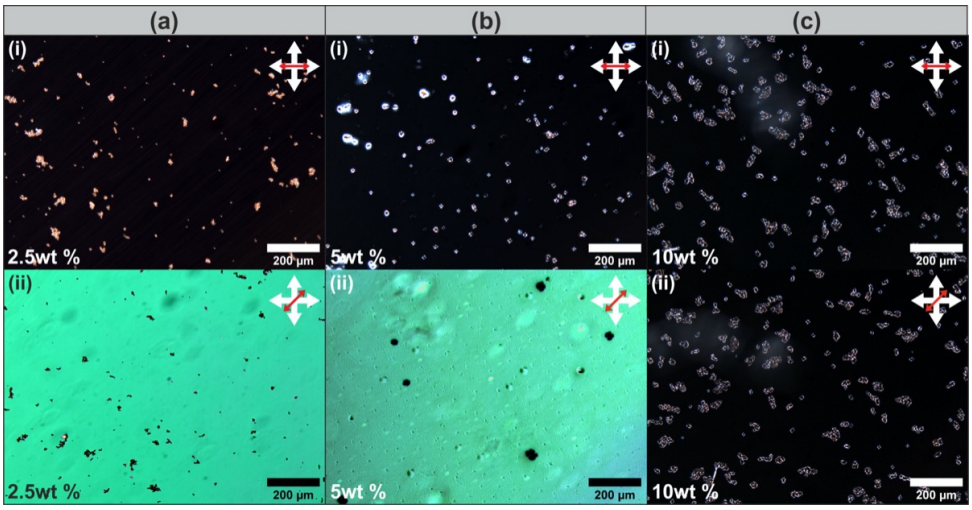


FIGURE 5.14: Optical polarisation microscope images of a nematic LC (E7) doped with $CsPbI_3$ perovskite nanocrystals at (a) 2.5 wt. %, (b) 5 wt.% and (c) 10 wt. % concentrations by weight. Samples were prepared using a stirring process at room temperature. Images are of a dark state (i) and a bright state (ii). The samples were 7 μm-thick and measurements were carried out at a temperature of 25°C.

surface of the cell and/or due to the interaction of long chain ligands with the nanocrystals as the ligands appeared to encourage a homeotropic alignment of the LC director. For high concentrations of the nanocrystals (i.e., 10 wt. %), the anchoring force due to the planar alignment layers appears to be suppressed by the LC-ligand interaction. The nanocrystals formed aggregates and the cluster size is highest for the case of 10 wt. % concentration.

The size of the aggregates was estimated using the edge-detection method and the average aggregate size for the 2.5 wt. %, 5 wt. % and 10 wt. % concentrations of $CsPbI_3$ nanocrystals were found to be 6 ± 1.2 μm, 9 ± 1.4 μm and 12 ± 0.4 μm, respectively, which is of a similar order to that observed for the 5 wt. % mixture that was heated to the isotropic temperature (Figure 5.11). The smallest aggregate size observed was for the 2.5 wt. % sample, which were $\geqslant 1$ μm in size.

Similarly, the samples prepared with $CsPbI_2Br$ nanocrystals were also inspected with the optical polarising microscope and example images are presented in Figure 5.15. Both samples showed bright and dark states when they were rotated through 45° under crossed polarisers, which suggests that the nanocrystals did not change the alignment of the LC. The samples showed a distribution of nanocrystals but again formed aggregates. The average sizes of the aggregates were found to be 5.5 ± 0.3 μm and 8 ± 1.5 μm for the 2.5 wt. % and 5 wt. % samples, respectively, using the edge-detection method described

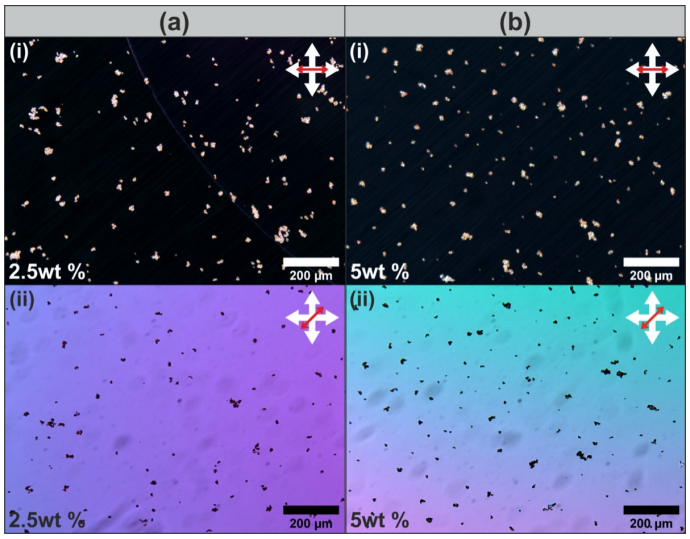


FIGURE 5.15: Optical polarisationmicroscope images of a nematic LC (E7) doped with $CsPbI_2Br$ perovskite nanocrystals at (a) 2.5 wt. % and (b) 5 wt. % concentrations by weight. Samples were prepared using a stirring process at room temperature. Images are of (i) a dark state and a bright state (ii). The samples were 7 μm-thick and measurements were carried out at a temperature of 25°C.

previously.

To further elucidate the distribution of the NCs in the LC host, the samples were investigated with the fluorescence optical microscope under UV (λ = 365 nm) illumination and images are presented in Figure 5.16. In this case, all of the samples exhibited bright red emission from the nanocrystals indicating that the perovskite nanocrystal structure had not been significantly altered during the mixing process. For the images of the samples consisting of 2.5 wt. % of the $CsPbI_3$ nanocrystals, small clusters can be seen that are distributed evenly across the sample area. These clusters appear to increase in size with the concentration by weight. It can be seen that the sample that contained 10 wt. % concentration of $CsPbI_3$ nanocrystals (Figure 5.16 (iii)) exhibits the largest clusters.

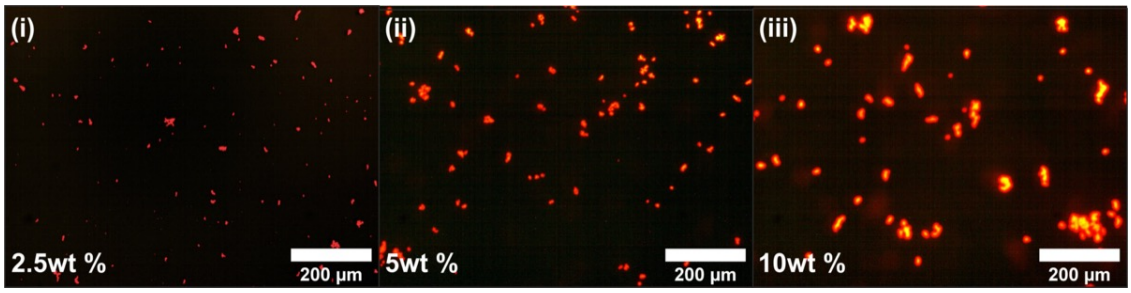


FIGURE 5.16: Fluorescence microscope images of a nematic LC E7 doped with $CsPbI_3$ perovskite nanocrystals at (**a**) 2.5 wt. %, (**b**) 5 wt. % and (**c**) 10 wt. % concentrations by weight and excited with UV (365nm) radiation. The samples were 7 μm-thick and measurements were carried out at a temperature of 25°C.

Similarly, the nematic LC samples doped with $CsPbI_2Br$ were also investigated on a fluorescence microscope. The example images are shown in Figure 5.17. Both samples exhibit red emission when excited with UV radiation and showed uniform distribution of nanocrystals across the thin film. The 2.5 wt. % sample formed smaller clusters compared to that observed for the 5 wt. % samples.

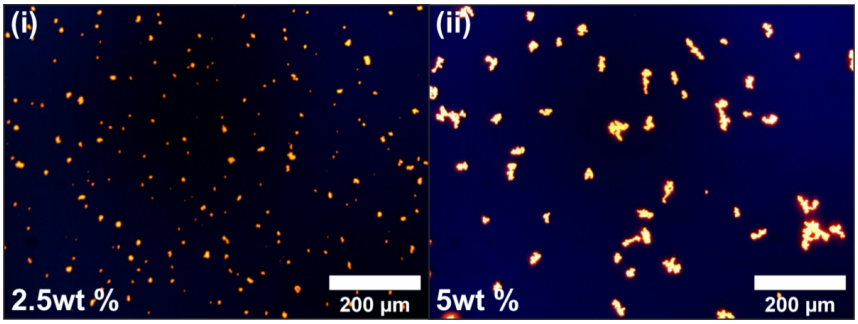


FIGURE 5.17: Fluorescence microscope images of a nematic LC E7 doped with $CsPbI_2Br$ perovskite nanocrystals at (i) 2.5 wt. % and (ii) 5 wt. %, and excited with UV (365 nm) radiation. The samples were 7 μm-thick and measurements were carried out at a temperature of 25°C.

Samples were excited with the UV-radiation (365 nm) using optical setup shown in Figure 3.15, Chapter 3. While taking the measurement, the power density of the excitation source was kept constant for comparison purpose. The PL emission spectra for the different samples are presented in Figure 5.18. It can be seen that the $CsPbI_3$ nanocrystals exhibit a peak emission wavelength at 675 nm, and the emission spectrum resembles that observed for the nanocrystals in hexane. It can also be seen that the peak intensity increased with the concentration of nanocrystals as shown in Figure 5.18 (a). There is also a slight reduction of 4 nm in the FWHM when the $CsPbI_3$ nanocrystals were combined with a nematic LC. Furthermore, the samples containing the $CsPbI_2Br$ nanocrystals exhibit a peak emission wavelength at 630 nm, which is blue-shifted by 45 nm compared with the spectrum observed for the same nanocrystals in hexane. This could be due to a solvatochromic shift, but is more likely due to structural change through a disintegration of the nanocrystals into its constituents (bromide and iodide) in the presence of oxygen and light, which would result in a blue-shift of the emission spectrum [254]. It is worth noting that there is an additional signal appearing at the short wavelength in the PL spectra which was due to the pump excitation as the cut-off filter was not present in these measurements. The FWHM of neat $CsPbI_2Br$ was found to be 29 ± 1 nm, which increased to 35 ± 1 nm when dispersed in the nematic LC.

Both types of nanocrystals exhibited PL emission for the 2.5 wt. % concentrations; however, for the sample with 10 wt. % of $CsPbI_3$ there was also a negative impact on the LC director alignment due to the interaction of the ligand of the nanocrystals with the LC host. Although the PL emission of the $CsPbI_2Br$ nanocrystal-doped LC samples exhibited a blue-shift in the emission spectrum, encouragingly both types of nanocrystals were found to be emissive when dispersed in the LC host.

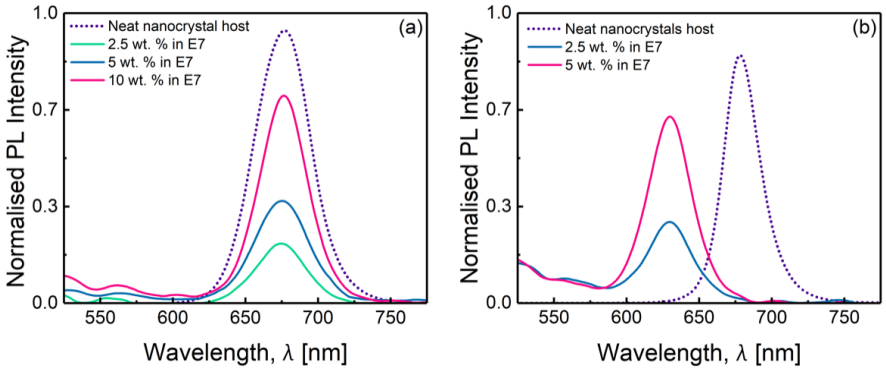


FIGURE 5.18: The PL emission spectrum from nematic LC (E7) samples doped with either (**a**) $CsPbI_3$ or (**b**) $CsPbI_2Br$ perovskite nanocrystals when excited with UV illumination (365 nm). The samples were 7 μm-thick and measurements were carried out at a temperature of 25°C.

Even though the nanocrystals formed clusters in the nematic LC, the peak emission wavelength for the $CsPbI_3$ did not appear to change, indicating that the nanocrystals had remained intact during the dispersion process. The next step was to disperse these nanocrystals into a chiral nematic LC. As the $CsPbI_2Br$ nanocrystals exhibited a shift in the PL emission, which is most likely due to a change in the perovskite structure, only the $CsPbI_3$ nanocrystals are considered further. A chiral nematic phase was prepared by mixing the nematic LC, E7, with 2.8 wt. % of the chiral dopant BDH1281. Using this chiral nematic LC mixture, the nanocrystal-doped CLC mixtures were prepared following the processing steps as explained for the nematic phase of LC. As it had been found that 10 wt. % nanocrystals in a nematic LC alters the alignment of the LC director, this concentration was also not considered further. For the purposes of comparison, a range of concentrations were used in this process. Therefore, CLC mixtures were doped with the $CsPbI_3$ nanocrystals (dispersed in hexane) at concentrations by weight of 1, 2.5 and 5 wt. %. Mixtures were stirred at 200 rpm at 25°C whilst repeatedly measuring the weight of the mixtures to monitor the evaporation of the hexane host. Once the hexane had been evaporated (no further change in the weight of the mixture), they were injected into 7

μm-thick glass cells with rubbed polyimide alignment layers. This results in a planar alignment of the LC director at the glass surfaces and consequently a Grandjean texture (standing helix).

Samples were inspected with an optical polarisation microscope under crossed polarisers and the corresponding microscope images are presented in Figure 5.19. The nanocrystal formed clusters, and the size of cluster increased as the concentration increased from 1 to 5 wt. %, as observed previously. It can be seen that the nanocrystals appeared to form clusters in the defect lines of the chiral nematic LC. Accumulation of nanocrystals in the defect lines is not surprising for the larger aggregates of colloidal nanoparticles and is something that has been observed previously [255–257]. As noted in these previous studies, large aggregates of quantum dots or nanocrystals prefer to localise at low energy states in the chiral nematic phase (i.e., at the defects). The nanocrystal cluster size was estimated using an edge-detection method and the average size of the clusters were found to be 5 ± 0.9 μm, 14 ± 0.2 μm and 18 ± 1.2 μm, respectively, for the samples with 1, 2.5 and 5 wt. % concentration, which has increased about 50% compared with the 2.5 and 5 wt. % concentration when doped in nematic LC. The aggregation of the nanocrystal at the disclination line is undesirable.

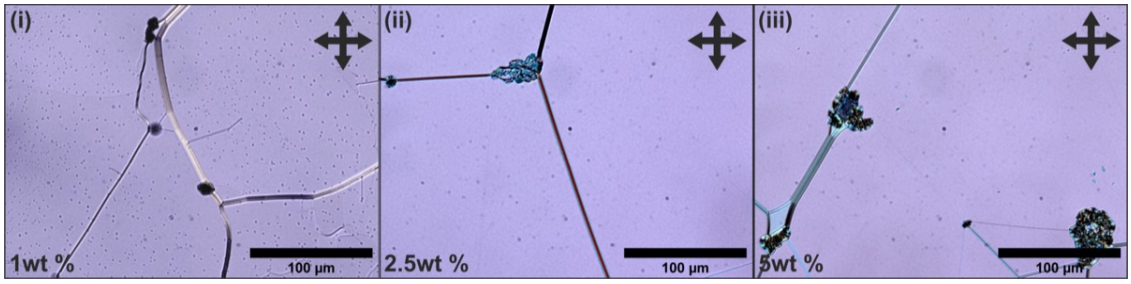


FIGURE 5.19: Optical polarisation microscope images of chiral nematic LC (E7+BDH1281) mixtures doped with $CsPbI_3$ nanocrystals at concentrations by weight of (a) 1, (b) 2.5 and (c) 5 wt. %. The samples were 7 μm-thick and measurements were carried out at a temperature of 25°C.

To confirm if the nanocrystals had indeed clustered at the disclination lines, the samples were studied on an optical fluorescence microscope, Figure 5.20. It is apparent from these images that the nanocrystals had aggregated around the disclination lines and were not homogenously dispersed throughout the bulk of the mixture. This aggregation and clustering is more noticeable for the larger concentrations.

Since the aggregation of the nanocrystals can influence the emission spectrum,

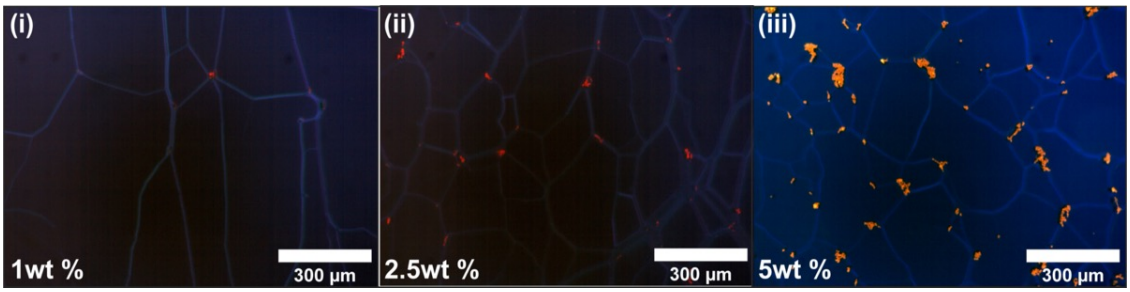


FIGURE 5.20: Fluorescence microscope images of the chiral nematic LC mixture (E7+BDH1281) doped with $CsPbI_3$ perovskite nanocrystals at concentrations by weight of (i) 1, (ii) 2.5 and (iii) 5 wt. % under UV (365 nm) radiation. The samples were 7 μm-thick and measurements were carried out at a temperature of 25°C.

each sample was excited with UV light and the corresponding PL emission spectra are presented in Figure 5.21. Results show that the 2.5 and 5 wt. % nanocrystal-doped CLC samples exhibit a clear PL emission spectrum whereas a weak PL emission spectrum is observed for the 1 wt. % sample; this is in accordance with the fluorescence micrographs presented in Figures 5.20 (i) which show a very low density of the nanocrystals. Overall, it is found that the PL emission increases as the concentration of nanocrystals increased up to 5 wt. %. The peak emission wavelength for all $CsPbI_3$ nanocrystal-doped CLC samples can be seen to be centred at 675 ± 2 nm, in agreement with the spectrum observed for the same nanocrystals in the hexane host, and indicates that the perovskite structure has been preserved. However, there appears to be no modification to the emission spectrum due to the presence of the band-gap and this is probably because the nanocrystals prefer to sit at the disclinations to minimise the free-energy rather than being dispersed in the bulk. This is clearly a problem from the perspective of band-edge laser emission as there is no evidence of resonant modes present in the chiral nematic LC influencing the emission from the perovskite nanocrystals. Typically, one would expect to see a series of peaks and troughs in the emission spectrum that reflects the variation in the density of photon states that occurs at the edges of a photonic band gap. No such modulation of the PL emission is observed here.

Nanocrystals have been combined into nematic and chiral nematic LC phases using a direct dispersion approach and a measurable PL emission from the chiral nematic LC samples containing nanocrystals with $\geqslant$1 wt. % has been observed. However, it was also found that as the concentration was increased the ligand-coated nanocrystals appear to have an adverse effect on the LC director alignment, as noted for the 10

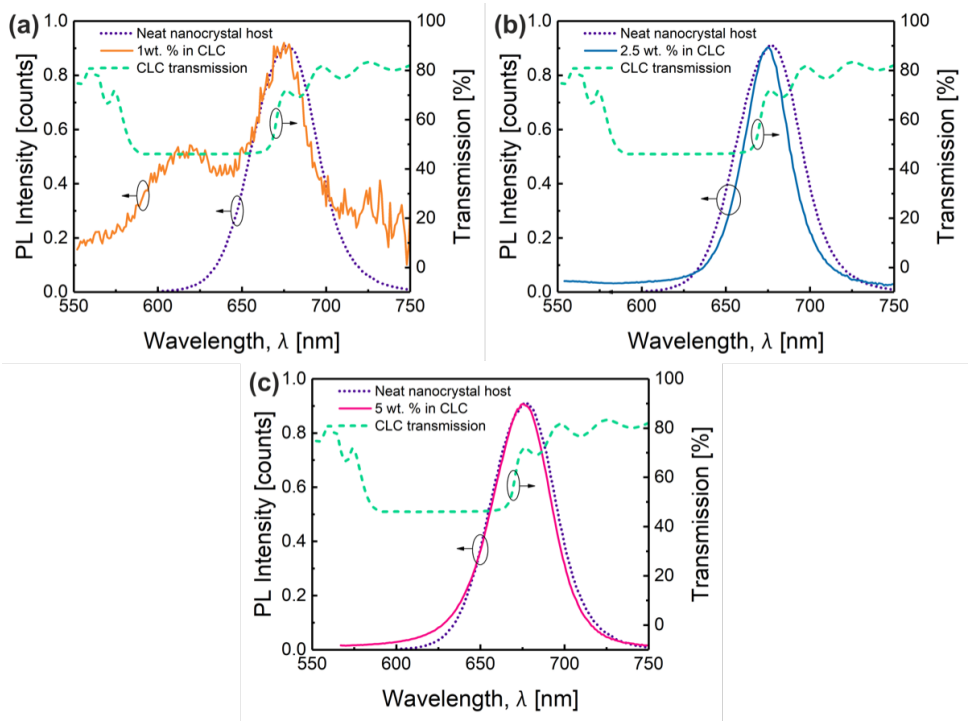


FIGURE 5.21: The PL emission spectrum from chiral nematic LC mixtures (E7+BDH1281) doped with $CsPbI_3$ perovskite nanocrystal samples at (a) 0.5, (b) 1 and (c) 5 wt. % concentrations by weight when excited with UV light (365 nm). The samples were 7 μm-thick and measurements were carried out at a temperature of 25°C.

wt. % nanocrystals in a nematic host. For the chiral nematic samples, 2.5 and 5 wt. % concentration appear to exhibit PL emission, but the nanocrystals were not found to be evenly dispersed and instead were found to aggregate around the disclination lines. Importantly, there appears to be no modification to the emission spectrum due to the presence of the band-gap, which is most likely due to coalescence of the nanocrystals around the disclinations. Nevertheless, while their applicability to band-edge LC lasers is not immediately clear, they can be combined with LC hosts to form novel nanocrystal-LC composites and their emission features can be retained, which is exciting for applications requiring narrow-bandwidth emission from anisotropic materials.

5.6 Summary

In summary, two types of inorganic perovskite nanocrystals $CsPbI_3$ and $CsPbI_2Br$ have been considered for dispersion in nematic and chiral nematic LC mixtures. The overall objective of this work being to determine whether such materials could replace the laser dyes conventionally used in band-edge LC devices. Towards this end, three different methods have been employed to explore whether dispersion of the

nanocrystals could be achieved and the impact of aggregation for each of these methods has been assessed. Specifically, these methods include the use of ultrasonication and thermally-assisted diffusion. The effect of temperature on the dispersion of the nanocrystals as well as the influence of the viscosity of the LC have also been considered.

TABLE 5.1: Summary of results showing the approximate cluster diameter of perovskite nanocrystals in nematic (NLC) and chiral nematic (CLC) mixtures prepared with different methods.

	Diameter (μm)		λ_{em} (nm)		
Methods	2.5wt. %	5wt. %	hexane	2.5 wt. %	5 wt. %
Sonication with dilute ($CsPbI_3$)	10±1.5	18±1.7	677	678	678
Sonication with dilute ($CsPbI_2Br$)	10±3.2	15±2.1	677	674.5	676
Thermal Dispersion at 60°C	3.5±4.8	8±2.3	677	543	543
RT Dispersion ($CsPbI_3$) NLC	6±1.2	9±1.4	675	675	675
RT Dispersion ($CsPbI_2Br$) NLC	5.5±0.3	8±1.5	675	630	630
RT Dispersion ($CsPbI_3$) CLC	14±0.2	18±1.2	675	675	676

Table 5.1 summarises the average aggregate size of the nanocrystals and peak emission when dispersed in the LC hosts using the different processing methods discussed in this chapter. Samples were prepared at a range of concentrations in either a nematic LC or chiral nematic LC host. Depending on the concentration of the nanocrystals and the preparation process employed, the size of the aggregates of the nanocrystal was found to vary. It was found that a measurable PL emission from samples containing nanocrystals with $\geqslant$1 wt.% could be observed. However, it was also found that as the concentration was increased the ligand-coated nanocrystals appear to have an adverse effect on the LC director alignment, as noted for the 10 wt. % nanocrystals in a nematic host. For the chiral nematic samples, 1 and 5 wt. % concentration appear to exhibit PL emission, but the nanocrystals were not found to be evenly dispersed and instead were found to aggregate around the disclination lines. Furthermore, perovskite nanocrystals ($CsPbI_3$) that were dispersed in nematic and chiral nematic hosts at room temperature did not appear to exhibit a shift peak emission wavelength of the nanocrystals. While the perovskite nanocrystals showed limitations in term of creating band-edge LC lasers, as no modification to emission spectrum was observed that mirrors the variation in the density of photon states, the narrow PL emission could be interesting for other photonic devices that employ the use of nanocrystals and anisotropic materials such as liquid crystals.

Chapter 6

Towards Perovskites Defect-Mode LC Lasers

6.1 Defect-mode structure

A defect-mode structure is an alternative architecture that could be used to form a laser cavity using liquid crystalline materials (LC). This structure has been employed previously for a number of different materials and fabrication techniques including 2D [258, 259], 3D photonic structures [260] and colloidal photonic crystals [261, 262]. Over the past two decades, a number of reports have focussed on the development and characterisation of LC-based defect-mode devices [102, 263–265]. These include forming the defect-mode configuration with an isotropic [264, 266] or anisotropic [53, 57, 94, 267–269] defect layer, a phase jump in the pitch of helix [42, 270, 271] or a combination of both defect-layer with a phase jump [49]. In this work, a structural defect has to be created within the macroscopic helical arrangement of the chiral nematic LC phase. This in turn leads to a resonant cavity inside the band-gap where the energy is confined within a very small volume, resulting in a higher density of states (DOS) for photons [45]. When the spectral position of this resonant channel overlaps with the photoluminescence peak of a suitable gain material, laser emission can be observed [53]. A summary of the underlying physics of a defect-mode laser is presented in Chapters 2.

Advanced gain materials such as organic and inorganic quantum dots [272–275] and perovskites [226, 232, 276] are attractive for numerous reasons including wavelength tuneability, colour purity, compatibility with solution processing techniques and the potential for electrically-driven laser emission [60]. Perovskite, either as a bulk thin-film

or in the form of nanocrystals [201], has been incorporated into various device configurations such as Fabry-Perot resonators [277], whispering gallery modes [224], spherical resonators [278], and nanowire architectures [225]. Furthermore, these materials have also been used to demonstrate random laser emission [279] and wavelength tuneable lasing [280, 281].

As shown in the previous chapter, the dispersion of perovskite nanocrystal into an LC host is by no means trivial and is plagued by numerous issues such as aggregation, alteration of LC director alignment, and disintegration of the perovskite structure. Rather than dispersing the nanocrystals directly into an LC host, an alternative approach is to incorporate the gain material into a separate layer (such as the defect layer) [53, 94, 282]. To this end, a defect-mode structure is used to combine perovskite (as the defect layer) with thin-films of CLC. In this chapter, two different types of defect layer are considered: 1) a bulk perovskite layer and 2) perovskite nanocrystals embedded in a polymer matrix. However, before developing the laser, it is essential to understand how the parameters of a defect-mode LC laser influence both the number and spectral position of the cavity modes. In the following, we consider a range of different defect-mode configurations and the impact of the thickness of the layers on the performance of full device stack.

6.1.1 Background on the simulations of the Defect-mode

An example of a defect-mode structure is one that consists of three separate layers: CLC/Defect Layer/CLC. The defect layer can be either an isotropic or anisotropic material [49]. Parameters such as thickness (d), refractive index (n), and for CLC layers, the pitch (p), must be carefully chosen as these dictate the number of cavity modes present within the band-gap and the corresponding wavelengths of these modes, which in turn govern the laser emission wavelength(s). A thick defect layer can support multiple modes within the gap whereas a thin defect-mode layer supports as little as a single mode. To simulate the mode structure of our defect-mode architectures, the 4×4 Berreman matrix method was employed, which was implemented using code written in MATLAB [283].

To begin with, a single CLC layer illuminated with unpolarised white light was modelled using the 4×4 Berreman matrix method as shown in Figure 6.1. The dip in the transmission spectrum for unpolarised white light is found to be only 50%. This is

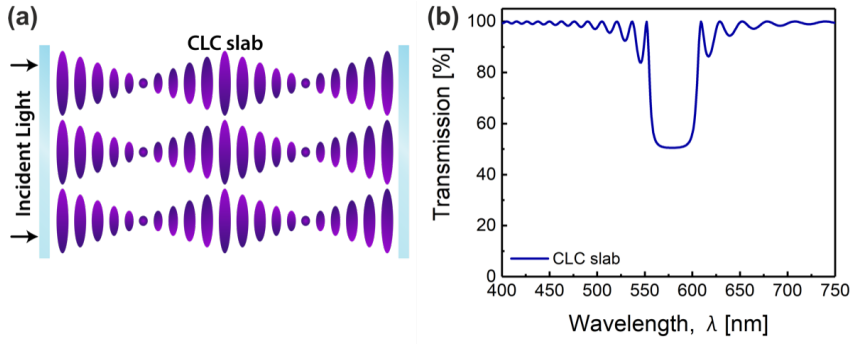


FIGURE 6.1: (**a**) Illustration of a CLC aligned in the Grandjean texture between glass substrates and (**b**) 4×4 Berreman simulation results on the corresponding transmission spectrum for unpolarised white light that propagates along the helical axis of the CLC (d_{CLC} = 5026 nm, p = 359 nm, d/p = 14). The dip in the transmission spectrum corresponds to the band gap, which only exists for one handedness of incident light.

because the reflection band only exists for circularly polarised light that matches the rotation sense (left or right hand) of the CLC helix. This dip in the transmission spectrum is referred to as the reflection band or photonic band-gap. In this case, the example transmission spectrum was obtained using the following parameters: CLC d_{CLC} = 5026 nm, p = 359 nm, n_o = 1.52 and n_e = 1.72.

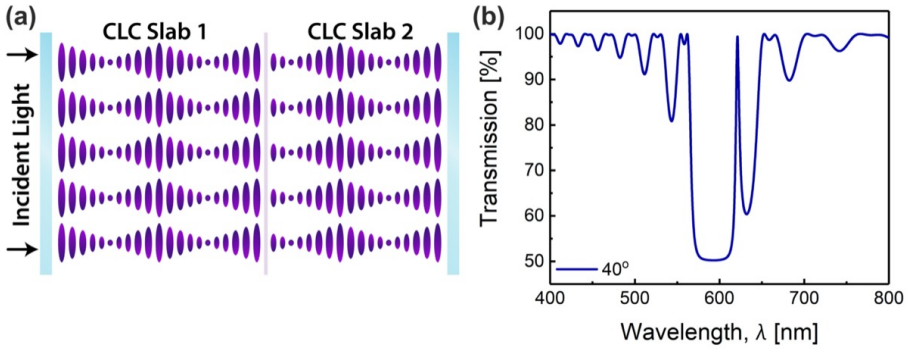


FIGURE 6.2: (**a**) An example of a twist defect-mode with a phase jump of $\phi = 40^\circ$ and (**b**) the corresponding transmission spectrum for unpolarised white light. For this example, in each CLC, d_{CLC} = 2555 nm, p = 365 nm (d/p =7), n_o = 1.58, n_e = 1.71 and $\phi = 40^\circ$ were used.

One configuration that is often considered for the fabrication of defect-mode LC lasers involves introducing a pitch or phase jump between two adjacent CLC slabs; this configuration is known as a twist defect-mode [42, 270]. Figure 6.2 (a) shows a schematic illustrating a twist defect structure that shows a phase jump or a phase shift (ϕ) between two neighbouring CLC layers. Using 4×4 Berreman simulations, a single mode is observed when using two identical layers of CLC with a phase jump or shift of $\phi = 40^\circ$ is introduced and is shown in Figure 6.2 (b).

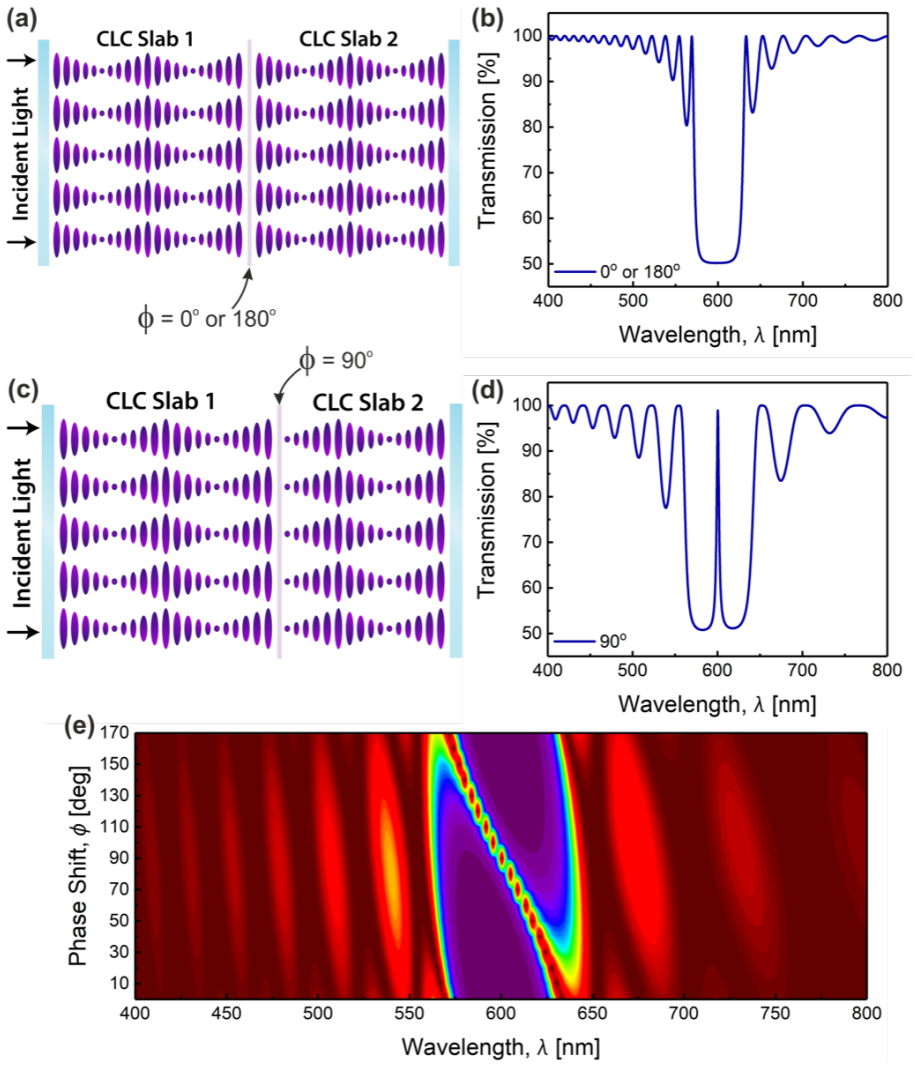


FIGURE 6.3: (**a**) An example of the twist defect-mode structure with a phase jump of (**a**) $\phi = 0^\circ$ or 180° and (**b**) the corresponding transmission spectrum for unpolarised white light. (**c**) phase jump of $\phi = 90^\circ$ and (**d**) the corresponding transmission spectrum for white light. (**e**) Contour plot of the transmission spectrum for different phase shifts in the twist defect-mode structure. The plot highlights the variation in the wavelength of the defect-mode as the phase shift increases from $\phi = 0^\circ$ to 170°. For this example, of each CLC film the parameters were: $d_{CLC} = 2555$ nm, $p = 365$nm ($d/p = 7$), $n_o = 1.58$, $n_e = 1.71$.

For a twist defect structure, the position modes can also be controlled. To demonstrate this, a number of simulations were conducted and the results are presented in Figure 6.3. The mode position can be controlled by changing the phase shift (ϕ) between adjacent CLC films. For instance, when $\phi = 0^\circ$ or 180° (Figure 6.3 (a)) no mode is observed as the helix in the two CLC films can be seen as being continuous for the incoming white light, Figure 6.3 (b). However, when $\phi = 90^\circ$, (Figure 6.3 (c)) a mode appears within the photonic bandgap as shown in Figure 6.3 (d). The contour plot in Figure 6.3 (e) illustrates the spectral shift in the position of the single mode due to the variation in

the phase shift between the neighbouring CLC layers.

The twist-defect mode configuration offers benefits in terms of simplicity of fabrication as it requires just two CLC layers to create a single mode laser. However, the gain material in the twist defect mode structures is dispersed within the CLC layers [284]. This configuration therefore is unsuitable for our needs: as shown in the previous chapter, dispersion of the perovskite nanocrystals directly into the chiral nematic phase results in aggregation and at high concentrations an alteration in the director profile. It was therefore deemed necessary to find an alternative configuration in which the gain material is separate from the chiral nematic phase. One such configuration uses a separate defect layer, either with an isotropic or anisotropic material as a defect layer and is explained below.

6.1.2 Simulation on isotropic defect layer in Defect-Mode configuration

For the work in this thesis, the objective is to fabricate defect-mode structures consisting of either an isotropic or anisotropic defect layer that will contain the perovskite emitters. As noted in the work [285], for a defect mode at the centre of photonic bandgap, the defect layer optical thickness $\bar{n}^d d$ (for an anisotropic defect) satisfies the relation:

$$\bar{n}^d d = \left(m + \frac{1}{2}\right)\frac{\lambda^d}{2} = \left(m + \frac{1}{2}\right)\frac{\bar{n}\sigma}{2} \tag{6.1}$$

This includes the refractive indices of the chiral nematic LC ($\bar{n}$), the refractive indices of the defect layer ($\bar{n}^d$), and the pitch of the helix (σ), and $m = 0, 1, 2, ...$ Using the notation employed in this thesis, the defect layer thickness is given by:

$$d_{def} = \left(m + \frac{1}{2}\right)\frac{\bar{n}p}{2\bar{n}_d} \tag{6.2}$$

An illustration of such a structure where an optically isotropic defect layer is presented in Figure 6.4 (a), which is arranged as follows CLC/Defect Layer/CLC. In this example, results from the Berreman matrix reveal the presence of a single mode at λ = 580 nm in the transmission spectrum as shown in Figure 6.4 (b). Since the position of the defect-mode is sensitive to the thickness of the defect-layer, simulations were also run to demonstrate the variation in the wavelength of the mode, and this is illustrated in Figure 6.5. Figure 6.5 (a – c) represents when the defect thickness is varied up to a few hundreds of nanometers: in this case, the structure creates a single mode with a wavelength that changes with the defect layer thickness. It can be seen that as the thickness of the defect

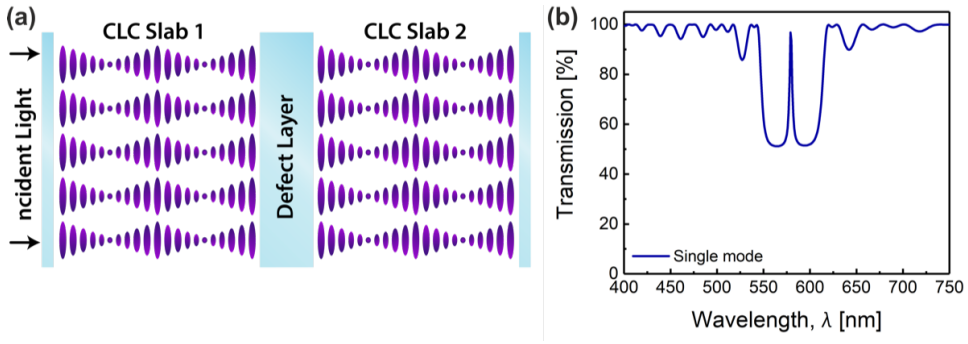


FIGURE 6.4: (**a**) An example of a defect-mode structure comprising two identical CLC slabs with an integral d/p ratio and an isotropic defect layer. (**b**) The corresponding transmission spectrum when unpolarised white light propagates along the helical axis. For this example, the following parameters were used: $d_{CLC} = 5026$ nm, $p = 359$ nm ($d/p = 14$), $n_o = 1.52$ and $n_e = 1.72$ and for the defect layer, thickness and refractive index were $d_{def} = 670$nm and $n = 1.50$, respectively.

layer increases the mode shifts from the short-wavelength band-edge for $d_{def} = 50$ nm to the long-wavelength band-edge for $d_{def} = 135$ nm.

When the defect thickness was set to $d_{def} = 57$ nm, a resonant mode can be seen at $\lambda = 608$ nm, as shown in Figure 6.5 (a), whereas for a 100 nm-thick defect layer a mode is seen to occur at $\lambda = 626$ nm, Figure 6.5 (b). By increasing the thickness of the defect layer from 57 nm to 135 nm, this single mode is found to red-shift to $\lambda = 641$nm as shown in Figure 6.5 (c). A contour plot in Figure 6.5 (d) highlights the variation in the wavelength of a single mode within the band-gap when the thickness of the defect layer is increased from 10 nm to 200 nm.

Multiple resonant modes can also be observed when the thickness of the defect layer is further increased. Figure 6.6 (a – c) illustrates results from 4×4 Berreman simulations showing the presence of multiple modes in the band-gap for a 'defect-mode' structure with a larger thickness of the defect layer. Firstly, Figure 6.6 (a) shows two modes located at $\lambda = 610$ nm and $\lambda = 639$ nm when the thickness of the defect layer is set to $d_{def} = 3000$ nm. However, three resonant modes appear (600 nm, 624 nm and 650 nm) when the thickness is increased to 3500 nm as shown in Figure 6.6 (b). Further increasing the thickness of the defect layer up to 10,000 nm adds yet more modes, as illustrated in Figure 6.6 (c), resembling more of a conventional resonant cavity. Figure 6.6 (d) is a contour plot that shows the variation in the number of modes in the defect-mode structure when the thickness of the defect layer is increased from 1μm to 20μm while keeping other parameters such as the refractive index of the defect layer unchanged.

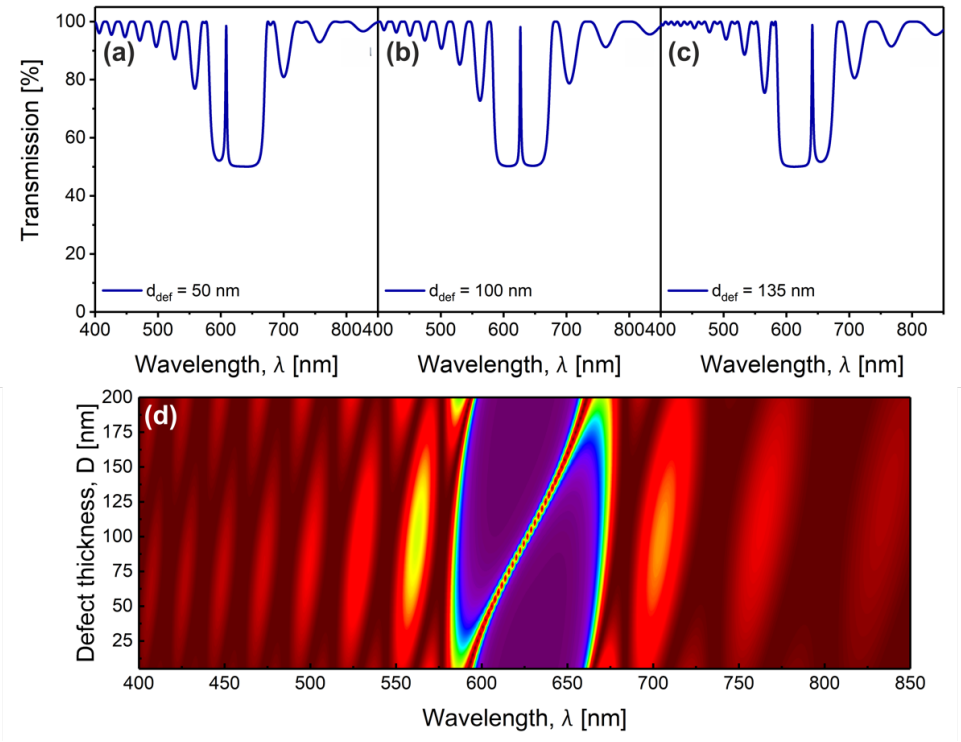


FIGURE 6.5: (**a - c**) The variation in the wavelength of the single resonant mode in a defect-mode structure of the form shown in Figure 6.4 (a) when the thickness of the defect layer, d_{def}, is varied. (**d**) Contour plot shows the variation in the wavelength of the single mode across the band-gap when the defect layer is varied between $d_{def} = 10$ nm and 200 nm. These simulations were run for the CLC layer parameters as follows: $d_{CLC} = 5376$ nm, p=384, d/p =14, n_o =1.56 and n_e =1.67, the refractive index of the defect layer was n = 1.50.

Based upon the findings in the previous chapter, the defect mode structure created with an isotropic layer is perhaps more suited as it avoids the potential for aggregation in an LC host and the degradation of the perovskite structure during the dispersion process, which rules out the use of an anisotropic defect layer (e.g., a nematic host) or the twist defect configuration. Therefore, the following sections explores the possibility of fabricating LC-perovskite defect mode lasers using an isotropic defect layer that comprises of either a solid perovskite thin-film or a polymer film dispersed with perovskite nanocrystals.

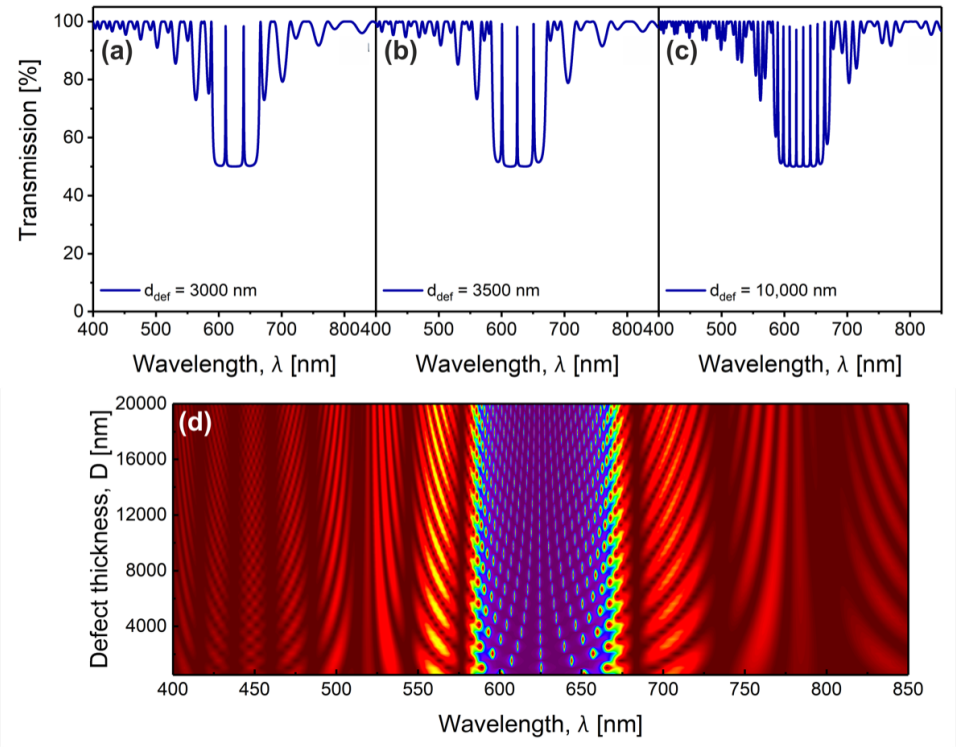


FIGURE 6.6: (**a - c**) The appearance of multiple modes in the band-gap when the thickness of the defect layer is increased for d_{def} ranging from 3 μm to 10 μm. (**d**) Contour plot showing the appearance of multiple modes within the band-gap for relatively thick defect layers from 1 μm to 20 μm. These simulations were run for the CLC layer parameters as follows: $d_{CLC} = 5376$ nm, $p = 384$, $d/p = 14$, $n_o = 1.56$ and $n_e = 1.67$, the refractive index of the defect layer was $n = 1.50$.

6.2 Defect-mode structure using bulk perovskite

A thin-film of perovskite was created using vapour-assisted solution processing (VASP), which is a tried and tested process for fabricating bulk perovskite layers [286–288]. The development process employed in this thesis to create a thin-film of organic-inorganic methyl ammonium lead iodide ($CH_3NH_3PbI_3$) perovskite was adopted from [89]. Figure 6.7 shows the absorbance of the thin film of perovskite, which indicates strong absorbance in the UV and a secondary peak/shoulder at ≈ 550 nm. The photoluminescence emission spectrum shows a peak at $\lambda = 770$ nm when the film was excited with UV light ($\lambda = 365$ nm) using a Horiba Fluorolog-3 with FluorEssence.

The CLC films were prepared by collaborators at the Eindhoven University of Technology (TU/e), Netherlands in the team of Professor Albert Schenning. For the CLC films, it was necessary for the pitch of the CLC film to be adjusted so that the central position of the band-gap overlapped with the peak emission of the perovskite layer, which in

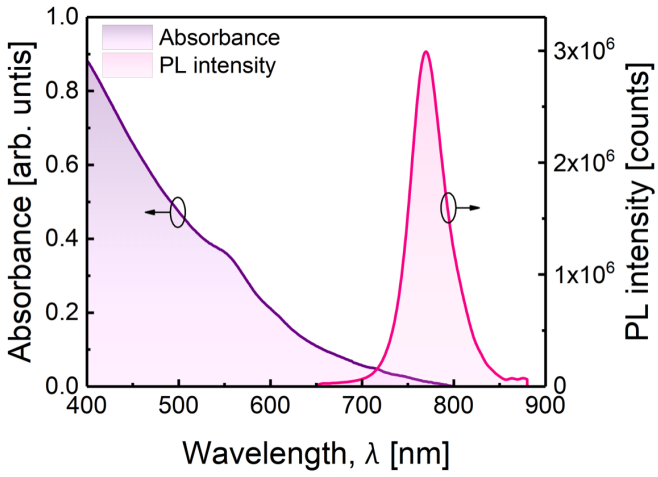


FIGURE 6.7: The absorbance and photoluminescence emission spectra of a methyl ammonium lead iodide ($CH_3NH_3PbI_3$) perovskite thin film. For PL emission spectrum, the thin-film was excited with UV light. The measurements were provided by the Prof Henry Snaith's team.

this case was 770 nm. The fabrication steps required to create the CLC/perovskite/CLC defect-mode structure are illustrated in Figure 6.8. The process begins with the cleaning of the glass substrates with acetone followed by treatment with UV-O_3 plasma for 25 min. The polyimide (PI) solution was then spin-coated onto a glass substrate at 4500 rpm for 30 sec before it was heated to 120°C for 20 min to evaporate any residual solvent from the polyimide solution. The substrate was then rubbed with a rotating drum covered with a clean velvet cloth so as to create a planar alignment; these steps are shown in Figure 6.8 (i – iii). The thin-films of chiral nematic LC comprised of: 94.8 wt. % RM-257 nematic LC (Merck KGaA), 3.2 wt. % chiral dopant LC-765 (BASF), 1 wt. % photoinitiator Irgacure 651 (Ciba Specialty Chemicals Ltd) and 1 wt. % surfactant 2-(n-ethylperfluorooctanesulfonamido)-ethyl methacrylate (Acrose Organics), which were first dissolved in 1.1 wt. % of xylene and mixed for 60 minutes at 40°C. The mixture was then dispensed onto rubbed polyimide glass substrates and spin-coated at 1000 rpm for 30 seconds. The substrate was photo-polymerised by illuminating with UV light (365 nm) at 7.5 mW/cm^2 for 4 minutes. The thickness of the polymerised CLC layer was found to be $\sim 7 \pm 1\mu$m. These fabrication steps are illustrated in Figure 6.8 (iv – vii).

The perovskite layer was deposited using the VASP technique reported elsewhere [94, 279] and was performed by the team of Professor Henry Snaith, Department of Physics, University of Oxford. PbI_2 was thermally evaporated with a base-pressure of

3×10^{-6} bar onto the top of the first CLC layer using an Edwards 306 evaporator. To remove the moisture, the substrate was heated up to 100°C for 10 min in ambient conditions and then transferred to a nitrogen glovebox. There the substrate was heated to 155°C for three hours in a closed dish containing methyl ammonium iodide power that reacts with PbI_2 to form perovskite. Next, the substrate was washed with isopropanol and heated for 30 min at 100°C in the glovebox. On top of the perovskite, PMMA (Poly(methyl methacrylate), dissolved in chlorobenzene at 10 mg/ml) was spin-coated at 700 rpm under ambient conditions to form a layer thickness of the PMMA of ∼200 nm. The reason for the addition of PMMA was to protect the perovskite layer from the environment. The fabrication stages used to deposit perovskite are shown in Figure 6.8 (viii – xiii). At this stage the stack consisted of CLC/PI/perovskite/PMMA.

In the final stages of the process, another thin film of CLC was deposited on top of the perovskite layer. Before deposition of the CLC layer, an alignment layer was created by spin coating 1 wt. % PVA solution (DI water) at 4500 rpm for 30 sec. The device was heated to 40°C for 15 min to remove any residual moisture and then rubbed with the rotating drum covered with a velvet cloth to create a planar alignment layer, as described previously. After this, the CLC mixture (as explained earlier in this section) was deposited using spin-coating and photo-polymerised with UV light (365 nm). These steps are illustrated in Figure 6.8 (xiv – xvii).

The complete device stack is shown in Figure 6.8 (xviii). It consists of Glass/PI/-CLC/perovskite/PMMA/PVA/CLC. The thickness of each layer is critical in determining whether the device would have a single or multimode laser emission as well as the position of the corresponding resonant mode(s). Interferometry measurements revealed that the thickness of the CLC films was $\sim 7\mu$m; the pitch and refractive indices of the CLC material were found to be $p = 486$ nm and $n_o = 1.53$ and $n_e = 1.68$ (obtained from TU/e), respectively. Since the process used here to form the perovskite layer is the same as that employed in [94], the thickness was estimated to be 50 nm and the refractive index was $n = 2.3$. Similarly, the thickness and refractive index of the PMMA layer was approximated to be 200 nm and 1.5, respectively. Finally, the thickness of the alignment layers was expected to be of the order of a few tens of nanometres.

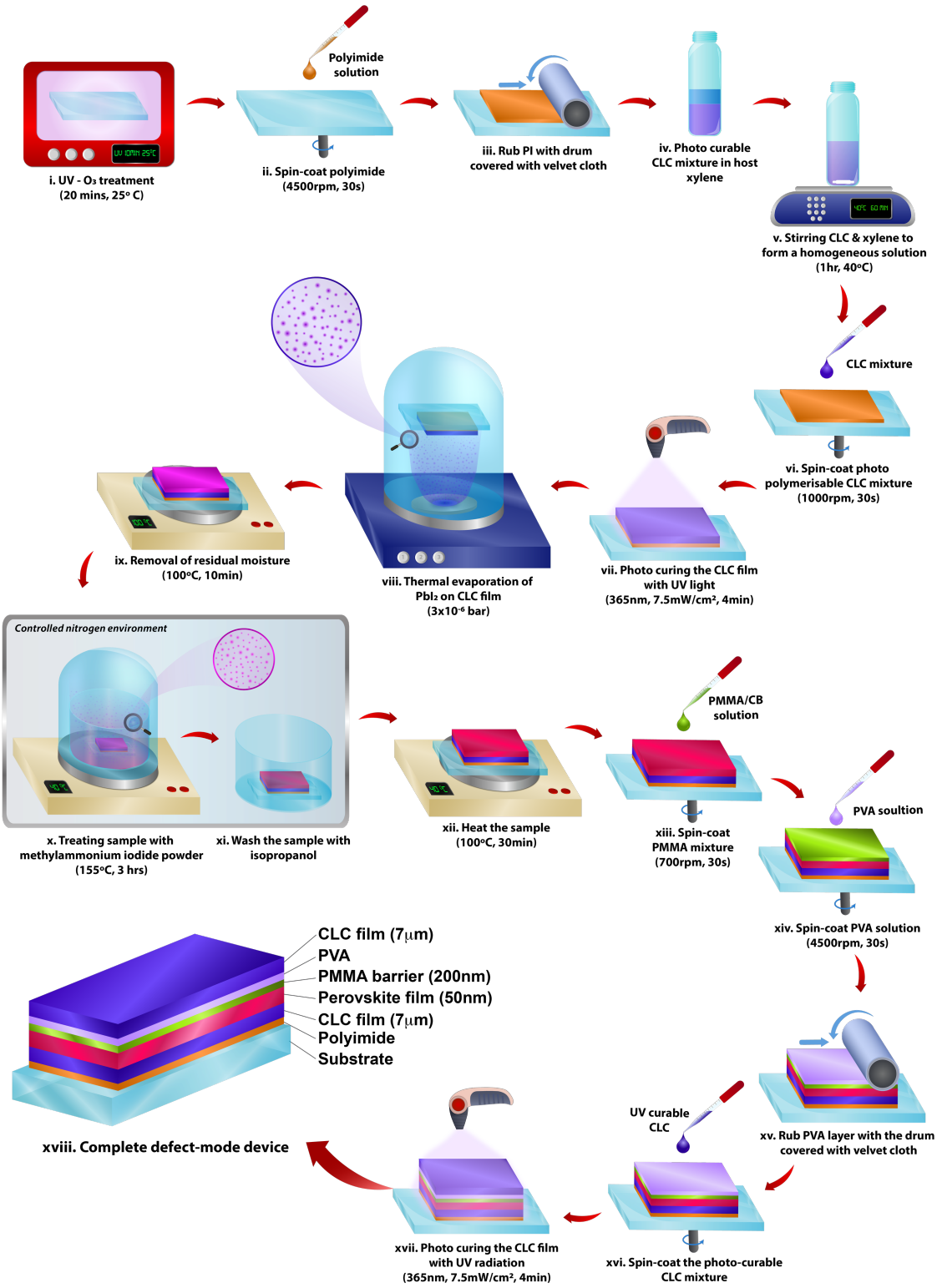


FIGURE 6.8: The process for creating a defect-mode structure consisting of a thin-film of perovskite ($CH_3NH_3PbI_3$) 50nm, which acts as the defect-layer, and polymerisable CLC layers, which act as the reflectors. Sub-figures details: (i – vii) Spin-coat deposition of photo-polymerisable bottom CLC film, (viii – xii) VASP deposition of thin-film of perovskite, and (xiii – xvii) Spin-coat deposition of photo-polymerisable top CLC film.

The film quality was studied using optical polarising microscopy and an example image is presented in Figure 6.9 (a), which shows reasonably uniform colour and appears to consist of relatively large domains (larger than the size of the pump laser beam). The different domains indicate regions of slightly different pitch. It is difficult to say with any real certainty that the image confirms that the alignment is good for both CLC layers. The microscope image indicates that the top CLC layer has a good Grandjean alignment. However, if the bottom CLC layer were poorly aligned then we would expect the scattering from this layer to significantly reduce the transmission through the sample and the crossed polarisers. In order to inspect this, the transmission/refection spectra from CLC films were studied. Figure 6.9 (b) shows the reflection spectra of the CLC when the device was illuminated with white unpolarised light using the setup presented in Figure 3.12 in Chapter 3. In reflection, the spectrum from both sides of the stack was recorded and the band gap was found to be centred at 778$\pm$1 nm in both cases, which is close to the PL emission peak ($\lambda_{PL} = 770$ nm) as intended. The shape and position of the spectrum on either side of the stack was almost identical. This can be used to infer that both CLC layers are relatively well-aligned as confirmed by the presence of a noticeable band gap in the reflection spectrum for the top and bottom layers. A simulation of the transmission spectrum of the complete device CLC/defect/CLC is also presented in Figure 6.9 (b) (blue solid line), which was generated using the 4$\times$4 Berreman model. The parameters input in the simulations matched that of the fabricated device (i.e. $d_{CLC} = 7\mu$m, $p = 480$nm, $n_0 = 1.53$, $n_e = 1.68$ and for the defect layer: $d_{def} = 50$ nm and $n = 2.3$). The modelling results predict the existing of a single resonant mode at 775 nm.

The stack was optically excited with the second harmonic from a nanosecond pulsed Nd:YAG (532 nm) laser (see Figure 3.23 Chapter 3 for experimental details). Figure 6.10 shows the emission characteristics of the device when it was pumped with the Nd:YAG laser. Figure 6.10 (a) shows a comparison of the PL emission when the device was pumped with excitation energy of $E_{exc} \approx 0.9\text{k}\mu\text{J/cm}^2$/pulse with the amplified spontaneous emission that is observed when the pump energy $E_{exc} \approx 1.8\text{k}\mu\text{J/cm}^2$/pulse. Figure 6.10 (b) shows the evolution of the PL emission spectrum from the complete device stack when the excitation fluence was increased, highlighting the appearance

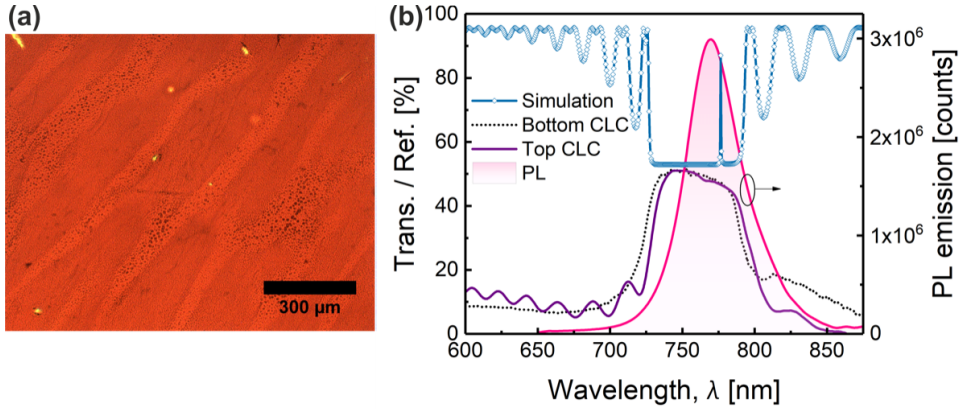


FIGURE 6.9: (**a**) Optical polarisation microscope image of the device stack examined in reflection taken at 25°C. (**b**) The reflection spectra of both photo-polymerised CLC films (solid blue and dotted lines) as well as the transmission spectrum for the complete device stack obtained from simulations using the 4×4 Berreman model (blue line with open circles). The photoluminescence (PL) emission from the neat perovskite thin-film when excited with UV light is overlaid on the transmission/reflection spectra to show the alignment of the PL peak emission wavelength with the centre of the band gap.

of an amplified spontaneous emission (ASE) peak at 789 nm. The PL emission intensity from the device was found to increase as the pump energy was increased from 120μJ/cm^2/pulse to 990μJ/cm^2/pulse. A further increase of the pump energy was also found to result in a narrowing of the linewidth at the ASE peak. Increasing the fluence from 1220muJ/cm^2/pulse to 3100μJ/cm^2/pulse leads to the ASE peak growing in intensity relative to the PL emission at other wavelengths.

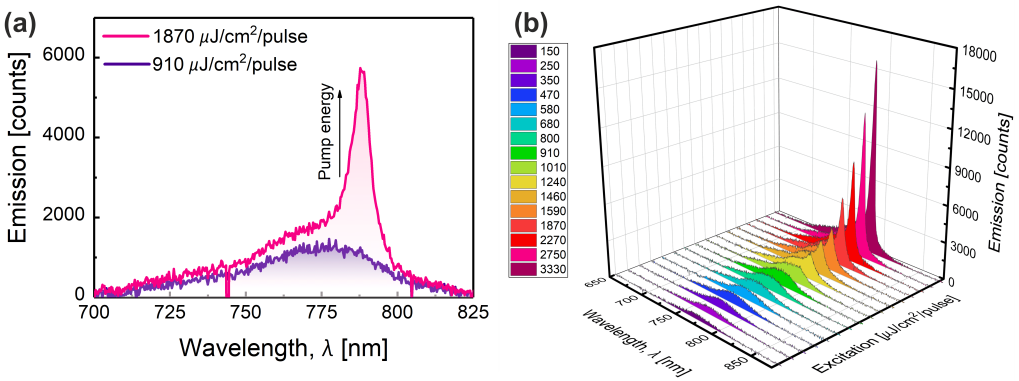


FIGURE 6.10: (**a**) The PL emission from the perovskite/CLC defect-mode stack when optically excited at 532 nm with a pulsed Nd:YAG laser. (**b**) The enhanced amplified spontaneous emission from the complete stack (CLC/perovskite/CLC) following photoexcitation (532 nm, 4 ns) pulsed laser.

The input-output characteristics of the amplified emission from the device are shown in Figure 6.11 (a). The discontinuity in the gradient is an indication of the ASE excitation threshold fluence for the stack, which in this case was found to be

E_{th} =1kμJ/cm^2/pulse. Figure 6.11 (b) depicts the change in the full width at half maximum (FWHM) of the spectrum as a function of the excitation fluence. It can be seen that the FWHM decreases from 52 nm at a fluence of 775 μJ/cm^2/pulse to 8 nm at a fluence of 2515 μJ/cm^2/pulse. Overall, the reduction in the FWHM is recorded to be 85% when the fluence increases from 120 μJ/cm^2/pulse to 3100μJ/cm^2/pulse.

ASE has been observed previously from perovskite films and a variety of ASE threshold values have been reported, largely due to differences in the device architecture, material composition, and the pump pulse length. In terms of magnitude, the ASE excitation threshold that has been reported thus far for the different geometries and configurations varies in range from a few tens of μJ/cm^2/pulse to several hundreds of μJ/cm^2/pulse for devices that contain methylammonium, formamidinium or Cs-based perovskite [289]. For methylammonium-based perovskite films the ASE threshold is found to vary from 7.6 μJ/cm^2/pulse [89] up to 600 μJ/cm^2/pulse [290]. In a configuration presented in [89], using $CH_3NH_3PbI_3$ and metal reflectors a control stack was created with glass / Al_2O_3 / $CH_3NH_3PbI_3$ / PMMA / Au (without any CLC) and was found to exhibit a pump threshold as high as 600 μJ/cm^2/pulse. Although the ASE threshold observed in our device is larger than that recorded for a comparable control sample, it is similar in magnitude. We believe that the lack of evidence of laser emission (i.e. a narrow linewidth emission line) and the high ASE threshold are a result of a degradation of the perovskite thin-film during the fabrication process.

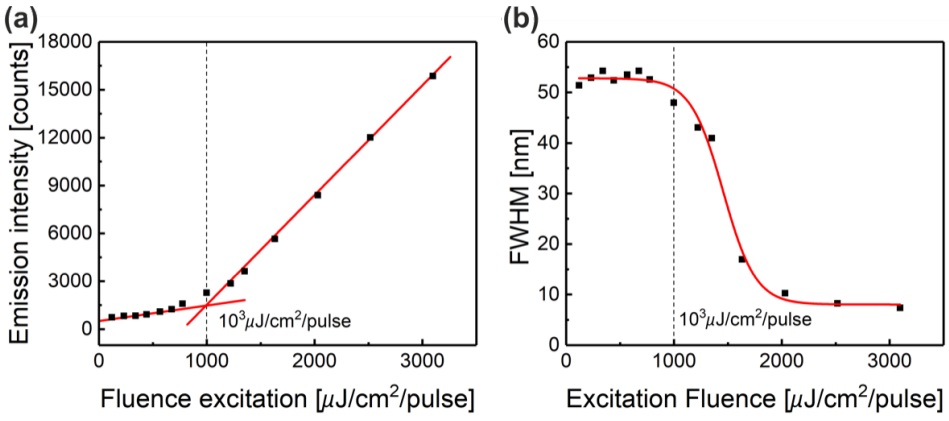


FIGURE 6.11: (**a**) The peak intensity as a function of the excitation fluence showing an excitation threshold of $10^3\mu$Jcm^{-2} per pulse and (**b**) the full-width at half maximum (FWHM) as a function of the excitation fluence.

For the CLC/defect/CLC structure, the fabrication process involved in creating

the top CLC presents challenges that can either adversely affect the gain material (defect layer) or the quality of CLC film or both. In [89], the defect-mode configuration was created with a CLC layer as one reflector whereas gold (Au) was used as the second reflector in a stack CLC/Al_2O_3/$CH_3NH_3PbI_3$/PMMA/Au, this is because at the time it was not possible to deposit a second CLC layer without disintegrating the perovskite layer. The use of a metal reflector limits the fabrication compatibility with solution processing techniques. In contrast, in the current study, our device was fabricated using solution processing techniques for both reflectors created with thin films of chiral nematic LC. This is the first demonstration of creating a perovskite-based defect-mode structure with both reflectors formed using chiral nematic LCs. However, as stated, only signatures of ASE were observed in the CLC/perovskite/CLC structure and the device stack did not exhibit laser emission under any of the optical pumping conditions considered in this study; this is considered to be due to the low gain of the perovskite film or poor quality of CLC film. In this regard, alternative methods were employed to create robust CLC films that could be deposited so that the perovskite and CLC films would not be damaged during the fabrication process.

6.3 Defect-mode structure using perovskite nanocrystals

As explained in the previous section, the fabrication process for depositing a thin-film of perovskite on a CLC film requires stringent processing conditions such as the use of high temperatures that could, in principle, negatively affect the quality of the CLC film. Further, the processing conditions could lead to a variation in the position of the band-gap of the CLCs due to solvent induced swelling/contraction of the film, which would in turn could result in the absence of any resonant modes due to a mismatch of the band-gap and the PL emission perovskite layer. Therefore, alternative fabrication processes were adopted to deposit a thin-film of perovskite that does not require high temperature processing.

To make the perovskite disposition process compatible with CLCs, instead of depositing a thin-film of perovskite using VASP, a thin film of perovskite nanocrystals in a polymer matrix was used for the defect layer. In this regard, $CsPbI_2Br$ perovskite nanocrystals were used and the PL emission was tailored by changing the composition of

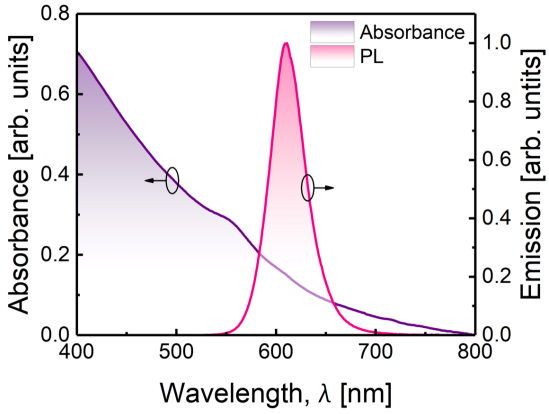


FIGURE 6.12: Absorbance and photoluminescence spectra of $CsPbI_2Br$ perovskite nanocrystals in hexane when excited with UV (365 nm) radiation. These measurements results were provided by Professor Henry Snaith's group in the Department of Physics.

the halide group. The absorbance and PL emission spectrum of the perovskite nanocrystals is shown in Figure 6.12 where it can be seen that the emission wavelength was centred at $\lambda_C = 610$ nm. Polymethyl methacrylate (PMMA) was used as the polymer host to embed the perovskite nanocrystals as PMMA is transparent to visible light, shows good compatibility with solution processing techniques and has been demonstrated to enhance the performance and emission stability of perovskite nanocrystals [291]. The CLC films were deposited independently either using a printing technique or via a delamination process, as explained in detail in the following sub-sections.

6.3.1 Defect-mode structure with printed CLCs

To begin with, a device stack was formed using CLC films that were prepared by our collaborators at the Eindhoven University of Technology (TU/e) using a flexography printing technique on Melinex 401-polyester film. The LC mixture consisted of Paliocolor 33.44% LC242 (nematic) + Paliocolor 1.566% LC756 (right-handed chiral nematic) dissolved in 59.95% cyclopentanone host solvent with 5% Irgacure 369 photoinitiator and 0.05% Byk 361N additive. The concentration of chiral dopant was chosen so that the central wavelength of the photonic bandgap would be close to the peak emission wavelength of the perovskite nanocrystals. Further detail of the chemical and physical characteristics of the materials used in the preparation of the CLC films can be found in Appendix B. The flexo-printing parameters were anilox force: 200 N, printing speed: 0.5 $^{m}/_{s}$, anilox speed: 5% and pre-ink revolutions: 3. After printing, the CLC stacks were dried in an oven for 3 minutes at 90°C followed by photocuring by passing them through a IGT

UV dryer once. The thickness was 2 μm and the central wavelength (λ_C) of the CLC was 595 nm; the spectral details are presented later.

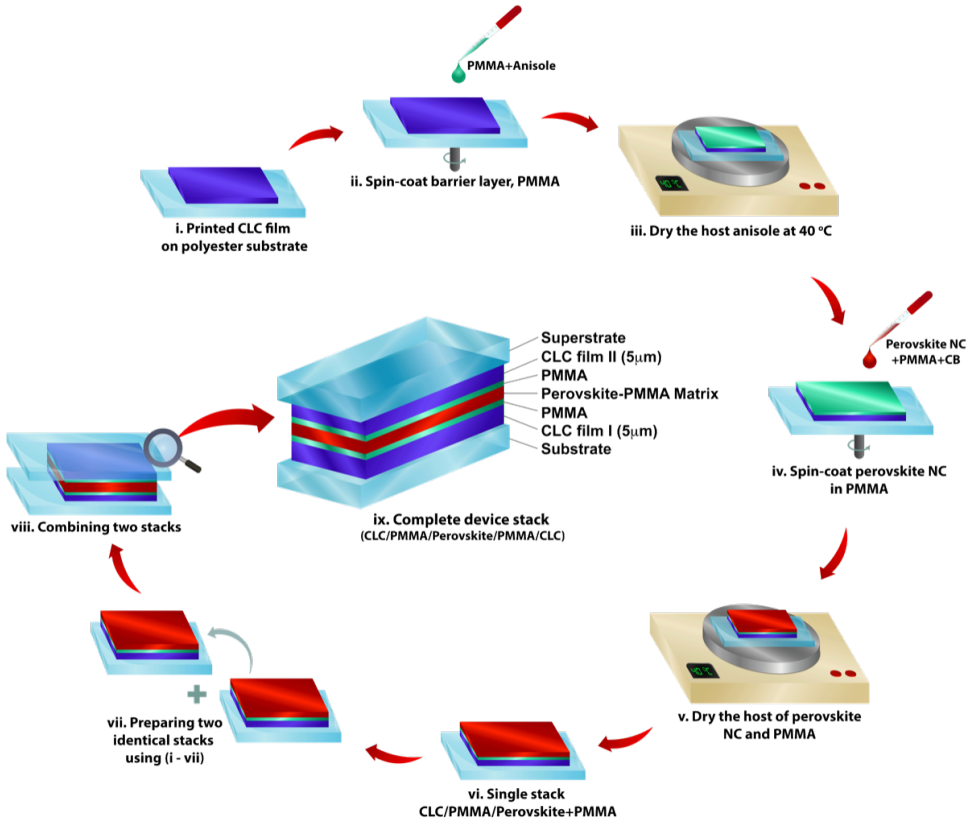


FIGURE 6.13: The fabrication process for creating defect-mode structures by using two identical CLC films fabricated with a flexography printing technology.

The printed CLC films on polyester substrates were used to create a defect-mode device with perovskite nanocrystals that were dispersed in PMMA. The fabrication process of the defect-mode structure using flexo-printed CLC films is illustrated in Figure 6.13. To protect the CLC films from the perovskite, the CLC films were coated with a light transparent polymer such as PMMA. Once the films had been received, commercially available MicroChem PMMA/anisole (4 wt. % anisole) was spin-coated on the CLC film at 4000 rpm for 30 sec followed by heating the stack to 40°C for 50±5 min to evaporate the anisole. The mixture containing perovskite nanocrystals in PMMA was then spin-coated at 3000 rpm for 30 sec at 25°C and the stack was then heated to 40°C for 10 min. Once the stack was dried, the combination of layers was then CLC/PMMA/perovskite + PMMA and is shown in Figure 6.13 (i – vi). Another identical stack was prepared, and both stacks were then combined to form a defect mode device comprising CLC/PMMA/perovskite/PMMA/CLC (Figure 6.13 (vii – viii)).

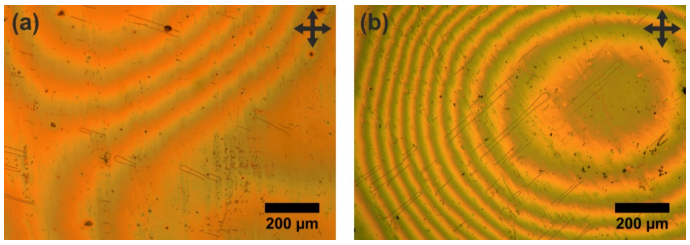


FIGURE 6.14: Optical polarisation microscope images of (**a**) neat CLC film prepared with a flexography printing technique and (**b**) single stack with CLC/PMMA/perovskite+PMMA observed from the CLC side.

Before combining these stacks to form a complete defect-mode structure, each individual stack was investigated using optical polarisation microscope under reflection of white light to study the quality of the film. Results are presented in Figure 6.14. The neat CLC film, Figure 6.14 (a) showed reflected colour that is expected from a standing helix in the CLC; however, the pitch may not be entirely uniform across the sample. The different regions of colour correspond to a variation in the thickness of printed the CLC film, which result in a slight variation in the pitch of the helix as a result of a slight bowing in the centre of the cell. The fringes appeared on the samples because they were fabricated on flexible substrates and were not completely flat when examined. It can also be seen that the stack comprising CLC/PMMA/perovskite+PMMA layer, Figure 6.14 (b), showed a slight change in colour from bright orange to pale orange − an indication of a small blue-shift in the band-gap after depositing the perovskite+PMMA.

To investigate the optical characteristics of each single stack (CLC/PMMA/Perovskite + PMMA), the reflection spectrum from the CLC side of each stack was recorded and is presented in Figure 6.15. The neat CLC films exhibited a band-gap with a central wavelength at 595 nm (shown with black dotted lines). After depositing the PMMA barrier layer, while Stack 1 did not show any change in the position of the band-gap, a small blue shift of 5 nm was seen for Stack 2 (shown as solid blue lines). Both samples, however, blue-shifted to 575 nm when the perovskite nanocrystal + PMMA matrix was deposited on the stack. This blue-shift could be due to a contraction of the CLC film after evaporation of the host solvent (anisole) in which PMMA was dispersed, which in turn would lead to a change in the helical pitch of the CLC.

After inspecting the CLC films in both stacks, they were then combined together

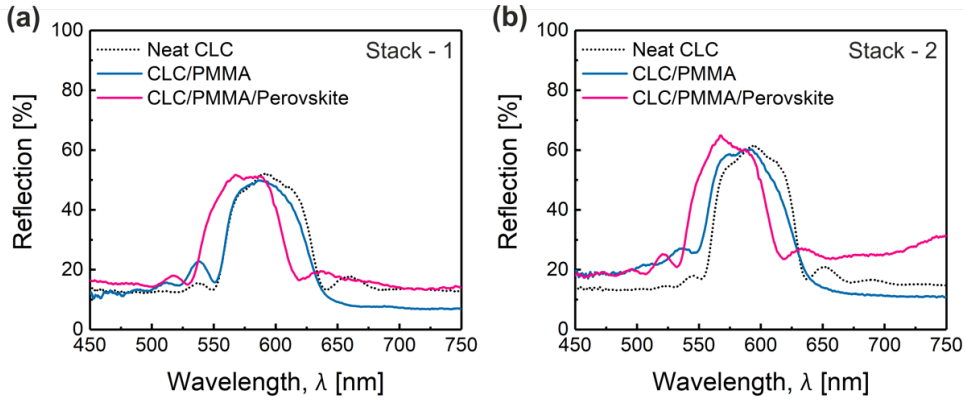


FIGURE 6.15: The refection spectra of the CLC film at various stages of the fabrication process of the defect-mode structure (CLC/PMMA/perovskite NC) with PMMA as barrier layer (**a**) Stack 1 and (**b**) Stack 2.

to form a defect-mode structure as illustrated in Figure 6.13 (vii – viii). Following assembly, the complete device was optically pumped with the Nd:YAG (532 nm) pulsed laser. The emission spectrum was captured and is presented in Figure 6.16 where it can be seen that the peak emission intensity occurs at a wavelength of 580 nm, which is at a slightly shorter wavelength than the peak observed for neat perovskite films ($\lambda_{PL} = 610$ nm). Clearly, the presence of the CLC films in the stack has altered the emission spectrum from the perovskite: in addition to the blue-shift in the peak emission, the spectrum reveals considerable narrowing of the FWHM from 42 nm to 24 nm compared to the neat perovskite film. Single mode laser emission was not observed. However, the spectrum appears to exhibit a shoulder (potentially an additional emission peak) at around 600 nm. This may be evidence of multimode emission that could not be readily discerned from the emission spectrum.

One possible reason for the lack of unequivocal evidence of laser emission is that the PL emission from the perovskite nanocrystals was centred at 610 nm, whereas the central wavelength of the band gap after fabrication of the stack was at 575 nm. This means that the gain maximum of the nanocrystals was not ideally matched to the defect-mode. Further, as seen in the microscope images, the pitch across each CLC layer was not very uniform, which could also explain the multimode nature of the emission.

It is known that the reflectance (R) of a chiral nematic LC typically increases with the number of pitches before it reaches a value of $R = 1$ for sufficiently thick films and for one handedness of circularly polarised light. The reflectance of a chiral nematic

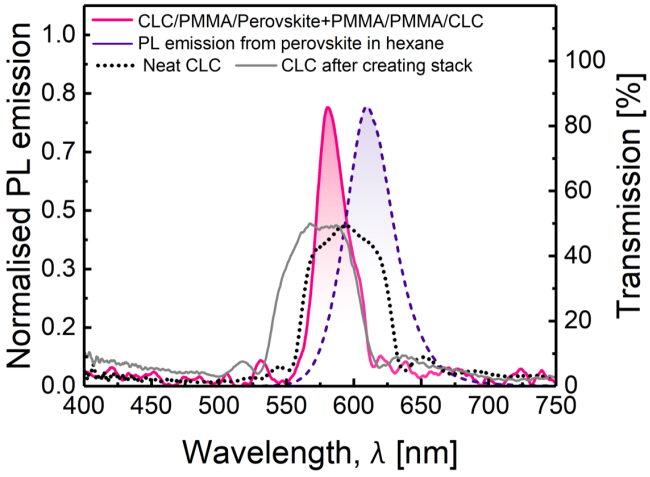


FIGURE 6.16: Emission spectrum from the defect-mode perovskite stack upon excitation with the second harmonic (532 nm) from an Nd:YAG laser.

LC can be expressed as [292]:

$$R = \frac{1 - \exp\left(-\frac{2\Delta n d}{\bar{n} p}\right)}{1 + \exp\left(-\frac{2\Delta n d}{\bar{n} p}\right)} \tag{6.3}$$

where Δn is the birefringence, p is the pitch, d is the thickness, and n is the average refractive index. It should be noted that the reflectivity of the printed CLC films (used in stack, Figure 6.13 (ix)) would be rather low as they were only 2 μm-thick; this is also illustrated with the simulation as presented in Figure 6.17 by comparing the reflectivity of a 2-micron thick CLC with a 5-micron thick CLC film with the identical film parameters.

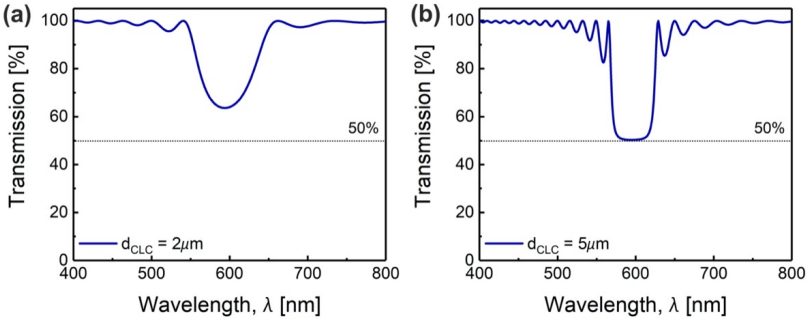


FIGURE 6.17: Example transmission spectra of a CLC film with thickness of either (**a**) 2μm and (**b**) 5μm showing the improvement in the reflectivity of light. The simulation parameters in both cases are $p = 370$ nm, $n_o = 1.52$ and $n_e = 1.66$.

6.3.2 Defect-mode structure using delamination

In order to improve the reflectivity of the CLC film, the printing fabrication process was replaced with a delamination method. Instead of creating a CLC film from a

bottom-up approach, the CLC film was fabricated by filling a glass cell with a photo-polymerisable mixture that could be photocured and delaminated from the glass substrates.

A photo-polymerisable CLC mixture from Merck (RMS11-068, $\lambda_C = 620 \pm 10$ nm) was used that was dissolved into the solvent toluene. The mixture was first stirred continuously at 200 rpm at 25°C until the toluene had evaporated. The weight of the mixture was repeatedly measured and once no change in the weight was observed, it was considered that the host solvent had completely evaporated. Upon photo-polymerisation, the mixture exhibited a band-gap with a central wavelength of 620 ± 5nm. The uncured mixture was found to have a clearing temperature of 79 ± 1°C.

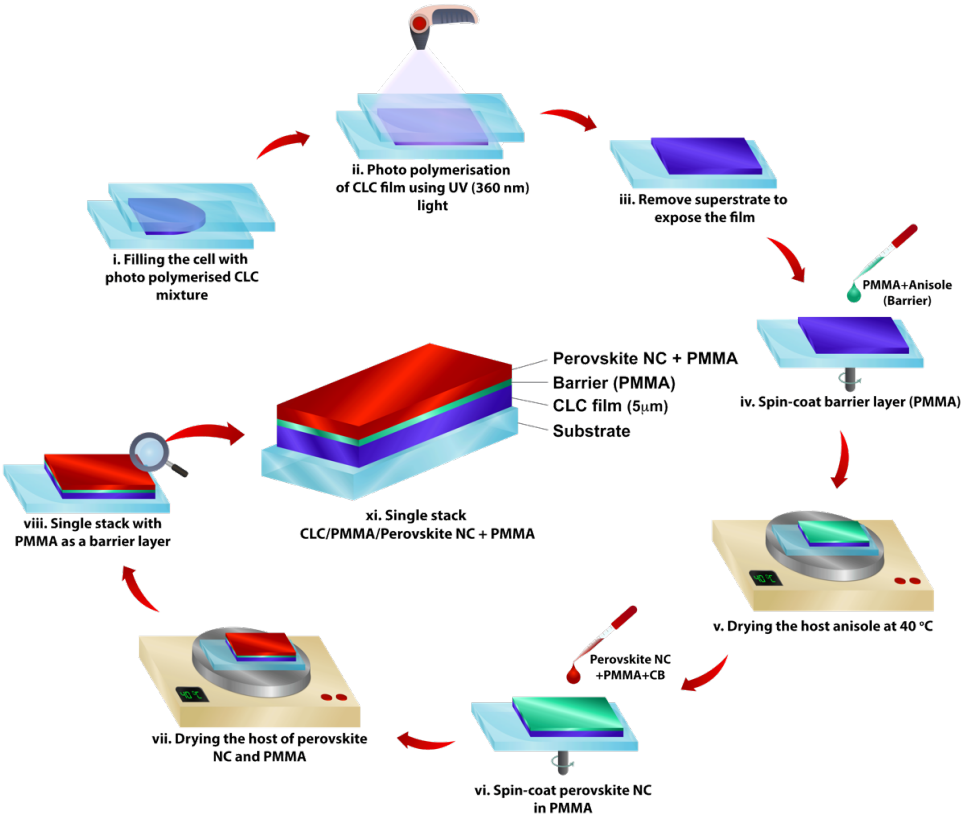


FIGURE 6.18: The fabrication process for creating a one side of the defect-mode perovskite stack using a delamination method for preparing the photo-polymerised CLC films with PMMA as a barrier layer.

Using this mixture, a defect-mode stack was created as illustrated in Figure 6.18. The process begins by injecting the CLC mixture into a 5 μm planar glass cell at the clearing temperature (79°C) of the mixture and the glass cell was filled via capillary action. The device was inspected with an optical polarisation microscope using a yellow filter

over the bulb to prevent unwanted photocuring of the mixture during inspection. The device exhibited a number of disclination lines that were undesirable as the regions separated by disclination lines would have different pitch. In order to remove (or minimise them) to prepare a sample with a uniform pitch, the device was thermally annealed by re-heating the device to the clearing temperature and placing it on a cooler surface at room temperature to cool it down. The regions separated by the disclinations represent regions where the helix axis is normal to the substrate surfaces. While the device was cooling, it was mechanically rubbed multiple times along one direction to encourage a uniform alignment of the helix axis parallel to the normal of the glass substrates. The device was then placed in dark conditions for 48 hours and left to settle to reduce the number of disclinations.

The device was photo-polymerised using UV light (365 nm) at 14±2 mW/cm^2 for 40 sec and then one of the substrates was delaminated to expose the photo-polymerised CLC film. This is shown in Figure 6.18 (ii – iii). To add a barrier layer onto the CLC film so as to protect it from dispersing with the gain media layer, a PMMA/anisole mixture was spin-coated onto the CLC film at 4000 rpm for 30 sec to form a barrier layer of thickness 180±10 nm. The host solvent (anisole) was then evaporated by heating the sample to 40°C for 50±5 min. These processes are illustrated in Figure 6.18 (iv – v). Finally, perovskite nanocrystals dispersed in chlorobenzene (CB) and PMMA was dispensed onto the CLC/PMMA stack and spin-coated at 3000 rpm for 30 sec to from a thin-film of perovskite nanocrystal in PMMA. The stack was then heated to 40°C for 10 min to evaporate the chlorobenzene to form a nanocrystal-PMMA thin-film as shown in Figure 6.18 (vi – vii). An identical stack was also prepared to make a defect-mode device. The single stack consists of glass substrate/CLC/PMMA/perovskite+PMMA and is shown in Figure 6.18 (ix).

In order to confirm whether the CLC remained intact during the fabrication process, the reflection spectrum was recorded at various stages of the process from both stacks and is presented in Figure 6.19. The position and shape of the reflection spectra from the neat photo-polymerised CLC film in both stacks are found to be identical and shown by the black dotted line. The band-gap was centred at 625 nm as expected. When the barrier layer of PMMA is added to the CLC film, it was found that the centre of the

gap shifted to 585 nm. It is believed that this 40 nm blue-shift occurred due to a combination of the penetration of the PMMA mixture into the CLC film and subsequent evaporation of the PMMA host solvent during heating, which resulted in a contraction of the film and thus a shorter pitch of the helix. Similarly, when the perovskite nanocrystal-doped PMMA mixture was added to the CLC/PMMA stack, there also appeared a further blue-shift in the spectrum, again due to a further contraction of the CLC film. For Stack 1, the band-gap was centred at 540 nm whereas for Stack 2 it was centred at 555 nm.

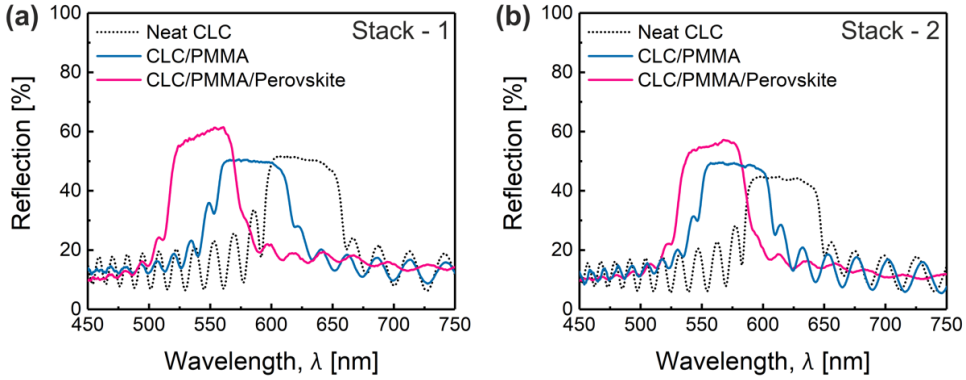


FIGURE 6.19: The refection spectra of the CLC at various stages of the fabrication process of the stack (CLC/PMMA/perovskite NC) with PMMA as barrier layer. Two identical stacks (**a**) Stack-1 and (**b**) Stack-2 were combined to form the full device stack.

The blue-shift in the band-gap during processing is undesirable and deserves further comment. The magnitude of the shift is difficult to predict and control, which means that when the barrier and defect layers are deposited onto two different CLC films, the corresponding reflection spectra may reveal that the band-gaps are not located at the same wavelengths (as seen in Figures 6.19 (a & b)). When these films are combined to create a defect-mode structure, they would be difficult to estimate position of mode as the shift in the position of photonic bandgap is unpredictable due to the evaporation of host.

In this regard, it was decided to replace PMMA with a UV curable Norland glue. Among the range of UV curable glues, NOA-81 was chosen as its transmittance is quoted as being $\geqslant$ 97% in the visible region and it has a lower viscosity (300cps) at 25°C, which means that it is easier to spin-coat and to create a thin-film of uniform thickness. Furthermore, it is also critical that the host solvent used for the perovskite nanocrystals should not damage NOA-81. Therefore, before creating a complete defect-mode structure with perovskite nanocrystals, four test samples were prepared with CLC/NOA-81 layers,

as shown in Figure 6.20 (a). The motivation for preparing these samples was to study the effect of the host solvent used for the perovskite nanocrystals on a layer of NOA-81. The refection from the neat CLC film and a film consisting of CLC/NOA-81 are shown in Figure 6.20 (b), where it can be seen that in both cases $\lambda_c = 615$ nm, which suggests that NOA-81 did not penetrate into the CLC.

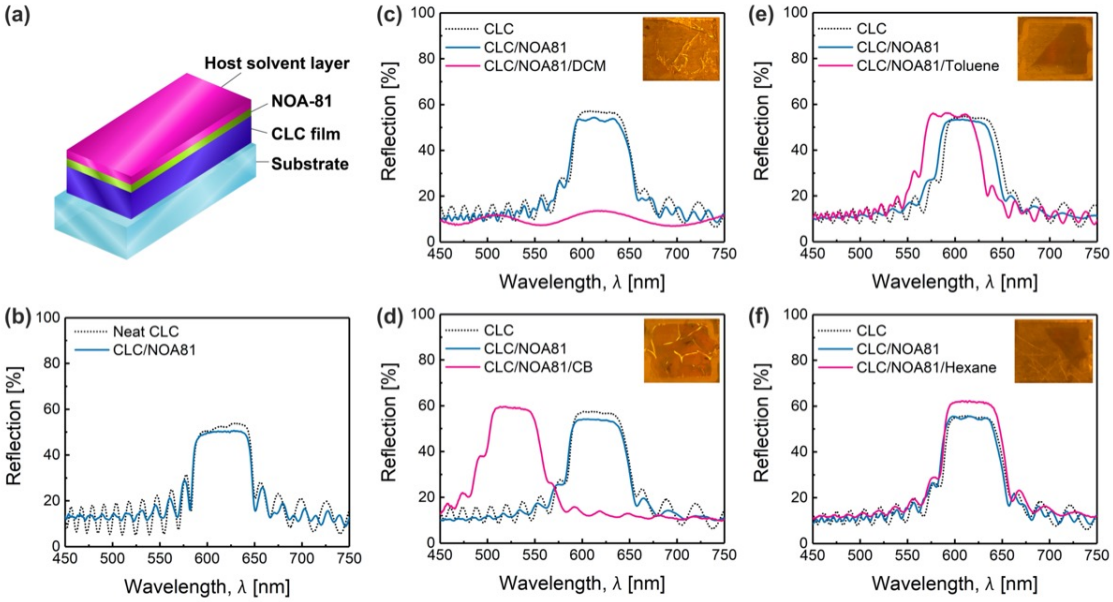


FIGURE 6.20: (**a**) Illustration of the device stack (CLC/NOA-81/host solvent) used to test the impact of the host solvent on the NOA-81 barrier. The reflection spectra for a CLC film (**b**) before and after spin-coating a barrier layer of NOA-81, and with the addition of a test host solvent (**c**) dichloromethane (DCM), (**d**) chlorobenzene (CB) (**e**) toluene and (**f**) hexane on CLC/NOA-81. The inset images shown in (**c – f**) are of the film after depositing the respective host solvent.

Four possible host solvents that are suitable for the perovskite nanocrystals were tested to determine their compatibility with the barrier layer, NOA-81: dichloromethane (DCM), chlorobenzene (CB), toluene, and hexane. These mixtures were spin-coated onto CLC/NOA-81 test samples and their refection spectra are presented in Figures 6.20 (c – f). Clearly, the use of DCM resulted in damage to the stack as no reflection band was seen when the sample was illuminated with white light (evidence of damage can also be seen in the inset in Figure 6.20 (c)). Chlorobenzene, however, did not appear to damage the stack but did result in a shift in the band-gap to $\lambda_C = 525$ nm, possibly due to a contraction of film after evaporation of the solvent. The contracted CLC film is shown in the inset of Figure 6.20 (d). Toluene also appeared to introduce a small blue-shift in the band-gap, shifting it to 595 nm from 615 nm, however, the stack appeared to remaining intact, Figure 6.20 (e). On the other hand, the CLC/NOA-81 stack tested with hexane

did not appear to affect the CLC layer. The band-gap for the CLC/NOA-81 stack after drying off the hexane was found to remain unchanged, Figure 6.20 (f) and the CLC film was intact, inset Figure 6.20 (f).

As the NOA-81 layer is able to protect the CLC film and using hexane as the solvent for the nanocrystals did not appear to effect the spectral position of the band-gap after processing, a defect-mode device was fabricated using the NOA-81 as a barrier layer and hexane as the host solvent for the nanocrystals. First, a thin-film of CLC was created using the fabrication steps as explained earlier in the Figure 6.18 with a Merck photo-polymerised CLC mixture that has a central wavelength at 620±10 nm. The process involves filling a 5 μm planar device, thermal annealing it to minimise the number and density of the disclination lines, photo-curing with UV radiation followed by delamination of the top substrate from the cell to expose the CLC film. These steps are shown in Figure 6.21 (i – iii). After this, the UV-curable NOA-81 glue was spin-coated onto the CLC film at 5500 rpm for 30 sec and the glue was photo-polymerised with UV (365 nm) radiation for 50 sec at 20±2 mW/cm^2. The perovskite nanocrystals dispersed in hexane and PMMA were then spin-coated onto the CLC/NOA-81 stack at 3000 rpm for 30 sec. The stack was heated at 40°C for 10 min to evaporate the solvent that was used to form a thin layer of the perovskite nanocrystal in PMMA. These steps are illustrated in Figure 6.21 (iv – vii). Another identical sample was also prepared using the process explained in Figure 6.21 (i – vii). Each sample forms a stack comprising CLC/NOA-81/Perovskite+PMMA. Both stacks were then combined together and glue was applied at the edges of the stack, Figure 6.21 (viii – ix). This formed a defect-mode structure with substrate/CLC/NOA-81/Perovskite+PMMA/NOA-81/CLC/substrate, Figure 6.21 (x).

The film quality was studied with an optical polarisation microscope under the reflection mode with white light and example images are presented in Figure 6.22 (a). The reflection from a neat CLC (Figure 6.22 a(i)) film shows uniform colour that corresponds to the central wavelength of the reflection band of this material and is expected to be 620±10nm. The film also shows a monodomain structure with the presence of some disclination lines as expected from the uniform standing helix. The optical polarisation microscope image of a single stack CLC/NOA-81/perovskite nanocrystals in PMMA is shown in Figure 6.22 a(ii) and exhibits uniform colour and a polydomain structure. The

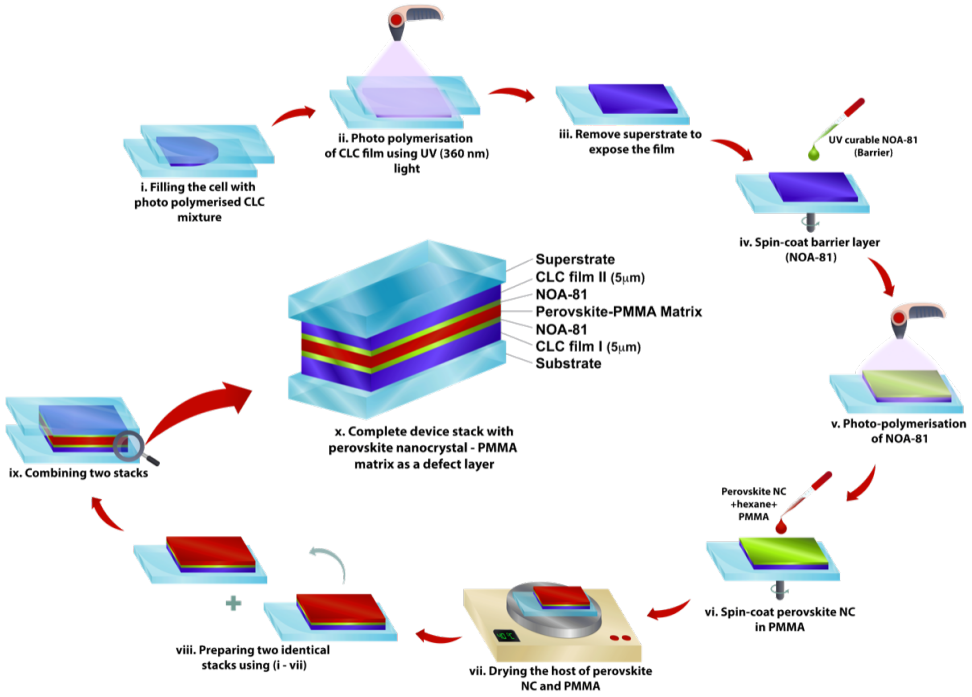


FIGURE 6.21: The fabrication process for creating a defect-mode device using a delamination process with NOA-81 as the barrier layer on photo-polymerised CLC films.

image reveals that the film remained intact after depositing the perovskite nanocrystals in PMMA. The reflection spectrum from the CLC films are crucial in determining the quality of the optical cavity. The reflection spectra from the CLC films was therefore recorded at various stages during the fabrication of the stack and are presented in Figure 6.22 (b). The central wavelength $\lambda_C = 618$ nm after photo-polymerisation and is shown as a dotted line in Figure 6.22. Encouragingly, after depositing the barrier layer of NOA-81 and the perovskite nanocrystal matrix in PMMA, no spectral shift was observed in the reflection band-gap suggesting the barrier layer had protected the CLC film.

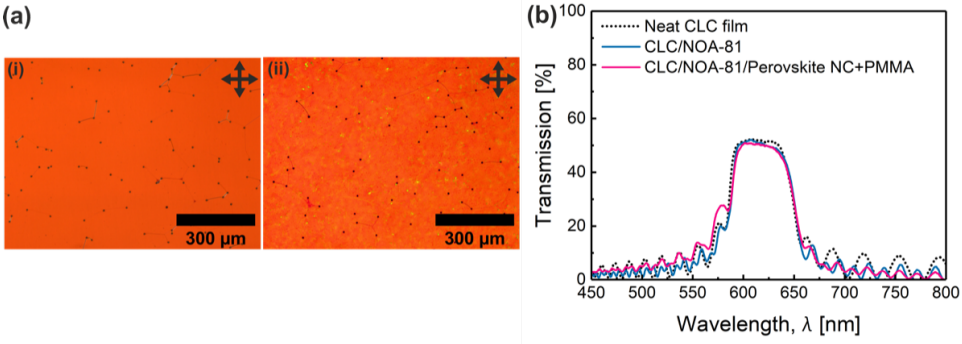


FIGURE 6.22: (**a**) Optical polarising microscope images (in reflection mode) of (i) neat CLC and (ii) single stack consisting of CLC/NOA-18/Perovskite nanocrystals in PMMA matrix. The images were taken from the CLC side. (**b**) The refection from the CLC film at various stages during the fabrication process showing $\lambda_C = 616$nm. All measurements were taken at 25°C.

The stack was photopumped with the Nd:YAG (532 nm) pulsed laser at a range of different repetition levels and the resulting emission spectra are presented in Figure 6.23, which shows enhanced PL emission from the stack. When the repetition rate was increased, the emission spectrum shows gain narrowing in the presence of the CLC reflectors. The laser emission and number of the modes from the defect-mode structure depends on factors such as the thickness and refractive index of the defect layer – a thicker defect layer would support multiple lasing modes. For example, a single mode is observed when the defect layer thickness was 100 nm (Figure 6.5 (b)) whereas multiple modes appear with a thick defect layer of 10 μm as demonstrated in Figure 6.6 (c). It is believed that in addition to a PL emission, in this device stack, multiple laser modes may present.

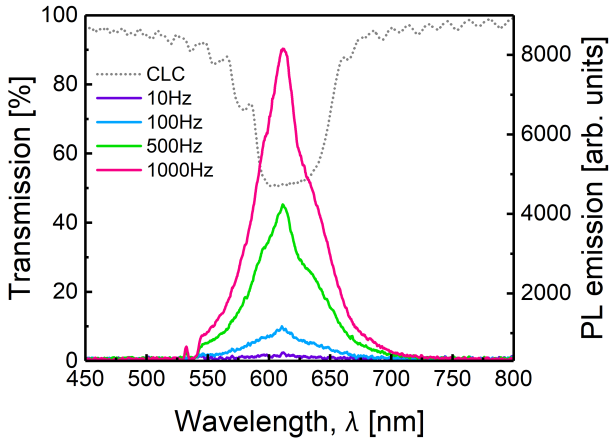


FIGURE 6.23: Emission spectra of CLC/NOA-81/Perovskite+PMMA/NOA-81/CLC stack for different repetition rates of the pump laser (Nd:YAG, $\lambda_{ex} = 532$ nm).

To further understand this behaviour, 4×4 Berreman simulations were run of the stack CLC/defect/CLC for which the approximate device parameters and the simulation results are presented in Figure 6.24. Figure 6.24 (a) shows the simulation model with the CLC parameters: $d_{CLC} = 5\mu$m, $n_o = 1.5$, $n_e = 1.7$, $p = 385$ nm, the barrier layer parameters: $d_{bar} = 2\mu$m and $n = 1.56$ and defect layer parameters: $d_{def} = 2\mu$m, $n = 2.3$. The modelling results support the presence of multiple modes with mode positions that agree approximately with the modes identified from the deconvolution. The multimodes observed in the real device could be a result of the larger thickness of the defect layer. Another possibility could be the non-uniform thickness of defect layer, which could also lead to the appearance of multiple modes.

Single mode emission could be possible from the device if the thickness of the defect layer were to be substantially reduced. An equivalent transmission spectrum of such a device was simulated using the 4×4 Berremen model and is presented in Figure 6.24 (b), which shows a single resonant mode centred at $\lambda = 620$ nm. The model uses the following parameters, CLC: $d_{CLC} = 5\mu$m, $n_o = 1.5$, $n_e = 1.7$, $p = 385$ nm, the barrier layers: $d_{Bar} = 170$ nm and $n = 1.56$ and defect layer: $d_{def} = 170$ nm, $n = 2.3$. It would therefore be possible to demonstrate a single mode laser, provided the thickness of the defect layer was substantially below 1 μm, in accordance with results from simulations.

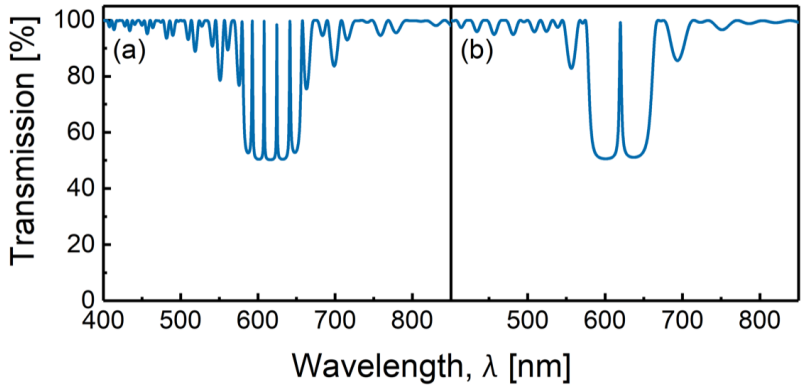


FIGURE 6.24: Transmission spectra simulated using the 4×4 Berreman model showing (**a**) multimode with 5μm thick defect layer (**b**) a single mode appears at 620 nm when a defect layer of 100nm is used.

As the simulations indicate, for a specific set of optical parameters (such as refractive index and pitch), the thickness of the defect-layer is critical in order to accurately control the spectral position and the number of modes in the LC defect-mode laser. With the addition of the defect or barrier layers (which are in solution) to the polymerised CLC films, it was found that the solvent/mixture would penetrate into the CLC polymer network, which caused a swelling/deswelling in the CLC films. In turn, this would elongate or contract the pitch of the helix and hence alter the position of the PBG (as observed in Figure 6.19).

For a defect-mode laser, it is important that the position of the refection band for both the top and bottom CLC reflectors should remain the same. A shift in the bandgap due to the contraction of the film by the addition of any additional layer to the CLC film can be a non-trivial and unpredictable process. For example, after fabricating the final device stack with barrier and defect layers, both CLC films would exhibit reflection bands at different wavelengths. Therefore, it is highly important that a reliable processing

technique is developed that does not result in an alteration in the optical characteristics of the CLC films.

An objective of this work has been to identify a process whereby these films can be made to be optically robust so that the position of the reflection band remained unchanged before and after the addition of either a barrier or defect layer. This has been achieved by first identification of a material that showed compatibility (as is explained in Figure 6.20), with the fabrication process (as illustrated in Figure 6.21), where it was shown that the refection spectra for the CLC films remained unchanged (Figure 6.22). Even though the experimental results have fallen somewhat short in terms of demonstrating single-mode defect-mode laser emission (Figure 6.23), this work has developed a methodology that enables robust multilayer CLC thin-film architectures to be assembled and studied, both in terms of their optical properties but also as their potential for defect-mode laser emission. If such a device is to be realised, then future work needs to concentrate on controlling the defect layer thickness and the uniformity of the layer.

6.4 Summary

In this chapter, a defect-mode LC-perovskite laser device has been proposed and fabricated: this configuration is well-suited to the incorporation of advanced gain materials such as quantum dots and nanocrystals. Several different defect-mode configurations have been discussed and results from 4×4 Berreman simulations have been presented to demonstrate how the spectral position and number of modes can be controlled.

Three different experimental approaches for forming these defect-mode structures have been presented. For the first method, a thin-film of perovskite was deposited via a VASP technique that was sandwiched between two CLC films. Due the presence of CLC films, the emission from the perovskite showed the signature of enhanced amplified emission when excited by a pulsed Nd:YAG laser. While the device exhibited gain narrowing of the photoluminescence, no evidence of laser emission was observed, possibly due to a low emission quantum yield of the perovskite and/or potential degradation of the perovskite structure during the fabrication process.

For the second technique, instead of employing the use of a bulk perovskite layer, perovskite nanocrystals were embedded into a PMMA matrix to form the defect

layer. The CLC films were fabricated using a flexography printing technique and a thin-film of perovskite nanocrystals embedded in a polymer host were deposited onto one of these. Even though this configuration overcomes the problem of depositing perovskite at higher temperatures, which may affect the structural integrity of the CLC films, the reflectivity of CLC film was rather low. Gain narrowing (FWHM from 42 nm to 24 nm) was observed in the PL spectrum although it was unclear whether the structure supported multimode laser emission. The overall profile of the spectrum was found to change noticeably with the appearance of a shoulder in the PL spectrum at 600 nm.

Finally, a new approach was introduced whereby the CLC films were first created using a delamination process and barrier layers consisting of NOA-81 were employed to protect the layers. The fabrication process was further developed by performing a compatibility test of the barrier layer with the host solvent used to disperse the perovskite nanocrystals and hexane was found to be the most suitable. In this regard, a defect-mode device was fabricated, and results have been presented on the characteristics of the thin CLC films. Optical microscope images and the refection spectra from the CLC layers before and after the creation of the device stack suggest that the CLC layers remained intact after the fabrication. Upon photoexcitation of the device with the Nd:YAG pulsed laser, a clear alteration in the emission spectrum was observed that indicates the presence of multiple modes, which is further supported by results obtained from a deconvolution of the spectra. It is believed that the multimode nature of the device is the result of either a larger thickness of the defect layer, which was difficult to control experimentally, or due to the non-uniformity in the thickness of the defect layers, both of which could lead to the appearance of multiple resonant modes. By accurately controlling the thickness of the defect layer, it could be possible to create a perovskite-LC defect mode structure that supports only a single mode. Nevertheless, the results show considerable promise in terms of the development of LC defect-mode photonic structures with advanced perovskite emitters. In the following chapter, it is demonstrated how the delamination fabrication process developed in this chapter can be taken further to create novel flexible defect-mode laser devices with single mode laser emission.

Chapter 7

Flexible Defect-Mode Laser

The self-organisation of liquid crystal (LC) molecules to form periodic structures is a particularly attractive feature as it represents a facile means of preparing a material with a photonic bandgap (PBG) for visible light. Combining this optical cavity with a suitable gain-medium can form the LC laser. One aspect of the LC laser is the band-edge laser, in which the gain medium is dispersed in the CLC. To form a flexible band edge lasing device [96], the CLC has to be doped with a gain material and photo-polymerised, which can potentially cause photo-bleaching of the guest molecules that can eventually reduce the laser efficiency. However, for an LC defect-mode laser, the gain medium can be contained in a separate layer between two CLC layers. This structure, as its name suggests, creates a defect in the PBG that can support laser modes due to the discontinuity in the helical structure formed by a defect layer or a phase jump [49]. These structures can also generate single or multiple laser modes by varying the defect thickness, refractive index of the defect layer and phase jump as explained in detail in Chapter 6.

Defect-mode structures, due to their device architecture, are compatible with a wide variety of gain materials that would be otherwise incompatible in band-edge LC laser devices due to the tendency to aggregate, which can result in photo-quenching. Aggregation can also disturb the helical structure because of the presence of large groups of guest molecules as observed in Chapter 5. Furthermore, the photo-physical characteristics of the gain medium can influence the laser efficiency, which can vary in the presence of different host materials.

7.1 PM597 Laser Dye

Laser dyes, in general, are composed of heavy molecules that possess a large number of overlapping excited states. When they are optically pumped, they exhibit a wide spectral range. This characteristic can be exploited to develop wavelength tuneable lasers when they are combined with a suitable optical cavity. For laser dyes, the radiative decay from the upper electronic state is typically in the nanosecond range and when they are excited with a pump laser of similar or longer pulse duration, they can generate pulses equal to the duration of the pump laser [293].

To-date, hundreds of dye-based lasers have been demonstrated either in the solid, liquid or gas phases with wavelength selectivity from the ultraviolet to the infrared [294–299]. The pioneering dye-based laser utilised a liquid medium to demonstrate laser emission using a dye that belonged to the Rhodamine (Rh) family showing emission from yellow to red. While rhodamine Rh-6G has been extensively studied as a gain medium for laser devices, one of the challenges is the large overlap of its absorbance and emission spectra, and as a consequence part of the output laser wavelength range has to be cut-off due by using a band filter that limits spectral tuning [300].

As explained in Chapter 2, for any laser dye, the triplet – triplet absorption plays a crucial role in the resulting laser performance. Lower triplet – triplet absorption yields better laser performance and improves stability. To enhance laser stability, in the early 1990s dipyrromethene·BF_2 complexes were developed that showed a low triplet – triplet absorption: approximately one-fifth of that of the Rhodamine dyes. Figure 7.1 (a) depicts the three most commonly used and commercially available dipyrromethene·BF_2 dye schemes. The dipyrromethene·BF_2 dyes are zwitterionic structures, which makes them highly polar covering an emission spectral range from green to yellow/red; the full range is determined by the chromophore group that is attached to the complex. Among the schemes shown in Figure 7.1 (a), the PM597 dye is used in the present study over another widely used laser dye, 4-(Dicyanomethylene)-2-methyl-6-(4-dimethylaminostyryl)-4H-pyran (commonly referred to as DCM). The molecular structure of DCM is shown in Figure 7.1 (b).

J-aggregate formation is a phenomenon observed in laser dyes causing the

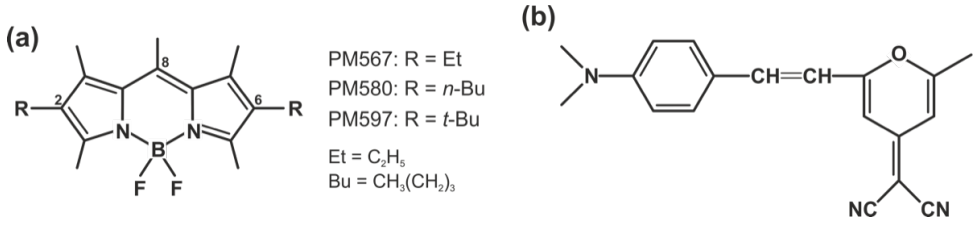


FIGURE 7.1: The chemical structure of (**a**) the pyrromethene class (**b**) the DCM laser dye.

bathochromatic or redshift of the absorption band of increasing the absorption coefficient when the dye aggregates due to the host solvent or change in the concentration [301]. In comparison of the emissive attributes of DCM with the pyrromethene dyes, the DCM dye shows a wider absorption spectrum ranging from blue to green, whereas the PM597 typically exhibit a narrower absorption spectra with a peak around 500 – 535 nm. Nevertheless, the pyrromethene dyes exhibit large absorption coefficients of the order of 10^5 $M^{-1}{\cdot}cm^{-1}$ [83], depending on the concentration of the dye and the nature of the host solvent. The quantum efficiency, which is the ratio of the photons emitted to the photons absorbed is crucial in estimating the laser performance and the excitation threshold. The pyrromethene dyes exhibit higher fluorescence quantum efficiency, in some cases, near unity [302]. In the nematic LC host, E49, the pyrromethene dyes exhibit a quantum efficiency of up to $\Phi = 70\%$. In comparison, the DCM laser dye was found to exhibit a quantum efficiency of $\Phi = 40\%$ for the same concentration in the same LC host [71].

TABLE 7.1: Photo-physics of Pyrromethene PM597 dye in a range of different solvents*.

Solvent	λ_{ab} ($\pm$ 0.1 nm)	λ_{fl} ($\pm$ 0.4 nm)	Φ ($\pm$0.05)	τ ($\pm$ 0.01 ns)	ϵ_{MAX} (10^4 M^{-1} cm^{-1})
Haxane	527.5	567.8	0.43	4.35	8.25
DMF	524.0	565.4	0.35	4.69	5.89
Acetone	522.5	563.6	0.44	4.34	7.44
Ethanol	524.3	563.2	0.43	4.09	7.63
Methanol	522.9	561.2	0.48	4.21	7.58
E49†	530	577	0.75	–	–
PMMA‡	530	580	0.63	6.22	–

Maximum of wavelength of absorbance (λ_{ab}) and fluorescence (λ_{fl}), fluorescence quantum yield (ϕ), lifetime (τ) and molar absorbance coefficient (ϵ_{MAX}). The data is adapted from * [83], † [71] and ‡ [303] with the concentration of PM597 of 2×10^{-6}M, 1wt. %, and 25μMg^{-1}, respectively.

One aspect of using laser dyes is that they are soluble in various solvents including isotopic liquids [83, 304–306], polymers [307, 308] and LCs [71, 309–311]. The solubility of PM597 in polymers such as polymethylmethacrylate (PMMA) ensures its

compatibility with solution processing techniques [303, 312]. As the photophysical and photochemical properties of any laser dye depends on the nature of the host solvent and to a large extent are determined by the polarity of the host. In general, the intramolecular charge transfer mechanism between the electron-accepting and electron-donating species is responsible for the emissive characteristics of a dye. Charge transfer interactions with the host can also affect the dye efficiency depending upon whether the excited states are radiative or non-radioactively favourable [71]. In this regard, the effect of the host on the photophysical properties of a laser dye has been widely studied. Table 7.1 summaries the photophysical characteristics such as quantum yield, lifetime and absorbance coefficient of the PM597 in commonly used isotropic solvents, polymer and LC hosts.

Due to the high quantum efficiency the PM597 laser dye was used in this work to create thin-film defect-mode liquid crystal lasers. For example, 1 wt. % of the PM597 laser dye is either dispersed into the nematic LC host (E7) or PMMA to create the defect layer; it is, therefore important to estimate the peak absorbance and emission of the PM597 in both hosts. Figure 7.2 shows the absorbance and emission characteristics of the 1 wt. % PM597 in the nematic LC, E7 and PMMA. The absorbance spectra suggests that the peak occurs at 530 nm, making it suitable for optical pumping with the second harmonic ($\lambda_{ex} = 532$ nm from a pulsed Nd:YAG laser. In either host, the PM597 dye exhibits a peak emission in the fluorescence at ~ 570 nm.

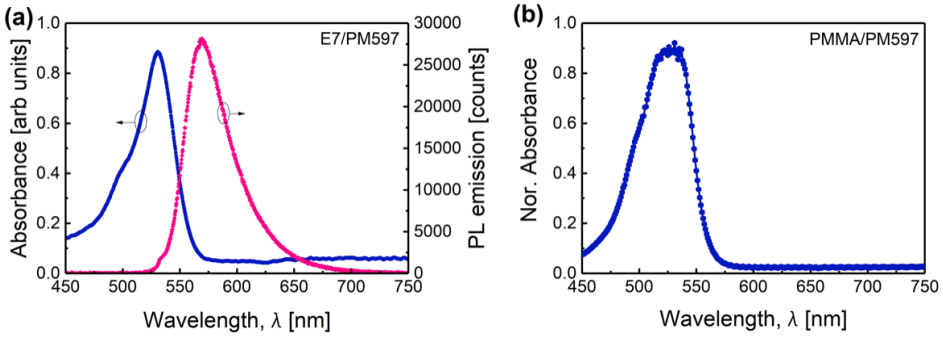


FIGURE 7.2: The absorbance and PL emission of 1 wt. % PM597 in (**a**) nematic E7 host and, (**b**) PMMA/anisole mixture when pumped by the second harmonic ($\lambda_{ex} = 532$ nm) of a Nd:YAG laser.

7.2 Device fabrication and characterisation

Photo-polymerisable chiral nematic LC mixture (RMS-68) was obtained from Merck and used to create the thin film of the CLC. Following the photo-polymerisation

process, it exhibited a central wavelength of the band gap of approximately $\lambda_c = 615 \pm 10$ nm. The mixtures were originally diluted in toluene to reduce its viscosity so that it could be easily spin-coated to form a uniform thin film. The uncured mixture was found to exhibit a clearing temperature of $79 \pm 1^{\circ}$C.

7.2.1 Spin-coating CLC films

As the CLC mixture was initially in a liquid state, it could be used to form a thin-film using a number of different methods. To begin with, the mixture was dispensed on a range of different glass substrates that were treated with different alignment layers using spin-coating. These alignment layers included polyvinyl alcohol (PVA), the sulphonic azo-dye-based photoalignment layer (SD1) and rubbed polyimide (PI). To prepare the alignment layer, PVA or SD1 solutions were dispensed and spin-coated on the glass substrates that were cleaned with IPA via ultrasonication. After spin coating, the substrate with PVA was rubbed with a velvet cloth that attached on a rubbing machine. The substrate with SD1 is, however, photoaligned to encouraged the planar alignment as reported in [313]. For the third substrate, commercially available planar aligned LC cells were used.

The glass plates of the LC cell that have rubbed PI layer were separated. The photopolymerisable CLC mixture was spin coated at 2000 rpm for 30 seconds on one of the substrates followed by photo-polymerisation with UV radiations (365 nm) at a power intensity $20 \pm 5 \text{mW/cm}^2$ for 60 seconds. The film quality for all substrates was inspected with the optical polarisation microscope that showed several defects lines, which suggested a poor alignment of the CLC film. The transmission spectrum for these samples was also recorded and it was found that exhibit the samples were not well-aligned. Therefore, the results are not included here and these samples are not considered further.

While all of these methods can create a thin-film of the CLC that is aligned with the helix axis normal to the substrates, the overall film quality was fairly poor. For all of the techniques considered thus far, only a single alignment layer at the substrate-film interface has been employed whereas the other side of the CLC film has an air/CLC interface. This would decrease the anchoring, resulting in a less well-aligned helix near the film-air interface, thereby reducing the film quality. To obtain higher quality films,

the combination of two substrates with alignment layers was considered, as will be discussed.

7.2.2 Delamination process

In the following attempts to create a photo-polymerised CLC thin film, RMS-68 mixture was used to test the procedure. Since the mixture was diluted in toluene, it was important to process the mixture before creating the thin film. The photo-polymerised RMS-68 mixture was continuously stirred at 200 rpm at room temperature (T = 25°C) and the weight of mixture was recorded repeatedly; this is shown in the Figure 7.3. After 40 hours of continuous stirring and monitoring no further change in weight of mixture, it was considered the toluene had completely evaporated and this mixture was then used to create the CLC film.

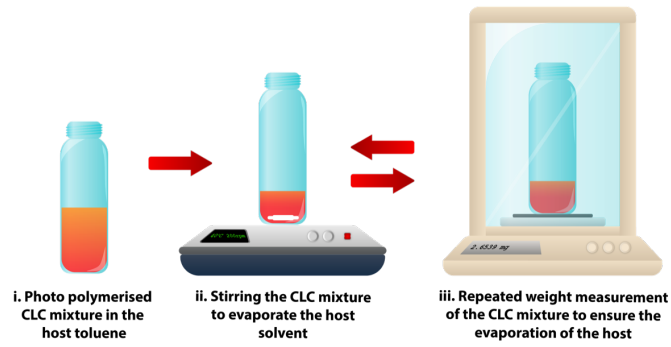


FIGURE 7.3: Experimental process employed to evaporate the host solvent from RMS-68 mixture that was used to form photo-polymerised thin film of CLC.

Three different defect-mode structures were created using RMS-68 mixture. While the device stack consists mainly of the photo-polymerised CLC films, they differ in the type of defect layer used. These defect layers include:

1. Dye-doped nematic LC (NLC) mixture as a defect layer
2. Thin film of dye-doped PMMA as a defect layer with no barrier layer
3. Thin film of dye-doped PMMA as a defect layer with a barrier layer

7.2.3 Dye-doped NLC defect layer

For this structure, dye-doped nematic LC is used to create the defect layer of the device. The nematic LC molecules in the defect-layer attain a planar alignment due to the uniform standing helix at the interface between CLC and the defect layer. The laser dye molecules have anisotropic shape and exhibit different absorption coefficients

along different directions. When combined with nematic LC (anisotropic host), the dye molecules are aligned along the director (in this case, it is a planar alignment), so that the dye molecules have higher absorption when illuminated at normal incidence to the device surface and therefore would exhibit lower pump excitation threshold.

A commercially available 5 μm planar cell was used. The cell consists of antiparallel rubbed PI layer as the alignment layers. The empty cell was heated to 80°C, which is above the clearing temperature of the chiral mixture, before the photo-polymerised chiral RMS-68 mixture (after evaporation of the host) was injected into the cell. The heating process ensures that the mixture is less viscous and fills easily into the glass cell via capillary action. Once filled, the cell was cooled down to room temperature. The cell was left on a flat surface in dark conditions for 48 hours and then inspected on an optical polarising microscope with a long pass filter to block UV wavelengths and prevent unwanted polymerisation. After confirming that the sample consisted of a low number of disclination lines, the cell was photo-cured on one side using UV (365 nm) radiation with a power density of 40 ± 5 mW/cm^2 for 15 secs. After photo-polymerisation, the cell was delaminated and the superstrate was removed; this exposed the photo-polymerised CLC thin film. The process is illustrated in Figure 7.4 a (i – iv).

Another identical photo-polymerised CLC film was created using the same procedure as described. Both exposed films were combined to form a stack of CLC/air/CLC and sealed with glue, Figure 7.4 a (v –vii). Clamps were attached at the edges of the stack to hold it together before glue was applied; this exerted pressure on the stack that minimised the gap between the two films. After curing the glue, 1 wt. % PM597 dye solution in the nematic LC, E7, was prepared and injected between the CLC layers. The mixture filled the gap via capillary action and formed a defect-layer with the dye-doped NLC, (Figure 7.4 a (viii – ix)).

The transmission spectrum and the film quality were studied at various stages of fabrication. Figure 7.4 (b) shows the transmission spectrum of the photo-polymerised CLC films (black & red line), which confirms that both films had identical band-gaps and that the alignment quality was good. The spectrum of the full stack (green line) shows a dip in the transmission at shorter wavelengths, which is due to the absorption of the laser dye in the defect layer. Overall, the spectral position of the band-gap remained

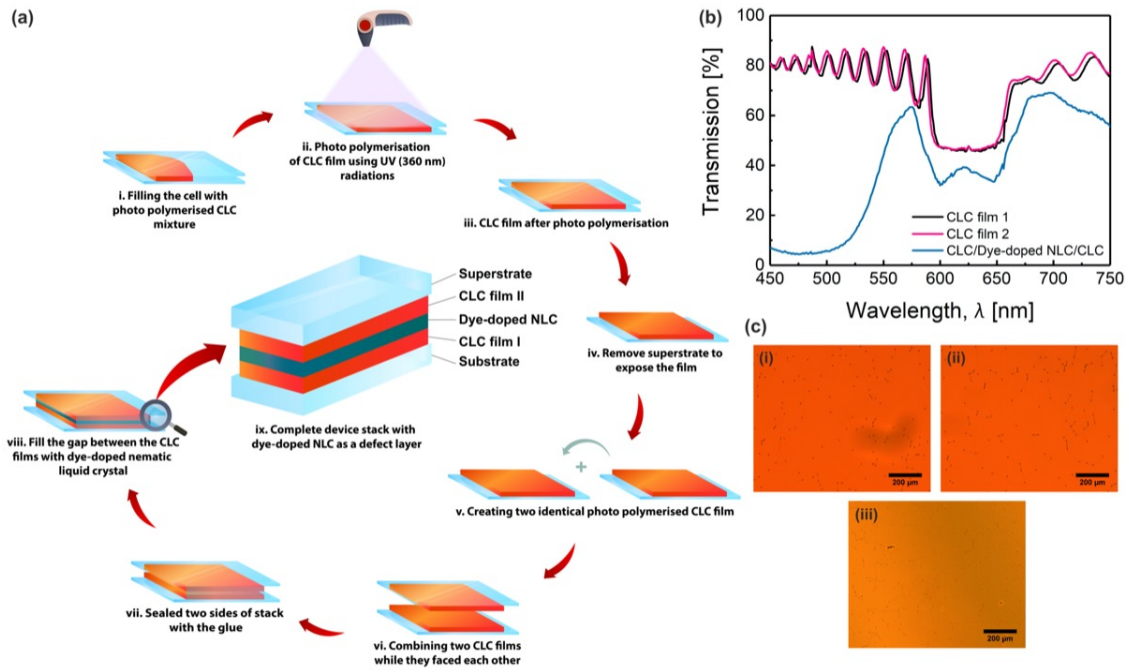


FIGURE 7.4: (**a**) The experimental process for creating a defect-mode laser using two identical photo-polymerised thin-films of CLC with a dye-doped nematic LC as a defect layer, (**b**) the transmission spectra of the different layers of the stack and (**c**) optical polarising micrographs (in reflection) at various stages during device fabrication.

unchanged but with a notch or peak broadening in the spectrum that is discussed later. The film and images of both photo-cured CLC films are shown in Figure 7.4 c (i & ii) where it can be seen that both exhibited a similar optical texture that was largely free of defects. Figure 7.4 c (iii) presents an equivalent image of the full stack. The single uniform colour in the image suggests that it is characterised by a helical structure with a single pitch value that exists over a region of at least 700 μm $\times$ 700 μm in area, which is significantly larger than the spot size of the pump laser used to excite the device.

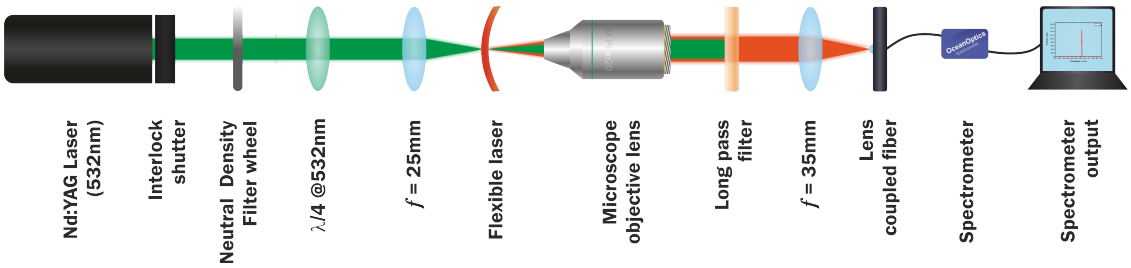


FIGURE 7.5: The free space optical setup for optically exciting the samples using a nanosecond Nd:YAG (532 nm) pump laser.

The stack CLC/dye-doped NCL/CLC was optically pumped by an Nd:YAG laser (CryLas) that emitted short-pulses (1.4 ns) at the second harmonic (λ_{ex} = 532 nm). The free space optical setup is shown in the Figure 7.5. In this case, the repetition rate

of the laser was set to 10 Hz to avoid bleaching of the laser dye. A neutral density filter wheel was used to adjust the excitation energy. The pump beam was focused onto the device using a 25 mm lens creating a spot size of 32.8 μm and the emission from the LC laser was then collected by a microscope objective and a focusing lens before it was directed to an optical fibre that was connected to an Ocean optics USB 2000+ spectrometer. A long pass filter was inserted between the objective lens and the fibre to prevent the pump laser beam from being detected.

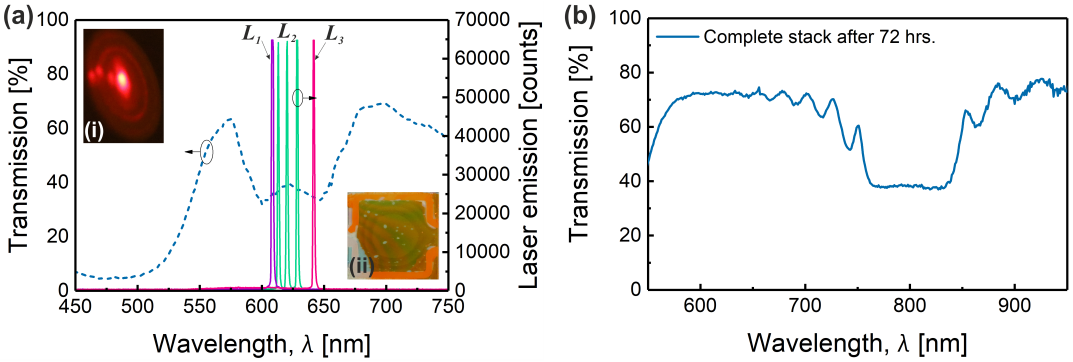


FIGURE 7.6: (**a**) Laser emission at three locations (indicated by the L_1, L_2, and L_3) from the defect-mode (CLC/dye-dope NLC/CLC) device when pumped at three different locations. Laser emission at locations L_1 and L_3 are single-mode whereas L_2 shows multi-mode emission. Insets images show (i) laser beam emission observed on a screen, and (ii) the defect-mode device. (**b**) the transmission spectrum of the complete device after 72 hours.

Figure 7.6 (a) shows the laser emission from the stack. The inset image in Figure 7.6 a (i) shows laser emission from the device while the inset image in Figure 7.6 a (ii) displays the fabricated device used in this study. When the stack was optically pumped at three different locations (I, II & III) resulting in either single or multimode emission depending on the location. It is clear from the spectra that the emission occurred at wavelengths corresponding to the band-gap, indicating that the emission originates from a defect-mode. As explained in Chapter 5, within the band-gap the density of photon states (DOS) is zero for the circular polarisation sense that matches the handedness of the helix [314]. However, when a discontinuity is introduced within the helical structure, either by introducing an isotropic/anisotropic layer or by introducing a phase slip, a leaky (defect) mode is created [49]. By overlapping the emission spectrum of the gain medium with the defect-mode(s), laser emission can be observed when optically excited at excitation fluences that exceed the laser threshold. From measurements of the transmission of the complete device stack, a broad peak or notch in the transmission spectrum is observed

and is expected from the defect-mode configuration with an anisotropic defect layer. This broad peak in the band gap is consistent with previous reports on similar device configurations when a dye-doped nematic LC layer is sandwiched between two identical CLC layers [53, 315].

It can be seen that the wavelength of emission varies as the device is scanned to different locations. This occurred due to the non-uniform thickness of the defect layer across the device; as a result, it supports different lasing modes (this is explained in detail in §6.1.2, Chapter 6). The thickness variation may have arisen due to the unequal penetration of the glue between the stack. While it proved challenging to experimentally determine the air gap (before filling with the NLC) between the CLC layers, using the 4×4 Berreman method, the gap thickness could be estimated from a combination of the CLC film parameters (i.e., thickness, refractive indices, pitch) and by adjusting the thickness of the defect layer to obtain the desired laser wavelength. The results are presented in Figure 7.7. To begin with, the photo-polymerised CLC parameters such as $d_{CLC} = 5\mu$ m, $n_o = 1.58$, $n_e = 1.71$ were used and the transmission spectrum is shown in Figure 7.7 (a). Then an anisotropic layer between the two identical CLC films was added using the parameters for E7 at 20°C ($n_o = 1.526192\ldots$ and $n_e = 1.757503\ldots$) and the thickness of the defect layer (d_{def}) was adjusted so that the defect-mode was consistent with emission at 607 nm (Figure 7.7 (b)). This resulted in a thickness of the defect-mode of 55 nm. Similarly, the thickness of the second mode (642 nm) was estimated and found to be 140 nm, as shown in Figure 7.7 (c). Furthermore, to add the multi-modes, a thicker defect layer needs to be added. However, due to the limitation of the model, it was difficult to add a thicker anisotropic defect layer as the model became unstable. The thickness of the defect layer was therefore estimated to have varied from a few tens to hundreds of nanometres.

To test the stability of the device, the device was stored in dark conditions and the transmission spectrum of the complete stack was further inspected after a period of 72 hours and was found to exhibit a 175 nm red-shift in the reflection band (from $\lambda_c \approx 625$ nm to $\lambda_c \approx 800$ nm), see Figure 7.6 (b). It is speculated that, over time, the dye-doped NLC molecules in the defect layer penetrated into the photo-polymerised CLC network, causing the film to swell, resulting in a red-shift of the band-gap that is due to either an extension of the pitch or a change in the refractive indices, or a combination of the

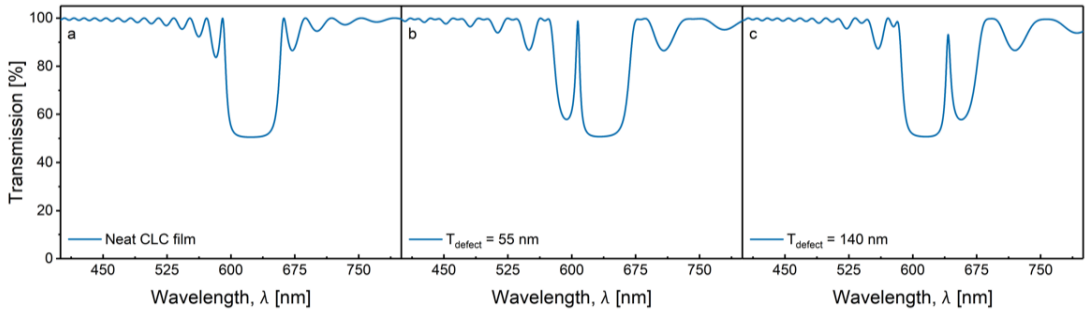


FIGURE 7.7: 4×4 Berreman simulations to estimate the thickness of the defect layer formed with a dye-doped nematic LC. (**a**) The transmission spectrum of a single CLC film, and with the dye-doped nematic LC (**b**) 55 nm and (**c**) 140 nm resulted in the single mode.

two. It is also interesting to note that the notch or broad peak at the centre of band gap of the transmission spectrum had disappeared after 72 hours. As a result, the defect-mode disappears. To better control the defect layer thickness and to stabilise the device performance, alternative approaches were considered.

7.2.3.1 Flexible laser with no barrier layer

The photo-polymerised CLC RMS-68 mixture (after evaporation of host, toluene) was used to create a thin film of CLC. In accordance with the process described in Figure 7.4 (a), a 5 μm antiparallel rubbed planar glass cell was capillary filled with RMS-68 mixture at a temperature of 80°C. After filling of the glass cell, it was left in dark for 48 hr to reduce the number of disclination lines. After inspection under the microscope to ensure only a low number of disclination lines were present, the sample was photo-cured using UV radiation (365 nm) with a power density of 40±5 mW/cm^2 for 15 secs. The superstrate of the cell was then delaminated to expose the CLC film. After removal from the glass cell, the photo-polymerised CLC film was transferred to a flexible substrate. To achieve this, the CLC film and underlying glass substrate were immersed in either acetone or isopropylalcohol (IPA) to release the CLC film from the glass substrate. When the CLC film was immersed in acetone, it was found that it started to damage the film within a few minutes. However, IPA did not show any effect on the film even after 48 hours.

A transparent flexible pressure sensitive adhesive substrate (made of polyethylene terephthalate) was then applied to the exposed CLC/glass substrate stack and the flexible substrate was gently rubbed in one direction. The flexible substrate was slowly peeled-off from the glass substrate which transferred the photo-polymerised CLC to the

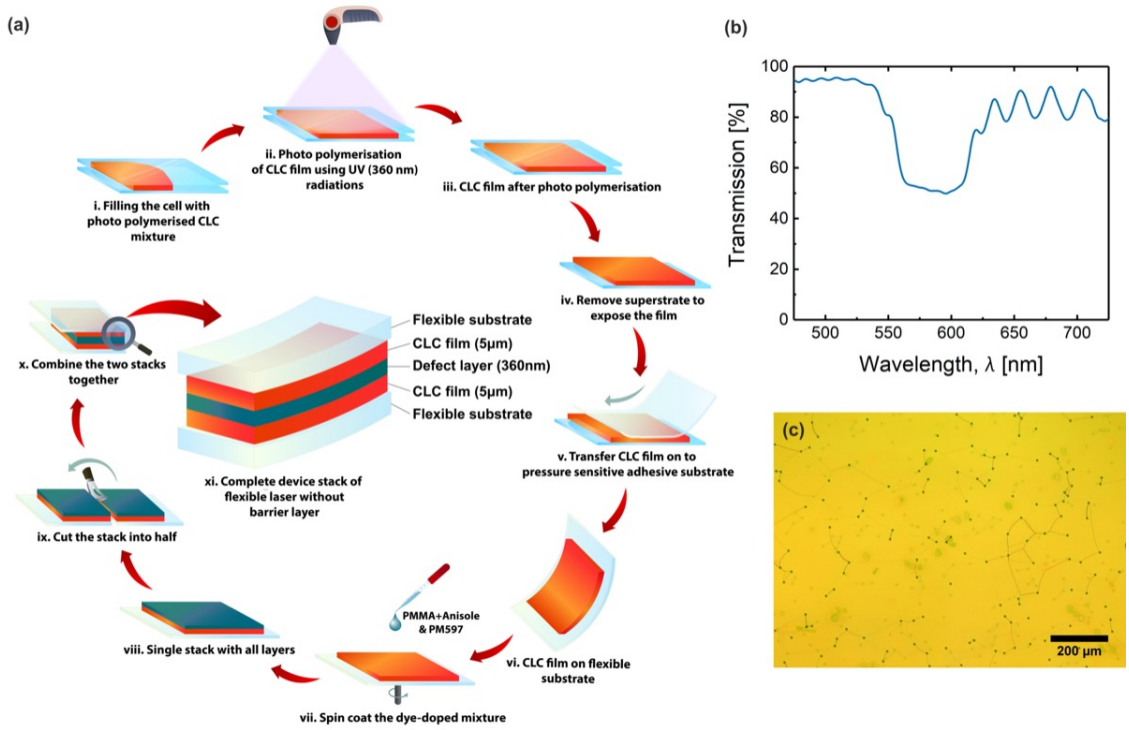


FIGURE 7.8: (**a**) The device fabrication process for creating a defect-mode laser using a flexible substrate without the use of a barrier layer, (**b**) the transmission spectrum of the complete device, (**c**) optical polarising microscope image in reflection using white light.

flexible substrate. This fabrication process is illustrated in Figure 7.8 a (i – vi). After transferring the CLC film onto the flexible substrate, the defect layer consisting of the gain medium was spin-coated at 4000 rpm for 30 secs, Figure 7.8 a (vii). The gain medium comprises 1 wt. % of laser dye pyrromethene, PM597 (Exciton), dispersed in commercially available MicroChem Polymethyl methacrylate (PMMA) and anisole (4wt. % anisole) mixture and stirred for 24 hours at 200 rpm at a temperature of 25°C. The CLC and gain medium stack was then heated to 40°C for 50 minutes so as to evaporate the anisole. The stack was cut into half and finally (Figure 7.8 a (ix), sandwiched together to form a defect structure comprising a flexible substrate/CLC/gain medium layer/CLC/flexible substrate, as shown in Figure 7.8 a (xi).

The film quality and the reflection band were then studied as before. The transmission spectrum of the film was recorded using the same optical setup (Figure 3.12) and the result is presented in Figure 7.8 (b). The transmission spectrum suggests that the CLC film created with this method forms a uniform standing helix configuration with the helix axis normal to the substrate. The reflection band is found to be centred at $\lambda_c = 585$ nm, which is blue-shifted slightly from the expected value and is likely due to the contraction

of the film as a result of the evaporation of the host material in which the PMMA was dissolved. Furthermore, the optical polarising microscopy image (Figure 7.8 (c)) reveals that the CLC film has a uniform area with few disclination lines. This is expected from a well-aligned uniform standing helix configuration.

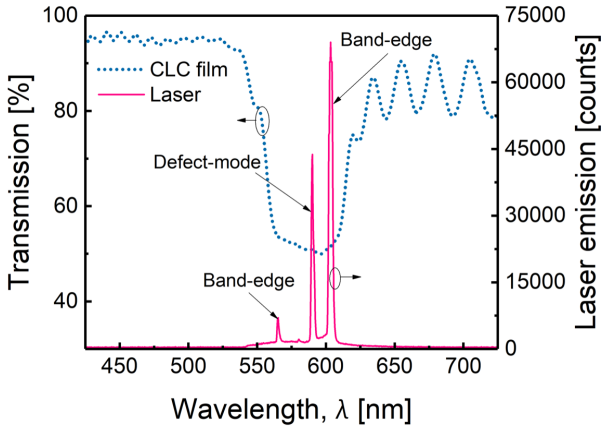


FIGURE 7.9: Band-edge and defect-mode laser emission from a flexible defect-mode film without barrier layers.

The complete device stack was optically pumped by the Nd:YAG laser (see Figure 7.5) and multimode laser emission was observed, as shown in Figure 7.9. In this case, laser emission is observed to occur both at the centre of the band-gap as well as towards the edges of the gap. It is possible that all three modes are defect-modes. However, it is also possible that the modes closer to the edge of the gap are actually band-edge laser modes, which occur at the short (λ_s = 565 nm) and long wavelength edges (λ_L = 605 nm) of the photonic band-gap. This might occur as a result of a small concentration of the NLC/laser dye mixture dispersing into the polymerised CLC reflectors, which are porous. Laser emission that occurs within the band-gap at λ_d = 590 nm, however, is clearly due to the presence of a defect-mode.

7.2.3.2 Flexible defect-mode laser with a barrier layer

Penetration of the dye-dope nematic LC mixture into the polymerised CLC layers is clearly undesirable and in order to avoid emission at the edges, a barrier layer was needed to protect the CLC films. This barrier layer can prevent the dye from penetrating into the CLC polymer network. The device fabrication steps are illustrated in Figure 7.10. As explained earlier, RMS-68 mixture (after evaporation of toluene) was used to fill the 5 μm planar cell and photo-polymerised with UV radiation (365 nm) with power density of 40$\pm$5 mW/cm^2 for 15 secs to create the CLC film, Figure 7.10 (i – iii). After creating

the CLC film, the superstrate was delaminated from the glass (Figure 7.10 (iv)) and a pressure-sensitive adhesive on a flexible substrate was applied and then slowly peeled-off, resulting in the transfer of the polymerised CLC film from the glass substrate to the flexible substrate (Figure 7.10 (v & vi)). The CLC film was found to have a thickness of 5.0± 0.1 μm.

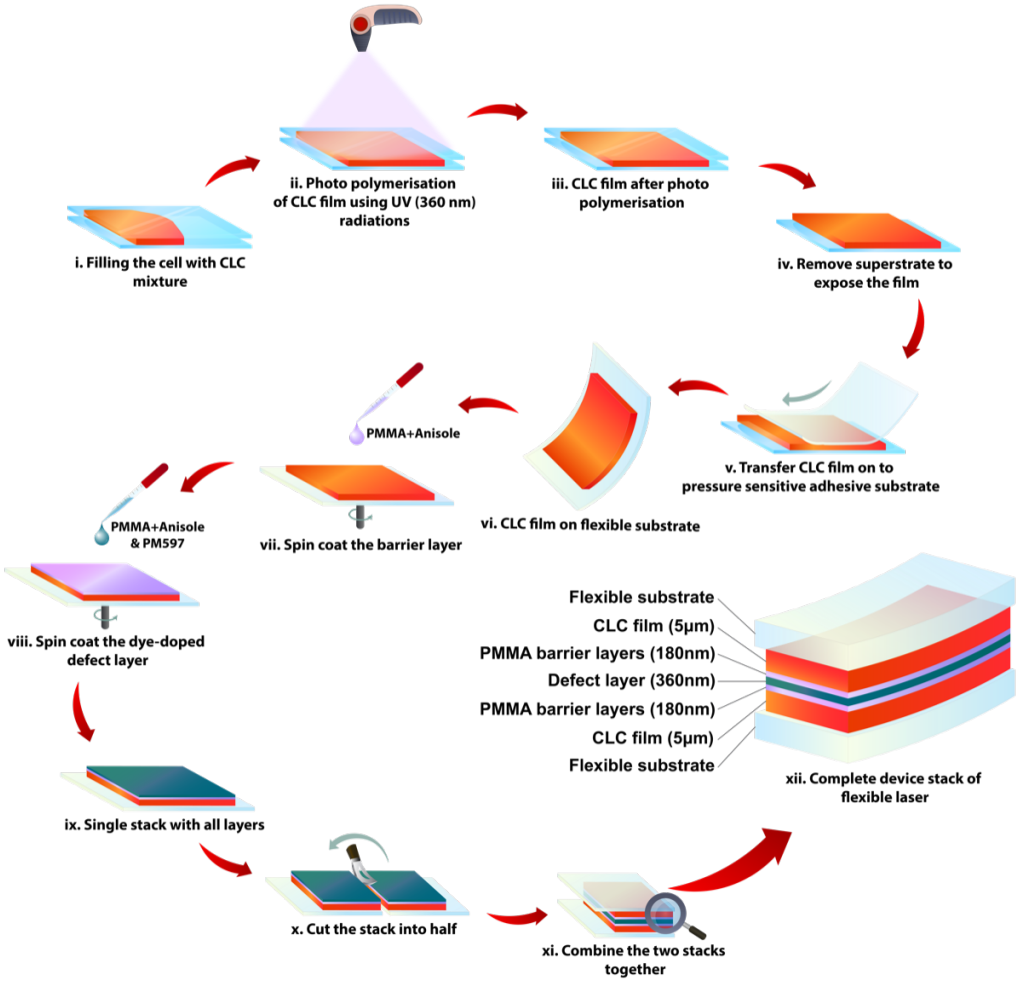


FIGURE 7.10: Fabrication process for creating a flexible defect-mode laser with barrier layers (i) injecting photo-polymerised CLC mixture into a LC cell with planar alignment, (ii) photo-polymerising the CLC mixture using UV (365 nm) light to create a thin film, (iii) the photo-polymerised CLC film, (iv) delaminating the top substrate to expose the CLC film, (v) apply the flexible substrate onto the CLC, (vi) transferring the CLC film onto a flexible substrate, (vii) spin-coat PMMA/anisole mixture to create a barrier layer, (viii) spin-coat the dye-doped PMMA/anisole solution, (ix) single stack with all layers, (x) cutting stack into two (xi) combining the two stacks and (xii) the complete device stack.

A neat PMMA/anisole (4wt. % anisole) mixture was spin coated at 4000 rpm for 30 seconds onto the CLC film (Figure 7.10 (vii)) and the sample was then baked for 50±5 min at 40°C to dry the solvent. This creates a barrier layer of PMMA of thickness 180± 10 nm on the CLC film [316]. The role of the barrier layer was to prevent the diffusion of

the dye into the CLC layers. For the defect-layer, the laser dye, PM597, (1wt. %) doped in a PMMA mixture was then spin-coated on top of the PMMA barrier layer at 4000 rpm 30 sec (Figure 7.10 (viii)). The sample is again baked at 40°C for 50±5 min to remove the residual solvent creating a dye-doped PMMA defect layer of thickness 180±10 nm [316]. At this stage, the stack now consists of flexible substrate/CLC film/PMMA/dye-doped PMMA and is shown in Figure 7.10 (ix). The stack is then cut in half resulting in two identical stacks, Figure 7.10 (x), which are then combined to complete the full device stack. In doing so, the dye-doped PMMA layer thickness, including barrier layers, becomes 720±20 nm (Figure 7.10 (xi)). The two stacks were then glued together and the complete flexible device is shown in Figure 7.10 (xii).

Figure 7.11 (a) shows examples of optical polarising microscopy images recorded of the sample when viewed in reflection at a magnification of 10× with a halogen white light source. Two images are presented: the first (Figure 7.11 a (i)) shows an example microscope image of the photo-polymerised CLC film after filling into the glass cell and before it was transferred to the flexible substrate while the second microscope image (Figure 7.11 a (ii)) shows the optical texture after assembling the complete device stack comprising flexible substrate/CLC/PMMA/dye-doped PMMA/PMMA/-CLC/flexible substrate. Encouragingly, a uniform (single colour) optical texture is observed in both images, indicating that the pitch was uniform over areas of at least 700 μm × 700 μm, which is significantly larger than the pump spot size of the Nd:YAG laser that was used to excite the thin-film laser device. Furthermore, the images confirm that the monodomain texture was retained after the CLC film was transferred onto the flexible substrate and after the addition of the barrier and defect layers. It should be noted that spacer beads are present in Figure 7.11 a (ii), which implies that these were transferred when the CLC film was delaminated from the glass substrate and attached to the flexible substrate.

To confirm that the CLC reflectors remain intact after device fabrication, Figure 7.11 (b) presents results of the reflection spectrum of the CLC film after polymerisation, but before the top glass substrate is removed, along with the reflection spectra from the top and bottom CLC layers after the device has been assembled. The centre of the band-gap of the photo-polymerised CLC is found to be located initially at λ_c = 615 nm, which

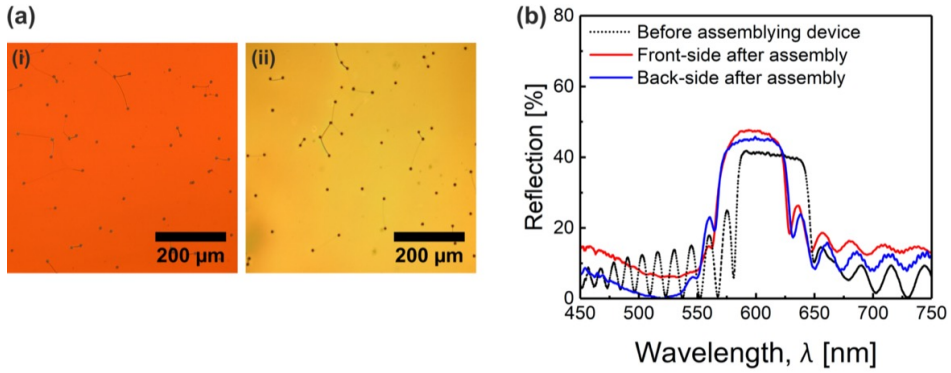


FIGURE 7.11: (**a**) Optical polarisation microscope images (viewed in reflection) of the photo-polymerised CLC film (i) before transfer to the flexible substrate and (ii) after assembling the flexible laser device. (**b**) Reflection spectra of the photo-polymerised CLC film before transfer onto the flexible substrate (black line) and after assembling the full device stack (red line – reflection from top CLC, blue line – reflection from the bottom CLC layer).

was then blue-shifted to λ_c = 595±5 nm after device construction. This relatively small shift in the band-gap is likely to be due to a slight contraction of the pitch of the helix during the removal of the anisole, which causes a deswelling of the CLC films as excess solvent, which was present during the capillary filling stage, was removed. It can also be seen that the position and overall shape of the reflection band for the top and bottom CLC layers are almost identical, indicating that the pitch was uniform throughout the device. Furthermore, the rotation sense of the CLC helix would not change when the CLC film was cut into half and placed at the top, the relative rotation remains the same. A right-handed helix is a right handed helix regardless of which direction it is viewed, but there might be a phase slip between the directors at each interface.

From measurement of the transmission spectrum of the complete stack, it is often difficult to discern the presence of the defect-mode as it is regularly the case that the spectral width of the defect-mode is very narrow and beyond the resolution of the spectrometer used to record the transmission spectrum of the band-gap [94, 284]. In this work, the spectrometer had a resolution of 1.5 nm; however, the defect-mode is likely to have a width of no more than 0.04 nm as noted in previous reports [284]. Nevertheless, it is believed that a defect-mode was present as evidenced from the laser emission characteristics.

When the sample was optically excited with an Nd:YAG laser (as shown in Figure 7.5) with fluences that are below the excitation threshold, for example at 5.60

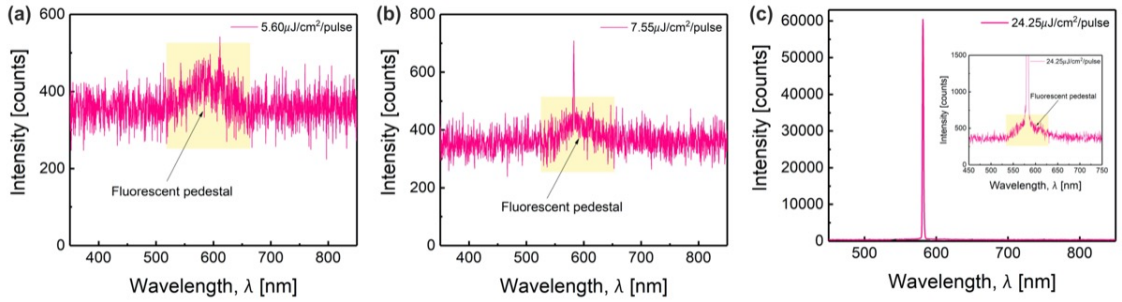


FIGURE 7.12: Fluorescence and laser emission from the flexible laser when pumped by the Nd:YAG laser at different excitation fluences. The fluorescent pedestal is centred at 585 *nm* for excitation fluences (i) 5.6 μJ/cm^2/pulse, (ii) 7.55 μJ/cm^2/pulse, (iii) single-mode laser emission when the excitation fluence is 24.25 μJ/cm^2/pulse. The inset shows the fluorescent pedestal at the same excitation fluence.

μJ/cm^2/pulse and 7.55 μJ/cm^2/pulse, a broad fluorescence spectrum was observed, corresponding to the fluorescence spectrum of the laser dye PM597, Figure 7.12 (a & b). However, when the optical excitation was increased above the excitation threshold fluence, it was found that the flexible device generated single mode laser emission centred at λ_{LC} = 582 nm, Figure 7.12 (c). However, when the excitation fluence was increased, i.e., to 24 μ J/cm^2/pulse, the fluorescent pedestal can only be seen when the laser spectrum is enlarged around the low emission intensities (inset Figure 7.12(c)).

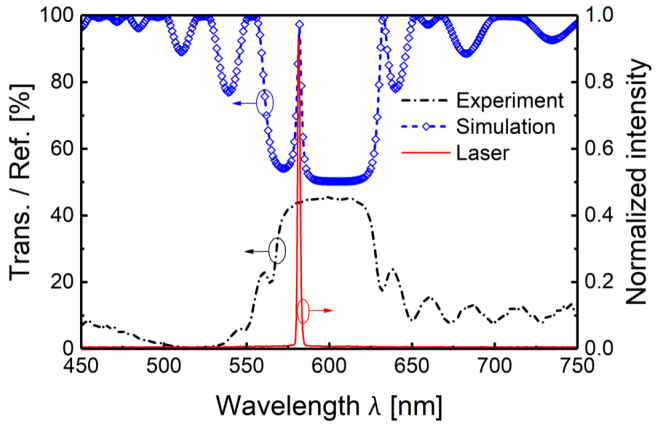


FIGURE 7.13: Reflection spectrum of the band-gap (black dashed line) of the full flexible device, 4×4 Berreman simulation (blue line) showing the transmission spectrum for the device stack with a transmission notch at 582 nm, laser emission spectrum (red line)for the flexible device centred at 582 nm with a linewidth of 1.97 nm.

Figure 7.13 shows the spectrum of the laser emission alongside the relative position of the reflection band of the CLC layers, where it can be seen that the laser emission is observed to occur within the band-gap, consistent with a defect-mode. This is also supported by results obtained for the transmission spectrum of the complete device stack

using a 4×4 Berreman matrix approach. The simulation shows that a defect-mode occurs at λ_d = 582 nm, which was consistent with our results for the laser emission wavelength. It is, therefore, considered that the laser emission is the result of the presence of a defect-mode within the band-gap.

Figure 7.14 (a) illustrates the evolution of the laser emission spectrum as the excitation fluence was increased, highlighting the appearance of a laser emission line centred at λ_d = 582 nm, which grew in magnitude with the excitation fluence. An example of the input-output characteristics for the laser is shown in Figure 7.14 (b) which shows a discontinuity in the gradient, corresponding to the excitation threshold, at E_{th} = 12.3± 0.5 μJ/cm^2/pulse. The slope efficiency of the laser was determined to be approximately 6.0 ± 0.3% while the divergence (Θ) of the flexible laser was found to be 8.8°± 1° when the pump energy was set to E_{th} = 340± 10 nJ. The divergence was estimated using $\Theta = \tan^{-1}\left(w_f/f\right)$, w_f is the width of spot and f is the distance between curved LC laser and screen. Previous reports indicate that the divergence of band-edge CLC lasers varies from a few degrees to tens of degrees and is found to depend on parameters such as the pump energy, CLC film thickness and boundary conditions of the active layer [317]. The results presented here reveal a divergence angle that is comparable in magnitude.

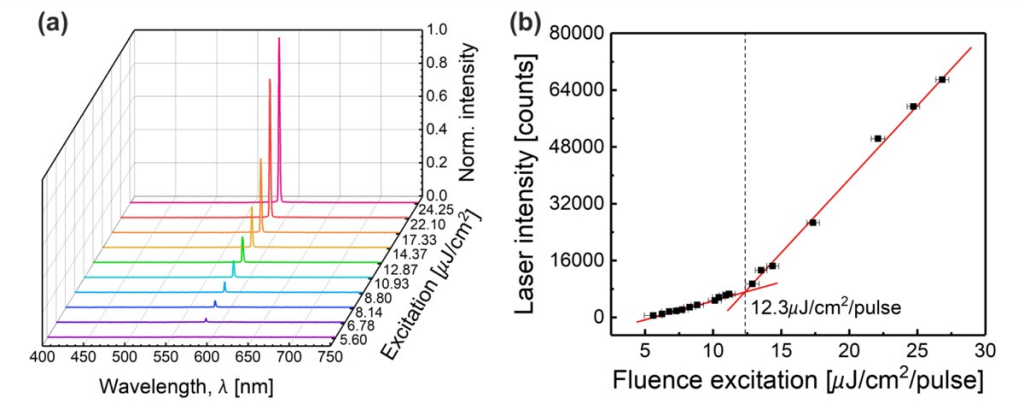


FIGURE 7.14: (a) Laser emission spectrum as a function of the excitation fluence, (**b**) peak laser intensity as a function of the excitation fluence showing an excitation threshold of 12.3μJ/cm^2/pulse when optically excited with a second harmonic (532 nm) Nd:YAG pulse laser with 10Hz repetition rate.

The threshold fluence presented here is low compared to previously reported LC band-edge/defect-mode lasers and deserves further comment [42, 53, 64, 94, 98, 100, 102, 105, 318]. In the literature, the excitation threshold of LC defect-mode lasers is typically found to lie within the range of hundreds of μJ/cm^2/pulse to tens of

mJ/cm^2/pulse[42, 53, 94, 102], whereas the lowest laser threshold reported for band-edge LC lasers is of the order of a few mJ/cm^2/pulse [64, 98, 100, 105]. The lower threshold observed for defect mode lasers is generally understood to result from the higher density of states at the defect-mode compared to that of the modes located at the band-edges [15]. Even though the threshold value in this flexible laser is on the lower end of the regime for other reported defect-mode lasers it is not out of line with other organic thin film lasers that have reported excitation fluences as low as a few tens of nJ/cm^2/pulse [64]. For the flexible device presented here, the low threshold is believed to be due to a combination of the high quantum efficiency (>70%) of the laser dye [71] and the confinement of the gain medium to the defect layer, which avoids the photo-bleaching of the dye when the gain medium is dispersed within the CLC mixture [42, 94, 102].

In order to determine the polarisation of the laser device, two CLC test samples with opposite handedness were prepared using the nematic host HTW114200-100 (obtained from Fusol) with the addition of a chiral dopant. The left-handed chiral dopant S811 (25 wt. %) was doped into the nematic host to form the left-handed test CLC while the right-handed chiral dopant R811 (25 wt. %) was used for the right-handed test CLC. The concentration of the chiral dopant was chosen so that the reflection band overlapped the LC laser emission wavelength (λ_{LC} = 582 nm). The transmission spectra of these samples are shown in Figure 7.15 (a). These test samples were inserted separately in between the flexible laser device and the collection optics, as shown in Figure 7.15 (c) to test the polarisation state of the LC laser.

When the right-handed CLC test sample is placed in the experimental rig, the handedness of the LC laser emission is found to match the handedness of CLC helix of the test sample, since most of the LC laser emission is reflected and only a small amount of laser light is observed at the detector (Figure 7.15 b(i)). However, when the left-handed CLC test sample was inserted into the set-up, it is noted that the laser emission is of a notably higher intensity (see Figure 7.15 b(ii)). These results reveal a dominant right circularly polarised component with a small amount of left circularly polarise light. For an isotropic defect layer, which is the configuration used here, previous research has shown that the polarisation of the mode is typically observed to be circularly polarised of the same handedness as that of the CLC helix [263, 266, 319]. These results are in broad

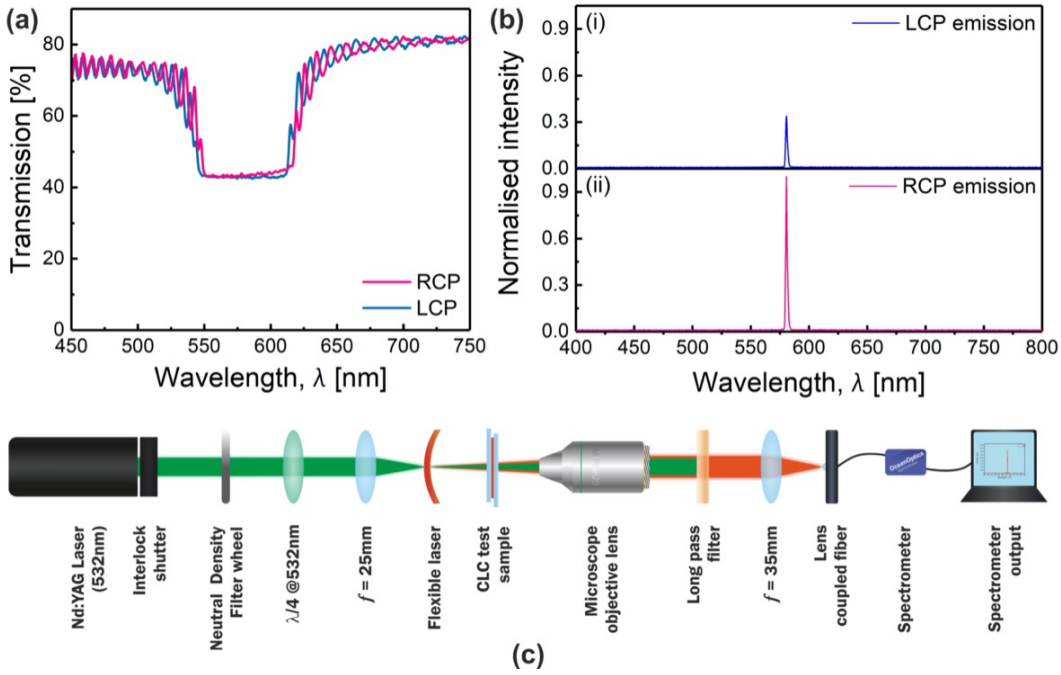


FIGURE 7.15: (**a**) The transmission spectra of two test samples used to determine the handedness of the flexible laser, (**b**) Laser emission spectra for the right circularly polarized component (red line) and left circularly polarized component (blue line) of the laser emission, and (**c**) Free space optical setup used to determine the polarisation state of the LC laser emission by using CLC test samples of known handedness. The test samples were inserted in between the flexible laser and the microscope objective lens.

agreement in that we see a dominant right circularly polarised component in accordance with the right-handed helix of our CLC layers. It is, however, unclear why we see both left and right circularly polarised light.

7.2.3.3 Beam steering

Figure 7.16 shows images of the flexible laser captured from different perspectives (Figure 7.16 (a), side view and Figure 7.16 (b), front view) when the laser is curved and optically pumped by the Nd:YAG laser. The laser exhibits an emission colour that corresponds to the spectral position of the laser mode as observed in Figure 7.13.

To demonstrate the flexibility of the device, the pump beam from the Nd:YAG laser was scanned across the device so as to illuminate different active regions in the thin film laser when it was mechanically deformed. Figure 7.16 (c) shows a schematic illustrating the concept of the experiment where, in this case, the flexible laser device was pumped at five separate active locations, labelled I to V in the figure, across the thin film. In accordance with the deformation of the thin film and thus the different orientations of the helix axis, this resulted in LC laser emission at different locations on the illumination

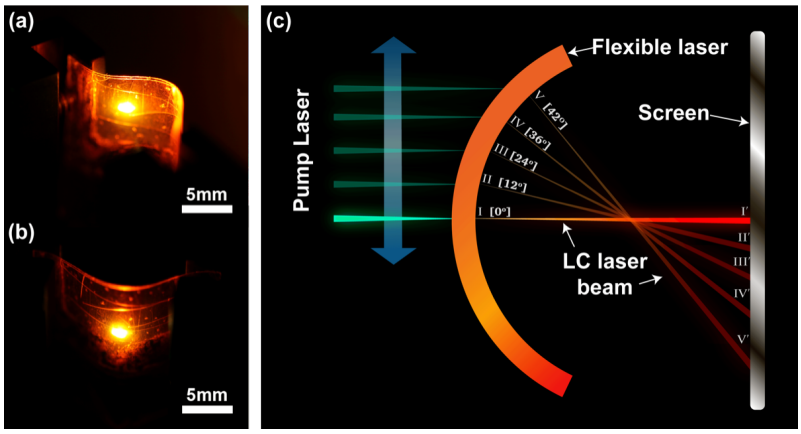


FIGURE 7.16: Photographs of the flexible laser device when subjected to a mechanically-induced deformation and optically excited by an Nd:YAG laser (**a**) side-view and (**b**) front-view, (**c**) diagram illustrating the beam steering concept when the flexible laser is deformed and the pump beam from the Nd:YAG laser is scanned across the device.

screen, shown with the corresponding Roman numerals.

A photograph of the flexible laser when it is held in a curved configuration and optically excited by the Nd:YAG laser is shown in Figure 7.17 (a), where the corresponding LC laser emission (red light) and the pump laser (at the centre) can be seen illuminating the screen. The following set of images in Figures 7.17 (b – f) show the beam steering phenomena of the flexible laser device.

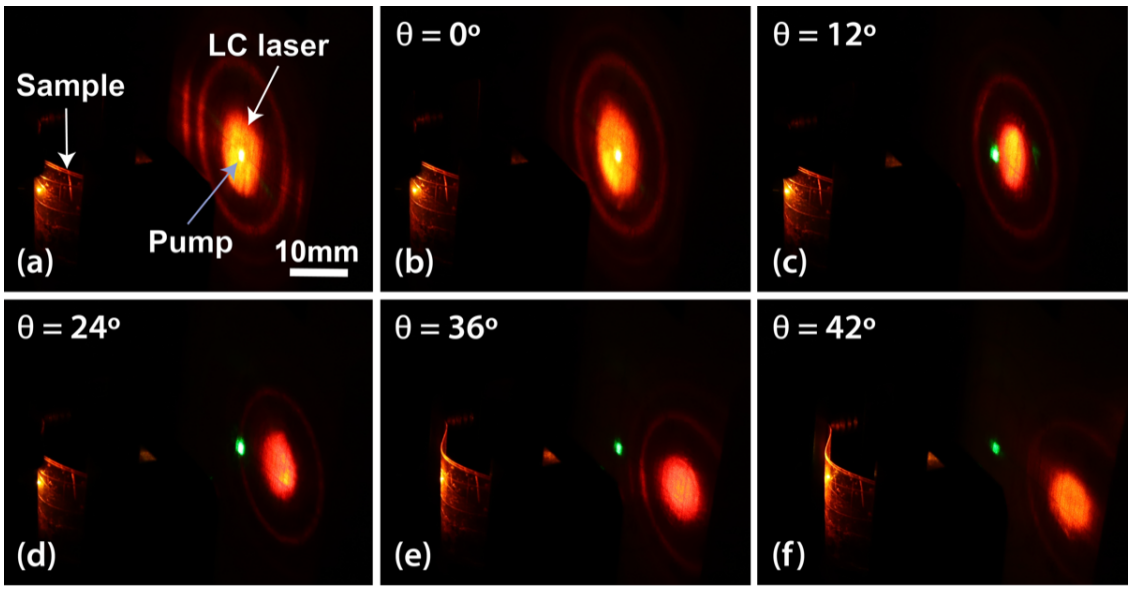


FIGURE 7.17: (**a**) Photograph showing the flexible laser, the pump beam and the LC laser emission observed on the white illumination screen. (**b – f**) Photographs demonstrating the steering of the LC laser beam as the pump beam is scanned across the curved flexible laser device.

In Figure 7.17 (b), optical pumping at the centre of the device corresponds to

location I and therefore both the pump spot and LC laser emission are observed on the viewing screen. The angle (θ) represents the angle between the propagation direction of the pump beam and the normal to the surface of the thin-film. At the central location (labelled as I), the normal to the substrate of the thin film laser is parallel to the propagation direction of the pump and therefore $\theta = 0^{\circ}$. Since the helix axis in the CLC layers is oriented along the normal to the substrates this means that the helix axis and the propagation direction of the pump beam are collinear. As a result, no deflection in the LC laser beam is observed on the illumination screen (Figure 7.17 (b)). By continuing the scanning from locations, I to V, the LC laser beam is translated in the opposite direction on the screen. In this case, the LC laser emission is found to occur at larger values of θ as the alignment of the substrate normal relative to the propagation direction of the pump beam increases. For example, at the location labelled as II (Figure 7.17 (c)), the LC laser is deflected by an angle of $\theta = 12^{\circ}$ which increases through values of $\theta = 24^{\circ}$, 36° and 42°, as the pump beam is scanned through the active regions, III, IV, and V, respectively.

Adjusting the radius of curvature of the flexible laser enables the amount of beam steering to be controlled, that is, a larger radius of curvature leads to shallower beam steering and vice-versa. In the illustration, the radius of curvature of the flexible device is 5 mm resulting in beam-steering of the LC laser of up to 42°. This feature means that the LC laser emission can be propagated in a range of directions without tilting the laser device.

The angle of pump laser is important in terms of LC lasing emission and needs further comments. Previous work has shown that the angle of incidence of the pump laser can affect the laser emission properties by altering the pumping conditions and the absorption of the dye. In the case of oblique incidence of light on a chiral nematic LC there are some distinctions from the case of normal incidence. First of all, higher reflection orders can be observed at frequencies that are multiples of the Bragg frequency. At very large angles of incidence, there is a region where the reflection becomes polarisation insensitive [320–325]

Theoretical studies have considered the variation in the pumping conditions for different angles of incidence and have identified potential regions where very large absorption may occur. However, experimental studies have not unequivocally confirmed

these findings, with results showing that the threshold typically increases with an increase in the incident angle [326]. Further studies are needed to truly understand how the emission characteristics vary with the incident angle of the pump beam.

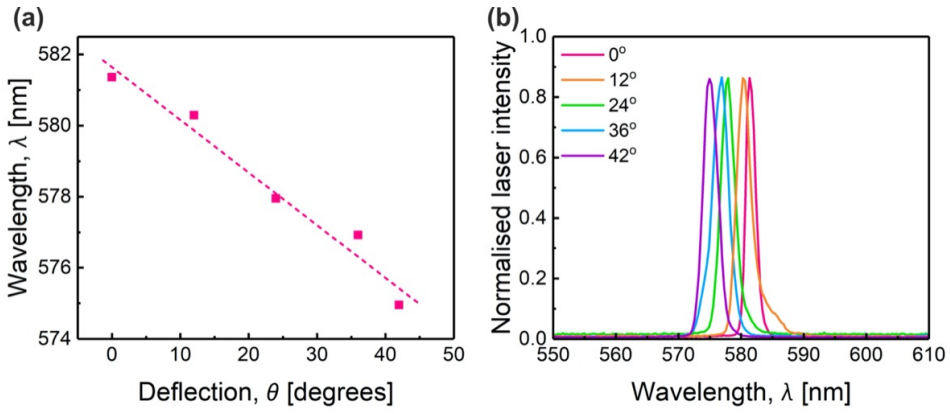


FIGURE 7.18: (**a**) The laser emission wavelength as a function of laser deflection angle when sample is scanned at various locations, and (**b**) the variation in the laser emission spectrum due to bending of the flexible device.

In addition, it should be noted that when the device is held in a curved configuration, there is the potential for a slight change in the film thickness at a given location, which can result in a small alteration in the laser emission wavelength in accordance with a shift in the defect-mode as observed in §6.1.2, Chapter 6. These results are also summarised in Figure 7.18 (a). This causes a small shift in the peak emission of the LC laser from 582 nm (flat) to 7 nm blue-shift (bent), Figure 7.18 (b).

7.2.4 Summary

In conclusion, a flexible defect-mode thin-film LC laser has been demonstrated using the pyrromethene laser dye, PM597, as a gain medium. Results are presented that highlight the challenges in fabricating a flexible defect-modes laser, such as the effect of different types of alignment layer on the formation of the photo-polymerised CLC layers.

A defect-mode laser is created using a dye-doped anisotropic defect layer (dye-doped nematic LC) between two identical CLC layers. The penetration of the dye-doped nematic into the CLC layers can result in the removal of the defect-mode as well as the possible appearance of band-edge laser modes. Different experimental procedures are then considered to avoid the penetration of the gain medium into the polymerised CLC. Using a film transfer technique, both single mode and multimode laser emission are demonstrated with the flexible defect-mode laser.

Finally, a flexible and mechanically robust defect-mode laser that exhibits single-mode laser emission at 582 nm, with an excitation threshold of 12.3$\pm$ 0.5 μJ/cm^2/pulse and a slope efficiency of 6.0 $\pm$ 0.3%, has been demonstrated. The experimental results are supported by the results from simulations using the 4$\times$4 Berreman model. By virtue of the flexibility of the device, beam steering has been demonstrated by simply bending the device without the need for any additional optical components. The properties of this laser device are particularly attractive for conformable platforms and potentially wearable photonics technologies.

Chapter 8

Polarisation Controllable Band-Edge LC Laser

Manipulating the polarisation state of light is becoming increasingly important in various optical applications including high-contrast LC displays [327], optoelectronic devices [328], optical communication systems [329], optical measurements [330], fibre optics [331], polarimetric [332] and holographic imaging [333], 3D displays [334] and virtual/augmented reality displays [335]. For example, polarisation controllers have been created with silicon lab-on-chip photonic integrated systems by forming waveguides and structures that can encode and process the optical information [336]. Such systems, however, require sophisticated fabrication processing that eventually increases the device cost as well as displaying limitations in terms of tuneability. Liquid crystals, on the other hand, are relatively easy to process and are compatible with cost-effective fabrication techniques. They exhibit electro-optic characteristics that enable them to be used in a variety of optical devices ranging from polarisation rotators [337–339], waveplate retarders [340], filters [341, 342] to pixelated displays [343, 344] and spatial light modulators (SLM) [345]. As an example, the first LC-based optical rotator was demonstrated by Ye [346] using two quarter waveplates with an optical modulator and later David *et al* showed two-dimensional polarisation phase encoding in a LC SLM [347].

It is well-known that when an electric field is applied across a nematic LC layer, the reorientation of the director results in a change in the optical retardation ($\Delta n \times d$), which enables the optical properties to be tuned from a quarter wave to a full waveplate condition etc. As a result, depending on the strength of the electric field, circular polarisation can be changed into elliptical or linear polarisation. By making use of this

electro-optic behaviour, various device configurations have been presented that use nematic [348], chiral nematic [349] or both phases [350] to manipulate the polarisation state of light [351–355]. Furthermore, a polarisation tuneable chiral nematic LC laser has been demonstrated previously [356] that can change the polarisation state of the output; however, similar to other reported devices, it has limitations in not being able to control the orientation of the polarisation state. In another configuration [357], the orientation and polarisation state of a defect-mode laser created with two identical 1D photonic crystals comprising alternate SiO_2 – TiO_2 layers was controlled with a nematic LC layer by applying an in-plane field. However, the number of alternate layered structures of SiO_2 – TiO_2 was crucial in creating an accurate polarisation states. In addition, the fabrication process was rather involved as it uses six in-plane electrodes and requires repeated fabrication steps to create the 1D photonic crystal with a multiple layered structure.

In this study we present the development of a bench-top demonstration of polarisation tunability of a band-edge LC laser with an all-LC based device using a four in-plane electrode assembly. The in-plane electrode configuration allows an applied electric field to provide control of the azimuthal orientation as well as the tilt of the LC director, allowing control of both the orientation and retardation of the LC waveplate. Using this it is then possible to control fully the polarisation state of the LC laser output. By engineering both the ellipticity and orientation of the polarisation state of the light emitted this can be beneficial for astronomical optical systems, holographic imagining tools and VR/AR applications.

In the following sections, the development of the polarisation controller device is discussed in detail by presenting the relevant theory and experiments on the electro-optic characteristics of the nematic LC. Before that, a general background on the operation of a waveplate is also presented to aid with the understanding of the use of a nematic LC as a tuneable waveplate.

8.1 Waveplate

Waveplates are optical retarders that are used to modify the polarisation state of light without attenuating the light intensity or diverting the beam direction. This is achieved by the use of a special type of optical material. After travelling through such a

material, light can attain a different polarisation state that is defined by the optical properties of the material and the device thickness. Such optical materials are birefringent (Δn) in nature (i.e., optically anisotropic), that is, have different refractive indices along different directions. Since the refractive index (n) of any material defines the speed that light attains while travelling through it (defined as $n = c/v$, where c: speed of light in vacuum and v: speed of light in material); this implies that a larger refractive index slows down the propagation of light compared to a material that has a lower refractive index. The extraordinary refractive index, which is the refractive index parallel to the optic axis of a birefringent material with uniaxial refractive index anisotropy. In birefringent materials n_e can be larger than n_o (e.g., quartz, positive birefringence), or n_e smaller than n_o (e.g., calcite, negative birefringence); the optical anisotropy being defined as $\Delta n = n_e - n_o$. In nematic phase of LC, the component of light that travels along a direction that exhibits the extraordinary refractive index would slow down compared with the component of light that travels along the direction described by the ordinary refractive index. And therefore, the direction or axis with n_e is known as the slow axis whereas the axis along n_o is the fast axis.

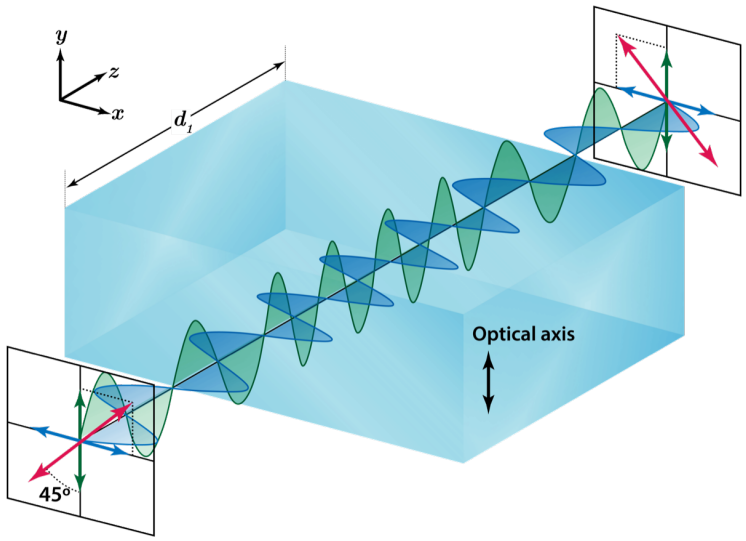


FIGURE 8.1: A typical waveplate showing two in-phase orthogonal components of light travelling through a birefringent material. After leaving the material, the components are out-of-phase by π. This results in rotating the orientation of linear polarised input light by 90°.

A waveplate is described by the amount of phase difference (Γ) it introduces between the two components of incident light and it is related to the thickness (d) and birefringence (Δn) as:

$$\Gamma = \frac{2\pi\Delta n \times d}{\lambda} \tag{8.1}$$

where λ is the wavelength of light. Using this principle, waveplates are designed to retard one component of light with respect to the other to a certain level and hence alter the polarisation state. This is illustrated in Figure 8.1 showing a typical waveplate when two in-phase orthogonal components of light enter the birefringent material and after passing through it, they exit the material with a π phase shift. This results in rotating the orientation of the polarisation state of the light by 90°; that is, inverting the orientation of the linear polarised light, as shown in Figure 8.1.

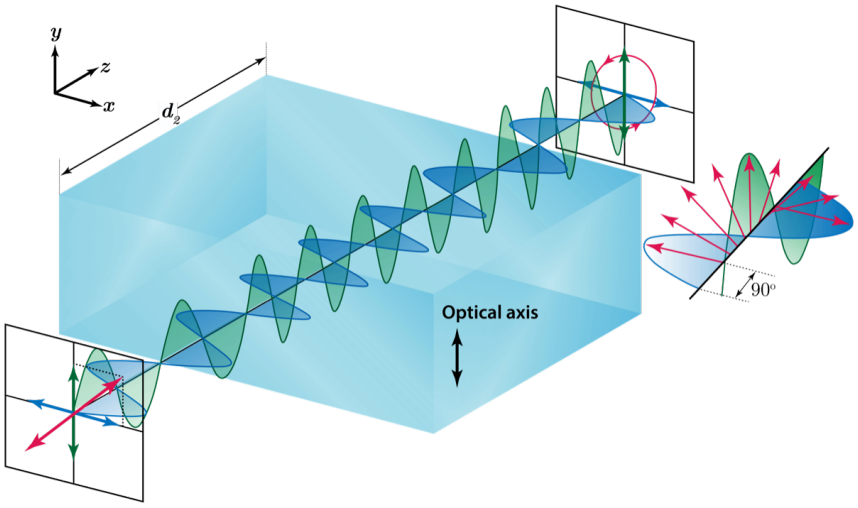


FIGURE 8.2: A typical waveplate showing two in-phase orthogonal components of light travelling through a birefringent material. After leaving the material, the components are phase shifted by $\pi/2$, this results in circular polarised light.

In order to achieve a particular state of polarisation (linear, elliptical or circular), it is vital to retard the components of light to a specific level. For example, if two components leave the material with a phase shift of odd integer multiple of π, the polarisation state would invert by 90° (as shown in Figure 8.1). For a given birefringence, this can be achieved by choosing a correct thickness (d) of the material. If, however, the thickness is altered (either increased or decreased), the material would not add the correct level of retardation, and as a result an incorrect polarisation may observed. For example, Figure 8.2, the same material is used as in Figure 8.1 but for a different thickness (say d_2), the components of light that leave the material would now have a phase difference of $\pi/2$. The resultant E-field of the output light would have a constant level, but its direction is continuously changing as if it is rotating – this is circular polarised light.

If the waveplates change the input polarisation state of light by adding a π-phase shift to the linearly polarised light or by retarding one of the components by half of the wavelength, that is, $\lambda/2$, this is called a half-wave plate (HWP). Similarly, the waveplate that can convert the linear polarised light into circular polarised light by adding a phase shift of $\pi/2$ or retarding one of the components by a quarter of the wavelength, $\lambda/4$, is known as a quarter waveplate (QWP). These are illustrated in Figure 8.3.

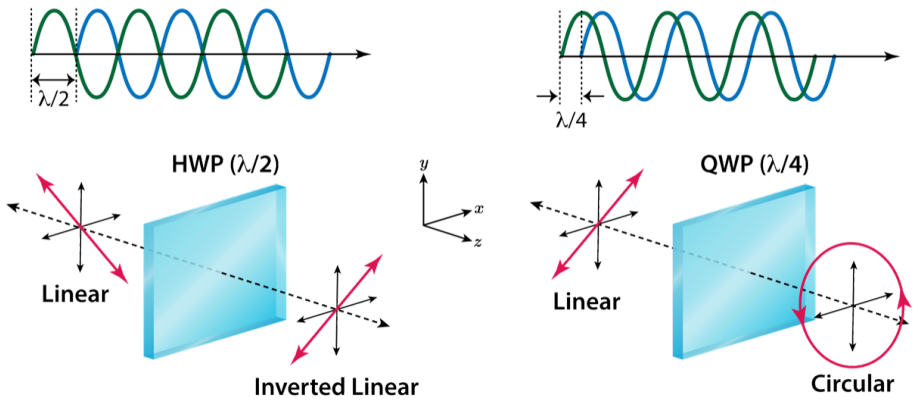


FIGURE 8.3: An illustration of a half waveplate (HWP) demonstrating a phase shift in the linearly polarised light (**left**) and a quarter waveplate (QWP) converting linear polarised light into circular and vice-versa (**right**).

Furthermore, when the components of the linearly polarised light have a phase shift between 0 to π ($\neq \pi/2$), then an elliptical polarisation is achieved. This can be attained by further varying the thickness of device of a given birefringent material. In essence, a waveplate made with a given birefringent material can convert a linearly polarised input light into circular or elliptical by adjusting the device thickness. This implies a need for a separate physical device with a fixed device thickness to attain each polarisation state. However, this can be achieved in one single device while keeping the device thickness constant but varying the effective birefringence of the material.

8.1.1 A tuneable waveplate

One way to achieve a tuneable waveplate is to use nematic liquid crystals (LC) as they offer optical anisotropy that can be changed when an electric field is applied across the LC device. This can be understood from Figure 8.4 (a) whereby unpolarised light is first converted into linearly polarised light after passing through a polariser. The LC device shown in Figure 8.4 (a) has a planar alignment and the director configuration under $V_1 = 0$ is shown in Figure 8.4 b(i). As the field is increased, due the positive dielectric anisotropy, the LC director tilts (θ). This tilt increases as the applied field amplitude

increases and since the LC is birefringent in nature, this tilt implies a change in the optical anisotropy (from Δn_2 to Δn_5) for the light that is propagating along the normal of the device, Figure 8.4 b(ii – v). For a given tilt in the director, the effective birefringence retards one of the two components of incident light to a certain level that results in a certain polarisation state. For example, if the director is tilted at an angle (θ_1), where the effective birefringence retards one of the components of light by π corresponding to propagation over a distance of $\lambda/2$ (as seen earlier for the HWP) the result is a reorientation of the input polarisation state by 90°. Similarly, if the LC director is tilted so that the device retards one of the two components of linear polarised input light by $\pi/2$ then circular polarisation is obtained (as seen for a QWP). Thus, by applying an electric field across a planar-aligned nematic LC device the polarisation state of the input light can be varied.

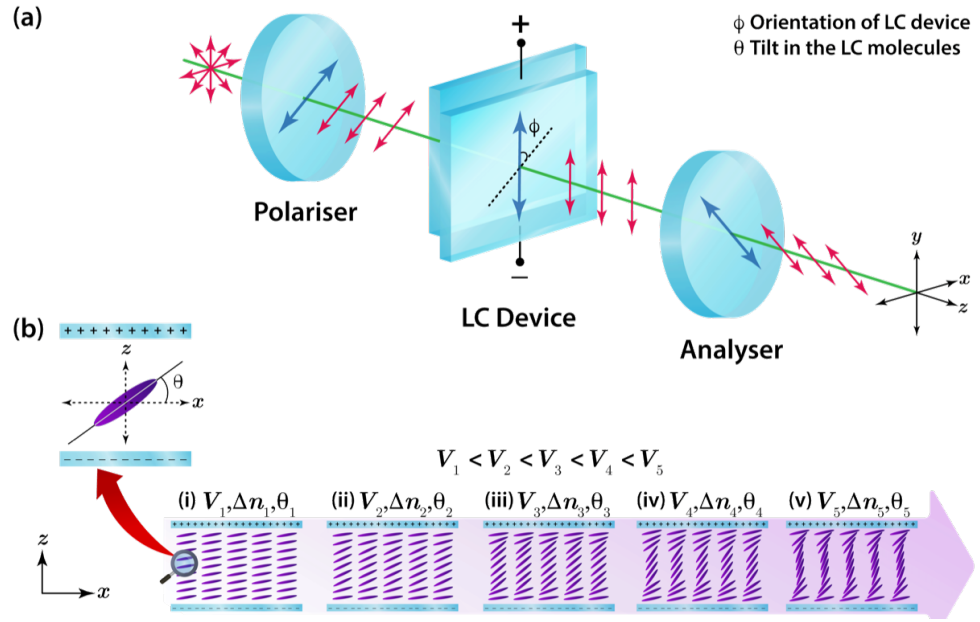


FIGURE 8.4: (**a**) Schematic illustration of a planar aligned nematic LC device showing the rotation of the polarisation state of light when a transverse electric field is applied across the LC device. (**b**) Depicts the alignment of the LC director when a varying electric field is applied across the device which results in a change in the effective birefringence.

The light intensity, when collected after the analyser and studied as a function of applied input voltage, behaves as shown in Figure 8.5 (a). The variation of the light intensity as a function of the applied voltage is a result of the change in the polarisation state of the light that passes through the LC device. To understand this behaviour, consider what happens if the applied voltage is increased to the maximum value, ideally to infinity, this tilts the LC director to a perfect homeotropic position, that is, $\theta = 90°$.

This implies that the input light travelling normal to the plane of device can only see one refractive index, i.e., the optical anisotropy (Δn) is zero in this situation. As a result, light cannot pass through the analyser and therefore no transmission is observed – this corresponds to a zero-waveplate (0-WP) condition – a situation identical to an isotropic material, i.e., glass. This means that light after passing through the LC device would be of the same polarisation state as that when it enters the device; it is shown with an example of linearly polarised light in Figure 8.5 (b) with label (i) at the 0-WP condition position.

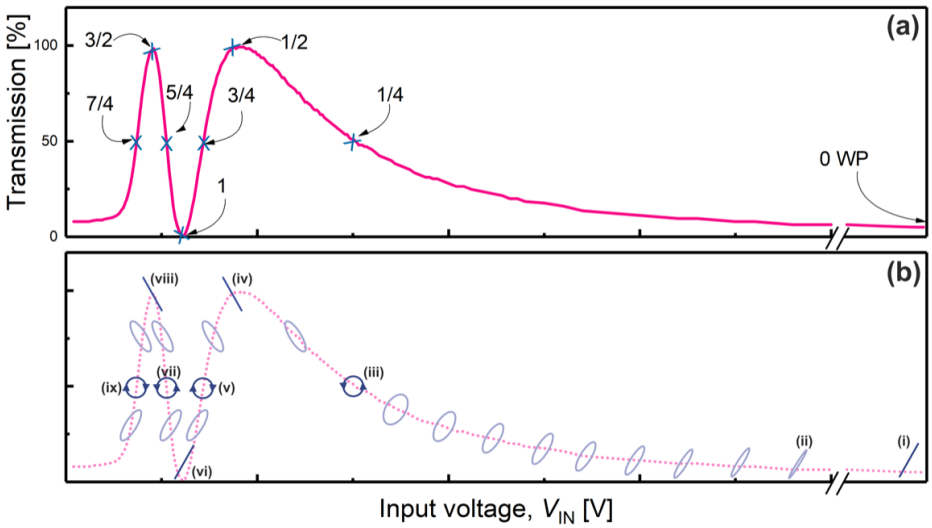


FIGURE 8.5: (**a**) A typical light transmission behaviour for transmission of a planar nematic LC device when it is placed between two crossed polarisers and a varying electric field is appled across the device. (**b**) Illustration of the corresponding polarisation states on the Fréedericksz transmission curve generated with a planar-aligned nematic LC device.

If the applied voltage is now reduced to a certain value such that the intensity of light is at a maximum (100%), it means that the polarisation state of the light after passing through the LC is now reoriented by 90° – this situation represents the $^1/_2$-WP condition and is indicated with $^1/_2$ in Figure 8.5 (a) (which corresponds to half-waveplate condition). The respective position on the transmission curve in Figure 8.5 (b) is labelled as (iv) and implies an inverted linear polarisation state. If the applied voltage is adjusted to between the 0-WP and $^1/_2$-WP conditions, the halfway point would correspond to the $^1/_4$ waveplate condition or a QWP that can convert linear polarised light into circularly polarised (Figure 8.5 (b) with label (iii)). Alternatively, if the applied voltage is adjusted to between the position for $^1/_2$-WP an 0-WP ($\neq$ $^1/_4$-WP), the polarisation state would be in between linear and circular polarisation states – i.e. an elliptical polarisation state. An example of such a situation is shown with the light blue ellipses in Figure 8.5 (b) (between

(i) & (iii)).

Starting from the 1/2 WP position, if the applied voltage is further decreased so that the light intensity is again reduced to zero transmission we end up with a full-waveplate $\left(\frac{\Delta n \times d}{\lambda} = 1\right)$ and is represented at '1' in Figure 8.5 (a). It implies that light passing through the LC device would have the same polarisation state as that before entering the device, Figure 8.5 (b), label (vi). As seen earlier, the halfway point between full waveplate (1-WP) condition and half waveplate (1/2) is now a three-quarter waveplate (3/4). Although, the 3/4-WP would give circularly polarised light, its handedness would be opposite to that obtained for 1/4-WP. Depending on the device thickness and optical anisotropy of LC, if the applied voltage is further reduced from the full waveplate condition, the device can behave as either a five-quarter waveplate (5/4), a three-half waveplate (3/2) or seven-quarters waveplate (7/4) as shown in Figure 8.5 (a & b).

8.1.2 A tuneable LC waveplate

In order to demonstrate the characteristics of a tuneable LC waveplate, a commercially-available, Instec, 5 μm-thick LC device with planar alignment was used. The cell gap was confirmed by studying the Fabry-Perot fringes as explained in Chapter 3. The device was filled with a well-studied nematic LC, E7, and then two wires were connected onto each of the electrodes of the device. A continuous wave He-Ne laser (JDS Uniphase, 632.8 nm, <4 mW), was used to study the Fréedericksz transmission characteristics of the LC device by using the free-space optical setup as shown in Figure 8.6 (a).

A neutral density filter wheel was used to control the intensity of laser for safety purposes. A polariser and an analyser were placed so that their optical axes were crossed, i.e. oriented 90° with respect to each other. The LC device was placed between the polariser and analyser with a device orientation ϕ = 45° with respect to the optical axis of the polariser and analyser. The translational position of the LC device was then adjusted such that the laser beam would pass through the active area. The laser passing through the analyser was then detected with a photodiode (Thorlab PDA36A-EC, ±12V/200mA) that was connected to the computer via an analogue-to-digital (A/D) converter (National Instrument USB-6008). The MATLAB built-in toolkit app, Analogue Input Recorder, was used to extract the data from the A/D converter.

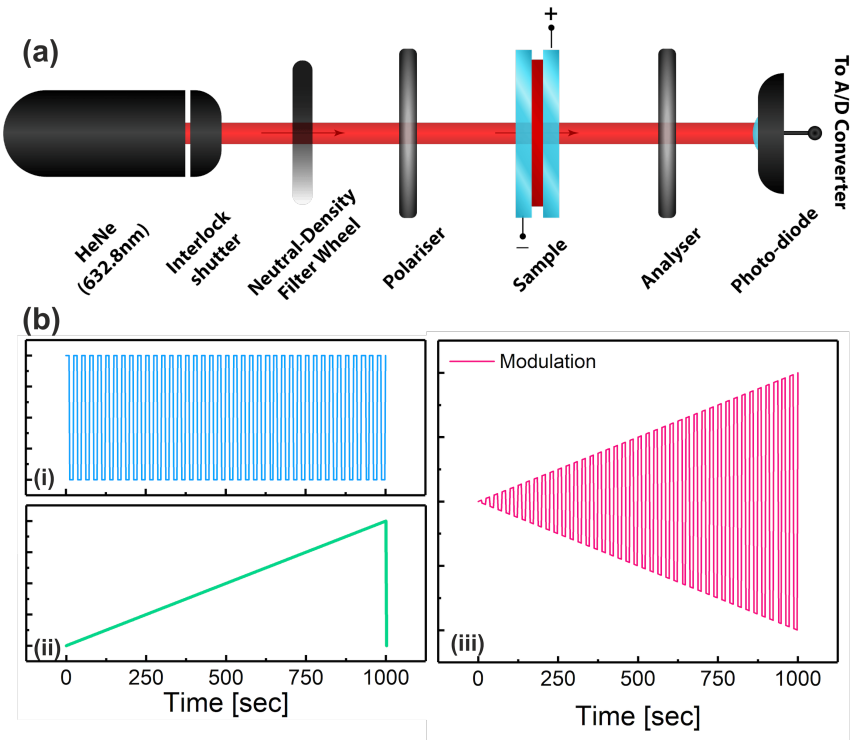


FIGURE 8.6: (**a**) The top view of the free-space optical setup used to study the Fréedericksz transmission characteristics of the nematic LC, E7 using CW 632.8nm He-Ne laser at 25°C. (**b**) Example of the voltage waveforms used to generate the modulation signal (i) 1 kHz square wave, (ii) the 1 mHz ramp was used to amplitude modulate (i) in order to generate (iii) the modulated signal.

The LC device was switched with a square wave signal at a fixed frequency of 1 kHz. In order to continuously increase the amplitude of the applied signal, the square wave was modulated with a ramp signal. The frequency of the ramp signal was chosen to be at a lower frequency of 1 mHz so that the LC director can switch completely and would allow a reasonable time for the A/D to sample the output correctly. Example signals, and their modulated output are shown in Figure 8.6 (b).

The modulation signal (square wave & ramp function) was applied to the LC device and the light intensity through the LC device was detected by the photodiode and recorded by the A/D converter as a photodiode voltage. The normalised output signal intensity as a function of applied voltage for one modulation cycle is shown in Figure 8.7. The variation in the level of voltage over one cycle (1 mHz) of modulation suggests a variation in the retardance of the LC due to the applied electric field. As explained earlier in Figure 8.5, the variation in the optical anisotropy is due to the tilt (θ) of the LC director and offers different levels of retardation for the components of the input light and as a result the output light has different polarisation states as indicated in Figure 8.5 (b). This

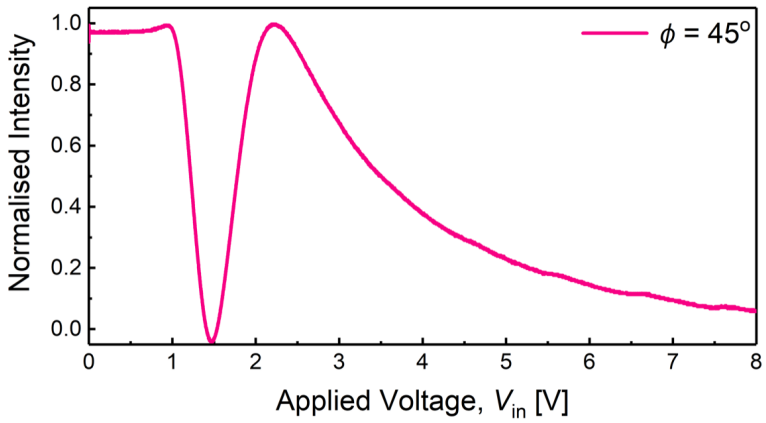


FIGURE 8.7: The Fréedericksz transmission behaviour of a planar-aligned LC device when placed between two crossed polarisers. A CW He-Ne at λ = 632.8 nm was used to study the behaviour of the LC device when a modulated electrical signal of 8V was applied across the device.

is how a LC device can be used to create any polarisation state and thus act as a tuneable waveplate.

To investigate directly the change in the polarisation states, the experimental arrangement shown in Figure 8.6 (a) was altered to a new scheme as depicted in Figure 8.8 (a). In the new arrangement, instead of using a single beam to study the polarisation state, two light beams, 1) Reference and 2) Signals were used to analyse and extract the polarisation states. The laser beam splits into a Signal beam and Reference beam by a 50:50 beam splitter. Both beams were then passed through two fixed polarisers, Polariser-1 & -2 to create linearly polarised light. The orientation of the optical axis of both polarisers were set to be the same. The Signal beam was then passed through the LC device that is connected to a waveform generator. Finally, both Signal and Reference beams were passed through a rotating polariser. The rotation of this polariser was controlled by a variable DC power supply. The laser beams were detected at their respective photodiodes that were separately connected to an oscilloscope and to the A/D converter. Since the input light is linearly polarised, after passing through the rotating polariser, a modulation signal (identical to a sinewave) was observed on the oscilloscope channel that was connected to Photodiode-2. Before taking any measurements, the alignment of the optical components was carefully adjusted. To achieve this, the LC device was first removed from the rig and the optical axes of both fixed polarisers was oriented so that the signals detected at both photodiodes were in-phase on the oscilloscope channel, Figure 8.8 (b). After achieving this, the LC device was inserted in the path of the Signal beam as

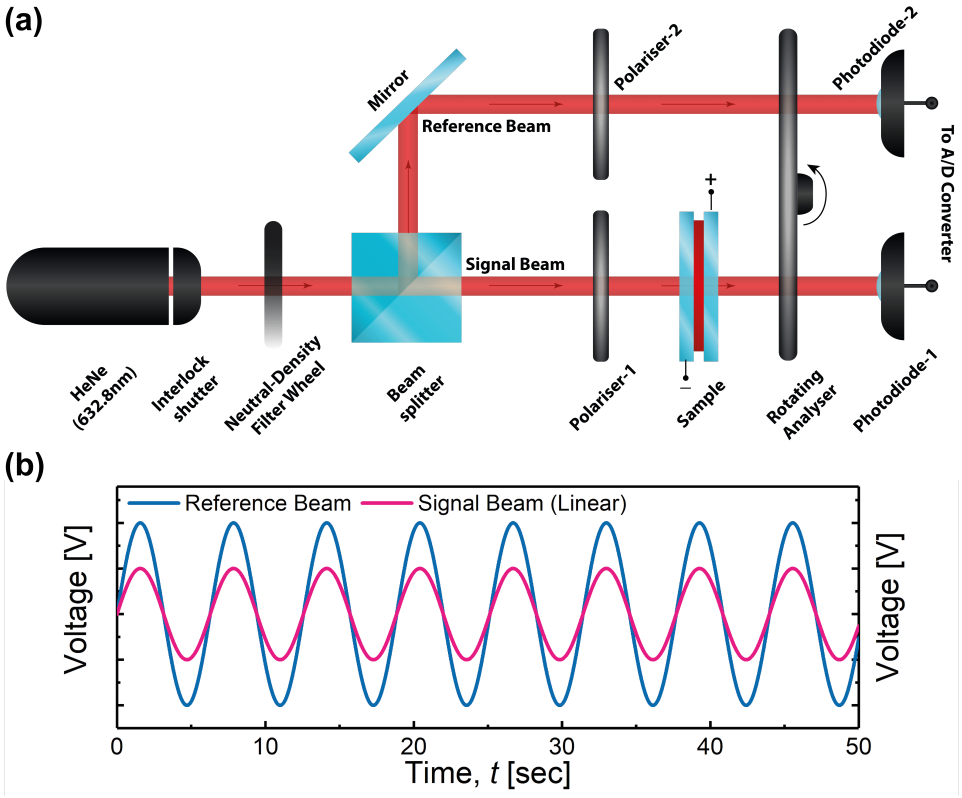


FIGURE 8.8: (**a**) Top view of the free-space optical setup used to study the Fréedericksz transmission characteristics of the nematic LC, E7 using a He-Ne laser at 25°C with a rotating analyser arrangement. The arrangement consists of Signal and Reference beams. (**b**) An example of the voltage recorded for the Reference and Signal beams for the initial experimental arrangement.

shown in Figure 8.8 (a). The LC device was placed by orientating the optical axis at 45° with respect to the optical axis of Polariser-1.

After setting up the experiment, a modulation signal (as shown in Figure 8.6 b (iii)) was applied across the LC device. The scan duration of the A/D converter was set to match with the period of the ramp function to record the data for one cycle of modulation signal. A low frequency (1 mHz) ramp function was used that allows the device to go through the transition slowly and lets the A/D record a suitable number of data points for a modulation cycle (recorded dataset is presented in C.1, Appendix C. The useful information was extracted from the dataset to analyse the polarisation states such as: 1) the phase-difference between Signal and Reference beams and 2) the variation in intensity of the Signal with respect to the Reference beam (i.e., the strength of modulation). Before analysing the data, it is important to understand the background.

The polarisation states created by the LC device (as seen in Figure 8.5 (b)) are

presented in further detail in Figure 8.9 (a). In order to understand the behaviour, again consider when the applied electric field reaches the maximum value, this means that the LC director attains the arrangement identical to homeotropic alignment and incoming light only sees one refractive index. In this case, the device does not change the polarisation state. Thus, the polarisation state of the Signal beam would match that of the Reference beam – after rotating the polariser, the signals for the Signal & Reference beams are detected to be 'in-phase'. As the applied voltage is reduced, the retardation of the LC device would also change and hence the polarisation state changes. The Signal beam after attaining circular polarisation state starts attaining the linear polarisation which has a phase-shift of $\pi/2$ with respect to Reference beam – this is refer to here as 'out-of-phase'. Example output polarisation states are labelled with 'IN' and 'OUT' for the in-phase and out-of-phase conditions, respectively, and are shown in Figure 8.9 (a).

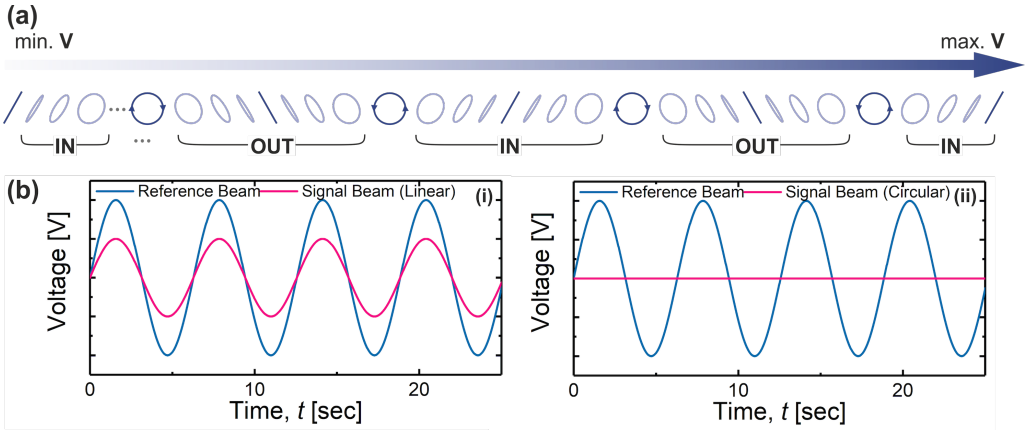


FIGURE 8.9: (**a**) Example polarisation states that can be generated with a planar-aligned LC device with the application of an electric field. (**b**) Example plots showing the Signal and Reference beams to extract the ellipticity in a polarisation state, that is, a (i) linear and (ii) circular state.

The modulation intensity of the Signal beam tells us about how much the polarisation state of the light is circular or linear in nature at a given voltage or alternatively the degree of ellipticity associated with each polarisation state. To understand this behaviour, two example situations are presented in Figure 8.9 (b) in order to compare the modulation intensity of the Signal beam and Reference beam. Figure 8.9 b (i) illustrates the case when the Signal beam has maximum modulation, which implies a linear polarisation state. However, in Figure 8.9 b (ii), the Signal beam has effectively no modulation in intensity, which indicates a circular polarisation state as the signal amplitude remains constant.

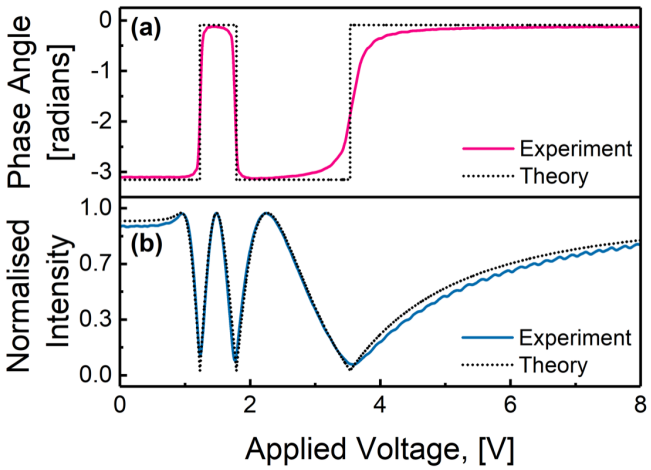


FIGURE 8.10: (**a**) Example polarisation states that can be generated with a planar-aligned LC device with the application of an electric field. (**b**) Example plots showing the Signal and Reference beams to extract the ellipticity in a polarisation state, that is, a (i) linear and (ii) circular state.

By using the abovementioned method, the phase difference between the Signal and Reference beams and the modulation intensity of the Signal beam can be extracted from the data recorded with A/D converter using a MATLAB script. The change in phase is presented in Figure 8.10 (a) with a solid line whereas the equivalent theoretical model is presented with a dotted line. When the applied voltage is a maximum (8V), the phase difference between the Signal and Reference beams is zero. As the applied voltage is reduced to 3.5±0.2V, a change in the phase is observed; the position where it occurs corresponds to the $^1/_4$ waveplate condition as seen in Figure 8.7. This implies that the polarisation of light has changed from linear to elliptical to circular and now elliptical, that is $\pi/2$ out-of-phase. The next change in phase is observed at about 1.75V when the Signal beam becomes in-phase with the Reference beam; this corresponds to the $^3/_4$-waveplate condition in Figure 8.5. The Signal then remains in-phase with the Reference until the applied voltage reaches 1.25V, after that the Signal beam is again out-of-phase, this is equivalent to $^5/_4$-waveplate condition in Figure 8.7 after that the Signal beam remained out-of-phase.

The modulation intensity of the Signal beam is presented in Figure 8.10 (b), the Signal intensity varies as the phase between the Signal and Reference beams changes. The modulation is minimum (close to zero) at 3.5V when the light becomes circularly polarised and therefore no modulation is observed. Similarly, minimum modulation in

intensity is observed at 1.75V and 1.25V, corresponding to 3/4- and 5/4-waveplate conditions, respectively – a circular polarisation state. In contrast, the intensity modulation is maximum at 2.25V; this corresponds to the 1/2-waveplate condition. Ater passing through a HWP the light has a linear polarisation, therefore a maximum modulation in intensity is seen. Likewise, a maximum modulation in intensity of the Signal beam is seen at 1.5V and 1.0V, corresponding to 1- and 3/2-waveplate conditions, respectively.

To demonstrate the behaviour at other angles, the LC device is oriented to a number of different angles such as $\phi = 0^\circ$, 11.25°, 22.5°, 33.75°, 56.25°, 67.5°, 78.75° and 90°. For each orientation of the LC device, the Fréedericksz transmission characteristics of the device were studied using the same setup as shown in Figure 8.6 (a) while the phase difference and the modulation in the Signal beam was recorded and extracted using the experiment presented in Figure 8.8 (a). These results are presented in Figure 8.11.

The intensity of the Fréedericksz transmission (that is, the light intensity after passing through the LC device) can be understand in terms of equation 8.2 (9.2)

$$T = \sin^2(2\phi) \times \sin^2\left(\frac{\pi d n(\theta, \phi)}{\lambda}\right) \tag{8.2}$$

where ϕ is the orientation of the optical axis with respect to the input polarisation. When $\phi = 45^\circ$, a maximum intensity is achieved, which is seen in Figure 8.7. However, when ϕ varies, the intensity reduces by the factor that is given as $\sin^2(2\phi)$ and is observed in Figure 8.11 (a – h) (for each sub-figure labelled as 'i'). It is important to note that the intensity is reduced to almost zero when $\phi = 0^\circ$ or 90°; in this condition the LC layer is aligned with the polariser axis and does not affect the polarisation of the incoming light, as incoming linear polarised light only sees one of the refractive indices.

Similarly, the phase difference between the Signal and Reference beams is presented in the sub-figure (ii) of Figure 8.11. The change in the phase difference occurs at the applied voltages for which the device changes its waveplate condition. For example, in case $\phi = 33.75^\circ$ at 1.5V, the LC device acts as a full-waveplate, and therefore the phase difference is zero. Also, it can be seen from the phase difference plot that the change in phase for the orientation of the LC device $0^\circ \leqslant \phi < 45^\circ$ is positive, whereas it is negative for $45^\circ < \phi \leqslant 90^\circ$.

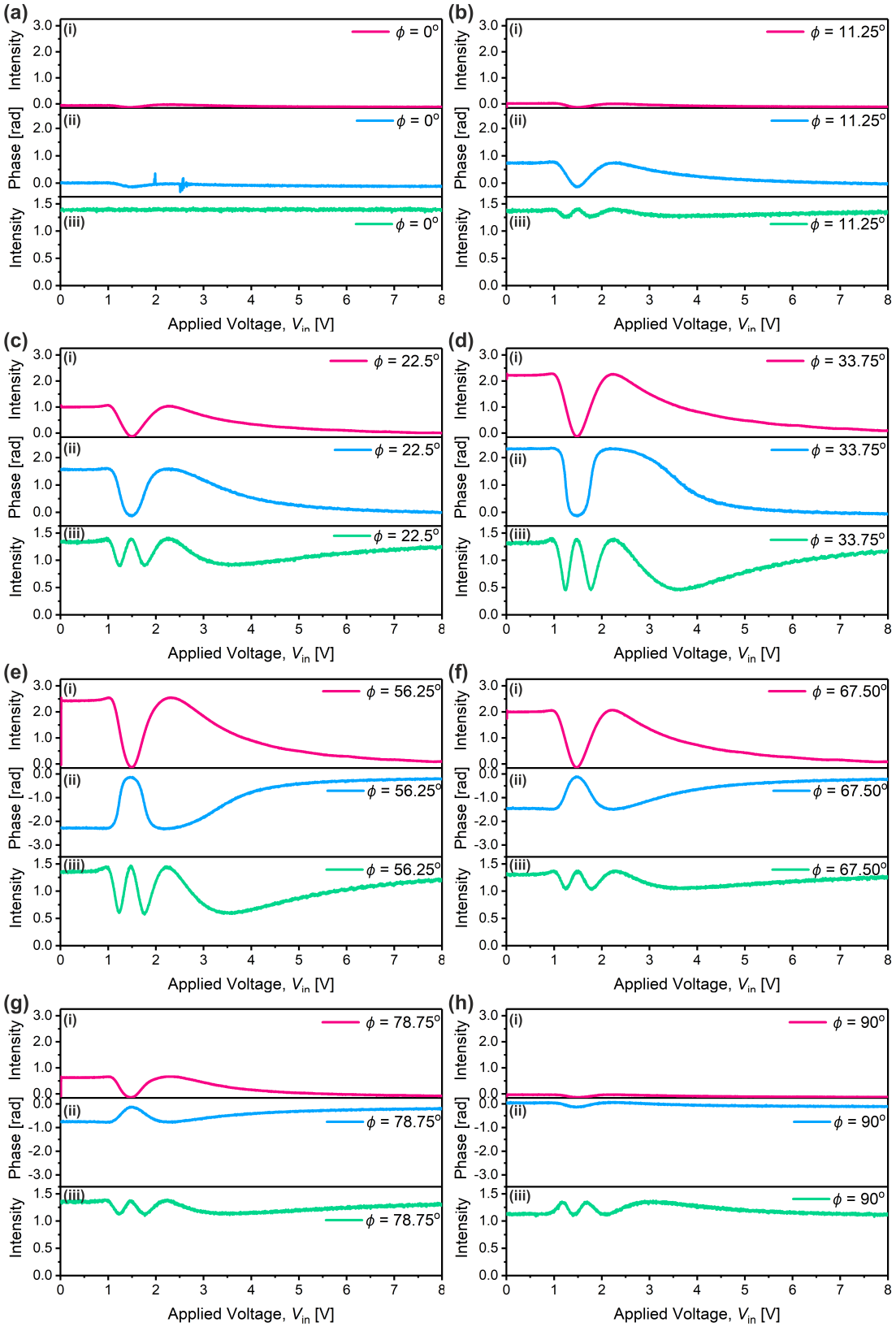


FIGURE 8.11: The polarisation study of the He-Ne (632.8nm) laser after passing through a 5μm LC device when a modulated signal is applied across the device and device is placed at different orientation (ϕ). Sub-figures show the (i) Fréedericksz transmission curve, (ii) phase difference between Signal and Reference beam and (iii) modulation intensity of the Signal beam.

The modulation is also presented in sub-figure (iii) of Figure 8.11, which follows the behaviour as explained in Figure 8.10 (b). The variation in the modulation intensity is more obvious when the orientation of the LC device is close to $\phi = 45^{\circ}$, however it follows the expected behaviour. That is, the applied voltage where the device gives rise to a circular polarisation exhibits no modulation in the intensity; however, for the position where it has a linear polarisation, a maximum modulation in the intensity is seen. For example, for $\phi = 33.75^{\circ}$, the device acts as a $1/4$-waveplate at 1.75V, and therefore the modulation intensity is minimum, whereas it behaves as a $1/2$-waveplate at 2.25V and therefore has a maximum modulation. For the device angle close to $\phi = 45^{\circ}$, in which, light changes the polarisation states after passing through the LC device. However, when the device is placed $\phi = 0^{\circ}$ or 90°, the modulation curve is constant, i.e., this implies that the LC device does not change the polarisation state of the input light (which was linearly polarised).

The planar LC device has been shown to produce a polarisation state from linear, elliptical to circular and so on when a varying electric field is applied across the device. The change in the polarisation state is a result of a variation in the optical retardance of the device. While an arbitrary polarisation state can be produced by changing the retardance of the LC device, the orientation of the given polarisation state remained fixed, therefore, the LC device is needed to be oriented through a certain angle ϕ to achieve the polarisation state in the desired orientation. The orientation of polarisation can nevertheless be controlled electrically, which is explained in following section.

8.2 In-plane switching device

As seen in the previous section a planar-aligned nematic LC device can act as tuneable waveplate when a transverse electric field is applied across the device. In this case, it is possible to vary the polarisation state depending on the retardation introduced by the LC layer. The orientation of the polarised light however is arbitrary and depends on the optical axis of the LC director, that is, the orientation angle of device. As seen previously, the orientation can be changed if a planar-aligned nematic LC device is physically re-oriented to a specific angle to attain the polarisation state in a particular direction. In order to electrically control the orientation of the polarised state, here we propose

another type of device configuration. Instead of using a planar aligned nematic LC with a transverse electric field, the proposed device uses an in-plane electrode configuration with a homeotropically-aligned nematic LC. A typical in-plane electric field and corresponding switching mechanism of an in-plane switching (IPS) is illustrated in Figure 8.12.

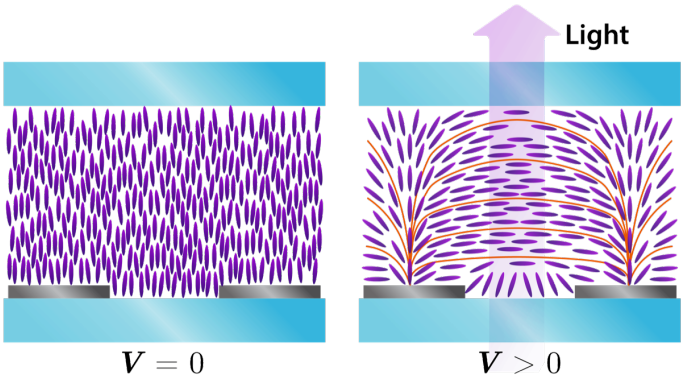


FIGURE 8.12: An example illustration of the different polarisation states generated at various orientation angles ($0° \leqslant \phi \leqslant 360°$) by varying the voltage across the LC device.

When $E = 0$, the LC director adopts a homeotropic alignment as shown in Figure 8.12 (a). When such a device is placed between a crossed polariser and analyser pair, and then illuminated with light, no transmission is observed as the incoming light only sees one of the refractive indices. However, when $E > 0$ (Figure 8.12 (b)), and for a nematic LC with a positive dielectric anisotropy, the LC director tilts under the influence of the electric field. This results in a change in the optical path length ($\Delta n_{eff} \times d$) of the LC device and therefore, light can transmit through and is seen as a bright state when the applied field is greater than the threshold voltage of the device, which is given as [358]:

$$E_{th}^{IPS} = \frac{\pi}{d}\sqrt{\frac{K_{IPS}}{\epsilon_o|\Delta\epsilon|}} \tag{8.3}$$

where E_{th}^{IPS} is the threshold electric field required to drive the LC, d is the cell gap, K_{IPS} is elastic constant of LC, which is a combination of splay, bend and twist deformations, ϵ_o is the vacuum dielectric constant and $\Delta\epsilon$ is dielectric anisotropy of the LC. For IPS switching, four identical electrodes were designed to achieve in-plane switching by applying different combinations of voltages.

The device layout showing the top view of the electrodes is shown in Figure 8.13 (a). When four independent voltages are applied at each electrode, they generate an electric field in a particular direction that can then switch the LC device. To understand

this, example images are presented in Figure 8.13 (b – d) when combinations of voltages were selected as so to generate an electric field and switch the LC in either the horizontal or vertical directions referred to here as $\psi = 0°$, $90°$ or $+45°$ with respect to the $+x$-axis.

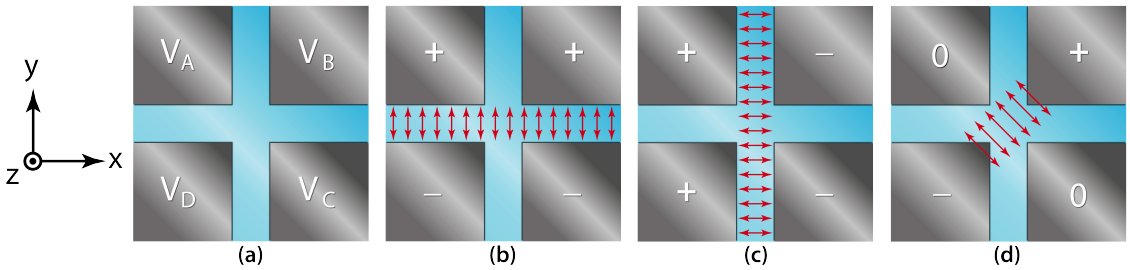


FIGURE 8.13: (**a**) The in-plane electrode assembly with four patterned electrodes. Each electrode is electrically isolated with voltage V_A, V_B, V_C and V_D. Example images showing three situations for generating an electric field in direction (ψ) (**b**) $0°$, (**c**) $90°$ and (**d**) $+45°$ direction by applying different combinations of voltages to the electrodes.

The magnitude and polarity of the applied voltages on the electrodes are critical in terms of generating the electric field along a certain orientation. It is therefore important to estimate the applied voltages on the electrodes. For this, consider the electrode assembly as shown in Figure 8.13. For simplicity, consider that the voltages at the corner of each electrode are V_A, V_B, V_C and V_D and that the electrode gap is 'l'. The desired field to be generated at the centre region is $\boldsymbol{E} = \boldsymbol{E}_x + \boldsymbol{E}_y$ where $\boldsymbol{E}_x$ and $\boldsymbol{E}_y$ are the electric fields along the x and y directions, respectively and are given as:

$$\boldsymbol{E}_x = E_i \cos(\psi) \tag{8.4}$$

$$\boldsymbol{E}_y = E_i \sin(\psi) \tag{8.5}$$

where ψ is the orientation with respect to $+x$-direction of the desired field and E_i is the target field required. Using these expressions, the voltage at each electrode is approximated as:

$$V_A = \frac{l}{2}\Big(- E_x + E_y \Big) \tag{8.6}$$

$$V_B = \frac{l}{2}\Big(E_x + E_y \Big) \tag{8.7}$$

$$V_C = \frac{l}{2}\Big(E_x - E_y \Big) \tag{8.8}$$

$$V_D = \frac{l}{2}\Big(- E_x - E_y \Big) \tag{8.9}$$

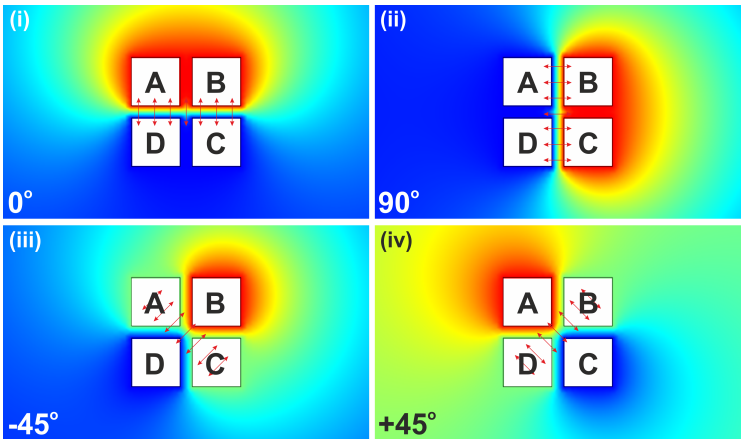


FIGURE 8.14: COMSOL Multiphysics model for IPS device with four electrodes **A**, **B**, **C** and **D** so as to generate an electric field at the following orientations (ψ): (**i**) 0°, (**ii**) 90°, (**iii**) -45° and (**iv**) +45° with respect to the $+x$-direction when different combinations of voltages were applied to the electrodes.

Using equations (8.4 – 8.9), the voltage on each electrode can then be estimated to create an electric field along a desired orientation. In this regard, an equivalent COMSOL Multiphysics model for the IPS device was created and simulated to demonstrate the electric field along various orientations ψ = 0°, +45°, 90°, -45° (with respect to $+x$-direction) , and example simulation results are presented in Figure 8.14. It can be seen that the field in the vertical orientation (i.e., along 0°) is generated when $V_A = V_B$ and were set to positive values whereas $V_C = V_D$ were set as negative voltages, Figure 8.14 (i). For the +45° case, $V_A = V_D = 0$V, $V_B = +$V, and $V_C = -$V, Figure 8.14 (iv). This implies that by correctly choosing the combinations of voltages, the electric field can be generated in a certain orientation.

8.2.1 IPS Device Preparation

After estimating the voltages and running the model for the IPS device, the four-electrode IPS device configuration (as shown in Figure 8.13) was fabricated using the process illustrated in Figure 8.15. The device was fabricated using commercially available indium tin oxide (ITO) coated glass substrate to form the patterned electrodes. The process began by ultra-sonication of the ITO substrates in acetone for 20 min at 25°C to remove any organic components. Any residual particles on the surface of the substrate were removed with an optical tissue dipped in acetone as shown in Figure 8.15 (ii). The substrate was further treated with O_3 plasma for 4 min at 25°C before coating the photoresist. A positive photoresist (Microposit S9-1813) was spun coated on the ITO substrate at 400rpm for 45 sec. The substrate was left on the spin coater for a couple of

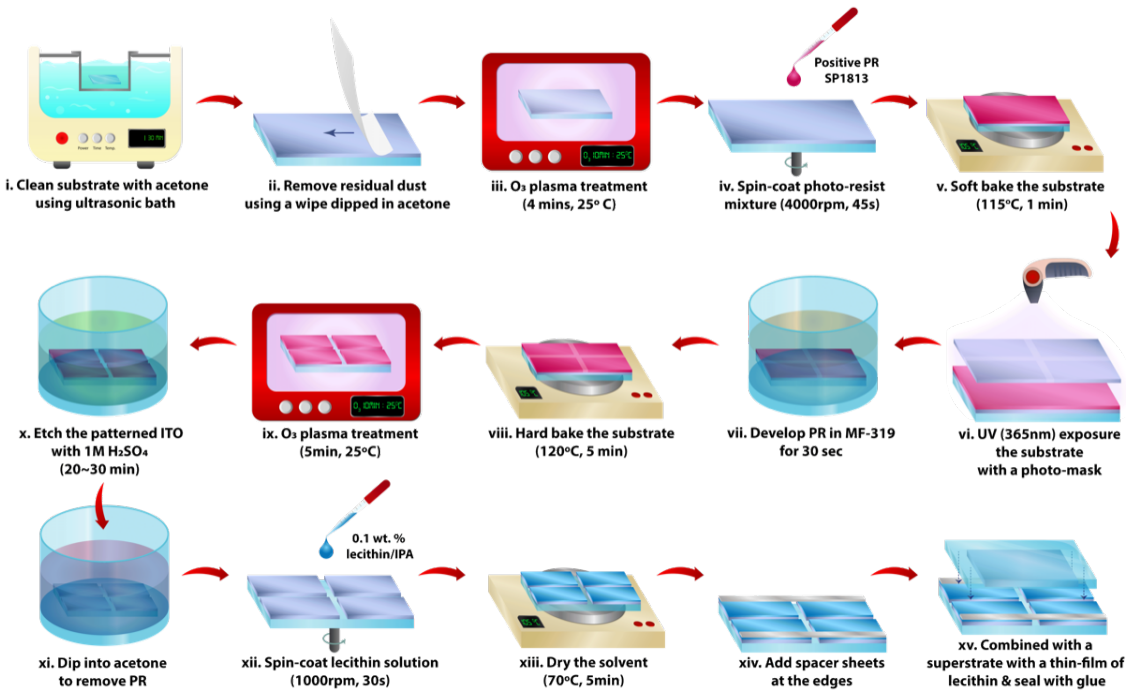


FIGURE 8.15: Illustration of fabrication process for the four-electrode in-plane switching (IPS) device using photolithography. The IPS substrate was created by patterning an ITO substrate with a photo-resist, which was followed by wet etching of the ITO before the application of lecithin to create a homeotropic aligned nematic LC cell.

minutes to let it dry before it was transferred to a hot-plate where it was soft baked at 115°C for 60 sec, Figure 8.15 (iv – v). Once a thin film of photoresist had been deposited, a glass-chrome mask was placed above the photoresist-coated ITO substrate and irradiated with UV light (365 nm) for 60 sec at 15 mW/cm^2 as shown in Figure 8.15 (vi). The substrate was then dipped into a developer (Microposit MF-319) for 30 sec at 25°C. Since the photoresist is a photo sensitive compound, and as it was a positive photoresist, the regions that were exposed to UV radiation underwent chemical changes and when the substrate was immersed into the developer, those areas interacted with the developer and were removed to form the desired pattern with the photoresist. The substrate was then hard baked on a hot plate at 120°C for 5 mins followed by O_3 plasma treatment to remove any residual developer/reacted photoresist, Figure 8.15 (vii – ix).

The substrate was then studied under a fluorescence microscope to confirm the desired pattern had been obtained without any defects. The substrate was then immersed into a 0.1M HCl solution, which was prepared by mixing 36.5 % HCl ACS Regent into deionised water. The device was left in HCl solution to etch the ITO between the photoresist pattern. The substrate was then taken from the HCl solution and thoroughly rinsed

with water and dried with nitrogen air. Using a digital multi-meter, the impedance of the etched region was studied to see if the ITO had been completely etched (Figure 8.15 (x)). It was found that the ITO was etched after immersing the substrates into HCl for 20-30 min. The substrate was then held and dipped into acetone solution for 15-20 sec to remove the remaining photoresist, Figure 8.15 (xi). The substrate was then dried with a nitrogen gun and 0.1 wt. % solution of lecithin in isopropyl alcohol (IPA) was dispensed and spin coated on the substrate at 1000 rpm for 30 sec; this was was followed by drying the host solvent on a hot plate at 70°C for 5 mins, Figure 8.15 (xii - xiii).

Another clean glass substrate was prepared by spin coating lecithin. Thin strips of spacer sheets of 45μm thickness were added at the edges of the patterned ITO substrate (Figure 8.15 (xiv)) and combined with the glass substrate (that has a thin film of lecithin). Glue was applied to the edges of the substrates to hold them together. The device thickness in the central region was inspected with the UV-Vis spectrometer and found to be 50 $\pm$ 2μm. The LC mixture was then injected into the cell and the device was left on a flat surface for a couple of hours to allow the LC director to adopt a uniform homeotropic alignment. Finally, four electrical wires were connected to the electrodes. To confirm the alignment of the LC, the device was observed between crossed polarisers on an optical polarising microscope and a dark field of view was observed, which is expected from homeotropic aligned nematic LC.

After creating the IPS device, the electro-optic switching behaviour was investigated by generating an electric field along a certain orientation. To test this, the device was observed between crossed polarisers on an optical polarisation microscope and each electrode of the device was connected to a waveform generator (FLC WFG 500) that can generate a square wave of 100 kHz up to $\pm$100V. The square wave voltages were applied to the electrodes had same phases; however, a possible alternative is to add phase change between these voltages. The frequency of the device was optimised to 100 kHz as it was observed that at this frequency the defects were minimum. A four-channel oscilloscope was also used to test the level of each signal from the waveform generator to confirms the peak amplitude of the applied voltage. A combination of voltages was chosen such that the central region between the electrode areas switched ON by creating a field along field along $\psi = 45°$. The magnitude of the voltages was varied to estimate the threshold

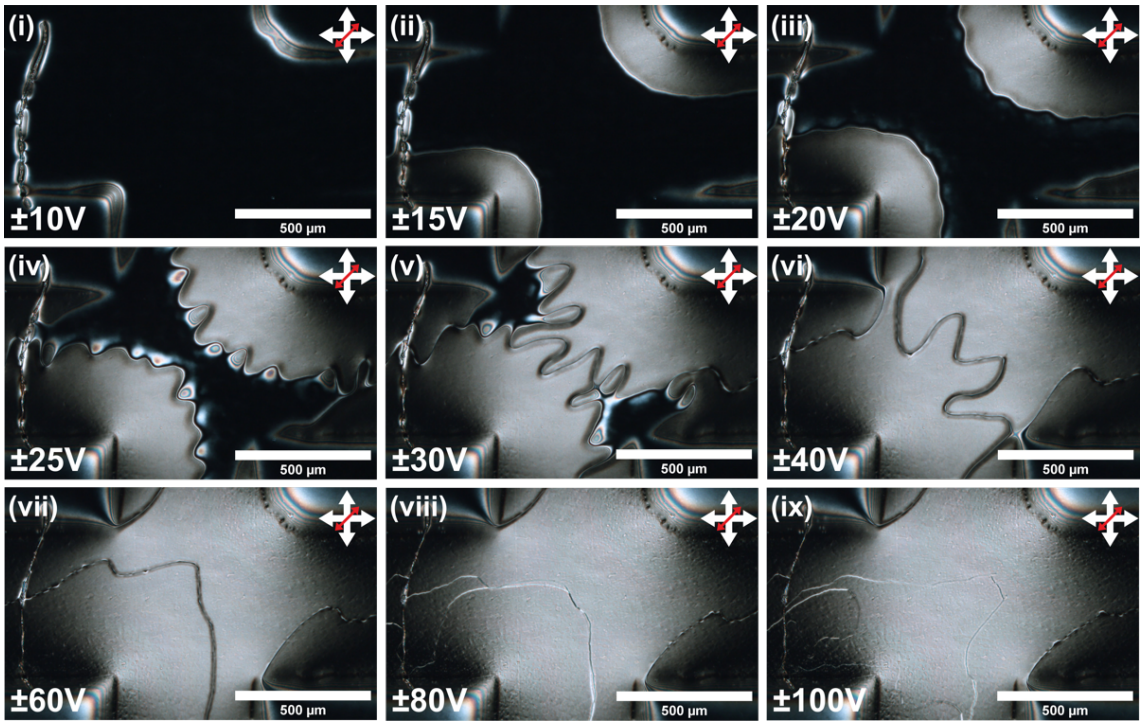


FIGURE 8.16: Optical polarisation microscope images of the IPS device used to estimate the threshold voltage to switch the device. Images were taken with the optical axis of the device at $\psi = 45^\circ$ to the transmission axes of the polariser and analyser. Measurements were conducted at 25°C and the amplitude of the applied voltage is labelled on each image. The scale bars are 500 μm.

voltage required to switch the device.

Figure 8.16 shows the optical polarisation microscope images when different levels of voltages were applied at the electrodes to create an electric field that was oriented at $\psi = 45^\circ$. It was found that the device showed switching at the electrode edges when $\pm$10V was applied but the complete region was switched when the applied voltage was between $\pm$30 and $\pm$40V, Figure 8.16 (v – vi). Furthermore, a defect line also appeared in the central region that settles down within a few minutes time after the application of an electric field. This defect line appeared due to the asymmetric tilt of the LC director; that is, the LC director in the region left of the defect line may tilt in one direction (say clockwise) when the field was applied whereas the LC director on the right side of the defect line tilted in the opposite direction and thereby a defect appeared where the two domains meet. These defect lines can affect the wavefront of the light and voltages were adjusted so as the defect could move towards the corner region.

The next stage was to confirm that the device can generate an electric field along any orientation. To confirm this, the voltages that were estimated using equations (8.4 –

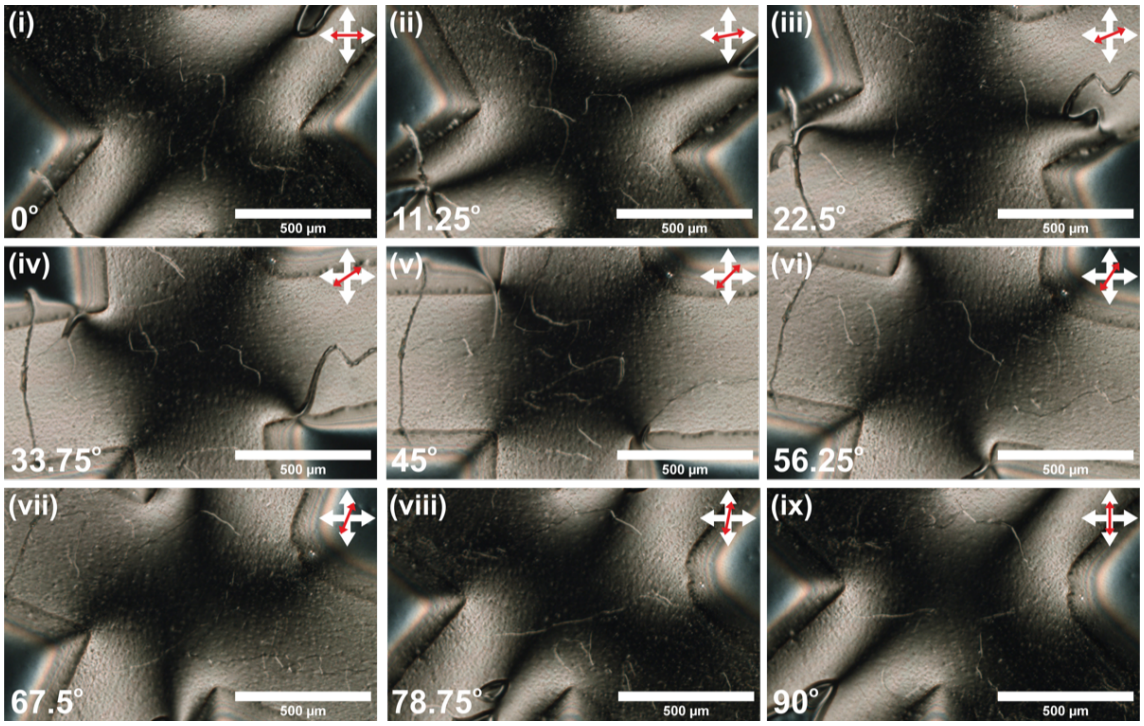


FIGURE 8.17: Optical polarisation microscope images of the IPS device when different combinations of electric field were applied across the electrodes and the device was rotated through an angle (χ) so that the switched region turned dark field. The rotation angle (χ) of microscope corresponds to the angle (ψ) along which the electric filed is generated and represented with a red arrow in each sub-figure. The scale bar reads 500mum.

8.9) to generate fields along a certain direction from $\psi = 0° \sim 180°$ were applied to the four electrodes of the IPS device. The voltage combination was applied to attain the field in the desired orientation and to observe this, the microscope stage on which IPS device was placed was rotated through an angle (χ) until a dark state was seen in the central region that corresponds to the desired orientation. The angle χ at which the extinction was seen corresponds to the field orientation ψ. The optical polarisation microscope images are presented in Figure 8.17 and show that by adjusting the voltage combination to the electrodes, an electric field can be generated along a certain direction (ψ) in the centre of the electrode region. Table C.1 summaries the values of the voltages required to generate the field in different orientation and is presented in Appendix C.

8.2.2 Polarisation controllability with an LC IPS device

As seen in the previous section, the IPS device can generate an electric field along any orientation (ψ) when a certain combination of voltages are applied to the electrodes. This demonstrates that we can now control both the polarisation state of the light (e.g. circular, linear etc.) and the orientation of the polarisation. To demonstrate this, the

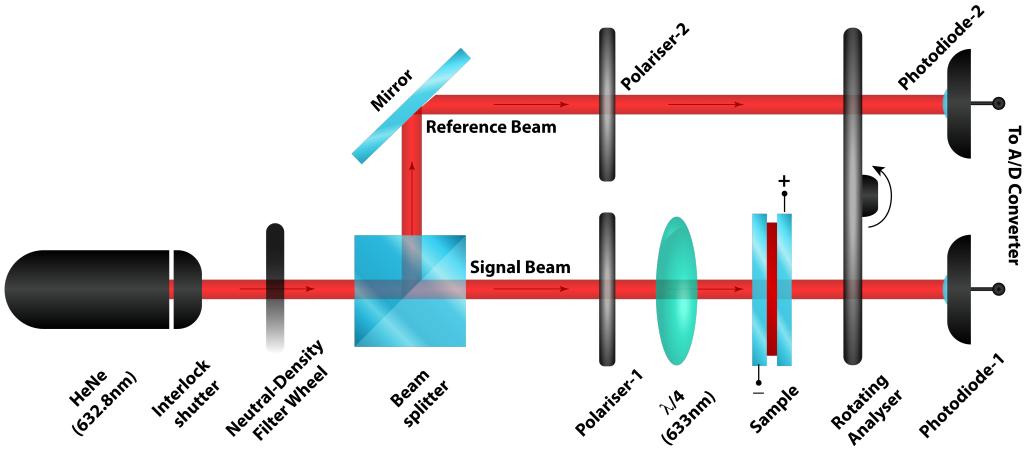


FIGURE 8.18: Top-view of the free-space optical setup used to study the polarisation state and orientation of light using an IPS device.

IPS device was placed in the experimental rig as shown in Figure 8.18, which also has the addition of a quarter waveplate (QWP) for 632.8 nm in the setup shown in Figure 8.8 (a). The QWP converts the input linear polarised light into circular and is relevant for the later demonstration of the LC-based polarisation controllable laser.

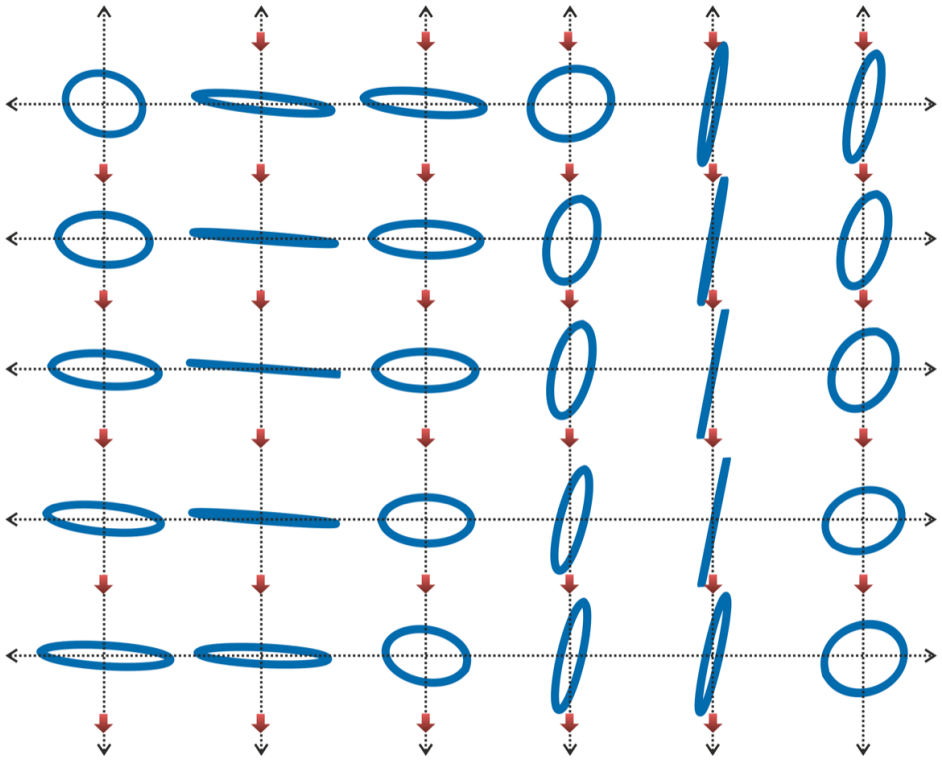


FIGURE 8.19: The polarisation states generated with the IPS device by apply a varying voltage so as to create an electric field oriented at $\psi = \pm 45^{\circ}$, where horizontal and vertical axes are x and y component of the light intensity in the polarisation ellipses, respectively.

In §8.2, the polarisation states were obtained by applying a modulated signal;

however, in the current setup a fixed combination of voltages were applied to each electrode. For each combination of electric field, the polarisation states were recorded via the A/D converter and then numerically extracted (example Signal and Reference waveforms recorded at circular, elliptical and linear polarisation are shown in Figure C.2, Appendix C. Since this IPS device can generate any polarisation state with a particular orientation, to demonstrate this, a combination of voltages was chosen so as to generate an electric field at $\psi = 45^\circ$ so as to give an orientation of the polarisation at 0° and 90° and then the magnitude of the field was varied to change the retardance of the LC layer and hence change the polarisation state from circular, elliptical, linear and so on. Alternatively, to achieve an electric field along 0°, the voltages at the electrodes were set as $V_A = V_B = +\text{V}$, $V_C = V_D = -\text{V}$ and for the field along 90°, $V_A = V_C = +\text{V}$, $V_B = V_D = -\text{V}$. After this, the voltages were varied to change the retardance of the LC and thereby the polarisation state. The results of the polarisation states that were generated with the electric field along the $\psi = +45^\circ$ orientation (with respect to the $+x$-direction) are presented in Figure 8.19.

It can be seen that the polarisation state starts from being circular (of one handedness) before changing to elliptical and then linearly polarised as the voltage amplitude is increased. While the different polarisation states are achieved by changing the magnitude of the applied electric field along the $\psi = \pm 45^\circ$ direction, there appeared to be some deviation of the orientation of the generated polarisation state. Theoretically, the electric field along the $\psi = \pm 45^\circ$ direction should result in linear polarisation along 0° and 90°. However, the experimentally generated (linear) states (as shown in Figure 8.19) deviated from theoretical predictions by $\pm 3^\circ$. This small discrepancy may be due to the non-uniform electric field distribution in the region where the laser passes through the device. One of the reasons for the non-uniform electric field could be the non-symmetrical shape of the fabricated ITO electrodes.

The next stage was to change the orientation of the electric field to demonstrate the manipulation alter the orientation of the polarisation state. Instead of presenting a detailed set of polarisation states at each orientation angle, the results are demonstrated as a 'constellation of polarisation states' and is presented in Figure 8.20 which can be thought of as a two-dimensional Poincaré sphere. The orientation of the polarisation

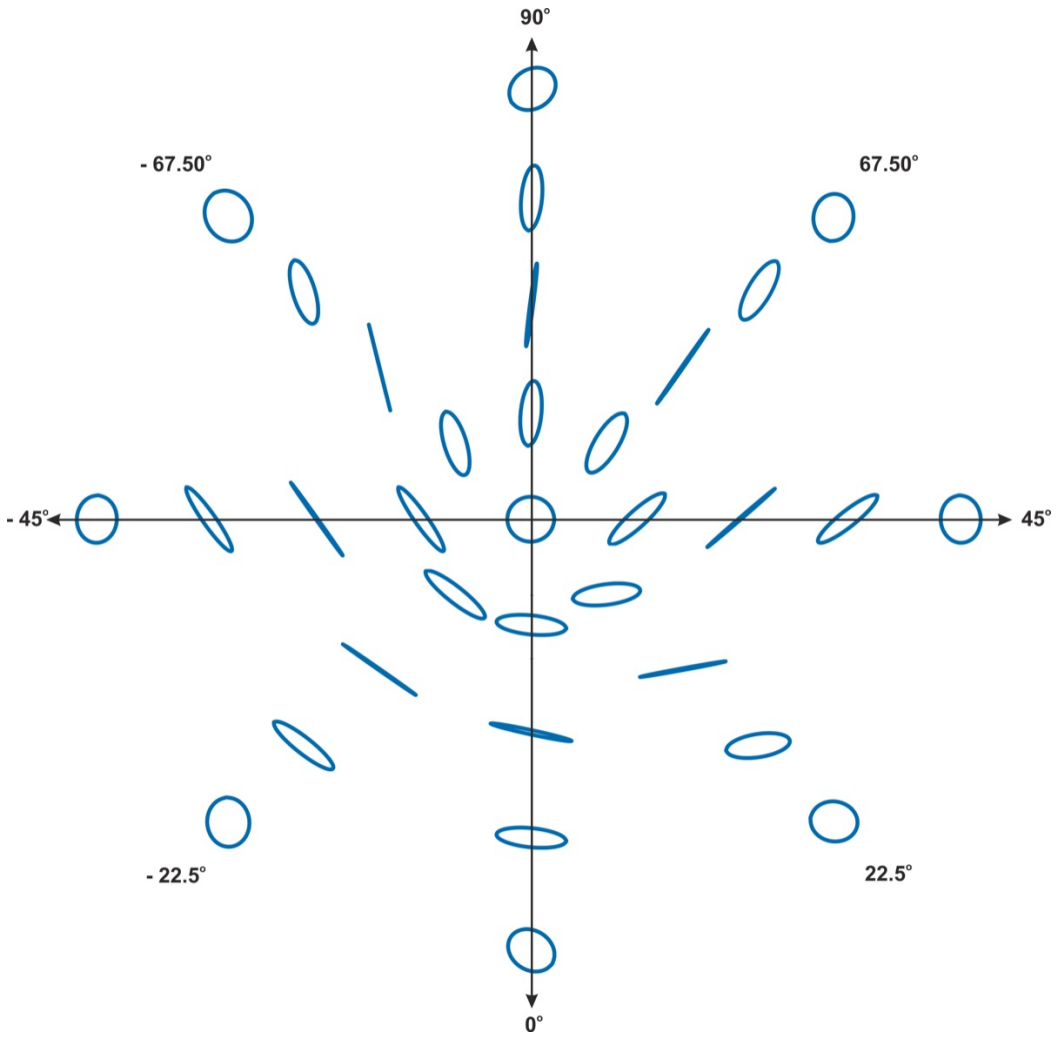


FIGURE 8.20: The constellation showing the different polarisation states of the He-Ne laser after passing through the nematic LC filled into an IPS device. The various polarisation states were created by selecting the necessary combination of voltages to define the orientation of the polarisation states whereas the magnitude of the applied electric field defines the actual polarisation state.

states was generated at $0°$, $22.5°$, $45°$, $67.5°$, $90°$, $-67.5°$, $-45°$, and $-22.5°$. While the field was applied to create the orientation of the polarisation states at the chosen angles, the experimental results showed some level of deviation from the orientation at the said angles. This may be due to imperfection in the symmetry of the four electrodes or a slight deviation of the applied voltage from the waveform generator or a combination of both factors.

8.3 Polarisation Controllable Band-Edge LC Laser

As seen in the last section, the IPS device can control both the orientation of the polarisation and the polarisation state through the combination of applied voltages. This

can now be used to demonstrate the polarisation controllability of either a LC band-edge or defect-mode laser. Since the fabrication process of a dye-doped LC band-edge laser is rather straightforward compare to a LC defect-mode, a band-edge LC laser is prepared and used to demonstrate the polarisation controllability; the illustration of the concept is shown in Figure 8.21. A defect-mode LC laser can also be employed to demonstrate the polarisation manipulation with an IPS device. Band-edge LC lasers are explained in detail in Chapter 2. In summary, a LC band-edge laser comprises a suitable gain-medium, such as a laser dye, dispersed into a chiral nematic LC. In principle, the gain material is chosen so that its peak PL emission wavelength overlaps the long-wavelength edge of the photonic bandgap. When the band-edge LC device is optically pumped, single mode laser emission is achieved at the edge of the bandgap.

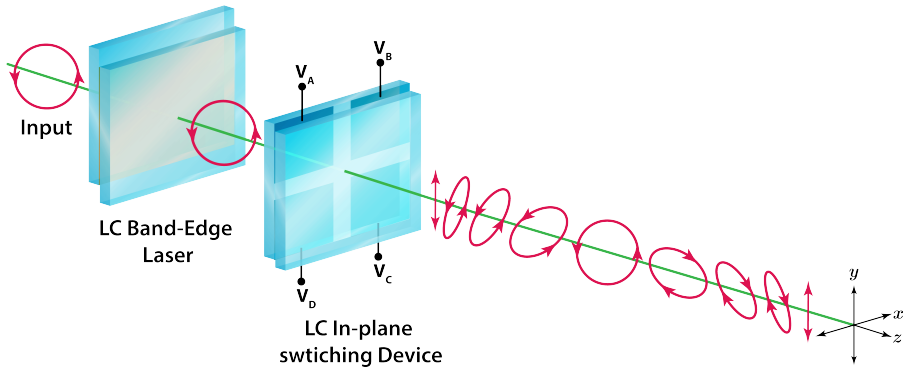


FIGURE 8.21: An illustration depicting the polarisation and orientation controllability of a band-edge LC laser with an in-plane switching (IPS) nematic LC device.

In order to demonstrate control of the polarisation state, a LC band-edge laser was prepared using the laser dye, PM597. The chiral nematic LC was prepared by doping the nematic LC, E7, with 3wt. % of the chiral dopant R5011. The concentration of chiral dopant was chosen so that the long-wavelength edge of the photonic bandgap overlapped with the peak emission of the laser dye (λ = 585 nm depending on host). To begin with, E7 (97 wt.%) and R5011 (3 wt. %) were added to a vial by carefully measuring their weights using a precision microbalance. The mixture was then heated to the isotropic phase (70°C) while constantly being stirred at 200 rpm for 24 hours. To confirm that the constituents had mixed as well as the position of the bandgap, a small quantity of the mixture was added into an Instec 5 μm-thick cell. The sample was then inspected with an optical polarising microscope equipped with a reflection arm using white light;

an example image is presented in Figure 8.22 (a). The sample showed a Grandjean texture with disclination lines as expected from the uniform standing helix. The average mono-domain area was about 400 μm^2 which is greater than the size of the pump laser beam (325 μm^2).

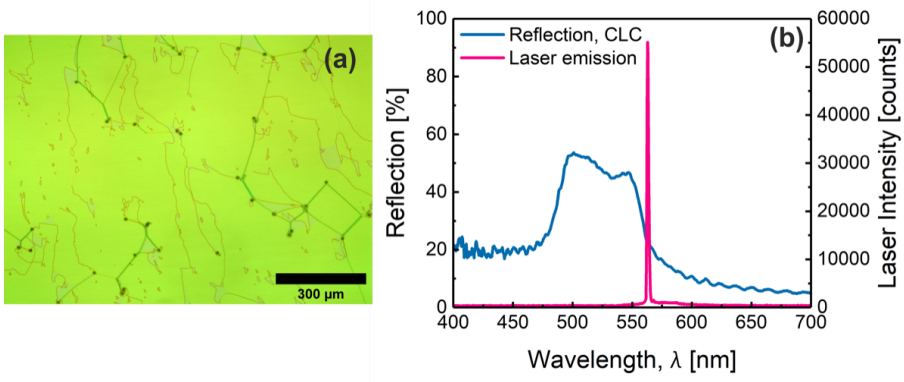


FIGURE 8.22: (**a**) Optical polarising microscope image (viewed in reflection) of the chiral nematic LC phase showing a Grandjean texture, (**b**) the reflection spectrum of the dye-doped chiral nematic LC sample (the primary axis, blue line) exhibiting a photonic bandgap centred at 525 nm and the single-mode laser emission at the long-wavelength band-edge (the secondary axis, red).

The chiral nematic LC mixture was then doped with the laser dye PM597. This was achieved by adding 1 wt. % of PM597 into the E7+R5011 mixture and a homogeneous mixture was obtained by stirring the mixture for 24 hr at 25°C at 200rpm. The mixture was then filled into an Instec 5 μm-thick planar-aligned glass cell. The reflection spectrum from the dye-doped chiral nematic LC was studied with white light using the free-space optical setup as shown in Figure **??**, Chapter 3 and is presented on the primary axis in Figure 8.22 (b). The central wavelength λ_C = 525 nm that corresponds to the reflected colour (green) from the chiral nematic can be seen in the optical microscope image in Figure 8.22 (a).

The emission characteristics of the device were studied with a pulsed Nd:YAG laser (532 nm, 10 Hz) using the optical rig as presented in Figure 3.23, Chapter 3. The device showed a single mode laser emission peak at 562 nm with a FWHM of 1.5 nm. The peak emission of the laser coincides with the position of the long-wavelength edge of the photonic bandgap (λ_L = 565nm$\pm$3nm), which confirms the laser emission is a band-edge laser (see Figure 8.22).

The linearity of the polarisation of the Nd:YAG laser was first tested by using a pair of polarisers (polariser and analyser). The analyser is oriented at different directions

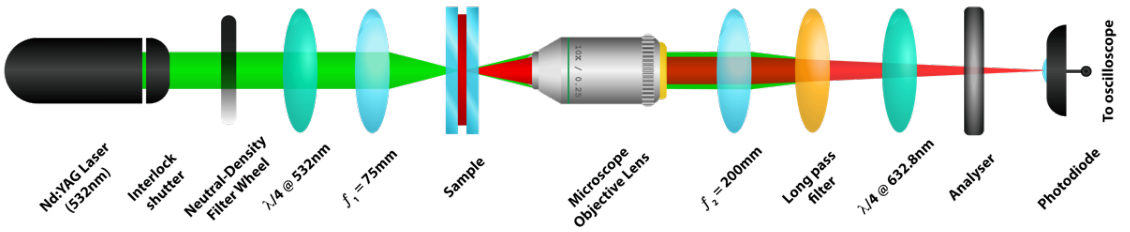


FIGURE 8.23: Free space optical setup used to determine the polarisation state of the LC band-edge laser when pumped with an Nd:YAG (532 nm) pulsed laser.

and the Nd:YAG light intensity was recorded at the photodiode, these results are shown together with the model results in Figure C.3, Appendix C. After this, the polarisation state of the LC laser was studied before demonstrating the polarisation controllable characteristic with an IPS device by adding a QWP in the optical pump setup. The modified optical pump setup is shown in Figure 8.23 when a QWP is added after the long pass filter followed by an analyser and a photodiode. The photodiode was connected to an oscilloscope that reads the collected LC laser light as a voltage pulse. Since the LC laser has a circular polarisation, by adding a QWP after the LC laser, the polarisation state of the LC laser converts into a linear state. When the analyser is rotated, due to the linear polarisation, a variation in the voltage level was seen on the oscilloscope. The photodiode response was recorded on the oscilloscope and is presented in Figure 8.24.

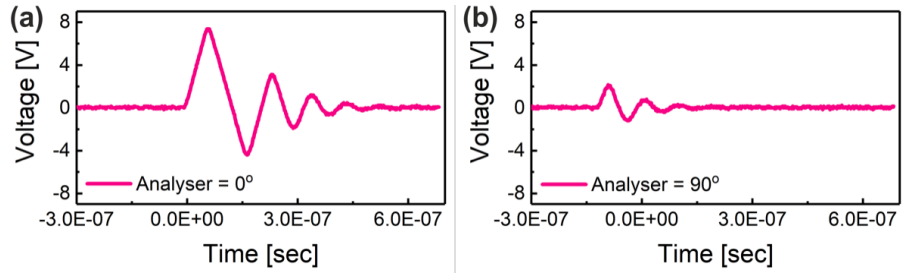


FIGURE 8.24: The band-edge LC laser response detected at the photodiode connected to the oscilloscope when the optical axis of the analyser is oriented at either (**a**) 0° or (b) 90° with respect to the linearly polarised LC laser. The repetition rate of pump Nd:YAG laser was 10 Hz.

First, the analyser was oriented so that the optical axis of the analyser and the orientation of the polarisation of the LC laser after passing through the QWP coincides and results in a maximum signal level on the oscilloscope. The orientation of the analyser was marked as 0° (i.e., parallel) and the corresponding response is shown Figure 8.24 (a). Now, the analyser was rotated through 90° to get a response with a minimum voltage level, which is shown in Figure 8.24 (b). For an ideal linearly polarised state, the voltage

level should drop to zero; however, for the LC laser, the voltage level did not reduce to zero, suggesting that the light that had passed through the QWP was not completely linear but had some degree of ellipticity. This may either be due to a difference in the LC laser wavelength (562 nm) and the QWP operation wavelength (632.8 nm) or the imperfect circular polarisation of the LC laser, or a combination of the two. Using a quarter waveplate designed for operation at 632.8 nm with light of wavelength 562 nm gives about ∼10% error in the measurement.

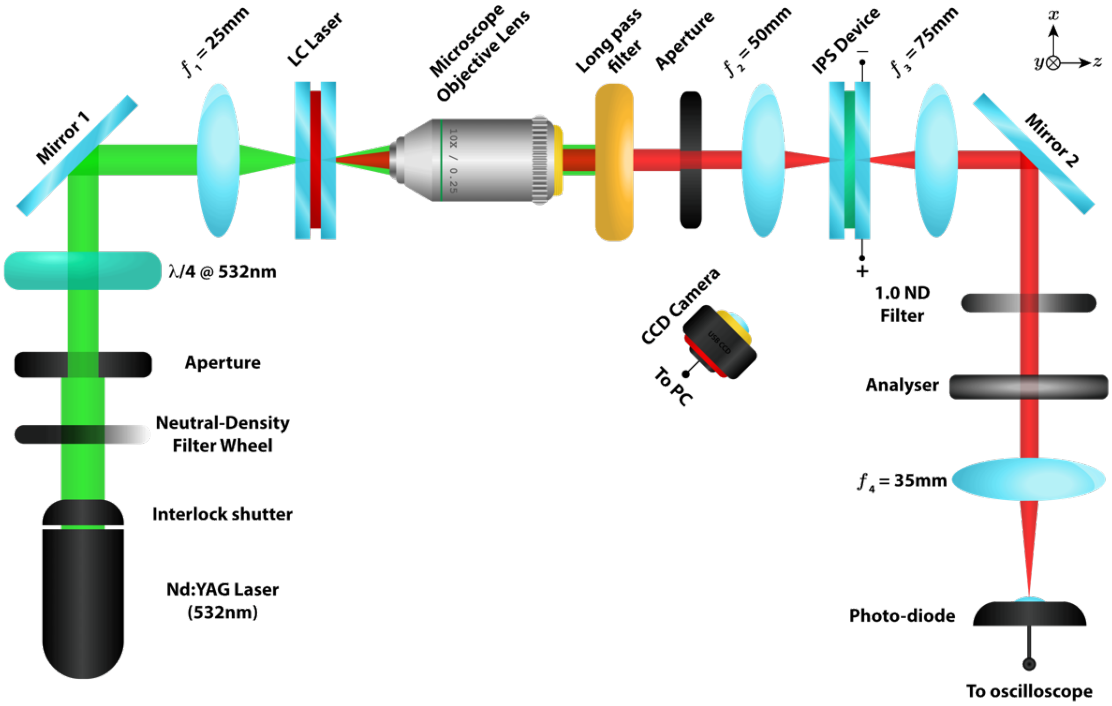


FIGURE 8.25: The free-space optical setup showing the bench-top demonstration of polarisation controllability of a dye-doped (E7+R5011+PM597) band-edge LC laser with an in-plane switching (IPS) device (E7) with four patterned electrodes.

The polarisation controllability of the LC laser was then demonstrated with a bench-top experiment as shown in Figure 8.25, which is modified from the optical pump setup. The setup mainly consists of two parts: 1) an optical pump setup: from the Nd:YAG laser to a long pass filter and 2) IPS optics: from aperture slit to the photodiode. The first part is to pump the LC band-edge laser and is discussed in detail in Figure 8.25, Chapter 3. The later part of the setup, however, was built to focus the LC laser beam onto the IPS electrode device. Because LC lasers are divergent in nature, an aperture was added to get a uniform waist and two-lenses of focal lengths f_2 and f_3 were added. While the lens f_2 focuses the LC laser beam onto the IPS device, the lens f_3 collimates the beam.

To accurately control the position of the LC laser on the active region (500 μm $\times$ 500μm) between the four electrodes, a CCD camera was used to monitor the beam position. To achieve this, the area between the electrodes of the IPS device were switched by applying an electric field along the diagonal orientation. Whilst looking at the CCD camera video, the position of the IPS device was adjusted by moving the translational stage on which the IPS device was mounted to ensure that the LC laser passed through the centre of the active region.

In this arrangement, the polarisation state was extracted in another way. To take the measurements, a manual method was adopted that consists of rotating the analyser from 0° through 90° while looking at the photodiode output voltage levels on the oscilloscope. Depending on the applied voltage on the IPS device, the photodiode response shows a maximum (V_{max}) or a minimum (V_{min}) level as the analyser was oriented through 0° to 90°. For example, if the applied voltage combination on the IPS device creates linear polarised light, rotating the analyser from 0° to 90° appears as a modulation signal with voltage V_{max} to V_{min}, respectively. However, for circularly polarised light, the modulation is zero and that is $V_{max} = V_{min}$ as the analyser is rotated from 0° to 90°.

For each applied electric field to the IPS device, the photodiode voltage level (V_{max} and V_{min}) was recorded. As any polarisation state can be represented as an ellipse with the dimensions of the major and minor axes changed if the state is circular, elliptical or linear. The V_{max} and V_{min} levels define the major and minor axes of the ellipse. While rotating the analyser, the position where V_{max} and V_{min} occur were also recorded as they provide the orientation of the corresponding major and minor axes for the ellipse and they were termed as α_{max} and α_{min} and respectively. To ensure the measurements were taken with a minimum error, a voltage level V_{avg} was also recorded at the orientation of the analyser half-way ($\approx 45°$) between the angles, α_{max} and α_{min}. The voltage levels V_{max}, V_{min}, V_{avg} and corresponding orientations α_{max}, α_{min} and $\alpha_{avg} \approx 45°$ were recorded to demonstrate the polarisation controllability of the band-edge LC laser.

To show the various polarisation states of the LC band-edge laser when combined with the IPS device, the voltage levels were chosen as so to generate an electric field in the horizontal, vertical and then diagonal directions on the active region between the electrode area of IPS device. The voltages combination were set as $V_A = V_B = +$V and

$V_C = V_D = -$V, which created an electric field in the vertical direction (i.e. $\psi = 90°$) with respect to $+x$-direction. Then the magnitude of the field was changed which in turn varied the retardation of the LC, thus exhibiting polarisation states from circular to elliptical and so on (as demonstrated previously). Similarly, the voltage combination was altered so as to generate an electric field in the horizontal direction within the in-plane electrode region and finally along the various diagonal orientations. For each combination of applied voltage, the minimum and maximum voltage levels recorded by the photodiode were read on the oscilloscope whilst the analyser was rotated and the corresponding angles on the analyser were noted.

Using this approach, a constellation diagram showing the different polarisation states was created, and the result is presented in Figure 8.26. The main polarisation states: circular of one sense of handedness, elliptical, reverse elliptical and circular with opposite sense of handedness oriented at $0°$, $\pm 45°$ and $90°$ were created. For example, the polarisation states created along the $0°$ direction is the result of a voltage combination that generates a vertical electric field ($\psi = 90°$) and similarly the polarisation states along $90°$ are produced by creating a horizontal electric field ($\psi = 0°$) between the in-plane electrodes.

For each orientation, the IPS device showed a range of polarisation states from circular with one handedness to elliptical to circular with opposite handedness and so on. However, the device showed limitations in terms of a linear polarisation state. This may be due to the imperfect nature of the circular polarisation of the band-edge LC laser. As seen in Figure 8.24, the band-edge LC laser showed some level of ellipticity that may limit to creating a linear polarised light. Furthermore, the device demonstrates a different polarisation state along the other orientations such as $+22.5°$, $+67.5°$, $-22.5°$ and $-67.5°$.

The previous reports although show the polarisation controllability either using LC device [348–356], these configuration does not control the orientation of the polarisation states. The six-electrodes based IPS device with SiO_2 - TiO_2 can control the polarisation and orientation, it however offers both in terms of fabrication complexity [357]. The bench-top demonstration presented here suggests that a nematic IPS device combined with a band-edge LC laser can be used to control and create any polarisation state along any orientation by correctly choosing the appropriate voltage combination. A LC

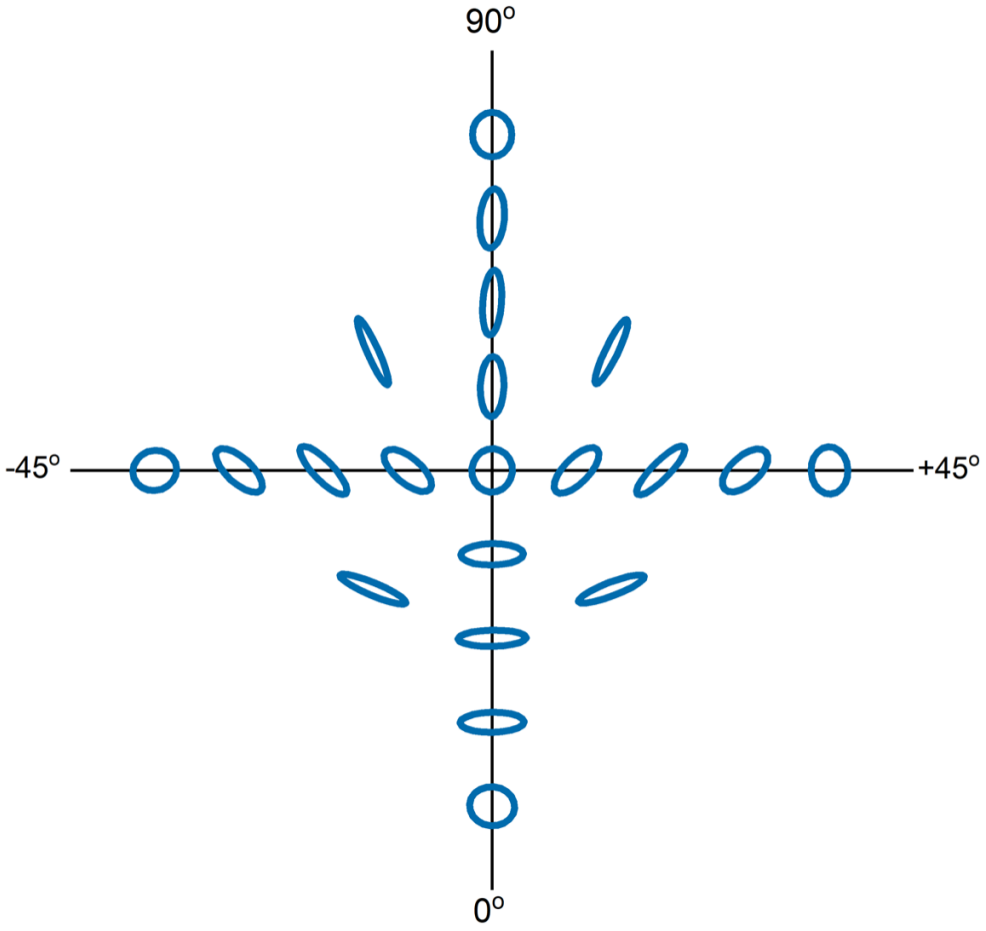


FIGURE 8.26: The polarisation constellation diagram created by controlling the polarisation states of the band-edge LC laser with an in-plane switching (IPS) nematic LC device. The various polarisation states at different orientations were generated by applying different combinations of voltages to the nematic IPS device.

band-edge laser offers benefits due to simple fabrication and wavelength tuneability, integrating the LC band-edge laser with an in-plane switching device to form an integrated polarisation controllable LC band-edge laser device.

8.4 Summary

The polarisation state of a band-edge LC laser is manipulated with a nematic LC device with a bench top demonstration. For the demonstration, the development stages of the different experimental setups were presented. To begin with, a nematic LC phase is used in a planar-aligned device to form a tuneable LC waveplate. Using a continuous wave He-Ne (632.8 nm) laser, the Fréedericksz transmission characteristics of the nematic LC device were investigated in order to demonstrate the control of the polarisation state.

The controllability of the orientation of the polarisation state generated with a planar-aligned nematic LC device was also presented by mechanically rotating the LC device to various orientations and results were presented on the transmission characteristics, phase difference, and modulation intensity of the signal that passes through the nematic LC device.

An in-plane four electrode device configuration in which the LC director was aligned homeotropically was fabricated to demonstrate control of both the orientation and the polarisation state of light emitted from a laser source. COMSOL modelling results were presented that estimate the electric field orientation, which is critical in determining the orientation of the polarisation state. Fabrication of the in-plane switching (IPS) device consisting of a nematic LC was explained in detail. The device operation and control of the polarisation states for different orientations of the electric field was demonstrated.

A liquid crystal band-edge laser was fabricated using a dye-doped chiral nematic LC and results were presented of the reflection spectrum of the chiral nematic LC, the emission characteristics of the laser and the resulting polarisation state. The polarisation state (e.g. linear, circular or elliptical) and the orientation (e.g. along the horizontal, vertical, diagonal axes) of the band-edge LC laser were investigated with the addition of the nematic LC-based IPS device. The bench top demonstration developed in this study shows that the circular polarisation of the LC band-edge laser can be tuned to any polarisation state with any desired orientation by correctly choosing the polarity and the magnitude of the applied electric field to the nematic IPS device. Control of the polarisation state of a band-edge LC laser is of particular interest in augmented reality, virtual reality, and holographic displays. Furthermore, it could be employed to create a laser-based 3D imaging system without the need for other optical components, which could be of importance for biomedical and astronomical imaging systems.

Chapter 9

Conclusion and Future Work

This Thesis considers a variety of materials including different liquid crystal (LC) phases and advanced emissive materials for use in thin-film photonic devices and investigates the fabrication challenges associated with manufacturing thin-film LC lasers using advanced materials. It studies the birefringence and electro-optic characteristics of a newly developed LC material and investigates the fabrication processes required to create photo-polymerised thin-films of chiral nematic LC that form the basis of a LC laser. It also discusses the need for and explores the use of alternative emissive materials that could potentially provide a route to an electrically-pumped LC laser. As LC and emissive materials show compatibility with solution processing techniques, this Thesis presents the successful demonstration of a flexible LC laser that exhibits mechanically-induced beam steering. Finally, this Thesis demonstrates an LC laser with polarisation control with the addition of a second LC layer. This system could potentially be integrated into 3D imaging systems. In the following sub-sections, the conclusions drawn from each study are discussed along with how this work could be taken forward in the future.

9.1 Optical Characteristics of a Novel LC Dimer

LCs are the core material considered in this Thesis for the creation of the optical cavity in thin-film laser technologies, and it is therefore important to understand the optical and electro-optical properties of these materials. A new LC dimer, developed by our collaborators at Hull, was characterised in terms of the birefringence, ratio of the LC elastic constants, the dielectric permittivities and the flexo-elastic ratio. The experiment was designed to first study the birefringence of a well-known LC material, E7, in order

to confirm the reliability of the measurement process as explained in detail in Chapter 4. The nematic phase of the new LC compound showed a high birefringence of $\Delta n = 0.312$ ($\lambda = 550$ nm) at 150°C, which is particularly high for an LC dimer and possibly the highest recorded to date [108, 164, 359]. The birefringence of the dimer varies with temperature reaching a value of $\Delta n = 0.184$ at 207°C just before the clearing temperature. Other physical parameters that were also studied include the ratios $k_1/\Delta\epsilon = 9 \sim 4$ and $k_3/k_1 = 0.40 \sim 0.42$ whereas the dielectric permittivities were estimated to be of the order of $\epsilon_\perp = 11$ and $\epsilon_\parallel = 16$ at 1kHz at a temperature of 140°C. Lastly, by studying the flexoelectro-optic effect in a chiral nematic LC that consists of the dimer, results have been presented on the flexoelastic ratio and were found to be $e/k = 2.59 \sim 2.60 V^{-1}$. The tilt angle and flexo-elastic ratio together with the high birefringence imply that the dimer would be an excellent candidate for a fast flexoelectro-optic phase modulator that can attain a 1/2-waveplate modulation in a thin device driven at lower operating voltages. In addition, the high birefringence of the dimer means its chiral nematic phase exhibits a wider photonic bandgap, which could potentially cover a larger portion of the visible spectrum [108]. When combined with a suitable gain material, it enables the possibility of creating a wavelength tuneable LC laser without changing the device geometry; for example, a band-edge LC laser in which the longer wavelength edge of the photonic bandgap can be tuned with an external electric field.

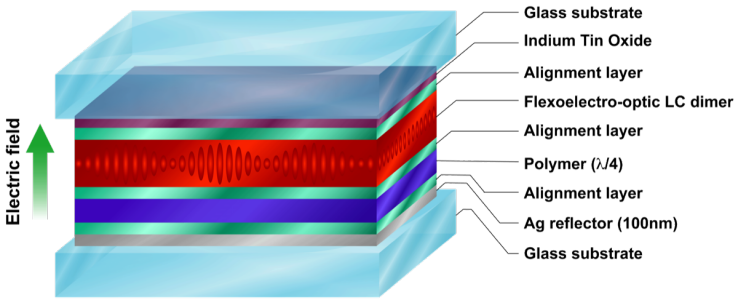


FIGURE 9.1: A fast switching flexoelectro-optic modulator with the LC dimer.

While the birefringence study of the dimer revealed the compound to possess a high birefringence, no LC laser could be demonstrated with this material. This is because the dimer exhibits a nematic (or a chiral nematic) phase at very high temperatures >132°C, which limits its use with conventional laser dyes that are typically used to form either band-edge or defect-mode LC lasers. In the future, mixtures could be formulated

with this compound to try to reduce the operating temperature whilst maintaining a relatively high birefringence and flexoelectro-optic switching. Furthermore, there is scope for creating a fast switching flexoelectro-optic modulator (Figure 9.1) with this new LC compound as it can exhibit half-waveplate modulation for low device thicknesses, thereby reducing the voltage required to achieve full 2π phase modulation.

9.2 Perovskites for LC Lasers

Gain materials are critical in the design of a laser system as their photophysical characteristics determine the resulting LC laser parameters such as emission wavelength and excitation fluence threshold. Laser dyes based on organic materials have widely been used in the study of LC lasers; however, these are limited in terms of the prospects for electrical pumping. Advanced emissive materials such as light emitting polymers and perovskites show remarkable emission characteristics that potentially provide a route towards electrically pumped LC lasers. In this regard, thin films of either bulk methylammonium (MA) perovskite ($\lambda_{em} = 770$ nm) or Caesium (CS)-based perovskite nanocrystals ($\lambda_{em} = 675$ nm , size = $5 \sim 10$ nm, host = hexane) were incorporated to form band-edge and defect-mode LC lasers in this Thesis. In the pursuit of a band-edge laser, a study was conducted to attempt to disperse perovskite nanocrystals into nematic and chiral nematic LC hosts using a number of different processing routes with the goal of achieving uniform dispersion. These include: 1) ultrasonic, 2) thermal and 3) room temperature dispersion. While certain processes were identified that did not result in a degradation of the nanocrystals, as determined from the photoluminescence emission properties, aggregation was found to be a problem. In chiral nematic LCs, the average cluster size of nanocrystals with the room temperature method was found to be 14 nm (2.5 wt. %) and 18 nm (5 wt. %). The nanocrystals were found to reside at the disclination lines and there was no evidence of alteration in the photoluminescence spectrum as a result of the modification of the density of photon states at the band-edges.

To avoid direct dispersion of the nanocrystals in the LC host, a defect-mode configuration was investigated. In this regard, a thin-film of MA-based perovskite in bulk form was first used as a defect layer to form a defect-mode structure with two CLC reflectors. The stack showed the signature of amplified spontaneous emission

when pumped with a pulsed Nd:YAG laser with excitation fluence threshold E_{th} = 1000μJ/cm^2/pulse. The MA-based perovskite showed an ASE excitation fluence threshold up to 600 μJ/cm^2/pulse [290]. Although laser emission could not be achieved, this is the first demonstration of a defect-mode structure created with two CLCs layers and perovskite. To improve the structure and move towards laser emission, the device was further modified. Since the deposition of the perovskite layer requires several stages at relatively higher temperatures (>150°C), it was decided to replace the thin film of bulk perovskite with Cs-based perovskite nanocrystals that were dispersed into a polymer matrix. Different fabrication processes were investigated for the creation of a defect-mode structure with perovskite nanocrystals dispersed into the polymer. Upon photoexcitation the devices showed a notable modification in the PL emission spectrum in terms of gain narrowing, with the possible indication of multimode laser emission. This multimode behaviour is believed to result from the non-uniform thickness of the defect layer, which was difficult to control during the fabrication process.

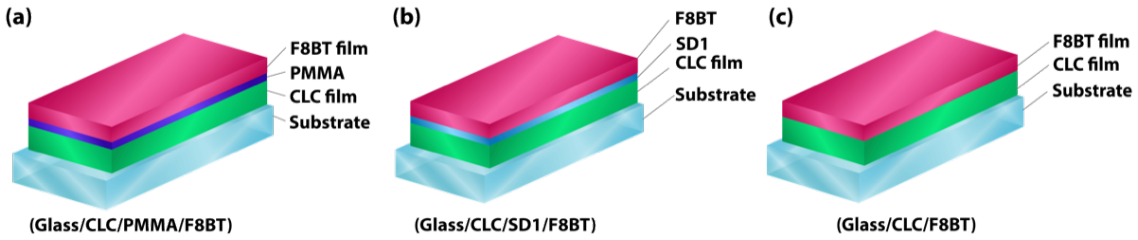


FIGURE 9.2: The device stacks with (**a**) CLC/PMMA/F8BT, (**b**) CLC/SD1/F8BT and (**c**) CLC/F8BT.

In future, there is huge promise to further investigate this area by refining the fabrication of the defect layer. This could be achieved by using either an alternative fabrication process or by replacing the material that can form a thin layer (of a few tens of nanometres) of the barrier layer or by completely replacing the barrier layer with the material in which perovskite nanocrystals can be uniformly dispersed as well as it protect the CLC film. The perovskite materials used to create the defect-mode structure can also be replaced with a light emitting conjugated polymer. In this regard, a liquid crystal conjugated polymer, poly(9,9-dioctylfluorene-co-benzothiadiazole) (F8BT) is considered as an alternative gain material for the defect-mode LC laser. The following three device stacks were fabricated with the delamination process that was considered in Chapters 6 & 7 and shown in Figure 9.2:

- CLC/PMMA/F8BT
- CLC/SD1/F8BT
- CLC/F8BT

The samples prepared with barrier layers of PMMA, SD1 and no barrier layer are then excited by a UV (365 nm) LED using the optical setup as shown in the Figure 3.15, Chapter 2. The photoluminescence emission is presented in Figure 9.3 that shows a modification in the photoluminescence – oscillations at the longer edge of the PL spectra – from a liquid crystalline conjugated polymer due the presence of a band gap. The oscillations in the photoluminescence are considered to be due to the variation in the density of photon states around the band-edges, although it can equally be thought of as the result of constructive and destructive interference in the PL that arises due to the helical structure.

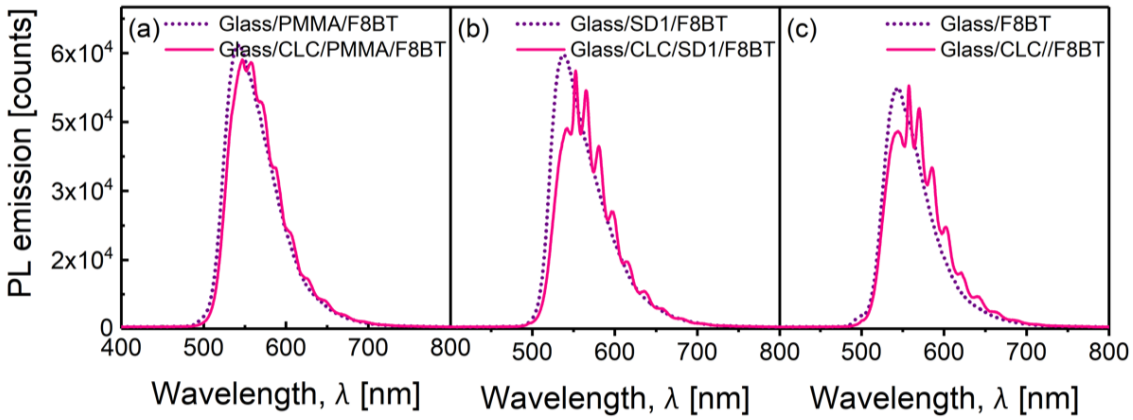


FIGURE 9.3: The PL emission spectra of CLC/F8BT stack with barrier layer of (**a**) PMMA, (**b**) SD1 and (**c**) no barrier layer.

A defect-mode LC laser comprising CLC/Barrier layer/F8BT/Barrier layer/-CLC can be created by combining two identical stacks of each CLC/Barrier layer/F8BT. Depending on the defect layer parameters (such as thickness etc) and upon photo-excitation, such a device could demonstrate single or multimode laser emission. In addition, with a suitable gain material that can show a current density of 10^5 A/cm^2 with the combination of electron and hole transport layers, there is a potential to form an electrically-pumped LC defect-mode thin-film laser.

9.3 Thin-film flexible laser

Building upon the approach developed in Chapter 6, a flexible defect-mode laser was created using a conventional organic laser dye to demonstrate and confirm the resonant properties of the device stack. Since the defect-mode device requires a multiple layered structure, which brings with it the challenge of material incompatibility for the different layers used in the structure, various fabrication methods were explored in order to develop a thin-film flexible laser without affecting the properties of the materials used in the layered structure. The thin-film was created by the photo-polymerisation of chiral nematic LC films (5μm). A mechanically robust and flexible defect-mode laser was prepared using a film transfer technique on a transparent conformable polymer film. The complete stack consists of CLC/barrier layer/dye-doped defect-layer/barrier layer/CLC with 0.36μm dye-doped defect layer and 0.18μm of each barrier layer. The laser demonstrates a single mode emission at 582 nm with excitation fluence threshold $E_{th} = 12.3 \pm 0.5 \mu J/cm^2/pulse$. The bendable feature of the proposed flexible LC laser allows the demonstration of a beam steering with steering angle of 42° by mechanically inducing the deformation with a radius of curvature was 5 mm. This phenomenon could be useful for VR/AR applications without the need for additional optical components.

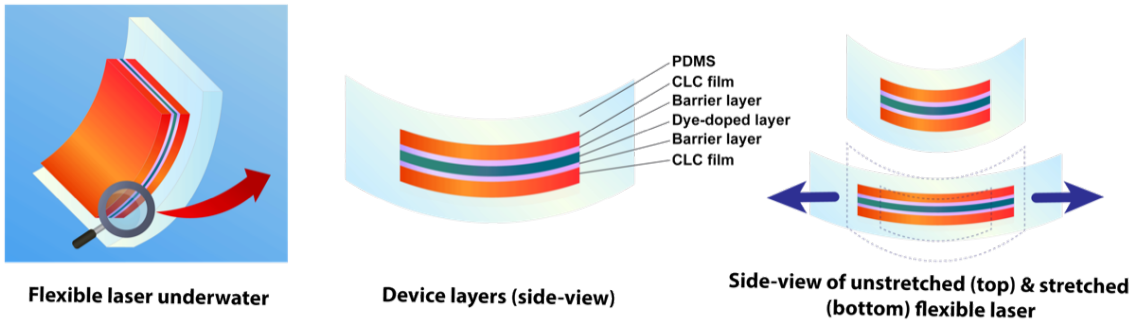


FIGURE 9.4: The proposed flexible, stretchable defect-mode laser with underwater communication.

The flexible laser developed in the Chapter 7 would be an excellent platform for advanced gain materials such as perovskites or light emitting polymers. It can further be explored by improving the mechanical properties to achieve wavelength tuning. One way to achieve this is to utilise a flexible and stretchable transparent polymer (such as Polydimethylsiloxane, PDMS) into which the thin-film laser can be embedded. When such a laser is stretched it can demonstrate wavelength tuning characteristics without

the need for replacing the gain material. Furthermore, by using water-resistant flexible polymers and embedding the thin-film lasers into them, weather resilient lasers could be created and by virtue of their mechanical flexibility, they form devices that could work underwater or be used for 3D imaging or communication applications without the need for additional optics components, Figure 9.4.

9.4 Polarisation Controllable LC laser

Manipulation of the polarisation is useful for a number of photonics applications such as in the creation of 3D images and holographic projection systems. To date, this has been achieved with various device configurations that generally require the use of sophisticated fabrication processes. LC materials are particularly attractive as they can be used to form tuneable waveplates – a device that can manipulate the polarisation state. Moreover, the fabrication processes required for these devices are compatible with solution processing techniques. By exploiting the characteristics of wave retardation in a nematic LC and combining this with a LC band-edge laser, the development of a polarisation controlled LC laser has been demonstrated in this Thesis. In addition to a change in the polarisation state from linear, elliptical to circular and so on, the orientation of the polarisation state is also important for many photonics and optoelectronic applications. To achieve this, a four-electrode assembly (electrode area $500 \times 500 \mu m^2$) was utilised that can create in-plane switching (IPS). With the different combination of voltages the orientation as well as the polarisation state of the laser light was electrically controlled. A band-edge LC laser device was combined with the nematic IPS device to conduct a bench-top demonstration of the control of the orientation and polarisation state of the LC laser when the direction and strength of the applied electric field was varied across the nematic IPS device.

This demonstration can pave the way for an integrated polarisation controllable LC laser which could be created by combining the IPS device with a band-edge LC laser in a single device configuration, Figure 9.5. For such a device, LC laser emission can be achieved by optically exciting the LC laser whereas the orientation and polarisation of the LC laser is controlled with the combination of electric fields across the IPS device. Such an integrated polarisation controllable LC laser could be of significant interest for

photonic applications ranging from imaging devices to VR/AR gadgets. Note: The refractive index matching between the chiral nematic structure and in-plane switching LC device and between the LC and glass would need to be optimised (i.e., refractive index differences minimised) in order to reduce the internal reflection and avoid influencing the lasing mode itself.

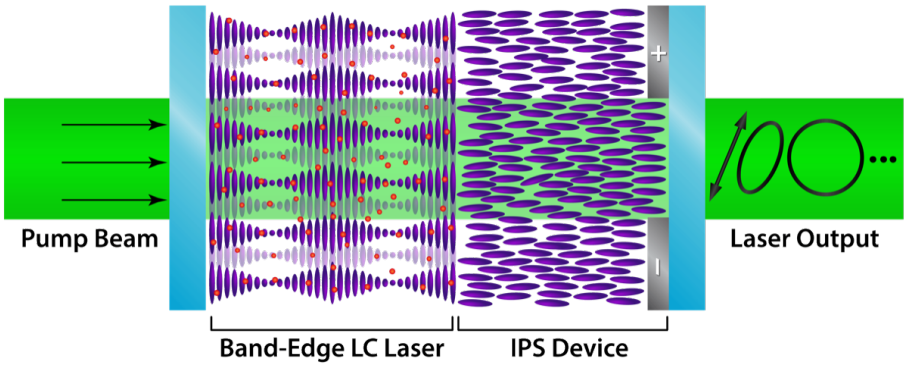


FIGURE 9.5: Illustration of proposed integrated polarisation controllable LC laser device.

Appendix A

High Birefringence LC Dimer

A.1 Twist-Bend Nematic ($N_{TB/X}$) phase of LC

In the $N_{TB/X}$ phase, the LC director is tilted at an angle (ϕ) that forms a helical periodic structure as shown in Figure A.1. Due to the tilt in the 'local' molecules of the nematic LC, the extra-ordinary refractive index (n_e) decreases while the ordinary refractive index (n_o) increases; thus resulting in an overall decrease in the Δn of the material.

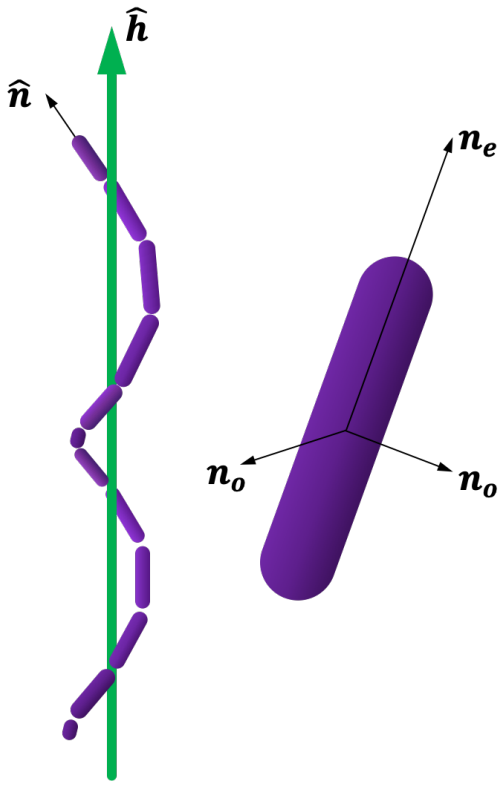


FIGURE A.1: The LC molecular arrangement forming the $N_{TB/X}$ phase that results in the variation in the local refractive index along the helical direction ($\hat{h}$) (left) and a typical nematic LC molecule illustrating n_o and n_e directions (right).

Appendix B

Towards Defect-Mode LC Laser

B.1 Material details on the printed LC

The nematic LC phase and chiral dopant used to prepare with the flexographic printed chiral nematic thin films is given below. The material details are provided by our collaborators in the Eindhoven University of Technology, Netherlands.

B.1.1 Paliocolor® LC 242 (Nematic phase)

- Phase behaviour: Heating = Cr 63 $\sim$ 70 N 120 $\sim$ 125 I & Cooling = I 125 N <30 Cr
- Birefringence: Δn = 0.15
- Purity: > 95 % (HPLC)
- Colour: Apha < 150
- Solubility: MEK, Toluene, PGMEA, Cyclohexanone

B.1.2 Paliocolor® LC 756 (Chiral Dopant)

- Right-handed chiral dopant
- Helical twisting power: HTP > 75 (in combination with Paliocolor® LC 242)
- Excellent compatibility with the Paliocolor® nematic LC materials (miscible with Palicolor® LC242 up to 15 weight-%)
- Purity: >75 % (HPLC)
- Colour: Apha < 100

Appendix C

Polarisation Controllable Laser

C.1 Signal and Reference waveforms

The Signal and Reference waveforms as recorded with A/D are shown in Figure C.1.

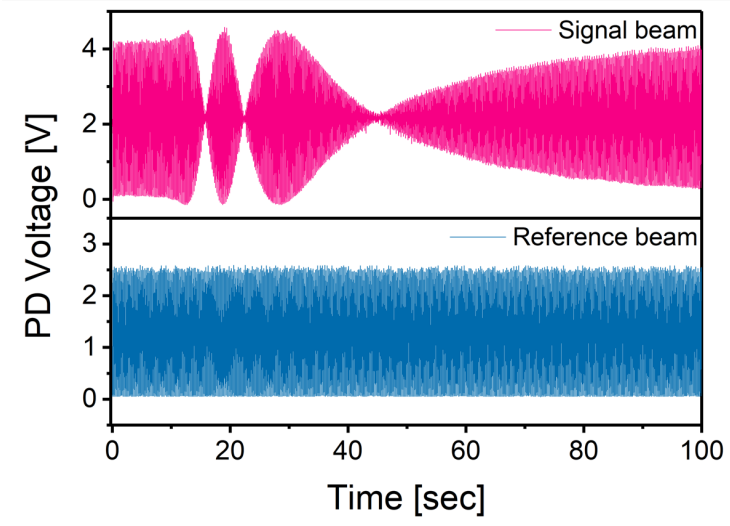


FIGURE C.1: Example plots of the Signal (**top**) beam and (**bottom**) the Reference beams recorded with an A/D converter to extract the polarisation states. .

Portion of Signal and Reference waveforms recorded with A/D converter. The Signal waveform depicts different polarisation states when compared with Reference waveform and are presented with their equivalent polarisation states in Figure C.2.

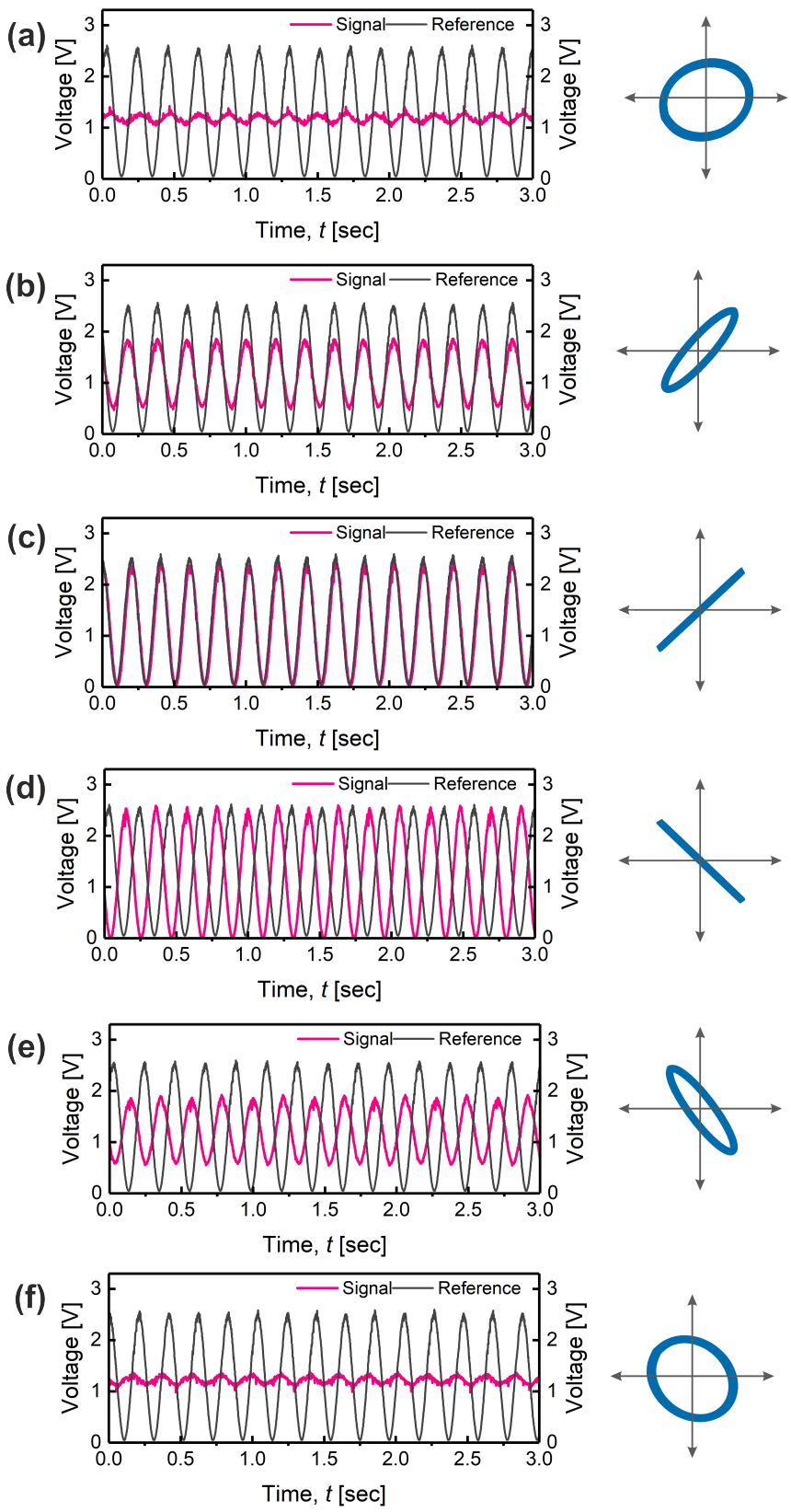


FIGURE C.2: The *Signal* and *Reference* waveforms of a few polarisation states that are presented in Figure 8.19. The corresponding polarisation states were extracted and shown with blue solid line on right side where sub-Figure (a) circular, (b) Elliptical ($+\psi$), (c) Linear ($+\psi$), (d) Linear ($-\psi$), (e) Elliptical ($-\psi$), and (f) circular (opposite hand as in (a)

.

C.2 Field estimation

Table C.1 summarises the voltage required on each electrode (A, B, C & D) of IPS device to generate the polarisation in a specific orientation.

TABLE C.1: The estimate of the applied voltage on the four electrodes (A, B, C and D) of the IPS device to generate the field in different orientations.

Field orientation, ϕ (°)	V_A (V)	V_B (V)	V_C (V)	V_D (V)
0	+70.71	+70.71	-70.71	-70.71
11.25	+55.55	+83.14	-83.14	-55.55
22.50	+38.26	+92.38	-92.38	-38.26
33.75	+19.51	+98.08	-98.08	-19.51
45	0	+100	0	-100
56.25	-19.51	+98.08	-98.08	+19.51
67.50	-38.26	+92.38	-92.38	+38.26
78.75	-55.55	+83.14	-83.14	+55.55
90	-70.71	+70.71	-70.71	+70.71

C.3 Linearity test of Nd:YAG pump laser

The variation in the intensity of Nd:YAG pump source as a function of rotation angle of the analyser is shown in Figure C.3.

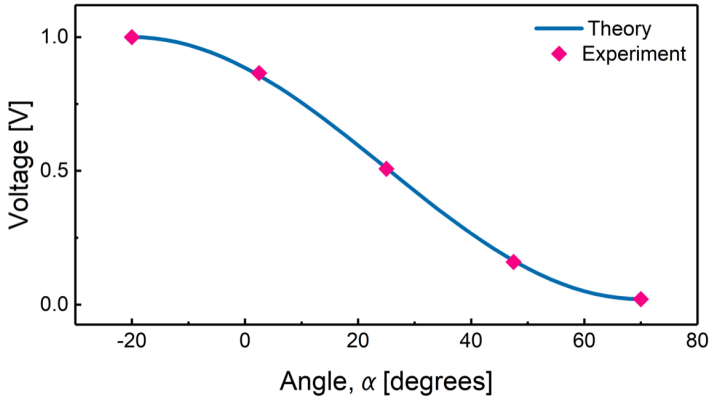


FIGURE C.3: The intensity level of the Nd:YAG laser as a function of orientation angle of the analyser (α). The experimental (markers) data that are taken at a few orientation angles of the analyser that follow the equivalent theoretical model (solid line) that is expected from linearly polarised light.

Bibliography

1. Goodby, J. W. Phase Transitions: General and Fundamental Aspects. *Handbook of Liquid Crystals, 8 Volume Set* **2** (2014).
2. Collings, P. J. & Hird, M. *Introduction to Liquid Crystals: Chemistry and Physics* (Taylor & Francis Group, 1997).
3. Goodby, J. W. in *Handbook of Visual Display Technology* (eds Chen, J., Cranton, W. & Fihn, M.) 1243–1287 (Springer Berlin Heidelberg, Berlin, Heidelberg, 2012).
4. Szydłowska, J., Krówczyński, A., Górecka, E. & Pociecha, D. Calamitic and discotic liquid crystalline phases for mesogens with triangular cores. *Soft matter* **15,** 7195–7202 (2019).
5. Bisoyi, H. K. & Kumar, S. Discotic nematic liquid crystals: science and technology. *Chemical Society Reviews* **39,** 264–285 (2010).
6. Hamley, I. *et al.* Orientational ordering in the nematic phase of a thermotropic liquid crystal: A small angle neutron scattering study. *The Journal of chemical physics* **104,** 10046–10054 (1996).
7. Jones, L. P. in *Handbook of Visual Display Technology* (eds Chen, J., Cranton, W. & Fihn, M.) 1387–1402 (Springer Berlin Heidelberg, Berlin, Heidelberg, 2012).
8. Hong, H., Shin, H. & Chung, I. In-plane switching technology for liquid crystal display television. *Journal of Display Technology* **3,** 361–370 (2007).
9. Pelzl, G. & Hauser, A. Birefringence and phase transitions in liquid crystals. *Phase Transitions: A Multinational Journal* **37,** 33–62 (1991).
10. Singh, S. in *Liquid Crystals Fundamental* (ed Scientific, W.) 221–311 ().
11. Taugerbeck, A. & Booth, C. J. Design and synthesis of chiral nematic liquid crystals. *Handbook of liquid crystals,* 1–63 (2014).
12. Ermakov, S., Beletskii, A., Eismont, O. & Nikolaev, V. in *Liquid Crystals in Biotribology: Synovial Joint Treatment* 37–56 (Springer International Publishing, Cham, 2016).
13. Khoo, I.-C. *Liquid crystals* chap. Cholesteric, Smectic, and Ferroelectric Liquid Crystals (John Wiley & Sons, 2007).
14. Yu, C.-H., Wu, P.-C. & Lee, W. Electro-thermal formation of uniform lying helix alignment in a cholesteric liquid crystal cell. *Crystals* **9,** 183 (2019).
15. Coles, H. & Morris, S. Liquid-crystal lasers. *Nature Photonics* **4,** 676–685 (2010).
16. Sandford O'Neill, J. J. *et al.* Robust measurement of flexoelectro-optic switching with different surface alignments. *Journal of Applied Physics* **125,** 093104 (2019).
17. Castles, F. & Morris, S. M. in *Handbook of Liquid Crystals* 1–28 (American Cancer Society, 2014).
18. Orzechowski, K. *et al.* Polarization properties of cubic blue phases of a cholesteric liquid crystal. *Optical Materials* **69,** 259–264 (2017).
19. Oton, E., Netter, E., Nakano, T., Inoue, F., *et al.* Monodomain blue phase liquid crystal layers for phase modulation. *Scientific Reports* **7,** 44575 (2017).
20. Blinov, L. M. *Structure and properties of liquid crystals* (Springer Science & Business Media, 2010).
21. Kikuchi, H., Yokota, M., Hisakado, Y., Yang, H. & Kajiyama, T. Polymer-stabilized liquid crystal blue phases. *Nature materials* **1,** 64–68 (2002).

22. Gray, G. W., Vill, V., Spiess, H. W., Demus, D. & Goodby, J. W. *Physical properties of liquid crystals* (John Wiley & Sons, 2009).
23. Kogelnik, H. & Shank, C. Coupled-wave theory of distributed feedback lasers. *Journal of applied physics* **43,** 2327–2335 (1972).
24. Mulder, D., Schenning, A. & Bastiaansen, C. Chiral-nematic liquid crystals as one dimensional photonic materials in optical sensors. *Journal of Materials Chemistry C* **2,** 6695–6705 (2014).
25. De Vries, H. Rotatory power and other optical properties of certain liquid crystals. *Acta Crystallographica* **4,** 219–226 (1951).
26. Xu, H., Trushkevych, O., Collings, N. & Crossland, W. Measurement of dielectric anisotropy of some liquid crystals for microwave applications. *Molecular Crystals and Liquid Crystals* **502,** 235–244 (2009).
27. Osman, M. A. Nematic Liquid Crystals with High Positive Dielectric Anisotropy. *Zeitschrift für Naturforschung B* **34,** 1092–1095 (1979).
28. Yang, D.-K. & Wu, S.-T. *Fréedericksz Transition, Fundamentals of liquid crystal devices* (John Wiley & Sons, 2014).
29. Dierking, I. *Surface Anchoring and Elasticity, Textures of liquid crystals* (John Wiley & Sons, 2003).
30. Coles, H. J. & Morris, S. M. in *Handbook of Visual Display Technology* (eds Chen, J., Cranton, W. & Fihn, M.) 1681–1694 (Springer Berlin Heidelberg, Berlin, Heidelberg, 2012).
31. Rudquist, P., Carlsson, T., Komitov, L. & Lagerwall, S. The flexoelectro-optic effect in cholesterics. *Liquid crystals* **22,** 445–449 (1997).
32. Eichler, H. J., Eichler, J. & Lux, O. *Lasers: basics, advances and applications* (Springer, 2018).
33. Mookherjea, S. Semiconductor coupled-resonator optical waveguide laser. *Applied physics letters* **84,** 3265–3267 (2004).
34. Komljenovic, T. *et al.* Widely-tunable ring-resonator semiconductor lasers. *Applied Sciences* **7,** 732 (2017).
35. Khoder, M., Radziunas, M., Tronciu, V. & Verschaffelt, G. Study of wavelength switching time in tunable semiconductor micro-ring lasers: experiment and travelling wave description. *OSA Continuum* **1,** 1226–1240 (2018).
36. Chen, G. Y. *et al.* Femtosecond-laser-written microstructured waveguides in BK7 glass. *Scientific reports* **8,** 1–7 (2018).
37. Li, L. *et al.* All-laser-micromachining of ridge waveguides in LiNbO 3 crystal for mid-infrared band applications. *Scientific Reports* **7,** 1–7 (2017).
38. Gardiner, D. J. *et al.* Paintable band-edge liquid crystal lasers. *Optics express* **19,** 2432–2439 (2011).
39. Morris, S., Ford, A., Pivnenko, M. & Coles, H. Enhanced emission from liquid-crystal lasers. *Journal of Applied Physics* **97,** 023103 (2005).
40. Lu, H. *et al.* Band-edge-enhanced tunable random laser using a polymer-stabilised cholesteric liquid crystal. *Liquid Crystals,* 1–8 (2020).
41. Ford, A. D., Morris, S. M. & Coles, H. J. Photonics and lasing in liquid crystals. *Materials Today* **9,** 36–42 (2006).
42. Ozaki, M., Ozaki, R., Matsui, T. & Yoshino, K. Twist-Defect-Mode Lasing in Photopolymerized Cholesteric Liquid Crystal. *Japanese Journal of Applied Physics* **42,** L472–L475 (May 2003).
43. Ozaki, R., Matsuhisa, Y., Ozaki, M. & Yoshino, K. Laser action based on electrically controllable defect mode in one-dimensional photonic crystal containing conducting polymer and liquid crystal defect layers. *Molecular Crystals and Liquid Crystals* **433,** 237–245 (2005).

44. Dowling, J. P., Scalora, M., Bloemer, M. J. & Bowden, C. M. The photonic band edge laser: A new approach to gain enhancement. *Journal of applied physics* **75,** 1896–1899 (1994).
45. Schmidtke, J. & Stille, W. Fluorescence of a dye-doped cholesteric liquid crystal film in the region of the stop band: theory and experiment. *The European Physical Journal B-Condensed Matter and Complex Systems* **31,** 179–194 (2003).
46. Huang, Y. *et al.* Incident angle and polarization effects on the dye-doped cholesteric liquid crystal laser. *Optics communications* **261,** 91–96 (2006).
47. Belyakov, V. Low threshold DFB lasing in chiral LC at diffraction of pumping wave. *Molecular Crystals and Liquid Crystals* **453,** 43–69 (2006).
48. Matsuhisa, Y. *et al.* Low-threshold and high efficiency lasing upon band-edge excitation in a cholesteric liquid crystal. *Applied Physics Letters* **90,** 091114 (2007).
49. Schmidtke, J. & Stille, W. Photonic defect modes in cholesteric liquid crystal films. *The European Physical Journal E* **12,** 553–564 (2003).
50. Shibaev, P., Tang, K., Genack, A., Kopp, V. & Green, M. Lasing from a stiff chain polymeric lyotropic cholesteric liquid crystal. *Macromolecules* **35,** 3022–3025 (2002).
51. Funamoto, K., Ozaki, M. & Yoshino, K. Discontinuous shift of lasing wavelength with temperature in cholesteric liquid crystal. *Japanese journal of applied physics* **42,** L1523 (2003).
52. Song, M. H. *et al.* Lasing from thick anisotropic layer sandwiched between polymeric cholesteric liquid crystal films. *Japanese journal of applied physics* **44,** 8165 (2005).
53. Song, M. H. *et al.* Effect of phase retardation on defect-mode lasing in polymeric cholesteric liquid crystals. *Advanced Materials* **16,** 779–783 (2004).
54. Song, M. H. *et al.* Defect-Mode Lasing with Lowered Threshold in a Three-Layered Hetero-Cholesteric Liquid-Crystal Structure. *Advanced materials* **18,** 193–197 (2006).
55. Song, M. H. *et al.* Electrotunable non-reciprocal laser emission from a liquid-crystal photonic device. *Advanced Functional Materials* **16,** 1793–1798 (2006).
56. Takanishi, Y. *et al.* Defect-mode lasing from a three-layered helical cholesteric liquid crystal structure. *Japanese journal of applied physics* **46,** 3510 (2007).
57. Huang, J.-C., Hsiao, Y.-C., Lin, Y.-T., Lee, C.-R. & Lee, W. Electrically switchable organo–inorganic hybrid for a white-light laser source. *Scientific reports* **6,** 28363 (2016).
58. Svelto, O. *Principles of lasers* (Springer, 2010).
59. Jaffé, H. H. & Miller, A. L. The fates of electronic excitation energy. *Journal of chemical education* **43,** 469 (1966).
60. Sutherland, B. R. & Sargent, E. H. Perovskite photonic sources. *Nature Photonics* **10,** 295 (2016).
61. Brichkin, S. B. & Razumov, V. F. Colloidal quantum dots: synthesis, properties and applications. *Russian Chemical Reviews* **85,** 1297 (2016).
62. Singh, G., Fisch, M. & Kumar, S. Emissivity and electrooptical properties of semiconducting quantum dots/rods and liquid crystal composites: a review. *Reports on Progress in Physics* **79,** 056502 (2016).
63. Schäfer, F. P., Schmidt, W. & Volze, J. Organic dye solution laser. *Applied Physics Letters* **9,** 306–309 (1966).
64. Kuehne, A. J. & Gather, M. C. Organic lasers: recent developments on materials, device geometries, and fabrication techniques. *Chemical reviews* **116,** 12823–12864 (2016).
65. Duarte, F. J. Organic dye lasers: brief history and recent developments. *Optics and photonics news* **14,** 20–25 (2003).

66. Li, Z. & Psaltis, D. Optofluidic dye lasers. *Microfluidics and Nanofluidics* **4,** 145–158 (2008).
67. Pal, P. *et al.* Spectroscopic and photophysical properties of some new rhodamine derivatives in cationic, anionic and neutral micelles. *Journal of Photochemistry and Photobiology A: Chemistry* **98,** 65–72 (1996).
68. Ion, R.-M. & Fara, L. *Photophysical and photochemical properties of dye molecules in polymers used for fluorescent solar concentrators* in *Proceedings of the Indian Academy of Sciences-Chemical Sciences* **107** (1995), 825.
69. Bourson, J., Doizi, D., Lambert, D., Sacaze, T. & Valeur, B. A derivative of laser dye DCM highly soluble in alcohols. *Optics communications* **72,** 367–370 (1989).
70. Nad, S. & Pal, H. Unusual photophysical properties of coumarin-151. *The Journal of Physical Chemistry A* **105,** 1097–1106 (2001).
71. Mowatt, C. *et al.* Comparison of the performance of photonic band-edge liquid crystal lasers using different dyes as the gain medium. *Journal of applied physics* **107,** 043101 (2010).
72. Shankarling, G. & Jarag, K. Laser dyes. *Resonance* **15,** 804–818 (2010).
73. Cao, D. *et al.* Coumarin-based small-molecule fluorescent chemosensors. *Chemical reviews* **119,** 10403–10519 (2019).
74. Shabir, G., Saeed, A. & Ali Channar, P. A review on the recent trends in synthetic strategies and applications of xanthene dyes. *Mini-Reviews in Organic Chemistry* **15,** 166–197 (2018).
75. Lopez Arbeloa, F., Banuelos, J., Martinez, V., Arbeloa, T. & Lopez Arbeloa, I. Structural, photophysical and lasing properties of pyrromethene dyes. *International Reviews in Physical Chemistry* **24,** 339–374 (2005).
76. Shah, M. *et al.* Pyrromethene–BF2 complexes as laser dyes: 1. *Heteroatom Chemistry* **1,** 389–399 (1990).
77. Boyer, J. H. *et al.* Pyrromethene–BF2 complexes as laser dyes: 2. *Heteroatom Chemistry* **4,** 39–49 (1993).
78. Hessz, D., Hegely, B., Kallay, M., Vidoczy, T. & Kubinyi, M. Solvation and protonation of coumarin 102 in aqueous media: a fluorescence spectroscopic and theoretical study. *The Journal of Physical Chemistry A* **118,** 5238–5247 (2014).
79. Sibbett, W. & Taylor, J. Passive Mode-Locking of the Flashlamp Pumped Coumarin 522 Dye Laser. *Optics Communications* **44,** 121–124 (1982).
80. Deutsch, T., Bass, M., Meyer, P. & Protopapa, S. Emission Spectrum of Rhodamine B Dye Lasers. *Applied Physics Letters* **11,** 379–381 (1967).
81. Govindanunny, T. & Sivaram, B. Solvation effects on the tunability of a fluorescein dye laser. *Optics Communications* **32,** 425–428 (1980).
82. Garcia-Moreno, I. *et al.* Structural changes in the BODIPY dye PM567 enhancing the laser action in liquid and solid media. *Advanced Functional Materials* **17,** 3088–3098 (2007).
83. Banuelos Prieto, J., Lopez Arbeloa, F., Martinez Martinez, V., Arbeloa Lopez, T. & Lopez Arbeloa, I. Photophysical properties of the pyrromethene 597 dye: solvent effect. *The Journal of Physical Chemistry A* **108,** 5503–5508 (2004).
84. Brus, L. Electronic wave functions in semiconductor clusters: experiment and theory. *The Journal of Physical Chemistry* **90,** 2555–2560 (1986).
85. Kalyuzhny, G. & Murray, R. W. Ligand effects on optical properties of CdSe nanocrystals. *The Journal of Physical Chemistry B* **109,** 7012–7021 (2005).
86. Mansur, H. S. Quantum dots and nanocomposites. *Wiley Interdisciplinary Reviews: Nanomedicine and Nanobiotechnology* **2,** 113–129 (2010).

87. Wood, S. M., Elston, S. J. & Morris, S. M. Wavelength-tuneable laser emission from a dye-doped achiral nematic liquid crystal dispersed into a chiral polymer scaffold. *Molecular Crystals and Liquid Crystals* **632,** 89–96 (2016).
88. Saliba, M. *et al.* Structured organic–inorganic perovskite toward a distributed feedback laser. *Advanced Materials* **28,** 923–929 (2016).
89. Stranks, S. D. *et al.* Enhanced amplified spontaneous emission in perovskites using a flexible cholesteric liquid crystal reflector. *Nano letters* **15,** 4935–4941 (2015).
90. Akkerman, Q. A. *et al.* Tuning the optical properties of cesium lead halide perovskite nanocrystals by anion exchange reactions. *Journal of the American Chemical Society* **137,** 10276–10281 (2015).
91. Freppon, D. J. *et al.* Photophysical properties of wavelength-tunable methylammonium lead halide perovskite nanocrystals. *Journal of Materials Chemistry C* **5,** 118–126 (2017).
92. Dai, G., Wang, L. & Deng, L. Flexible random laser from dye doped stretchable polymer film containing nematic liquid crystal. *Optical Materials Express* **10,** 68–75 (2020).
93. Varanytsia, A., Nagai, H., Urayama, K. & Palffy-Muhoray, P. Tunable lasing in cholesteric liquid crystal elastomers with accurate measurements of strain. *Scientific reports* **5,** 1–8 (2015).
94. Jeong, S. M. *et al.* Defect mode lasing from a double-layered dye-doped polymeric cholesteric liquid crystal films with a thin rubbed defect layer. *Applied physics letters* **90,** 261108 (2007).
95. Kim, S. W. *et al.* One-dimensional birefringent photonic crystal laser. *Journal of Applied Physics* **103,** 033103 (2008).
96. Matsui, T., Ozaki, R., Funamoto, K., Ozaki, M. & Yoshino, K. Flexible mirrorless laser based on a free-standing film of photopolymerized cholesteric liquid crystal. *Applied physics letters* **81,** 3741–3743 (2002).
97. Peterson, O., Webb, J., McColgin, W. & Eberly, J. Organic dye laser threshold. *Journal of Applied Physics* **42,** 1917–1928 (1971).
98. Watanabe, Y. *et al.* Extremely low threshold in a pyrene-doped distributed feedback cholesteric liquid crystal laser. *Applied Physics Express* **2,** 102501 (2009).
99. Wood, S., Castles, F., Elston, S. & Morris, S. Wavelength-tuneable laser emission from stretchable chiral nematic liquid crystal gels via in situ photopolymerization. *RSC advances* **6,** 31919–31924 (2016).
100. Normand, M. C., Chen, P., Can, C. & Hands, P. J. Overcoming repetition rate limitations in liquid crystal laser systems. *Optics express* **26,** 26544–26555 (2018).
101. Morris, S. M. *et al.* Liquid crystalline chromophores for photonic band-edge laser devices. *Optical Materials* **35,** 837–842 (2013).
102. Yoshida, H., Lee, C. H., Matsuhisa, Y., Fujii, A. & Ozaki, M. Bottom-Up Fabrication of Photonic Defect Structures in Cholesteric Liquid Crystals Based on Laser-Assisted Modification of the Helix. *Advanced Materials* **19,** 1187–1190 (2007).
103. Tomazio, N. B., De Boni, L. & Mendonca, C. R. Low threshold Rhodamine-doped whispering gallery mode microlasers fabricated by direct laser writing. *Scientific Reports* **7,** 1–5 (2017).
104. Grossmann, T. *et al.* Low-threshold conical microcavity dye lasers. *Applied Physics Letters* **97,** 173 (2010).
105. Uchimura, M. *et al.* Development of laser dyes to realize low threshold in dye-doped cholesteric liquid crystal lasers. *Advanced Materials* **22,** 4473–4478 (2010).
106. Morris, S., Ford, A., Pivnenko, M., Hadeler, O. & Coles, H. Correlations between the performance characteristics of a liquid crystal laser and the macroscopic material properties. *Physical Review E* **74,** 061709 (2006).

107. Morris, S. *et al.* The emission characteristics of liquid-crystal lasers. *Journal of the Society for Information Display* **14,** 565–573 (2006).
108. Ford, A., Morris, S., Pivnenko, M., Gillespie, C. & Coles, H. Emission characteristics of a homologous series of bimesogenic liquid-crystal lasers. *Physical Review E* **76,** 051703 (2007).
109. Mavrogordatos, T. K. *et al.* Density of photon states in dye-doped chiral nematic liquid crystal cells in the presence of losses and gain. *Phys. Rev. E* **86,** 011705 (1 July 2012).
110. Mavrogordatos, T. K., Morris, S. M., Wood, S. M., Coles, H. J. & Wilkinson, T. D. Spontaneous emission from radiative chiral nematic liquid crystals at the photonic band-gap edge - An investigation into the role of the density of photon states near resonance. *Phys. Rev. E* **87,** 062504 (6 June 2013).
111. Bransonic. *Ultrasonic Bath 3800* https://bransonic.com/ (2000).
112. ThorLabs. https://thorlabs.com/ (2000).
113. Norland. *Norland UV curable Adhesive NOA 81* https://norlandrod.com/ (2018).
114. Merck. *L Phosphatidylcholine Lecithin* https://sigmaaldrich.com/ (2020).
115. Wilson, M. R. & Earl, D. J. Calculating the helical twisting power of chiral dopants. *J. Mater. Chem.* **11,** 2672–2677 (11 2001).
116. Oiwa, M., Takeda, S., Araya, K., Tomioka, Y. & Mikami, Y. *Liquid crystal display* US Patents 8,848,157. 2011.
117. Ko, S.-W., Huang, S.-H., Fuh, A. Y.-G. & Lin, T.-H. Measurement of helical twisting power based on axially symmetrical photo-aligned dye-doped liquid crystal film. *Optics express* **17,** 15926–15931 (2009).
118. Yu, M. *et al.* Effect of biaxiality on chirality in chiral nematic liquid crystals. *Soft matter* **14,** 6530–6536 (2018).
119. Coles, H., Pivnenko, M. & Hannington, J. *Liquid crystal materials* US Patent 7,623,214. 2009.
120. Toledo, M. *AB104-S Analytical Balance* https://mt.com/ (2005).
121. Habibi, M. & Eslamian, M. Facile and low-cost mechanical techniques for the fabrication of solution-processed polymer and perovskite thin film transistors. *Journal of Physics Communications* **2,** 075018 (2018).
122. Diao, Y., Shaw, L., Bao, Z. & Mannsfeld, S. C. Morphology control strategies for solution-processed organic semiconductor thin films. *Energy & Environmental Science* **7,** 2145–2159 (2014).
123. Pasquarelli, R. M., Ginley, D. S. & O'Hayre, R. Solution processing of transparent conductors: from flask to film. *Chemical Society Reviews* **40,** 5406–5441 (2011).
124. Technologies, A. *Agilent Cary 8454 UV-Vis Spectrophotometer* https://agilent.com (2014).
125. Di Capua, R., Offi, F. & Fontana, F. Check the Lambert–Beer–Bouguer law: a simple trick to boost the confidence of students toward both exponential laws and the discrete approach to experimental physics. *European Journal of Physics* **35,** 045025 (2014).
126. Wu, S.-T., Efron, U. & Hess, L. D. Birefringence measurements of liquid crystals. *Applied optics* **23,** 3911–3915 (1984).
127. Mada, H. & Kobayashi, S. Wavelength and voltage dependences of refractive indices of nematic liquid crystals. *Molecular Crystals and Liquid Crystals* **33,** 47–53 (1976).
128. Olympus. *Polarizing Microscope BX51-P* https://olympus-ims.com/ (2006).
129. QImaging. *Regita R6* https://qimaging.com (2015).

130. Benzie, P. W. & Elston, S. J. *Optics of Liquid Crystals and Liquid Crystal Displays* (eds Chen, J., Cranton, W. & Fihn, M.) 1365–1385 (Springer Berlin Heidelberg, Berlin, Heidelberg, 2012).
131. OceanInsight. https://oceaninsight.com/ (2008).
132. Zeiss. *Zeiss Axioplan 2* https://zeiss.com/ (2002).
133. Ximea. *xiQ USB 3.0* https://ximea.com/ (2014).
134. 6FTSS355-Q4-S. *CryLaS Crystal Laser System GmbH* https://crylas.de (2005).
135. De Araujo, M. A., Silva, R., de Lima, E., Pereira, D. P. & de Oliveira, P. C. Measurement of Gaussian laser beam radius using the knife-edge technique: improvement on data analysis. *Applied optics* **48,** 393–396 (2009).
136. Wright, D., Greve, P., Fleischer, J. & Austin, L. Laser beam width, divergence and beam propagation factor—an international standardization approach. *Optical and quantum electronics* **24,** S993–S1000 (1992).
137. PE9-ES-C. *Ophir* https://ophiropt.com (2014).
138. BLP01-532R-25. *EdgeBasic* https://semrock.com/ (2011).
139. Ohtera, Y., Chiba, T. & Kawakami, S. Liquid crystal rotatable waveplates. *IEEE Photonics Technology Letters* **8,** 390–392 (1996).
140. Love, G. D. Liquid-crystal phase modulator for unpolarized light. *Applied optics* **32,** 2222–2223 (1993).
141. Brown, C. V. in *Handbook of Visual Display Technology* (eds Chen, J., Cranton, W. & Fihn, M.) 1953–1975 (Springer International Publishing, Cham, 2016).
142. Hird, M. *et al.* Synthesis, transition temperatures and optical anisotropy of some isothiocyanato-substituted biphenyls. *J. Mater. Chem.* **3,** 851–859 (8 1993).
143. Hird, M. *et al.* Synthesis, mesomorphic behaviour and optical anisotropy of some novel materials for nematic mixtures of high birefringence. *J. Mater. Chem.* **14,** 1731–1743 (11 2004).
144. Ahmed, Z., Welch, C. & Mehl, G. H. The design and investigation of the self-assembly of dimers with two nematic phases. *RSC Adv.* **5,** 93513–93521 (113 2015).
145. Pardaev, S. A. *et al.* Second harmonic light scattering induced by defects in the twist-bend nematic phase of liquid crystal dimers. *Soft Matter* **12,** 4472–4482 (2016).
146. Mather, P., Broer, D., Bunning, T., Walba, D. & Zentel, R. Advances in Liquid Crystalline Materials and Technologies. *Moleculary Inprinted Materials - Sensors and other Devices* **709,** 161–172 (2002).
147. Schadt, M., Buchecker, R., Villiger, A., Leenhouts, F. & Fromm, J. The cooperative effects of heterocycles, NCS-polar groups, and double bonds on the material properties of new nematic liquid crystals. *IEEE transactions on electron devices* **33,** 1187–1194 (1986).
148. Gauza, S., Wen, C.-H., Tan, B. & Wu, S.-T. UV stable high birefringence liquid crystals. *Japanese journal of applied physics* **43,** 7176 (2004).
149. Cross, G. J. *et al.* Synthesis, transition temperatures, and optical properties of compounds with simple phenyl units linked by double bond, triple bond, ester or propiolate linkages. *J. Mater. Chem.* **10,** 1555–1563 (7 2000).
150. Seed, A. J., Toyne, K. J., Goodby, J. W. & Hird, M. Synthesis, transition temperatures, and optical properties of various 2,6-disubstituted naphthalenes and related 1-benzothiophenes with butylsulfanyl and cyano or isothiocyanato terminal groups. *J. Mater. Chem.* **10,** 2069–2080 (9 2000).
151. Szczuciński, Ł. *et al.* Synthesis, mesogenic and dielectric properties of fluorosubstituted isothiocyanatoterphenyls. *Liquid Crystals* **42,** 1706–1729 (2015).
152. Smith, M. *Organic Synthesis* (Elsevier, 2011).

153. Miyaura, N., Yamada, K. & Suzuki, A. A new stereospecific cross-coupling by the palladium-catalyzed reaction of 1-alkenylboranes with 1-alkenyl or 1-alkynyl halides. *Tetrahedron Letters* **20,** 3437–3440 (1979).
154. Miyaura, N. & Suzuki, A. Stereoselective synthesis of arylated (E)-alkenes by the reaction of alk-1-enylboranes with aryl halides in the presence of palladium catalyst. *J. Chem. Soc., Chem. Commun.* **19,** 866–867 (1979).
155. Miyaura, N., Yano, T. & Suzuki, A. The palladium-catalyzed cross-coupling reaction of 1-alkenylboranes with allylic or benzylic bromides. Convenient syntheses of 1, 4-alkadienes and allybenzenes from alkynes via hydroboration. *Tetrahedron Letters* **21,** 2865–2868 (1980).
156. Miyaura, N., Yanagi, T. & Suzuki, A. The palladium-catalyzed cross-coupling reaction of phenylboronic acid with haloarenes in the presence of bases. *Synthetic Communications* **11,** 513–519 (1981).
157. Miller, D. S., Carlton, R. J., Mushenheim, P. C. & Abbott, N. L. Introduction to optical methods for characterizing liquid crystals at interfaces. *Langmuir* **29,** 3154–3169 (2013).
158. Li, J., Baird, G., Lin, Y.-H., Ren, H. & Wu, S.-T. Refractive-index matching between liquid crystals and photopolymers. *Journal of the Society for Information Display* **13,** 1017–1026 (2005).
159. Li, J. & Wu, S.-T. Two-coefficient Cauchy model for low birefringence liquid crystals. *Journal of applied physics* **96,** 170–174 (2004).
160. Tkachenko, V. *et al.* Nematic liquid crystal optical dispersion in the visible-near infrared range. *Molecular Crystals and Liquid Crystals* **454,** 263–665 (2006).
161. Fréedericksz, V. & Zolina, V. Forces causing the orientation of an anisotropic liquid. *Trans. Faraday Soc.* **29,** 919–930 (140 1933).
162. Ewings, R., Kischka, C., Parry-Jones, L. & Elston, S. Measurement of the difference in flexoelectric coefficients of nematic liquid crystals using a twisted nematic geometry. *Physical Review E* **73,** 011713 (2006).
163. Bradshaw, M., Raynes, E., Bunning, J. & Faber, T. The Frank constants of some nematic liquid crystals. *Journal de Physique* **46,** 1513–1520 (1985).
164. Babakhanova, G. *et al.* Elastic and viscous properties of the nematic dimer CB7CB. *Physical Review E* **96,** 062704 (2017).
165. Basu, R. & Iannacchione, G. S. Orientational coupling enhancement in a carbon nanotube dispersed liquid crystal. *Physical Review E* **81,** 051705 (2010).
166. Kempaiah, R., Liu, Y., Nie, Z. & Basu, R. Giant soft-memory in liquid crystal nanocomposites. *Applied Physics Letters* **108,** 083105 (2016).
167. Frank, F. C. I. Liquid crystals. On the theory of liquid crystals. *Discuss. Faraday Soc.* **25,** 19–28 (0 1958).
168. Oseen, C. W. The theory of liquid crystals. *Discussion of Faraday Society* **29,** 883–899 (1933).
169. Meyer, R. B. Piezoelectric effects in liquid crystals. *Physical Review Letters* **22,** 918 (1969).
170. Harden, J. *et al.* Giant Flexoelectricity of Bent-Core Nematic Liquid Crystals. *Phys. Rev. Lett.* **97,** 157802 (15 Oct. 2006).
171. Varanytsia, A. & Chien, L.-C. Giant flexoelectro-optic effect with liquid crystal dimer CB7CB. *Scientific reports* **7,** 1–7 (2017).
172. Schmidt, D., Schadt, M. & Helfrich, W. Liquid-crystalline curvature electricity: the bending mode of MBBA. *Zeitschrift Für Naturforschung A* **27,** 277–280 (1972).
173. Balachandran, R., Panov, V. P., Vij, J. K., Lehmann, A. & Tschierske, C. Effect of cybotactic clusters on the elastic and flexoelectric properties of bent-core liquid

crystals belonging to the same homologous series. *Phys. Rev. E* **88,** 032503 (3 Sept. 2013).
174. Patel, J. & Meyer, R. B. Flexoelectric electro-optics of a cholesteric liquid crystal. *Physical review letters* **58,** 1538 (1987).
175. Patel, J. & Lee, S.-D. Fast linear electro-optic effect based on cholesteric liquid crystals. *Journal of applied physics* **66,** 1879–1881 (1989).
176. Wild, J. *et al.* Synthesis and investigation of nematic liquid crystals with flexoelectric properties. *Chemistry of materials* **17,** 6354–6360 (2005).
177. Tidey, E., Parry-Jones, L. & Elston, S. Determination of the difference of flexoelectric coefficients in a nematic liquid crystal using a conoscopic technique. *Liquid Crystals* **34,** 251–255 (2007).
178. Kischka, C., Parry-Jones, L. A., Elston, S. J. & Raynes, E. P. Measurement of the Flexoelectric Coefficients e 1 and e 3 in Nematic Liquid Crystals. *Molecular Crystals and Liquid Crystals* **480,** 103–110 (2008).
179. Salter, P., Kischka, C., Elston, S. & Raynes, E. The influence of chirality on the difference in flexoelectric coefficients investigated in uniform lying helix, Grandjean and twisted nematic structures. *Liquid crystals* **36,** 1355–1364 (2009).
180. Castles, F., Green, S., Gardiner, D., Morris, S. & Coles, H. Flexoelectric coefficient measurements in the nematic liquid crystal phase of 5CB. *Aip Advances* **2,** 022137 (2012).
181. Albani, J. in *Structure and Dynamics of Macromolecules: Absorption and Fluorescence Studies* (ed Albani, J.) 141–192 (Elsevier Science, Amsterdam, 2004).
182. Fletcher, A., Knipe, R. & Pietrak, M. Laser dye stability. Part 7. Effects of temperature UV filter and solvent purity. *Appl. Phys. B* **27,** 93–97 (1982).
183. Ahmad, M., King, T. A., Ko, D.-K., Cha, B. H. & Lee, J. Performance and photostability of xanthene and pyrromethene laser dyes in sol-gel phases. *Journal of Physics D: Applied Physics* **35,** 1473 (2002).
184. Qi, H. & Hegmann, T. Multiple Alignment Modes for Nematic Liquid Crystals Doped with Alkylthiol-Capped Gold Nanoparticles. *ACS Applied Materials & Interfaces* **1.** PMID: 20355789, 1731–1738 (2009).
185. Urbanski, M. On the impact of nanoparticle doping on the electro-optic response of nematic hosts. *Liquid Crystals Today* **24,** 102–115 (2015).
186. Lee, W.-K. *et al.* CIS–ZnS quantum dots for self-aligned liquid crystal molecules with superior electro-optic properties. *Nanoscale* **5,** 93–199 (2013).
187. Singh, D. P. *et al.* CuInS2/ZnS QD-ferroelectric liquid crystal mixtures for faster electro-optical devices and their energy storage aspects. *Journal of Applied Physics* **123,** 034101 (2018).
188. Roy, A. *et al.* InP/ZnS quantum-dot-dispersed nematic liquid crystal illustrating characteristic birefringence and enhanced electro-optical parameters. *Applied Physics A* **124,** 1–8 (2018).
189. Joshi, T., Ganguly, P., Haranath, D., Singh, S. & Biradar, A. Tuning the photoluminescence of ferroelectric liquid crystal by controlling the size of dopant ZnO quantum dots. *Materials Letters* **114,** 156–158 (2014).
190. Kumar, A. *et al.* Enhancing the photoluminescence of ferroelectric liquid crystal by doping with ZnS quantum dots. *Applied Physics Letters* **100,** 134101 (2012).
191. Vimal, T., Singh, D. P., Agrahari, K., Srivastava, A. & Manohar, R. Analysis of optical properties and mechanism of photoluminescence enhancement of quantum dot-ferroelectric liquid crystal composite. *Photonics Letters of Poland* **8,** 23–25 (2016).
192. Chen, J. *et al.* Perovskite quantum dot lasers. *InfoMat* **2,** 170–183 (2020).

193. Khan, Y. *et al.* Waterproof perovskites: high fluorescence quantum yield and stability from a methylammonium lead bromide/formate mixture in water. *Journal of Materials Chemistry C* **8,** 5873–5881 (2020).
194. Protesescu, L. *et al.* Nanocrystals of cesium lead halide perovskites ($CsPbX_3$, X= Cl, Br, and I): novel optoelectronic materials showing bright emission with wide color gamut. *Nano letters* **15,** 3692–3696 (2015).
195. Maes, J. *et al.* Light absorption coefficient of $CsPbBr_3$ perovskite nanocrystals. *The journal of physical chemistry letters* **9,** 3093–3097 (2018).
196. Wei, Q. *et al.* Recent progress in metal halide perovskite micro-and nanolasers. *Advanced Optical Materials* **7,** 1900080 (2019).
197. Dong, H., Zhang, C., Liu, X., Yao, J. & Zhao, Y. S. Materials chemistry and engineering in metal halide perovskite lasers. *Chemical Society Reviews* **49,** 951–982 (2020).
198. Stylianakis, M. M., Maksudov, T., Panagiotopoulos, A., Kakavelakis, G. & Petridis, K. Inorganic and hybrid perovskite based laser devices: a review. *Materials* **12,** 859 (2019).
199. Zhang, Q. *et al.* High-quality whispering-gallery-mode lasing from cesium lead halide perovskite nanoplatelets. *Advanced Functional Materials* **26,** 6238–6245 (2016).
200. Park, K. *et al.* Light–matter interactions in cesium lead halide perovskite nanowire lasers. *The journal of physical chemistry letters* **7,** 3703–3710 (2016).
201. Yakunin, S. *et al.* Low-threshold amplified spontaneous emission and lasing from colloidal nanocrystals of caesium lead halide perovskites. *Nature communications* **6,** 1–9 (2015).
202. Sun, W., Wang, K., Gu, Z., Xiao, S. & Song, Q. Tunable perovskite microdisk lasers. *Nanoscale* **8,** 8717–8721 (2016).
203. Chen, L.-J. *et al.* Wavelength-Tunable and Highly Stable Perovskite-Quantum-Dot-Doped Lasers with Liquid Crystal Lasing Cavities. *ACS applied materials & interfaces* **10,** 33307–33315 (2018).
204. Mirzaei, J., Reznikov, M. & Hegmann, T. Quantum dots as liquid crystal dopants. *Journal of Materials Chemistry* **22,** 22350–22365 (2012).
205. Rodarte, A. L., Pandolfi, R. J., Ghosh, S. & Hirst, L. S. Quantum dot/liquid crystal composite materials: self-assembly driven by liquid crystal phase transition templating. *Journal of Materials Chemistry C* **1,** 5527–5532 (2013).
206. Kinkead, B. & Hegmann, T. Effects of size, capping agent, and concentration of CdSe and CdTe quantum dots doped into a nematic liquid crystal on the optical and electro-optic properties of the final colloidal liquid crystal mixture. *Journal of Materials Chemistry* **20,** 448–458 (2010).
207. Mirzaei, J., Urbanski, M., Yu, K., Kitzerow, H.-S. & Hegmann, T. Nanocomposites of a nematic liquid crystal doped with magic-sized CdSe quantum dots. *Journal of Materials Chemistry* **21,** 12710–12716 (2011).
208. Kumar, S. & Sagar, L. K. CdSe quantum dots in a columnar matrix. *Chemical Communications* **47,** 12182–12184 (2011).
209. Konshina, E., Gavrish, E., Orlova, A. & Artem'ev, M. Effect of dispersed CdSe/ZnS quantum dots on optical and electrical characteristics of nematic liquid crystal cells. *Technical Physics Letters* **37,** 1011–1014 (2011).
210. Singh, G., Fisch, M. R. & Kumar, S. *Electrically tunable photoluminescence of semiconducting quantum dots doped nematic liquid crystal nanocomposites* in *AIP Conference Proceedings* **1953** (2018), 060042.
211. Zhou, P., Li, Y., Liu, S. & Su, Y. Colour 3D holographic display based on a quantum-dot-doped liquid crystal. *Liquid Crystals* **46,** 1478–1484 (2019).
212. Hirst, L. S., Kirchhoff, J., Inman, R. & Ghosh, S. *Quantum dot self-assembly in liquid crystal media* in *Emerging Liquid Crystal Technologies V* **7618** (2010), 76180F.

213. Rodarte, A. L., Cisneros, F., Hein, J. E., Ghosh, S. & Hirst, L. S. *Quantum dot/liquid crystal nanocomposites in photonic devices* in *Photonics* **2** (2015), 855–864.
214. Schlaus, A. P. *et al.* How lasing happens in $CsPbBr_3$ perovskite nanowires. *Nature communications* **10,** 1–8 (2019).
215. Chen, D. & Chen, X. Luminescent perovskite quantum dots: synthesis, microstructures, optical properties and applications. *Journal of Materials Chemistry C* **7,** 1413–1446 (2019).
216. Wang, Y., Ding, G., Mao, J.-Y., Zhou, Y. & Han, S.-T. Recent advances in synthesis and application of perovskite quantum dot based composites for photonics, electronics and sensors. *Science and Technology of Advanced Materials* **21,** 278–302 (2020).
217. Rao, C. in *Encyclopedia of Physical Science and Technology (Third Edition)* (ed Meyers, R. A.) Third Edition, 707–714 (Academic Press, New York, 2003).
218. Green, M. A. *et al.* Solar cell efficiency tables (version 56). *Progress in Photovoltaics: Research and Applications* **28,** 629–638 (2020).
219. Van Le, Q., Jang, H. W. & Kim, S. Y. Recent advances toward high-efficiency halide perovskite light-emitting diodes: review and perspective. *Small Methods* **2,** 1700419 (2018).
220. Wang, K., Wang, S., Xiao, S. & Song, Q. Recent advances in perovskite micro-and nanolasers. *Advanced Optical Materials* **6,** 1800278 (2018).
221. Liu, Z., Huang, S., Du, J., Wang, C. & Leng, Y. Advances in inorganic and hybrid perovskites for miniaturized lasers. *Nanophotonics* **1** (2020).
222. Pourdavoud, N. *et al.* Room-Temperature Stimulated Emission and Lasing in Recrystallized Cesium Lead Bromide Perovskite Thin Films. *Advanced Materials* **31,** 1903717 (2019).
223. Tian, X. *et al.* Femtosecond Laser Direct Writing of Perovskite Patterns with Whispering Gallery Mode Lasing. *Journal of Materials Chemistry C* (2020).
224. Zhang, Q., Ha, S. T., Liu, X., Sum, T. C. & Xiong, Q. Room-temperature near-infrared high-Q perovskite whispering-gallery planar nanolasers. *Nano letters* **14,** 5995–6001 (2014).
225. Zhu, H. *et al.* Lead halide perovskite nanowire lasers with low lasing thresholds and high quality factors. *Nature materials* **14,** 636–642 (2015).
226. Zhang, N. *et al.* All-optical control of lead halide perovskite microlasers. *Nature communications* **10,** 1–7 (2019).
227. Chen, J., Messing, M. E., Zheng, K. & Pullerits, T. Cation-dependent hot carrier cooling in halide perovskite nanocrystals. *Journal of the American Chemical Society* **141,** 3532–3540 (2019).
228. Lim, J. W. M. *et al.* Hot Carriers in Halide Perovskites: How Hot Truly? *The Journal of Physical Chemistry Letters* **11,** 2743–2750 (2020).
229. Sun, S., Yuan, D., Xu, Y., Wang, A. & Deng, Z. Ligand-mediated synthesis of shape-controlled cesium lead halide perovskite nanocrystals via reprecipitation process at room temperature. *ACS nano* **10,** 3648–3657 (2016).
230. Zhang, F. *et al.* Brightly luminescent and color-tunable colloidal $CH_3NH_3PbX_3$ (X= Br, I, Cl) quantum dots: potential alternatives for display technology. *ACS nano* **9,** 4533–4542 (2015).
231. Tsiwah, E. A. *et al.* One-pot scalable synthesis of all-inorganic perovskite nanocrystals with tunable morphology, composition and photoluminescence. *CrystEngComm* **19,** 7041–7049 (2017).
232. Yuan, Z., Shu, Y., Tian, Y., Xin, Y. & Ma, B. A facile one-pot synthesis of deep blue luminescent lead bromide perovskite microdisks. *Chemical Communications* **51,** 16385–16388 (2015).

233. Li, G. *et al.* Highly efficient perovskite nanocrystal light-emitting diodes enabled by a universal crosslinking method. *Advanced materials* **28,** 3528–3534 (2016).
234. Han, T.-H. *et al.* Perovskite-polymer composite cross-linker approach for highly-stable and efficient perovskite solar cells. *Nature communications* **10,** 1–10 (2019).
235. Kim, Y.-H., Cho, H. & Lee, T.-W. Metal halide perovskite light emitters. *Proceedings of the National Academy of Sciences* **113,** 11694–11702 (2016).
236. Mashford, B. S. *et al.* High-efficiency quantum-dot light-emitting devices with enhanced charge injection. *Nature photonics* **7,** 407–412 (2013).
237. Dai, X. *et al.* Solution-processed, high-performance light-emitting diodes based on quantum dots. *Nature* **515,** 96–99 (2014).
238. Singh, M., Goyal, M. & Devlal, K. Size and shape effects on the band gap of semiconductor compound nanomaterials. *Journal of Taibah University for Science* **12,** 470–475 (2018).
239. Wright, A. D. *et al.* Electron–phonon coupling in hybrid lead halide perovskites. *Nature communications* **7,** 1–9 (2016).
240. Wolff, C. M., Caprioglio, P., Stolterfoht, M. & Neher, D. Nonradiative recombination in perovskite solar cells: the role of interfaces. *Advanced Materials* **31,** 1902762 (2019).
241. Motta, C., El-Mellouhi, F. & Sanvito, S. Charge carrier mobility in hybrid halide perovskites. *Scientific reports* **5,** 1–8 (2015).
242. Sutter-Fella, C. M. *et al.* High photoluminescence quantum yield in band gap tunable bromide containing mixed halide perovskites. *Nano letters* **16,** 800–806 (2016).
243. La-Placa, M.-G. *et al.* Photoluminescence quantum yield exceeding 80% in low dimensional perovskite thin-films via passivation control. *Chemical Communications* **53,** 8707–8710 (2017).
244. Xiao, Z. *et al.* Efficient perovskite light-emitting diodes featuring nanometre-sized crystallites. *Nature Photonics* **11,** 108–115 (2017).
245. Gunnarsson, W. B. & Rand, B. P. Electrically driven lasing in metal halide perovskites: Challenges and outlook. *APL Materials* **8,** 030902 (2020).
246. Peng, Y., Jing, G. & Cui, T. A hybrid physical–chemical deposition process at ultra-low temperatures for high-performance perovskite solar cells. *Journal of Materials Chemistry A* **3,** 12436–12442 (2015).
247. Huang, H. *et al.* Colloidal lead halide perovskite nanocrystals: synthesis, optical properties and applications. *NPG Asia Materials* **8,** e328–e328 (2016).
248. Song, J. *et al.* Quantum dot light-emitting diodes based on inorganic perovskite cesium lead halides ($CsPbX_3$). *Advanced materials* **27,** 7162–7167 (2015).
249. Hassan, Y. *et al.* Facile synthesis of stable and highly luminescent methylammonium lead halide nanocrystals for efficient light emitting devices. *Journal of the American Chemical Society* **141,** 1269–1279 (2019).
250. Feng, A. *et al.* Shape Control of Metal Halide Perovskite Single Crystals: From Bulk to Nanoscale. *Chemistry of Materials* **32,** 7602–7617 (2020).
251. Supreet & Singh, G. Recent advances on cadmium free quantum dots-liquid crystal nanocomposites. *Applied Materials Today* **21,** 100840 (2020).
252. Bondarev, S., Knyukshto, V., Stepuro, V., Stupak, A. & Turban, A. Fluorescence and electronic structure of the laser dye DCM in solutions and in polymethylmethacrylate. *Journal of Applied Spectroscopy* **71,** 194–201 (2004).
253. Mowatt, C. *et al.* Comparison of the performance of photonic band-edge liquid crystal lasers using different dyes as the gain medium. *Journal of Applied Physics* **107,** 043101 (2010).
254. Yuan, G. *et al.* The degradation and blinking of single $CsPbI_3$ perovskite quantum dots. *The Journal of Physical Chemistry C* **122,** 13407–13415 (2017).

255. Hirst, L. S., Kirchhoff, J., Inman, R. & Ghosh, S. *Quantum dot self-assembly in liquid crystal media* in *Emerging Liquid Crystal Technologies V* **7618** (2010), 76180F.
256. Evans, J., Wang, N., Khoo, I. C. & He, S. *Self-assembly in chiral nematic liquid crystal* in *Liquid Crystals XXI* **10361** (2017), 1036103.
257. Rodarte, A. L., Cisneros, F., Hein, J. E., Ghosh, S. & Hirst, L. S. *Quantum dot/liquid crystal nanocomposites in photonic devices* in *Photonics* **2** (2015), 855–864.
258. Painter, O. *et al.* Two-dimensional photonic band-gap defect mode laser. *Science* **284,** 1819–1821 (1999).
259. Mawst, L. *et al. Leaky defect modes of two-dimensional VCSEL arrays* in *Vertical-Cavity Surface-Emitting Lasers X* **6132** (2006), 61320G.
260. Evans, J. S., Ackerman, P. J., Broer, D. J., van de Lagemaat, J. & Smalyukh, I. I. Optical generation, templating, and polymerization of three-dimensional arrays of liquid-crystal defects decorated by plasmonic nanoparticles. *Physical Review E* **87,** 032503 (2013).
261. Zhong, K. *et al.* Defect mode passband lasing in self-assembled photonic crystal. *Acs Photonics* **3,** 2330–2337 (2016).
262. Li, M., Lai, X., Li, C. & Song, Y. Recent advantages of colloidal photonic crystals and their applications for luminescence enhancement. *Materials Today Nano* **6,** 100039 (2019).
263. Gao, S. *et al.* Coupling of Defect Modes in Cholesteric Liquid Crystals Separated by Isotropic Polymeric Layers. *Polymers* **10,** 805 (2018).
264. Gevorgyan, A. & Oganesyan, K. Lasing in cholesteric liquid crystal cells with an isotropic defect layer inside. *Laser Physics Letters* **12,** 125805 (2015).
265. Ilchishin, I., Tikhonov, E. & Mykytiuk, T. Narrowing the oscillation spectra of a cholesteric liquid crystal laser. *Molecular Crystals and Liquid Crystals* **670,** 112–118 (2018).
266. Yang, Y.-C. *et al.* Photonic defect modes of cholesteric liquid crystals. *Physical Review E* **60,** 6852 (1999).
267. Grzelczyk, D. & Awrejcewicz, J. *Reflectivity of Cholesteric Liquid Crystals with an Anisotropic Defect Layer Inside* in *Photonics* **7** (2020), 58.
268. Kopp, V. I., Shibaev, P. V., Bose, R. & Genack, A. Z. *Anisotropic photonic-bandgap structures* in *Photonic Bandgap Materials and Devices* **4655** (2002), 141–149.
269. Ozaki, R. *et al.* Defect mode in cholesteric liquid crystal consisting of two helicoidal periodicities. *Japanese journal of applied physics* **45,** 493 (2006).
270. Kopp, V. I. & Genack, A. Z. Twist defect in chiral photonic structures. *Physical review letters* **89,** 033901 (2002).
271. Wang, F. & Lakhtakia, A. Optical crossover phenomenon due to a central 90°-twist defect in a chiral sculptured thin film or chiral liquid crystal. *Proceedings of the Royal Society A: Mathematical, Physical and Engineering Sciences* **461,** 2985–3004 (2005).
272. Geiregat, P., Van Thourhout, D. & Hens, Z. A bright future for colloidal quantum dot lasers. *NPG Asia Materials* **11,** 1–8 (2019).
273. Roh, J., Park, Y.-S., Lim, J. & Klimov, V. I. Optically pumped colloidal-quantum-dot lasing in LED-like devices with an integrated optical cavity. *Nature communications* **11,** 1–10 (2020).
274. Reithmaier, J. P. & Eisenstein, G. *1.5 µm quantum dot lasers for data and telecom applications* in *2016 Compound Semiconductor Week (CSW) [Includes 28th International Conference on Indium Phosphide Related Materials (IPRM) 43rd International Symposium on Compound Semiconductors (ISCS)* (2016), 1–2.
275. Huang, H. *et al.* Epitaxial quantum dot lasers on silicon with high thermal stability and strong resistance to optical feedback. *APL Photonics* **5,** 016103 (2020).

276. Stylianakis, M. M., Maksudov, T., Panagiotopoulos, A., Kakavelakis, G. & Petridis, K. Inorganic and hybrid perovskite based laser devices: a review. *Materials* **12,** 859 (2019).
277. Deschler, F. *et al.* High photoluminescence efficiency and optically pumped lasing in solution-processed mixed halide perovskite semiconductors. *The journal of physical chemistry letters* **5,** 1421–1426 (2014).
278. Sutherland, B. R., Hoogland, S., Adachi, M. M., Wong, C. T. & Sargent, E. H. Conformal organohalide perovskites enable lasing on spherical resonators. *ACS nano* **8,** 10947–10952 (2014).
279. Dhanker, R. *et al.* Random lasing in organo-lead halide perovskite microcrystal networks. *Applied Physics Letters* **105,** 151112 (2014).
280. Wang, Y., Li, X., Nalla, V., Zeng, H. & Sun, H. Solution-processed low threshold vertical cavity surface emitting lasers from all-inorganic perovskite nanocrystals. *Advanced Functional Materials* **27,** 1605088 (2017).
281. Tang, X. *et al.* Room temperature single-photon emission and lasing for all-inorganic colloidal perovskite quantum dots. *Nano Energy* **28,** 462–468 (2016).
282. Takanishi, Y., Ohtsuka, Y., Suzaki, G., Nishimura, S. & Takezoe, H. Low threshold lasing from dye-doped cholesteric liquid crystal multi-layered structures. *Optics Express* **18,** 12909–12914 (2010).
283. Park, J. R. *et al.* Numerical modeling and simulation of a cholesteric liquid crystal polarizer. *Optical review* **9,** 207–212 (2002).
284. Schmidtke, J., Stille, W. & Finkelmann, H. Defect mode emission of a dye doped cholesteric polymer network. *Physical review letters* **90,** 083902 (2003).
285. Gevorgyan, A. H. & Harutyunyan, M. Z. Chiral photonic crystals with an anisotropic defect layer. *Phys. Rev. E* **76,** 031701 (3 Sept. 2007).
286. Chen, Q. *et al.* Planar heterojunction perovskite solar cells via vapor-assisted solution process. *Journal of the American Chemical Society* **136,** 622–625 (2014).
287. Ávila, J., Momblona, C., Boix, P. P., Sessolo, M. & Bolink, H. J. Vapor-deposited perovskites: the route to high-performance solar cell production? *Joule* **1,** 431–442 (2017).
288. Zhou, H., Chen, Q. & Yang, Y. Vapor-assisted solution process for perovskite materials and solar cells. *MRS Bulletin* **40,** 667 (2015).
289. De Giorgi, M. L. & Anni, M. Amplified spontaneous emission and lasing in lead halide perovskites: state of the art and perspectives. *Applied Sciences* **9,** 4591 (2019).
290. Ngo, T. T. *et al.* Enhancement of the performance of perovskite solar cells, LEDs, and optical amplifiers by anti-solvent additive deposition. *Advanced Materials* **29,** 1604056 (2017).
291. Yu, J. C. *et al.* Enhancing the Performance and Stability of Perovskite Nanocrystal Light-Emitting Diodes with a Polymer Matrix. *Advanced Materials Technologies* **2,** 1700003 (2017).
292. Yang, D.-K. & Wu, S.-T. *Fundamentals of liquid crystal devices* (John Wiley & Sons, 2014).
293. Littman, M. G. & Wang, X. in *Atomic, Molecular, and Optical Physics: Electromagnetic Radiation* (eds Dunning, F. & Hulet, R. G.) 137–169 (Academic Press, 1997).
294. Vojnovic, I., Winkelmeier, J. & Endesfelder, U. Visualizing the inner life of microbes: practices of multi-color single-molecule localization microscopy in microbiology. *Biochemical Society Transactions* **47,** 1041–1065 (2019).
295. Jitsui, Y. & Ohtani, N. Fabrication of near-infrared polymer light-emitting-diodes using dispersed laser dye. *Journal of the Korean Physical Society* **60,** 1557–1559 (2012).
296. Mulder, C. L. *et al.* Dye alignment in luminescent solar concentrators: I. Vertical alignment for improved waveguide coupling. *Optics Express* **18,** A79–A90 (2010).

297. Chandrahalim, H. & Fan, X. Reconfigurable solid-state dye-doped polymer ring resonator lasers. *Scientific reports* **5,** 1–8 (2015).
298. Bornemann, R., Lemmer, U. & Thiel, E. Continuous-wave solid-state dye laser. *Optics letters* **31,** 1669–1671 (2006).
299. Gromov, D. *et al.* Efficient plastic-host dye lasers. *JOSA B* **2,** 1028–1031 (1985).
300. Poelma, C., Westerweel, J. & Ooms, G. Turbulence statistics from optical whole-field measurements in particle-laden turbulence. *Experiments in Fluids* **40,** 347–363 (2006).
301. Wurthner, F., Kaiser, T. E. & Saha-Moller, C. R. J-aggregates: from serendipitous discovery to supramolecular engineering of functional dye materials. *Angewandte Chemie International Edition* **50,** 3376–3410 (2011).
302. Prieto-Montero, R. *et al.* Methylthio BODIPY as a standard triplet photosensitizer for singlet oxygen production: a photophysical study. *Physical Chemistry Chemical Physics* **21,** 20403–20414 (2019).
303. Krammer, S. M. M. *Dye-Doped Polymeric Lasers for Sensing Applications* PhD thesis (Universitat Karlsruhe, 2016).
304. Gupta, M., Kamble, P., Rath, M., Naik, D. & Ray, A. K. High laser efficiency and photostability of pyrromethene dyes mediated by nonpolar solvent. *Applied optics* **54,** 7013–7019 (2015).
305. Al-Aqmar, D. M., Abdelkader, H. & Abou Kana, M. T. Optical, photo-physical properties and photostability of pyrromethene (PM-597) in ionic liquids as benign green-solvents. *Journal of Luminescence* **161,** 221–228 (2015).
306. López Arbeloa, F., López Arbeloa, T. & López Arbeloa, I. in *Handbook of Advanced Electronic and Photonic Materials and Devices* (ed Singh Nalwa, H.) 209–245 (Academic Press, Burlington, 2001).
307. Perez-Ojeda, M. E. *et al.* Highly efficient and photostable photonic materials from diiodinated BODIPY laser dyes. *Optical Materials Express* **1,** 243–251 (2011).
308. Alvarez, M. *et al.* Linear and cross-linked polymeric solid-state dye lasers based on 8-substituted alkyl analogues of pyrromethene 567. *Applied Physics B* **80,** 993–1006 (2005).
309. Zhu, M., Chen, Y., Guo, H., Yang, F. & Song, X. Perylene liquid crystals with multiple alkyl chains: investigation of the influence of peripheral alkyl chain number on mesomorphic and photophysical properties. *New Journal of Chemistry* **42,** 8998–9005 (2018).
310. Shirvani-Mahdavi, H. & Ebrahimi-Azandariani, S. Effect of combined laser dyes on the efficiency of cholesteric liquid crystal lasers. *Journal of Theoretical and Applied Physics* **13,** 7–15 (2019).
311. Wu, R. *et al.* Random lasing in dye-doped chiral nematic liquid crystal. *Optik* **202,** 163616 (2020).
312. Costela, A., Garcia-Moreno, I. & Sastre, R. Polymeric solid-state dye lasers: Recent developments. *Physical Chemistry Chemical Physics* **5,** 4745–4763 (2003).
313. Zhang, H. *et al.* Azobenzene Sulphonic Dye Photoalignment as a Means to Fabricate Liquid Crystalline Conjugated Polymer Chain-Orientation-Based Optical Structures. *Advanced Optical Materials* **8,** 1901958 (2020).
314. Kopp, V., Fan, B., Vithana, H. & Genack, A. Low-threshold lasing at the edge of a photonic stop band in cholesteric liquid crystals. *Optics letters* **23,** 1707–1709 (1998).
315. Song, M. H. *et al.* Polarization characteristics of phase retardation defect mode lasing in polymeric cholesteric liquid crystals. *Science and technology of Advanced Materials* **5,** 437 (2004).
316. PMMA, N. & Copolymer. *MicroChem* https://kayakuam.com/wp-content/uploads/2019/09/PMMA_Data_Sheet.pdf (2019).

317. Ilchishin, I., Tikhonov, E. & Mykytiuk, T. Dye-doped CLC-lasers: Interdependence of spectral and angular characteristics and boundary conditions of the active layer. *Molecular Crystals and Liquid Crystals* **639,** 47–54 (2016).
318. Inoue, Y., Yoshida, H., Inoue, K., Fujii, A. & Ozaki, M. Improved lasing threshold of cholesteric liquid crystal lasers with in-plane helix alignment. *Applied Physics Express* **3,** 102702 (2010).
319. Stockley, J. E., Sharp, G. D. & Johnson, K. M. Fabry–Perot etalon with polymer cholesteric liquid-crystal mirrors. *Optics letters* **24,** 55–57 (1999).
320. Gevorgyan, A. Effects of angle of incidence and polarization in the chiral photonic crystals. *Optics and Spectroscopy* **105,** 624–632 (2008).
321. Dmitrienko, V. & Belyakov, V. Highest orders of selective reflections of light by cholisteric liquid-crystals. *Fizika Tverdogo Tele* **15,** 3540–3543 (1973).
322. Takezoe, H., Ouchi, Y., Hara, M., Fukuda, A. & Kuze, E. Experimental studies on reflection spectra in monodomain cholesteric liquid crystal cells: total reflection, subsidiary oscillation and its beat or swell structure. *Japanese journal of applied physics* **22,** 1080 (1983).
323. Takezoe, H. *et al.* Experimental observation of the total reflection by a monodomain cholesteric liquid crystal. *Japanese Journal of Applied Physics* **21,** L390 (1982).
324. Harutyunyan, M., Gevorgyan, A. & Mkhitaryan, S. Influence of dielectric boundaries, angle of incidence, and polarization of light on the optical properties of chiral photonic crystals. *Journal of Contemporary Physics (Armenian Academy of Sciences)* **42,** 271–276 (2007).
325. Takezoe, H., Ouchi, Y., Hara, M., Fukuda, A. & Kuze, E. A tunable 90° rotator using a total reflection by a monodomain cholesteric liquid crystal cell. *Japanese journal of applied physics* **22,** L185 (1983).
326. Huang, Y. *et al.* Incident angle and polarization effects on the dye-doped cholesteric liquid crystal laser. *Optics Communications* **261,** 91–96 (2006).
327. Shin, H. K., Lee, J. H., Kim, J.-W., Yoon, T.-H. & Kim, J. C. Fast polarization switching panel with high brightness and contrast ratio for three-dimensional display. *Applied physics letters* **98,** 063505 (2011).
328. Rahman, B. A., Obayya, S. S. & Somasiri, N. *Polarization issues in optoelectronic devices and systems* in *Physics and Simulation of Optoelectronic Devices XI* **4986** (2003), 363–374.
329. VanWiggeren, G. D. & Roy, R. Transmission of linearly polarized light through a single-mode fiber with random fluctuations of birefringence. *Applied optics* **38,** 3888–3892 (1999).
330. Clarke, D. & Grainger, J. in *Polarized Light and Optical Measurement* (eds Clarke, D. & Grainger, J.) 155–172 (Pergamon, 1971).
331. Kaminow, I. Polarization in optical fibers. *IEEE Journal of Quantum Electronics* **17,** 15–22 (1981).
332. Hickman, D. L., Smith, M. I., Kim, K. S. & Choi, H.-J. *Polarimetric imaging: system architectures and trade-offs* in *Electro-Optical and Infrared Systems: Technology and Applications XV* **10795** (2018), 107950B.
333. Cheng, F. *et al.* Polarization-switchable holograms based on efficient, broadband multifunctional metasurfaces in the visible regime. *Optics express* **26,** 30678–30688 (2018).
334. Iizuka, K. *3D microscope* in *Three-Dimensional and Multidimensional Microscopy: Image Acquisition and Processing XV* (eds Conchello, J.-A., Cogswell, C. J., Wilson, T. & Brown, T. G.) **6861** (SPIE, 2008), 227–237.

335. Chen, H., Weng, Y., Xu, D., Tabiryan, N. V. & Wu, S.-T. Beam steering for virtual/augmented reality displays with a cycloidal diffractive waveplate. *Optics express* **24,** 7287–7298 (2016).
336. Hou, Z.-S. *et al.* On-Chip Polarization Rotators. *Advanced Optical Materials* **7,** 1900129 (2019).
337. Ren, H. & Wu, S.-T. Liquid-crystal-based linear polarization rotator. *Applied physics letters* **90,** 121123 (2007).
338. Yang, F., Ruan, L., Jewell, S. & Sambles, J. Polarization rotator using a hybrid aligned nematic liquid crystal cell. *Optics Express* **15,** 4192–4197 (2007).
339. Zhuang, Z., Suh, S.-W. & Patel, J. Polarization controller using nematic liquid crystals. *Optics letters* **24,** 694–696 (1999).
340. Lavrentovich, M., Sergan, T. & Kelly, J. Switchable broadband achromatic half-wave plate with nematic liquid crystals. *Optics letters* **29,** 1411–1413 (2004).
341. Tripathi, U. & Rastogi, V. Liquid crystal-based widely tunable integrated optic wavelength filters. *JOSA B* **36,** 1883–1889 (2019).
342. Wu, S.-T. Design of a liquid crystal based tunable electrooptic filter. *Applied optics* **28,** 48–52 (1989).
343. Raynes, E. in *Reference Module in Materials Science and Materials Engineering* (Elsevier, 2016).
344. Chen, H. & Wu, S.-T. Advanced liquid crystal displays with supreme image qualities. *Liquid Crystals Today* **28,** 4–11 (2019).
345. Zhang, Z., You, Z. & Chu, D. Fundamentals of phase-only liquid crystal on silicon (LCOS) devices. *Light: Science & Applications* **3,** e213 (2014).
346. Ye, C. Construction of an optical rotator using quarter-wave plates and an optical retarder. *Optical Engineering* **34,** 3031–3036 (1995).
347. Davis, J. A., McNamara, D. E., Cottrell, D. M. & Sonehara, T. Two-dimensional polarization encoding with a phase-only liquid-crystal spatial light modulator. *Applied Optics* **39,** 1549–1554 (2000).
348. Chang, L. M., Yin, C. C., Lin, C. Y., Wang, C. T. & Hung, Y. J. Tunable polarizing reflector based on liquid crystal-clad guided-mode resonator. *Liquid Crystals,* 1–6 (2020).
349. Gevorgyan, A., Harutyunyan, M., Oganesyan, K. & Rafayelyan, M. Cholesteric liquid crystals with tunable defect inside as polarization azimuth rotation amplifiers and polarization azimuth stabilizers. *Optik* **123,** 2076–2081 (2012).
350. Gevorgyan, A. & Oganesyan, K. NLC-CLC-NLC cell as an electrically tunable polarization plane rotator. *Journal of Contemporary Physics (Armenian Academy of Sciences)* **45,** 209–214 (2010).
351. Yu, C.-J. & Hsieh, C.-M. Electrically controllable polarization element. *IEEE Photonics Technology Letters* **28,** 1229–1232 (2016).
352. Honma, M., Okitsu, K. & Nose, T. Reflective liquid crystal polarization rotator with ultraviolet-polymerizable liquid crystal retardation film. *Japanese Journal of Applied Physics* **52,** 022501 (2013).
353. Chung, T.-Y., Tsai, M.-C., Liu, C.-K., Li, J.-H. & Cheng, K.-T. Achromatic linear polarization rotators by tandem twisted nematic liquid crystal cells. *Scientific Reports* **8,** 1–13 (2018).
354. Kundikova, N., Popkov, I. & Popkova, A. Composite quarter-wave systems with adjustable parameters. *Applied optics* **49,** 6504–6511 (2010).
355. Safrani, A. & Abdulhalim, I. Liquid-crystal polarization rotator and a tunable polarizer. *Optics letters* **34,** 1801–1803 (2009).
356. Wang, C.-T. & Lin, T.-H. Polarization-tunable chiral nematic liquid crystal lasing. *Journal of Applied Physics* **107,** 123102 (2010).

357. Ozaki, R., Ozaki, M. & Yoshino, K. Electrically rotatable polarizer using one-dimensional photonic crystal with a nematic liquid crystal defect layer. *Crystals* **5,** 394–404 (2015).
358. Oh-e, M. In-plane switching electro-optical effect of nematic liquid crystals. *Liquid Crystals Today* **10,** 6–10 (2001).
359. Meyer, C., Luckhurst, G. & Dozov, I. The temperature dependence of the heliconical tilt angle in the twist-bend nematic phase of the odd dimer CB7CB. *Journal of Materials Chemistry C* **3,** 318–328 (2015).